

# Dipole-strength distributions below the giant dipole resonance in $^{92}\text{Mo}$ , $^{98}\text{Mo}$ and $^{100}\text{Mo}$

Gencho Yordanov Rusev

August 2007

Wissenschaftlich-Technische Berichte  
**FZD-478**  
August 2007

Gencho Yordanov Rusev

**Dipole-strength distributions below  
the giant dipole resonance in  
<sup>92</sup>Mo, <sup>98</sup>Mo and <sup>100</sup>Mo**

Bibliothek D 120



100102608



**Forschungszentrum  
Dresden** Rossendorf

Institut für Kern und Teilchenphysik  
Fakultät Mathematik und Naturwissenschaften  
Technische Universität Dresden

---

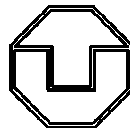
# Dipole-strength distributions below the giant dipole resonance in $^{92}\text{Mo}$ , $^{98}\text{Mo}$ and $^{100}\text{Mo}$

---

Dissertation  
zur Erlangung des  
Doktorgrades der Naturwissenschaften  
(Doctor rerum naturalium)

vorgelegt von  
**Gencho Yordanov Rusev**  
geboren am 23. September 1975 in Veliko Tarnovo, Bulgarien

DRESDEN 2006





# Zusammenfassung

In der vorliegenden Arbeit werden Dipolstärkeverteilungen in  $^{92}\text{Mo}$ ,  $^{98}\text{Mo}$  und  $^{100}\text{Mo}$  mit der Methode der Kernresonanzfluoreszenz untersucht. Die Experimente wurden am Dynamitron Beschleuniger der Universität Stuttgart und am ELBE Beschleuniger des Forschungszentrums Rossendorf durchgeführt. Photonen wurden während des Beschusses metallischer Strahlungskonverter mit Elektronen in Form von Bremsstrahlung erzeugt. Die am Target gestreuten Photonen wurden mit hochreinen Germanium-Detektoren gemessen, die Effektivitäten von 100 % relativ zu einem  $3'' \times 3''$  NaJ Szintillationsdetektor hatten.

Niedrigliegende Dipolanregungen in den Nukliden  $^{92}\text{Mo}$ ,  $^{98}\text{Mo}$  und  $^{100}\text{Mo}$  wurden in Photonenstreuungs-Experimenten am ELBE Beschleuniger bei einer Elektronenenergie von 6 MeV und am Dynamitron bei Elektronenenergien von 3.2 bis 3.8 MeV untersucht. Die Kombination verschiedener Elektronenenergien in den Experimenten zu  $^{98}\text{Mo}$  and  $^{100}\text{Mo}$  ermöglichte die Identifizierung von inelastischen Übergängen zu niedrigliegenden angeregten Zuständen. In diesen Experimenten wurden fünf Zustände mit Spin  $J=1$  im  $^{98}\text{Mo}$  and 14 im  $^{100}\text{Mo}$  im Energiebereich von 2 bis 4 MeV erstmalig beobachtet. Die experimentell gefundenen Anregungsenergien und Übergangsstärken wurden mit Vorhersagen des Schalenmodells und der sogenannten Quasiparticle-Random-Phase-Approximation (QRPA) in einer deformierten Basis verglichen. Letztere zeigen, dass Isektor-Orbital- und Isektor-Spin-Vibrationen etwa gleichermaßen zur magnetischen Dipolstärke ( $M1$ -Stärke) bis 4 MeV beitragen. Die QRPA-Rechnungen reproduzieren das Anwachsen der  $M1$ -Stärke mit wachsender Neutronenzahl. Ein besonderes Merkmal des  $^{98}\text{Mo}$  und des  $^{100}\text{Mo}$  ist die Abregung eines  $J=1$  Zustands sowohl zum  $0^+$  Grundzustand als auch zum ersten angeregten  $0^+$  Zustand. Die Existenz dieser Abregungen weist auf eine Mischung zweier Konfigurationen in den  $0^+$  Zuständen hin, die in Standard-Kernmodellen nicht beschrieben werden kann. Ein von Dr. F. Dönau und Prof. S. Frauendorf entwickeltes Modell erlaubt es, die Mischungskoeffizienten für die zwei in den formisomeren  $0^+$  Zuständen enthaltenen Konfigurationen aus dem experimentellen Verhältnis der Übergangsstärken vom  $J=1$  Zustand zu den zwei  $0^+$  Zuständen zu berechnen. Die Beobachtung der Abregungen zu den zwei  $0^+$  Zuständen liefert in Verbindung mit dem entwickelten Modell eine neue Methode zur Untersuchung der Struktur von  $0^+$  Formisomeren.

Als Bestandteil dieser Arbeit wurden zahlreiche GEANT Simulationsrechnungen durchgeführt, die der Optimierung des experimentellen Aufbaus für die Experimente mit Bremsstrahlung am ELBE Beschleuniger dienen, z.B. beim Entwurf der Kollimatoren und der Abschirmungen für die Germanium-Detektoren, bei der Wahl des Materials für das Strahlrohr und beim Entwurf des Photonen-Strahlfängers. Mit dem nun vorliegenden Aufbau wurde ein Detektionslimit von  $B(E1) \uparrow \approx 0.15 \times 10^{-3} e^2\text{fm}^2$  für die Messungen in dieser Arbeit erreicht. Monte-Carlo-Simulationen wurden ebenfalls in der Auswertung der Daten benutzt, so z.B. zur Bestimmung der Nachweisempfindlichkeiten der Detektoren, des durch einen Strahlhärter aus Aluminium modifizierten Bremsstrahlungsspektrums und zur Bestimmung der Endpunktsenergien aus den mit Si-Detektoren gemessenen Spektren der beim Deuteronenaufbruch emittierten Protonen bzw. aus den mit einem NaJ-Detektor gemessenen Spektren am Target gestreuter Photonen.

Am ELBE Beschleuniger wurden Dipolstärkeverteilungen in den Nukliden  $^{92}\text{Mo}$ ,  $^{98}\text{Mo}$  and  $^{100}\text{Mo}$  bis zu den Neutronenseparationsenergien untersucht. Die Photonenstreuungs-Experimente für die drei Isotope wurden unter gleichen experimentellen Bedingungen bei einer Elektronenenergie von 13.2 MeV

durchgeführt, die oberhalb der Neutronenseparationsenergien liegt. Um mögliche Übergänge in Nachbarkernen zu identifizieren, die über die  $(\gamma, n)$  Reaktion erzeugt wurden, wurden zusätzlich Messungen bei Elektronenenergien unterhalb der Neutronenseparationsenergie, bei 7.8 und 8.4 MeV, für  $^{98}\text{Mo}$  und  $^{100}\text{Mo}$  durchgeführt. Den Isotopen  $^{92}\text{Mo}$ ,  $^{98}\text{Mo}$  und  $^{100}\text{Mo}$  wurden 340, 485 bzw. 499 Übergänge zugeordnet, deren Mehrzahl Dipolübergänge sind. Eine Analyse der statistischen Eigenschaften der Übergänge zeigt, dass die Verteilung der Abstände nächst benachbarter Übergänge einer Wigner-Verteilung entspricht, die das quantenchaotische Verhalten eines Gaußschen orthogonalen Ensembles beschreibt. Die Verteilung der partiellen Breiten der Übergänge entspricht einer Porter-Thomas-Verteilung.

Die Porter-Thomas-Fluktuationen der Niveaubreiten führen dazu, dass bei hohen Energien eine große Zahl der Übergänge nicht als prominente Peaks im Spektrum erscheinen. Die hohe Niveaudichte oberhalb 5 MeV und die endliche Energieauflösung der Detektoren resultiert in einem Kontinuum überlappender Peaks. Ein Vergleich der für  $^{98}\text{Mo}$  und  $^{100}\text{Mo}$  erhaltenen Spektren zeigt, dass nahe der Neutronenseparationsenergie des  $^{98}\text{Mo}$  die Stärke im Kontinuum zweimal größer als die in den diskreten Peaks enthaltene ist. Mit Hilfe von GEANT-Simulationen wurde der nicht-resonante, aus atomaren Prozessen stammende Untergrund in den Spektren bestimmt. Dieser wurde von den Spektren abgezogen. Die resultierenden Kontinuumsspektren enthalten sowohl Grundzustandsübergänge als auch Übergänge zu niedrigliegenden Niveaus und deren Abregungen.

Im Rahmen dieser Arbeit wurde ein Monte-Carlo-Programm entwickelt, das Kaskaden von Gammaübergängen simuliert. Diese Simulationen erlauben es, (i) die Intensitätsverteilung der Grundzustandsübergänge aus dem Kontinuum und damit den Wirkungsquerschnitt für die elastische Streuung zu bestimmen und (ii) die Verzweigungsverhältnisse der Grundzustandsübergänge und damit den Photoabsorptionsquerschnitt abzuleiten. Die resultierenden Absorptionsquerschnitte für  $^{92}\text{Mo}$ ,  $^{98}\text{Mo}$  und  $^{100}\text{Mo}$  schließen glatt an gemessene Wirkungsquerschnitte für die  $(\gamma, n)$  Reaktion an. Das zeigt, dass diese Methode neuartige Informationen über die niederenergetischen Ausläufer der Riesendipolresonanzen unterhalb der Neutronenseparationsenergien erbringt.

Die erhaltenen Dipolstärkeverteilungen für  $^{92}\text{Mo}$ ,  $^{98}\text{Mo}$  und  $^{100}\text{Mo}$  zeigen, dass die Stärke mit der Neutronenzahl steigt. QRPA-Rechnungen in einer deformierten Basis beschreiben diesen Anstieg als eine Folge der ansteigenden Kerndeformation.

# Summary

Investigations of the dipole-strength distributions in  $^{92}\text{Mo}$ ,  $^{98}\text{Mo}$  and  $^{100}\text{Mo}$  were carried out by means of the method of nuclear resonance fluorescence. The experiments included in this work were performed at the Dynamitron accelerator of the Universität Stuttgart and at the ELBE accelerator of the Forschungszentrum Rossendorf. The photon beams were produced by deceleration of electrons in a metallic radiation converter. The photons scattered from the target were measured with high purity germanium detectors with efficiencies of 100 % relative to a  $3'' \times 3''$  NaI scintillation detector.

The low-lying excitations in the nuclides  $^{92}\text{Mo}$ ,  $^{98}\text{Mo}$  and  $^{100}\text{Mo}$  have been studied in photon-scattering experiments at an electron energy of 6 MeV at the ELBE accelerator and at electron energies from 3.2 to 3.8 MeV at the Dynamitron accelerator. Five levels were observed in  $^{92}\text{Mo}$ . Various electron-beam energies were used in the experiments on  $^{98}\text{Mo}$  and  $^{100}\text{Mo}$  in order to resolve branching transitions. Five levels in  $^{98}\text{Mo}$  and 14 in  $^{100}\text{Mo}$  were identified for the first time in the energy range from 2 to 4 MeV. The experimental results are compared with predictions of the shell model and with predictions of the quasiparticle random-phase approximation (QRPA) in a deformed basis. The latter show significant contributions of the isovector-orbital and isovector-spin vibration to the dipole strength below 4 MeV. The QRPA calculations reproduce the growing  $M1$  strength with increasing neutron number.

A specific feature of  $^{98}\text{Mo}$  and  $^{100}\text{Mo}$  is the deexcitation of one state with spin  $J=1$  to the  $0^+$  ground state as well as to the first excited  $0^+$  states, which cannot be explained in standard models. The existence of decay branches from  $J=1$  to the two  $0^+$  states indicates a mixture of the configurations in the two  $0^+$  states. A model developed by Dr. F. Dönau and Prof. S. Frauendorf allowed us to deduce the mixing coefficients for the two  $0^+$  shape-isomeric states from the experimental ratios of the transition strengths from the  $J = 1$  state to the  $0^+$  ground state and to the  $0^+$  excited state. The observation of decay branches to excited  $0^+$  states combined with the present model provides a new means to investigate the structure of  $0^+$  shape isomers.

As part of this work, numerous GEANT simulations were performed in order to optimize the design of the components of the bremsstrahlung facility at the ELBE accelerator and to reduce background radiation. The lead collimators and the lead shields of the detectors were designed by performing GEANT simulations. The photon-beam dump and the material of the photon-beam pipe were optimized to provide less photons scattered to the detectors. A detection sensitivity of  $B(E1) \uparrow \approx 0.15 \times 10^{-3} e^2 \text{fm}^2$  was achieved in the presented photon-scattering experiments. A discussion on the origin of the background in the measured spectrum is presented. Monte Carlo simulations are applied in the analysis of the data for determination of the detector efficiency, the bremsstrahlung spectrum modified by an aluminum hardener and the determination of its end-point energy from spectra of protons emitted during the photodisintegration of the deuteron or the spectra of scattered  $\gamma$ -rays from the target and detected with an NaI detector.

Dipole-strength distributions up to the neutron-separation energies in the nuclides  $^{92}\text{Mo}$ ,  $^{98}\text{Mo}$  and  $^{100}\text{Mo}$  have been investigated at the ELBE accelerator. The photon-scattering experiments were carried out at identical conditions and at an electron energy of 13.2 MeV such that the energy region around the neutron-separation energies in the three nuclides could be studied. Because of the possible observation of transitions in the neighboring nuclei produced via  $(\gamma, n)$  reaction, additional measurements at electron energies of 8.4 and 7.8 MeV, below the neutron-separation energy, were performed

on  $^{98}\text{Mo}$  and  $^{100}\text{Mo}$ , respectively. The number of transitions assigned to  $^{92}\text{Mo}$ ,  $^{98}\text{Mo}$  and  $^{100}\text{Mo}$  is 340, 485 and 499, respectively, the main part of them being dipole transitions. Statistical properties of the observed transitions are obtained. The distributions of the nearest-neighbor spacings and the transition widths do closely resemble Wigner and Porter-Thomas distributions, respectively, indicating a quantum chaotical behavior as predicted for a Gaussian orthogonal ensemble.

Because of the Porter-Thomas fluctuations of the level widths the most of the levels do not appear as prominent peaks in the experimental spectra. Due to the high level density above 5 MeV and the finite resolution of the detectors these weakly populated levels produce a continuum of overlapping peaks. It is shown from a comparison of the spectra of  $^{98}\text{Mo}$  and  $^{100}\text{Mo}$  that close to the neutron-separation energy of  $^{98}\text{Mo}$  the strength in the continuum is two times higher than the strength in the peaks. GEANT simulations were applied to determine the non-resonant background in the measured spectra, i.e. the counts in the spectrum which do not result from deexcitation of nuclear levels, and thus to extract the continuum. The continuum contains the ground-state transitions as well as the branching transitions to the low-lying levels and the subsequent deexcitations of these levels.

In this work, a Monte Carlo code for  $\gamma$ -ray cascade simulations was developed which allows us (i) to deconvolute the intensity distribution of the ground-state transitions from the continuum and thus to determine the cross section for elastic scattering and (ii) to calculate the branching ratios for deexcitations to the ground state and to obtain the photoabsorption cross section. Since the obtained photoabsorption cross sections for  $^{92}\text{Mo}$ ,  $^{98}\text{Mo}$  and  $^{100}\text{Mo}$  match with the measured cross sections for the  $(\gamma, n)$  reaction the method allows us to determine the tail of the Giant Dipole Resonance below the neutron-separation energy.

The obtained dipole-strength distributions for  $^{92}\text{Mo}$ ,  $^{98}\text{Mo}$  and  $^{100}\text{Mo}$  show that the strength increases with the neutron number. The experimental results are discussed in the frame of QRPA calculations in a deformed basis which describe the increasing strength as a result of the increasing deformation.



# Preface

This dissertation is a result of work carried out in the Nuclear Physics group of the Institute for Nuclear and Hadron Physics of the Research Center Rossendorf, Dresden, Germany. Results of this work were reported in the regular “Spring meeting” conference of the German Physical Society in follow talks and posters: HK10.12 in Münster (2002), HK10.15 and HK29.13 in Tübingen (2003), HK19.9 and HK43.1 in Köln (2004), HK10.7 and HK38.7 in Berlin (2005) and HK31.2 München (2006). Results of this work were presented in the XV (2003) and XVI (2003) “International School on Nuclear Physics, Neutron Physics and Nuclear Energy” in Varna, Bulgaria, in the “Second International Conference on Nuclear Physics and Astrophysics”, 2005, Debrecen, Hungary and in the “Second International Conference COMEX2”, 2006, Sankt Goar, Germany.

Results of this work are published in the annual reports of the Institute for Nuclear and Hadron Physics of the Research Center Rossendorf FZR-341 (2002) p. 77, FZR-372 (2003) p. 29, p. 34 and p. 35, FZR-401 (2004) p. 7 and p. 10, FZR-423 (2005) p. 8 and p. 9, FZR-111 (2006) p.11 and the annual reports of the Institute for Radiation Physics of the University of Stuttgart for 2002 p. 8 and p. 10.

Results of the present work were included in the follow publications in scientific journals:

“Systematics of magnetic dipole strength in the stable even-mass Mo isotopes”

G. Rusev *et al.*, Phys. Rev. C 73, 044308 (2006).

“Pygmy dipole strength close to particle-separation energies - The case of the Mo isotopes”

G. Rusev *et al.*, Eur. Phys. J. A 27, s1.135 (2006).

“Decay of  $1^+$  States as a New Probe of the Structure of  $0^+$  Shape Isomers”

G. Rusev *et al.*, Phys. Rev. Lett. 95, 062501 (2005).

“The photon-scattering facility at the superconducting electron accelerator ELBE”

R. Schwengner *et al.*, Nucl. Inst. Meth. A555, 211 (2005).

“The new bremsstrahlung facility at the superconducting electron accelerator ELBE”

A. Wagner *et al.*, J. Phys. (London) G31, S1969 (2005).

”The bremsstrahlung facility at the ELBE accelerator”

G. Rusev, BgNS Transactions Vol. 9, 173 (2004).

“Nuclear-structure and Nuclear-astrophysics Experiments at the Superconducting Electron Accelerator ELBE”

R. Schwengner *et al.*, BgNS Transactions, in print.

“Dipole-strength distributions up to the particle-separation energies and photodissociation of Mo isotopes”

R. Schwengner *et al.*, Nucl. Phys. A, submitted.

## Acknowledgements

First of all, I want to thank to Dr. R. Schwengner, Dr. F. Dönau and to Prof. E. Grosse giving me the opportunity to join the Nuclear Physics Group of the Institute for Nuclear and Hadron Physics of Research Center Rossendorf. I thank to the German Research Foundation (Deutsche Forschungsgemeinschaft) for the financial support of my work under contracts Do-466-1 and Do-466-2. My special graduate goes to my colleague from the Nuclear Physics group and to Prof. E. Grosse for the continuous support and nice working atmosphere.

I thank to Dr. R. Schwengner who introduced me to details of the photon-scattering experiments and the common work during Ph.D. I am especially grateful to Dr. F. Dönau for his calculations on the molybdenum isotopes. I thank to him and to Prof. S. Frauendorf for the discussions and their work on the interpretation of the obtained experimental results.

I would like to acknowledge the colleagues from the Institute for Radiation Physics at the University of Stuttgart for preparing the setup for the experiments at the Dynamitron accelerator and for the given shifts. I would like to thank to Prof. U. Kneißl and to H. Pitz accepting the proposal to continue with the photon-scattering experiments on  $^{98}\text{Mo}$  and  $^{100}\text{Mo}$  at various electron-beam energies in order to resolve the branching transitions.

I am grateful to my colleagues who shared with me the shifts during the photon-scattering experiments on the molybdenum experiments at the ELBE accelerator. I would like to thank to the ELBE crew with a head Dr. P. Michel for the smoothly running accelerator.

I want to thank to my colleagues from the Nuclear Physics Department for the discussions about the GEANT simulations for the bremsstrahlung facility during our regular weekly meetings. I would like to thank to the system administrators Dr. M. Schlett and J. Steiner for the care on the cluster systems “Mosix” in the Institute for Nuclear and Hadron Physics and “Hades” in the Computing Center of the Research Center Rossendorf. The two cluster systems allowed me to use up to 30 computers simultaneously.

I highly appreciate the discussions with Prof. F. Bečvář and Dr. M. Krτίčka from the Charles University of Prague about the cascade simulations. I thank to Prof. E. Grosse for the supervision during the development of the code for  $\gamma$ -ray cascade simulations.

Finally, I want to address my thanks to my family, relatives and friends for their love and encouragement.

## Declaration

The work described here is all my own, except where clear reference is made to the work by others. The work in here has not been submitted for a degree, diploma or any other qualification at this or any other university.

*Dresden*  
*August 2006*

Gencho Y. Rusev

# Contents

<b>1</b>	<b>Introduction and motivation</b>	<b>1</b>
<b>2</b>	<b>Nuclear Resonance Fluorescence</b>	<b>5</b>
2.1	Cross section for photon scattering . . . . .	5
2.2	Spin determination . . . . .	8
2.3	Transition probabilities . . . . .	9
2.4	Parity determination . . . . .	10
2.4.1	Usage of linearly polarized photon beam . . . . .	10
2.4.2	Usage of Compton polarimeter . . . . .	11
2.5	K-quantum number assignments . . . . .	12
<b>3</b>	<b>The bremsstrahlung facility at the ELBE accelerator</b>	<b>15</b>
3.1	The ELBE accelerator . . . . .	15
3.2	The bremsstrahlung facility at the ELBE accelerator . . . . .	16
3.2.1	Radiator and bremsstrahlung production . . . . .	17
	Production of bremsstrahlung . . . . .	17
	Production of polarized photons . . . . .	18
3.2.2	Beam hardener . . . . .	19
3.2.3	Beam collimator . . . . .	19
3.2.4	Polarization monitor . . . . .	20
3.2.5	Photon-beam dump . . . . .	21
3.2.6	Reconstruction of the bremsstrahlung spectrum using an NaI detector . . . . .	22
3.3	Detector setup for NRF experiments at ELBE . . . . .	23
	Pb collimators . . . . .	25
	Pb shields . . . . .	25
3.4	Investigation of background in the measured spectra . . . . .	26
3.4.1	“Detector background” . . . . .	26
3.4.2	“Target background” . . . . .	27
3.4.3	“Room background” . . . . .	29
3.5	Data acquisition . . . . .	33
<b>4</b>	<b>Data analysis</b>	<b>37</b>
4.1	Determination of peak energy . . . . .	37
4.2	Detector efficiency . . . . .	38
4.3	Spin assignment . . . . .	40
4.4	Photon flux . . . . .	40
4.4.1	Approximation of the bremsstrahlung spectrum . . . . .	41
4.4.2	Determination of the electron-beam energy . . . . .	43
4.5	Energy-integrated scattering cross section $I_S$ . . . . .	45
4.6	Detection limits . . . . .	46
4.7	Determination of the resonant continuum . . . . .	48

4.8	A Monte Carlo code for $\gamma$ -ray cascade simulations in photon-induced reactions . . . . .	52
<b>5</b>	<b>Experimental results</b>	<b>57</b>
5.1	Low-lying dipole excitations in $^{92}\text{Mo}$ , $^{98}\text{Mo}$ and $^{100}\text{Mo}$ . . . . .	57
5.2	Dipole excitations in $^{92}\text{Mo}$ , $^{98}\text{Mo}$ and $^{100}\text{Mo}$ up to the $(\gamma, n)$ threshold . . . . .	63
5.2.1	Statistical properties of the observed resonances . . . . .	68
5.2.2	Determination of the total strength . . . . .	69
<b>6</b>	<b>Discussion</b>	<b>77</b>
6.1	Systematics of magnetic dipole strength in the stable even-mass Mo isotopes . . . . .	77
6.1.1	QRPA calculations . . . . .	77
6.1.2	Shell-model calculations . . . . .	80
6.1.3	Comparison of experimental and calculated $M1$ strengths . . . . .	81
6.1.4	$M1$ strength predicted at high energy . . . . .	82
6.2	Shape coexistence in $^{98}\text{Mo}$ and $^{100}\text{Mo}$ . . . . .	83
6.3	Dipole-strength distributions in $^{92}\text{Mo}$ , $^{98}\text{Mo}$ and $^{100}\text{Mo}$ . . . . .	85
<b>7</b>	<b>Summary and conclusions</b>	<b>89</b>
	<b>Appendices</b>	<b>91</b>
<b>A</b>	<b>NRF calibration standards</b>	<b>91</b>
<b>B</b>	<b>Low-lying excitations in <math>^{92}\text{Mo}</math>, <math>^{98}\text{Mo}</math> and <math>^{100}\text{Mo}</math></b>	<b>93</b>
<b>C</b>	<b>Transitions in <math>^{92}\text{Mo}</math>, <math>^{98}\text{Mo}</math> and <math>^{100}\text{Mo}</math> up to the <math>(\gamma, n)</math> threshold</b>	<b>95</b>
<b>D</b>	<b>Photoabsorption cross sections up to the <math>(\gamma, n)</math> threshold</b>	<b>111</b>
	<b>Bibliography</b>	<b>113</b>
	<b>Erklärung</b>	<b>121</b>

# Chapter 1

## Introduction and motivation

Since the early days of subatomic research experimental studies of the response of atomic nuclei to electromagnetic radiation have delivered important information on many nuclear properties. The atomic nuclei are composite quantum systems which exhibit excited states. Their properties such as excitation energies, angular momenta and decay widths to the ground state or to other low-lying levels are test ground for the existing theoretical approaches. Photon scattering, frequently called nuclear-resonance-fluorescence (NRF), refers to the resonant excitation of a level by absorption of a real photon and the subsequent decay of this level by emission of radiation. The principal advantage of this method is that both the excitation and deexcitation processes take place via the best understood interaction in physics, the electromagnetic interaction. The NRF with bremsstrahlung provides a sensitive probe for the excitation of states with dominantly spin  $J = 1$  and possibly  $J = 2$  in even-even nuclei, and allows the determination of level lifetimes in the order of  $10^{-15}$  s. An overview of the method can be found, e.g. in Refs. [Metz59, Knei96].

A systematic investigation of the dipole-strength distributions in dependence on the deformation or on the neutron-to-proton ratio  $N/Z$  is of importance for comparison with nuclear models. The chain of stable molybdenum isotopes with  $Z = 42$  provides a good example for a study of the dipole-strength distributions at the onset of deformation. Since a permanent ground-state deformation was observed in the heavier  $^{104}\text{Mo}$  and  $^{106}\text{Mo}$  isotopes [Chei70] and the lightest  $^{92}\text{Mo}$  is a closed-shell nucleus, the intermediate isotopes  $^{98}\text{Mo}$  and  $^{100}\text{Mo}$  are expected to show characteristics of transitional nuclei. The deformation around mass  $A = 100$  was studied in the framework of Hartree-Fock-Bogoliubov model by P. Federman and S. Pittel [Fede78, Fede79] and, with enlarged valence space, by E. Kirchuk *et al.* [Kirc93]. They showed that the deformation is strongly correlated to the polarization of valence neutrons and protons into the spin-orbit partner orbitals  $g_{7/2}$  and  $g_{9/2}$ , respectively, resulting from the strong neutron-proton interaction. A sharp fall of the  $g$ -factors of the  $2^+$  states [Mant01] between the closed neutron shell nucleus  $^{92}\text{Mo}$  and  $^{94}\text{Mo}$  with two valence neutrons was suggested as result of weak coupling of the proton and neutron valence spaces. P. Regan *et al.* [Rega03] showed that the increasing deformation causes an evolution from vibrational to rotational shapes along the yrast line using a new empirical approach E-GOS (E-Gamma Over Spin) based on the connection between transition energy and spin.

In the transitional Mo isotopes the excited  $0_2^+$  states are found close to the  $2_1^+$  states indicating the coexistence of different shapes. In an early work by H. Taketani *et al.* [Take71] on the stable even-mass Mo isotopes with two neutron transfer reactions it was observed that the excited  $0_2^+$  states behave like ground states. The intruder  $0^+$  states in the Sr-Zr-Mo nuclei were studied in the framework of the shell model by K. Heyde *et al.* [Heyd87]. It was concluded that the appearance of  $0^+$  intruder states in the  $Z = 40$  region is a combined effect of the extra quadrupole proton-neutron binding energy and the large monopole shift, effectively causing the disappearance of the proton  $2p_{1/2}$ - $1g_{9/2}$  gap at  $N = 60$ . The shape of  $^{98}\text{Mo}$  [Ziel02] and  $^{96,100}\text{Mo}$  [Ziel05] was recently investigated by means of Coulomb excitation. It was found that the shapes of the considered Mo isotopes are soft and, moreover, the coexistence of different shapes shows up in the occurrence of low-lying  $0^+$  states. Observation of

states with spin  $J = 1$  in  $^{98}\text{Mo}$  and  $^{100}\text{Mo}$  which decay to the  $0^+$  ground state as well as to the first excited  $0_2^+$  states within the present work allowed the extraction of the shape mixing coefficients from the measured branching ratios [Ruse05]. Therefore, the properties of the chain of stable Mo isotopes are dominated by deformation. The response of the stable Mo isotopes to electromagnetic radiation provides an interesting test ground for the influence of the proton-neutron interaction on the nuclear structure in the onset of the deformation. The photon-scattering experiments included in this work are performed with bremsstrahlung. Due to the dominant dipole fraction of the bremsstrahlung mainly states with spin  $J = 1$  are populated which allows a study of magnetic-dipole ( $M1$ ) and electric-dipole ( $E1$ ) excitations in the nucleus.

The origin and the strength of the  $M1$  radiation emitted from excited nuclear states has been the subject of various experimental and theoretical investigations. In even-even nuclei there are basically two sources for the generation of  $M1$  radiation [Bohr75]. Firstly, based on large nucleonic  $g$  factors, considerable  $M1$  strength can be produced by spin-flip transitions arising from particle excitations between spin-orbit partner states with  $j = l \pm 1/2$ . Secondly, substantial  $M1$  strength can be formed in deformed nuclei by orbital-magnetic transitions between states in which high- $j$  proton and high- $j$  neutron orbits are reoriented. According to this possibility the existence of a particular isovector excitation with spin and parity  $1^+$  was predicted within a semiclassical two-rotor model [LoIu78] and observed a few years later first in electron-scattering experiments [Bohl84]. This so-called scissors mode is caused by a rotational oscillation of the neutron system against the proton system which manifests as a group of  $1^+$  states around 3 MeV with a summed transition strength of up to  $\sum B(M1, 0^+ \rightarrow 1^+) \approx 3 \mu_N^2$ . Such  $1^+$  states have been studied systematically in numerous photon-scattering experiments on rare-earth nuclei. Overviews about these experiments are given, e.g., in Refs. [Rich95, Knei96].

The present work aims to study the magnetic dipole strength in the isotopic chain of the stable even-mass isotopes from  $^{92}\text{Mo}$  to  $^{100}\text{Mo}$ .

It is found that in all nuclei, the absorption cross section exhibits a strong maximum in the energy region from 10 to 25 MeV, depending on the mass number. This excitation mode, called giant dipole resonance (GDR), has  $E1$  isovector character. Microscopically the GDR consists of particle-hole excitations across one major shell. The residual interaction shifts the energy to the GDR region. The  $E1$  strength distribution below the neutron separation energy is dominated by the isovector giant dipole resonance but still part of the strength of the particle-hole excitations remains around  $1\hbar\omega$  region and it can be observed as narrow resonances in high resolution experiments [Zilg02]. In the early work on the investigation of the strength function below the GDR was found that some nuclei exhibit a concentration of strength around 5.5 MeV. The strength function can be represented by a smooth tail of the GDR with a ‘‘pygmy resonance’’ superimposed on it at 5.5 MeV. A further investigation of the properties of the bump at 5.5 MeV turned out that the  $\gamma$ -rays in the bump are predominantly direct  $E1$  transitions. An overview of this early work is given in Ref. [Bart72].

The aim of the present work is to study the dipole-strength distributions in  $^{92}\text{Mo}$ ,  $^{98}\text{Mo}$  and  $^{100}\text{Mo}$  below the neutron separation energy. The investigation of the dipole-strength distributions below the GDR in dependence on the shell-structure and the neutron-to-proton ratio  $N/Z$  is important for understanding of the collective and single-particle motion in quantum many-body systems.

Results of from photon-scattering experiments up to the neutron threshold have consequences for the description of the nucleosynthesis since they cover the energy range for photon induced reactions in explosive stellar scenarios and can provide an important information for the interplay between  $(\gamma, \gamma')$  and  $(\gamma, n)$ ,  $(\gamma, p)$  or  $(\gamma, \alpha)$  reactions. The response of nuclei to dipole radiation is of importance for understanding the synthesis of approximately 30 – 40 neutron-deficient nuclei which can not be produced in neutron capture. The so-called p-nuclei may be produced from photo-disintegration of previously formed heavier ones in the thermal photon bath. As shown previously [Gori98], details of the dipole strength (now in n-rich nuclei) may as well have large consequences for the r-process path and also s-process branchings are influenced by nuclear excitations [Kapp89] induced by thermal photons.

For the understanding and the modeling of the astrophysical processes the photoabsorption cross

---

section  $\sigma_\gamma$  up to and near the particle thresholds has to be known accurately [Gori02]. This part of the cross section determines essentially the critical stellar temperatures (Gamov peak) at which in a photonic heat bath the neutron production is starting. The energy region around the neutron threshold belongs to the tail of the giant dipole resonance containing only a few percents of the large total cross section of the GDR. Concerning the measurement of  $\sigma_\gamma$  in the threshold region one is in the following dilemma. Below the neutron threshold  $\sigma_\gamma$  can be measured via  $\gamma$  rays emitted after photo-excitation. However, the increasing level density of nuclear states towards the threshold leads to complex deexcitation patterns that include not only the deexcitation to the ground state but also the deexcitation to many intermediate states. Hence, generally the intensity of the detectable gamma radiation falls rapidly towards higher energies. The statistical Porter-Thomas fluctuations of the widths of the levels lead to observation of small part of the nuclear excitations as peaks. Both problems make the extraction of desired transition strength near the threshold to rather demanding task. Above the threshold  $\sigma_\gamma$  is measured by detecting emitted neutrons after photo-excitation. Apparently, the cross-section is low near the opening of the neutron emission channel making a precise measurement problematic. The theoretical prediction of the distribution of the dipole transition strength around the neutron emission threshold is also a highly challenging task. A fair description of the qualitative features of the GDR has been achieved by in terms of empirical and microscopic models. However, the quantitative calculation of the width, in particular the spreading part, is missing such that extrapolations of the GDR distributions towards lower energies are not reliable. Summarizing, there is a lack of both nuclear data and nuclear theory impact for a better prediction of the photoabsorption cross section in the critical threshold region.

In this work, statistical methods are applied in order to correct the high-resolution spectra for the intensities of branching and feeding transitions and, hence, to deduce the dipole-strength distributions and about the continuation of the photoabsorption cross section below the threshold, i.e., the low-energy tail of the GDR.

In the next Chapters of this thesis, the NRF method will be presented (Chapter 2). In Chapter 3 the bremsstrahlung facility at the ELBE accelerator is described with respect to the performed Monte Carlo simulations for optimization and background reduction. The used methods for analysis of the data are presented in Chapter 4. An overview on the experimental results is given in Chapter 5. The results are discussed on the basis of QRPA calculations which were done in a deformed basis. The final conclusions and remarks are given in Chapter 6.





## Chapter 2

# Nuclear Resonance Fluorescence

The nuclear-resonance-fluorescence technique (NRF) will be briefly presented in this Chapter. The summary concentrates only on the case of even-even nuclei because such nuclei are the subject of investigation in this thesis. Detailed descriptions and applications of NRF can be found in review articles [Metz59, Knei96].

Usage of bremsstrahlung allows us in principle to excite simultaneously all low-spin ( $J = 1, 2$ ) levels in the investigated nucleus. Due to the low transfer of momentum of real photons mainly states with spin  $J = 1$  are populated. The following quantities can be extracted in a model independent way from NRF experiments on even-even nuclei:

- the excitation energies  $E_x$ ;
- the spins of the excited states  $J$ ;
- the parities of the excited states  $\pi$ ;
- the widths  $\Gamma$ ;
- the branching ratios  $\Gamma_f/\Gamma$ ;
- the reduced transition probabilities  $B(\pi, L)$ .

### 2.1 Cross section for photon scattering

Following Bohr, the nuclear reaction proceeds through a compound nucleus. The process can be described as follows: a particle  $A$  (e.g. a charged or neutral particle, or a photon) impinges on an initial nucleus  $B$  in its ground state and a compound nucleus  $C$  is formed. This nucleus then emits a particle  $D$  and a residual nucleus  $E$  is left that may or may not be in an excited state,  $A + B \rightarrow C \rightarrow D + E$ .

The nuclear resonance fluorescence represents an absorption and reemission of real photons. This leads to the transformation:  $A + \gamma \rightarrow C \rightarrow \gamma' + A$ . The process of photon scattering is shown in Fig. 2.1. An excited level is populated via resonant absorption of a real photon and it decays via emission of a photon. The residual nucleus may be in its ground state  $J_0^\pi$ . In this case the process of photon scattering is called elastic scattering. It is inelastic when the excited level  $J_x^\pi$  decays to an intermediate  $J_f^\pi$  level.

The cross section for resonance fluorescence was derived by H.A. Bethe and G. Placzek [Beth37] from Dirac radiation theory. In the case of pure resonance fluorescence where the deexcitation of a level  $E_x$  to the ground state is only possible mode the cross section is given [Metz59]:

$$\sigma_{\gamma\gamma}(E, \theta) = \pi \lambda^2 \frac{2J_x + 1}{2(2J_0 + 1)} \cdot \frac{\Gamma^2}{(E - E_x)^2 + \frac{1}{4}\Gamma^2} \cdot \frac{W(\theta)}{4\pi}, \quad (2.1)$$

where  $J_x$  and  $J_0$  are the angular momenta of the excited state and the ground state, respectively,  $E_x$  is the resonance energy and  $W(\theta)$  is the angular correlation function between the incident and the

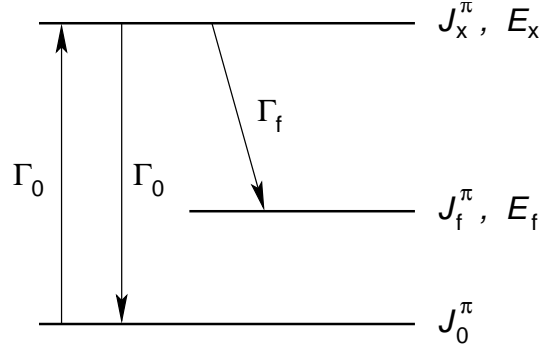


Figure 2.1: Resonance fluorescence on a nucleus with a ground state  $J_0^\pi$ . An excited level  $J_x^\pi$  is populated via resonance absorption of a photon. It can decay to the g.s.  $J_0^\pi$  (elastic scattering) or to one or more intermediate states  $J_f^\pi$  (inelastic scattering).

scattered photons,  $\lambda = \hbar c/E$  is the wavelength of the photon. The width of the excited level  $\Gamma$  is connected to the lifetime  $\tau$  of the level via the Heisenberg uncertainty relation:  $\Gamma \cdot \tau = \hbar$ .

In the general case of photon scattering the level with energy  $E_x$  may decay to the ground state or to one or more intermediate states  $E_f$ . If the absorbed energy is larger than the separation energy for protons or neutrons then the decay width for particle emission  $\Gamma_p$  has to be taken in to account. Finally the total width of the excited level is a superposition of the partial widths for decay to the ground state  $\Gamma_0$ , to the intermediate states  $\Gamma_f$  and for particle emission  $\Gamma_p$ :

$$\Gamma = \Gamma_0 + \sum_f \Gamma_f + \Gamma_p \quad (2.2)$$

The radiative decay is the only one considered in NRF. The decay width for particle emission is  $\Gamma_p = 0$ . The cross section for an excitation of the level  $J_x$  and its subsequent deexcitation to the level  $J_f$  is:

$$\sigma_{\gamma\gamma_f}(E, \theta) = \pi\lambda^2 \frac{2J_x + 1}{2(2J_0 + 1)} \cdot \frac{\Gamma_0\Gamma_f}{(E - E_x)^2 + \frac{1}{4}\Gamma^2} \cdot \frac{W(\theta)}{4\pi} \quad (2.3)$$

Summing  $\sigma_{\gamma\gamma_f}(E, \theta)$  over all possible modes of deexcitation and integrating over all scattering angles  $\theta$ , one obtains the total cross section for resonance absorption  $\sigma_\gamma(E)$  of photons of energy  $E$ :

$$\sigma_\gamma(E) = \pi\lambda^2 \frac{2J_x + 1}{2(2J_0 + 1)} \cdot \frac{\Gamma_0\Gamma}{(E - E_x)^2 + \frac{1}{4}\Gamma^2} \quad (2.4)$$

The cross section for elastic photon scattering, i.e. the deexcitation is to the ground state  $J_0^\pi$ , is related to the photoabsorption cross section:

$$\sigma_{\gamma\gamma}(E) = \frac{\Gamma_0}{\Gamma} \cdot \sigma_\gamma(E) = B_0 \cdot \sigma_\gamma(E), \quad (2.5)$$

where  $B_0 = \Gamma_0/\Gamma$  is the branching ratio for a ground-state transition.

The thermal moving of the nuclei leads to a Doppler broadening of the absorption lines given by Eq. (2.4). According to the Doppler effect, if a nucleus is moving with velocity  $v$  and emits a  $\gamma$ -ray with an energy  $E$ , then the observed radiation energy is shifted to:

$$E' = \frac{E(1 + \frac{v}{c})}{\sqrt{1 - (\frac{v}{c})^2}} \approx E(1 + \frac{v}{c}) \quad \text{for } v \ll c, \quad (2.6)$$

where  $c$  is the velocity of the light. A Maxwellian distribution may be assumed for the nuclear velocities  $v$ :

$$w(v)dv = (M/2\pi kT)^{1/2} \exp(-Mv^2/2kT)dv \quad (2.7)$$

where  $M$  is the mass of the nucleus,  $k$  Boltzmann's constant and  $T$  the absolute temperature of the absorber. Combining Eqs. (2.6) and (2.7), the distribution of the  $\gamma$ -ray energies is expressed as:

$$w(E')dE' = (1/\Delta\pi^{1/2}) \exp\{-(E' - E)/\Delta\}^2 dE', \quad (2.8)$$

where  $\Delta = (E/c)(2kT/M)^{1/2}$  is called the Doppler width.

In order to obtain the effective absorption cross section for gamma rays of energy  $E$ , the expression (2.4) has to be averaged over all possible values  $E'$  of the  $\gamma$ -ray energy:

$$\sigma_\gamma^D(E) = \int \sigma_\gamma(E')w(E')dE' = \sigma_\gamma^{\max}\psi(x, t) \quad (2.9)$$

$$\text{with } x = 2(E - E_x)/\Gamma; \quad t = (\Delta/\Gamma)^2$$

$$\sigma_\gamma^{\max} = \pi\lambda^2 \frac{2(2J_x + 1)}{2J_0 + 1} \cdot \frac{\Gamma_0}{\Gamma}$$

$$\psi(x, t) = \left[ \frac{1}{2(\pi t)^{1/2}} \right] \int_{-\infty}^{\infty} \frac{\exp[-(x - y)^2/4t]}{1 + y^2} dy \quad (2.10)$$

$$y = 2(E' - E_x)/\Gamma$$

For large  $t$  values ( $x \ll t$ ) the  $\psi(x, t)$  is well approximated by:

$$\psi(x, t) = (\pi^{1/2}/2t^{1/2}) \exp(-x^2/4t) \quad (2.11)$$

This means that for  $\Delta \gg \Gamma$  the effective absorption cross section  $\sigma_\gamma^D(E)$  has a "Doppler form", it can be written as:

$$\sigma_\gamma^D(E) = \sigma_\gamma^{\max}(\Gamma\pi^{1/2}/2\Delta) \exp\{-(E - E_x)/\Delta\}^2 \quad (2.12)$$

Considering Eq. (2.9) and the fact that  $\int_{-\infty}^{\infty} \psi(x, t)dx = \pi$  independently of  $t$ , it is clear that the integrated absorption cross section

$$\int_0^{\infty} \sigma_\gamma^D(E, t)dE = \sigma_\gamma^{\max}\Gamma \frac{\pi}{2} = \frac{2J_x + 1}{2J_0 + 1} \pi^2 \lambda^2 \Gamma_0 \quad (2.13)$$

does not depend on the relative size of the natural width and the Doppler form. For the case of pure resonance fluorescence, Eq. (2.13) takes the form:

$$I_s = \int_0^{\infty} \sigma_\gamma^D dE = \frac{2J_x + 1}{2J_0 + 1} \pi^2 \lambda^2 \Gamma. \quad (2.14)$$

For the case of non-pure resonance fluorescence and deexcitation to the ground state.

$$I_s = B_0 \int_0^{\infty} \sigma_\gamma^D dE = \frac{2J_x + 1}{2J_0 + 1} \left( \frac{\pi \hbar c}{E_x} \right)^2 \frac{\Gamma_0^2}{\Gamma}. \quad (2.15)$$

## 2.2 Spin determination

If a nucleus emits in a rapid succession two  $\gamma$ -rays  $\gamma_1$  and  $\gamma_2$  the angular distribution of  $\gamma_2$  with respect to  $\gamma_1$  is the relative probability  $W(\theta)d\Omega$  [Sieg65] that  $\gamma_2$  is emitted into the solid angle  $d\Omega$  at an angle  $\theta$  with respect to the direction of  $\gamma_1$ . The formalism describing the angular distributions in NRF is equivalent to the theory of  $(\gamma - \gamma)$  angular correlations. In case of NRF  $\gamma_1$  is the absorbed photon and  $\gamma_2$  the emitted one.

The measurement of the angular distribution of the scattered photons with respect to the incoming photon beam allows a spin assignment of the excited states. The angular correlation function  $W(\theta)$  of the scattered photons for the case  $L_n \leq 2$ , can be written as:

$$W(\theta) = \sum_{\lambda \text{ even}} B_\lambda(\gamma_1) A_\lambda(\gamma_2) P_\lambda(\cos \theta) \quad (2.16)$$

where the expansion coefficients  $A_\lambda$  and  $B_\lambda$  are given in the Krane-Steffen phase convention [Kran75]:

$$B_\lambda(\gamma_1) = \frac{F_\lambda(L_1 L_1 J_1 J_2) + (-1)^{L_1+L_1} 2\delta_1 F_\lambda(L_1 L'_1 J_1 J_2) + \delta_1^2 F_\lambda(L'_1 L'_1 J_1 J_2)}{1 + \delta_1^2} \quad (2.17)$$

$$A_\lambda(\gamma_2) = \frac{F_\lambda(L_2 L_2 J_3 J_2) + 2\delta_2 F_\lambda(L_2 L'_2 J_3 J_2) + \delta_2^2 F_\lambda(L'_2 L'_2 J_3 J_2)}{1 + \delta_2^2} \quad (2.18)$$

The mixing ratio is defined by the reduced matrix elements to:

$$\delta_1 = \frac{\langle J_2 \| \hat{L}'_1 \| J_1 \rangle}{\langle J_2 \| \hat{L}_1 \| J_1 \rangle} \quad \text{and} \quad \delta_2 = \frac{\langle J_3 \| \hat{L}'_2 \| J_2 \rangle}{\langle J_3 \| \hat{L}_2 \| J_2 \rangle}, \quad (2.19)$$

where  $L'_1 = L_1 + 1$  and  $L'_2 = L_2 + 1$ . The F-coefficients are defined as [Hage68]:

$$F_\lambda(LL' J_1 J_2) = (-1)^{J_1+J_2+1} \sqrt{(2L+1)(2L'+1)(2\lambda+1)(2J_2+1)} \cdot \begin{pmatrix} L & L' & \lambda \\ 1 & -1 & 0 \end{pmatrix} \cdot \left\{ \begin{matrix} J_2 & J_2 & \lambda \\ L & L' & J_1 \end{matrix} \right\}. \quad (2.20)$$

In the general case, one or more intermediate transitions may occur before the  $\gamma$ -ray of interest is observed. Those intermediate transitions may lead to a redistribution of the population of the substates, and may be taken into account by including appropriate coefficients  $U_\lambda$  in Eq. (2.16). The angular distribution function has the general form [Hami75]:

$$W(\theta) = \sum_{\lambda \text{ even}} B_\lambda(\gamma_1) U_\lambda(\gamma'_1) \cdots U_\lambda(\gamma'_n) A_\lambda(\gamma_2) P_\lambda(\cos \theta), \quad (2.21)$$

where

$$U_\lambda(\gamma) = \frac{U_\lambda(L) + \delta_2^2 U_\lambda(L')}{1 + \delta_2^2} \quad (2.22)$$

$$U_\lambda(L) = (-1)^{J_i+J_f+\lambda+L} \sqrt{(2J_i+1)(2J_f+1)} \left\{ \begin{matrix} J_i & J_i & \lambda \\ J_f & J_f & L \end{matrix} \right\}. \quad (2.23)$$

The ground state of even-even nuclei is  $0^+$ . States with spins 1 or 2 are mainly excited in NRF experiments with bremsstrahlung. The angular distribution for photons scattered from even-even nuclei is shown on Fig. 2.2 for pure dipole and quadrupole transitions. For these transitions the angular distribution (2.16) has a form:

$$W(\theta)_{\text{dipole}} = \frac{3}{4}(1 + \cos^2 \theta) \quad (2.24)$$

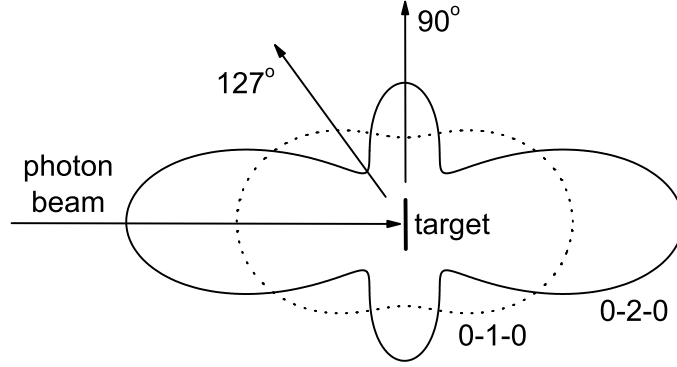


Figure 2.2: Angular distribution for photons scattered from even-even nuclei with respect to the direction of the incident photon beam. The distributions are labeled with the spin sequence  $J_{g.s.} - J_x - J_{g.s.}$ .

$$W(\theta)_{\text{quadrupole}} = \frac{5}{4}(1 - 3\cos^2\theta + 4\cos^4\theta). \quad (2.25)$$

As can be seen from Fig. 2.2 there are two important observation angles  $90^\circ$  and  $127^\circ$  with respect to the beam (the small angles are discarded because of the high background in the measured spectra). At  $127^\circ$  the quadrupole radiation angular distribution has a minimal value, and at  $90^\circ$  it has a local maximum. In contrast to the quadrupole radiation the dipole radiation shows a quite flat angular distribution. Therefore a ratio of  $W(90^\circ)/W(127^\circ)$  will give most differing values for the two multipole orders of radiation. From Eqs. (2.24) and (2.25) the expectation values for the ratio  $W(90^\circ)/W(127^\circ)$  can be specified, which are 0.737 and 2.28 for dipole and quadrupole transitions, respectively. These values are reduced due to the finite solid angles of the detectors and the size of the target.

## 2.3 Transition probabilities

The partial width for decay to the ground state  $\Gamma_0$  is proportional to the reduced transition probabilities  $B(\Pi L, E_\gamma) \uparrow$  ( $\Pi$  is  $E$  or  $M$ ) [Ring80]:

$$\Gamma_0 = 8\pi \sum_{\Pi L=1}^{\infty} \frac{(L+1)(E_\gamma/\hbar c)^{2L+1}}{L[(2L+1)!!]^2} \cdot \frac{2J_0+1}{2J_x+1} B(\Pi L, E_\gamma) \uparrow \quad (2.26)$$

For dipole and quadrupole transitions in even-even nuclei:

$$B(E1) \uparrow = 2.866 \cdot 10^{-3} \frac{\Gamma_0}{E_\gamma^3} \quad e^2 \text{fm}^2 \quad (2.27)$$

$$B(M1) \uparrow = 0.2598 \frac{\Gamma_0}{E_\gamma^3} \quad \mu_N^2 \quad (2.28)$$

$$B(E2) \uparrow = 6201 \frac{\Gamma_0}{E_\gamma^5} \quad e^2 \text{fm}^4, \quad (2.29)$$

where  $E_\gamma$  is taken in MeV and  $\Gamma_0$  in meV. The reduced transition probabilities  $B(\Pi L, J_0 \rightarrow J_x) = B(\Pi L) \uparrow$  and  $B(\Pi L, J_x \rightarrow J_0) = B(\Pi L) \downarrow$  are connected by the following relation:

$$B(\Pi L) \uparrow = \frac{2J_x+1}{2J_0+1} B(\Pi L) \downarrow. \quad (2.30)$$

## 2.4 Parity determination

Parity assignments are of crucial importance for the interpretation of the NRF experiments. Model independent parity assignments in photon scattering can be achieved by measuring the linear polarization of  $\gamma$  rays. There are two principle experimental possibilities: (i) the usage of linearly polarized photons in the entrance channel and (ii) the measurement of the linear polarization via the Compton scattering of photons. A review of the used methods is given in [Fagg59].

### 2.4.1 Usage of linearly polarized photon beam

A measurement of the azimuthal asymmetry of the resonantly scattered photons is used for parity determination in the NRF experiments with polarized photon beams. A schematic depiction of a NRF experimental setup using polarized off-axis bremsstrahlung beam is shown in Fig. 2.3. The electron beam hits a thin radiator under an angle relative to the axis of the collimator. The electric field vector  $\vec{E}$  is tangential to the bremsstrahlung intensity cone. The collimator separates a small part of the bremsstrahlung cone where a certain direction of  $\vec{E}$  dominates. The degree of polarization is about 30 – 40 % and depends strongly on the energy of the photons (see subsection 3.2.1). The angular distribution of scattered photons from the NRF target then depends on the polar angle  $\theta$  and the azimuthal angle  $\varphi$  (i.e. the angle between the electric field vector  $\vec{E}$  of the incoming photon beam and the scattering plane):

$$W(\theta, \varphi) = W(\theta) + (\pm)_{L'_1} \sum_{\lambda=2,4} B'_\lambda(\gamma_1) A_\lambda(\gamma_2) P_\nu^{(2)}(\cos \theta) \cos 2\varphi \quad (2.31)$$

where

$$B'_\lambda(\gamma_1) = \left( \frac{1}{1 + \delta_1^2} \right) \left\{ -k_\lambda(L_1 L_1) F_\lambda(L_1 L_1 J_0 J) + \right. \\ \left. + 2\delta_1 k_\lambda(L_1 L'_1) F_\lambda(L_1 L'_1 J_0 J) + \delta_1^2 k_\lambda(L'_1 L'_1) F_\lambda(L'_1 L'_1 J_0 J) \right\}. \quad (2.32)$$

$W(\theta)$  is the angular distribution for the unpolarized photon beam (see Eq. (2.16)) and  $A_\nu(2)$  is given in Eq. (2.17). The factors  $(\pm)_{L'_1}$  are +1 and -1 for electric and magnetic transitions  $L'_1$ , respectively.  $k_\nu(L_n, L'_n)$  are polarization coefficients [Fagg59].

The measured azimuthal asymmetry  $\epsilon(\theta, E_\gamma)$  is the product of the degree of polarization of the incoming photon beam  $P_\gamma(E_\gamma)$  and the analyzing power  $\Sigma(\theta)$  of the  $(\gamma, \gamma')$  reaction:

$$\epsilon(\theta, E_\gamma) = \frac{N_\perp - N_\parallel}{N_\perp + N_\parallel} = P_\gamma(E_\gamma) \Sigma(\theta) \quad (2.33)$$

where  $N_\perp$  and  $N_\parallel$  are the measured counting rates perpendicular and parallel to the polarization plane. The analyzing power  $\Sigma(\theta)$  is defined as a normalized difference of the angular distributions for the scattering plane perpendicular and parallel to the polarization plane:

$$\Sigma(\theta) = \frac{W(\theta, \varphi = 90^\circ) - W(\theta, \varphi = 0^\circ)}{W(\theta, \varphi = 90^\circ) + W(\theta, \varphi = 0^\circ)} \quad (2.34)$$

The analyzing power has a maximum under a scattering angle of  $\theta = 90^\circ$  for dipole and quadrupole transitions and values of:

$$\Sigma(\theta = 90^\circ) = \left\{ \begin{array}{l} +1 : E1 \\ -1 : M1 \\ -1 : E2 \end{array} \right\} - \text{radiation} \quad (2.35)$$

The production of off-axis bremsstrahlung polarized beams requires [Gova94]:

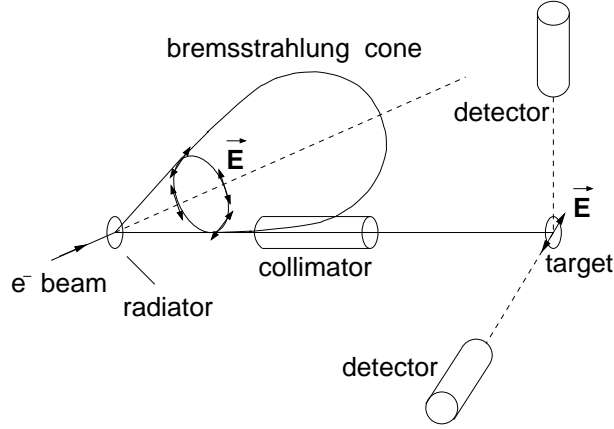


Figure 2.3: Schematic drawing for usage of linearly polarized photons for parity determination.

- a high intensity electron beam for sufficiently high count rates;
- a high pulse repetition rate to avoid pile-up;
- stable energy and position of the electron beam;
- a well defined and reproducible angle of incidence;

Facilities using off-axis bremsstrahlung polarized beams were in operation at Gießen [Berg87] and Gent [Gova94]. The new facility at Forschungszentrum Rossendorf also has been designed for production of polarized beams [Schw05]. Another technique using the back-angle Compton scattering of a laser light on an electron beam provides 100 % polarized photon beams. Facilities using such a method is in operation at Duke University [Piet02] and at the AIST, Tsukuba [Utsu05].

### 2.4.2 Usage of Compton polarimeter

Measurements of the linear polarization of resonantly scattered photons using Compton polarimeter allows model independent parity assignments. In the case of a polarization sensitive detector the angular distribution function depends additionally on the angle  $\varphi$  between the electric field vector  $\vec{E}$  of the scattered photon and the reaction plane defined by the incoming and scattered photons:

$$W(\theta, \varphi) = W(\theta) + (\pm)_{L'_2} \sum_{\lambda=2,4} B_\lambda(\gamma_1) A'_\lambda(\gamma_2) P_\nu^{(2)}(\cos \theta) \cos 2\varphi \quad (2.36)$$

where

$$A'_\lambda(\gamma_2) = \left( \frac{1}{1 + \delta_2^2} \right) \left\{ -k_\lambda(L_2 L_2) F_\lambda(L_2 L_2 J_f J) + 2\delta_1 k_\lambda(L_2 L'_2) F_\lambda(L_2 L'_2 J_f J) + \delta_1^2 k_\lambda(L'_2 L'_2) F_\lambda(L'_2 L'_2 J_f J) \right\} \quad (2.37)$$

Here the factors  $(\pm)_{L'_2}$  are also +1 and -1 for electric and magnetic transitions  $L'_2$ , respectively. The degree of linear polarization  $P_\gamma(\theta)$  can be defined by the relative difference of the scattering resulting in radiation with the electric field vector  $\vec{E}$  parallel and perpendicular to the reaction plane:

$$P_\gamma(\theta) = \frac{W(\theta, \varphi = 90^\circ) - W(\theta, \varphi = 0^\circ)}{W(\theta, \varphi = 90^\circ) + W(\theta, \varphi = 0^\circ)} \quad (2.38)$$

The degree of polarization has a maximum under a scattering angle of  $\theta = 90^\circ$  for dipole and quadrupole transitions in even-even nuclei and values:

$$P_\gamma(\theta = 90^\circ) = \left\{ \begin{array}{l} -1 : E1 \\ +1 : M1 \\ +1 : E2 \end{array} \right\} - \text{radiation} \quad (2.39)$$

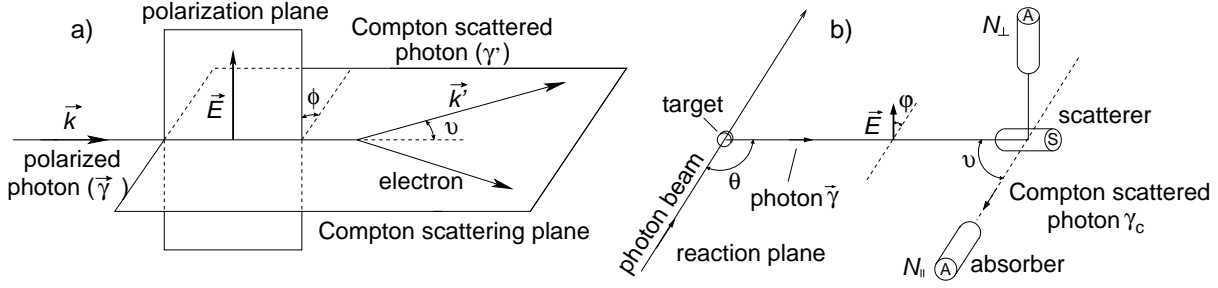


Figure 2.4: Kinematics of Compton scattering a) and schematic depiction of a Compton polarimeter setup b). The figures are taken from [Schl94].

The classical process, sensitive to the linear polarization of photons, is the Compton scattering. Fig. 2.4 a) shows the kinematics of the Compton scattering process. The Compton-scattering plane is defined by the momentum vectors  $\vec{k}$  and  $\vec{k}'$  of the incident and scattered photons, respectively. The scattering angle is denoted as  $\vartheta$ . The polarization plane is defined by the directions of the electric field vector  $\vec{E}$  of the incoming and its momentum vector  $\vec{k}$ . The angle between the scattering and polarization planes is denoted as  $\phi$ . The differential cross section for Compton scattering is given by the Klein-Nishina formula:

$$\frac{d\sigma}{d\Omega} = \frac{1}{2} r_0^2 \frac{E_{\gamma'}^2}{E_{\gamma}^2} \left( \frac{E_{\gamma'}}{E_{\gamma}} + \frac{E_{\gamma}}{E_{\gamma'}} - 2 \sin^2 \vartheta \cos^2 \phi \right) \quad (2.40)$$

where  $r_0 = e^2/m_0c^2$  is the classical electron radius,  $E_{\gamma'} = E_{\gamma}/(1 + \frac{E_{\gamma}}{m_0c^2}(1 - \cos \vartheta))$  is the energy of the scattered photon. As can be seen the Compton scattering predominantly takes place in a plane perpendicular to the electric field vector  $\vec{E}$  corresponding to  $\phi = 90^\circ$  (Eq. (2.40)).

To measure the linear polarization of photons one has to determine the count rates  $N_{\parallel}$  and  $N_{\perp}$  of Compton scattering events parallel and perpendicular to the reaction plane to which the polarization  $P_{\gamma}$  is defined. A schematic depiction of Compton polarimeter setup is shown in Fig. 2.4 b). The experimentally accessible quantity of the azimuthal asymmetry  $\varepsilon(\theta, E_{\gamma})$  is defined as the relative difference of the count rates  $N_{\parallel}$  and  $N_{\perp}$ :

$$\varepsilon(\theta, E_{\gamma}) = \frac{N_{\perp} - N_{\parallel}}{N_{\perp} + N_{\parallel}} = Q(E_{\gamma})P_{\gamma}(\theta) \quad (2.41)$$

the factor  $Q(E_{\gamma})$  is the polarization sensitivity of the polarimeter.

A setup for polarization measurements using two four-fold sectored Compton polarimeters [Knei92] was in operation in Stuttgart. The detector setup in Rossendorf also contains two four-fold sectored HPGc detectors (see Section 3.3) and allows for measurements of the linear polarization of the scattered photons.

## 2.5 K-quantum number assignments

In the case when an excited level can decay to the ground state and to intermediate levels in the NRF experiments the following ratio may be deduced:

$$R_{\text{exp}} = \frac{\Gamma_f}{\Gamma_0} \cdot \frac{E_{\gamma J_0}^3}{E_{\gamma J_f}^3} = \frac{B(J \rightarrow J_f)}{B(J \rightarrow J_0)} \quad (2.42)$$

for the case of pure dipole cascade. When a direct parity assignment is not performed some valuable information on the spin of the excited level is given by the Alaga rules [Alag55] stating that nuclear



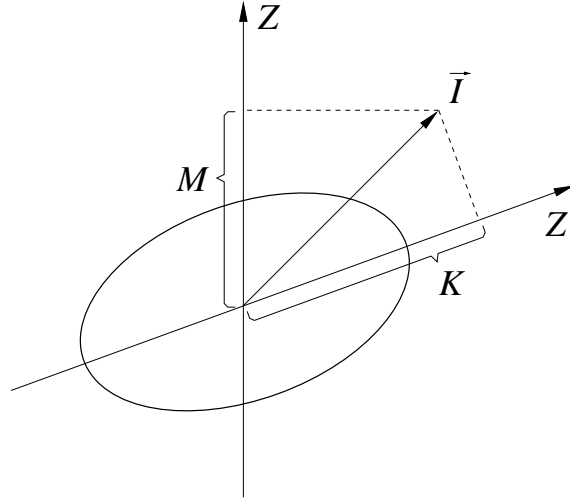


Figure 2.5: Angular momentum quantum numbers for a strongly axial deformed nucleus. The coupling scheme is characterized by the three constants of motion: the total angular momentum  $\vec{I}$ , its projection,  $M$ , on an axis  $z$  fixed in space, and its projection,  $K$ , on the nuclear symmetry axis  $z'$ . The figure is taken from [Alag55].

states with  $K = 1$  have parity  $\pi = +1$  and states with  $K = 0$  have  $\pi = -1$ . For axially deformed nuclei, in the rotational limit, the branching ratio  $R_{\text{theo}}$  is given by:

$$R_{\text{theo}} = \left| \frac{\sqrt{2J_f + 1} \langle J_f, K_f, L, K - K_f | J, K \rangle}{\sqrt{2J_0 + 1} \langle J_0, K_0, L, K - K_0 | J, K \rangle} \right|^2, \quad (2.43)$$

where  $K$  is the projection of the total angular momentum  $\vec{I}$  on the nuclear symmetry axis  $z'$  (cf. Fig. 2.5). Relation (2.43) allows  $K$ -quantum number assignments.

For even-even nuclei, the excited state has spin 1 and it can decay to the ground state ( $J_0=0_1^+$ ) or to the first excited  $2_1^+$  state. The  $K$ -quantum number can be assigned by comparison of the experimental branching ratio  $R_{\text{exp}}$  and the predictions of Alaga rule

$$R_{\text{Alaga}}(K = 1) = \frac{B(\pi 1; J = 1_1 \rightarrow J_f = 2_0)}{B(\pi 1; J = 1_1 \rightarrow J_0 = 0_0)} = 0.5 \quad (2.44)$$

$$R_{\text{Alaga}}(K = 0) = \frac{B(\pi 1; J = 1_0 \rightarrow J_f = 2_0)}{B(\pi 1; J = 1_0 \rightarrow J_0 = 0_0)} = 2.0$$

Here, the states with  $K = 1$  have parity  $\pi = +1$  and with  $K=0$  parity  $\pi = -1$ .



## Chapter 3

# The bremsstrahlung facility at the ELBE accelerator

The photon-scattering experiments in this work were performed at the bremsstrahlung facilities at the ELBE accelerator of the Forschungszentrum Rossendorf, Dresden and at the Dynamitron accelerator of the Institut für Strahlenphysik, Universität Stuttgart. Bremsstrahlung produced by deceleration of electrons in a radiation converter has the advantage that the continuous bremsstrahlung spectrum allows as to excite simultaneously all levels in the investigated nucleus. However, the non-resonantly scattered bremsstrahlung photons from the NRF target lead to continuous increasing background in the measured spectra. An investigation of the background radiation is presented in Section 3.4. Several solutions to the problem of reduction of the background were found using Monte Carlo simulations and applied for the setup in Rossendorf. The results of the simulations are compared with methodological measurements in the cases when such comparison is possible.

In this Chapter the main parts of the bremsstrahlung facility at the ELBE accelerator, the detector setup for NRF experiments and the data acquisition will be discussed. The investigation of the background radiation and the corresponding Monte Carlo simulations are reported.

### 3.1 The ELBE accelerator

A new superconducting electron linear accelerator of high brilliance and low emittance (ELBE) was built at the Forschungszentrum Rossendorf in order to deliver continuous wave electron beams with a maximum energy of 40 MeV at a maximum average current of 1 mA [Gabr00]. Electrons are pre-accelerated in a 250 keV-thermionic DC electron-gun and pre-bunched in a two RF-buncher section. Main acceleration is accomplished in two 20 MeV-superconducting linear accelerator modules operated at 1.3 GHz. Each accelerator module uses standing wave RF cavities designed for the TESLA test facility at DESY. Two 9-cell superconducting niobium cavities are operated in a cryo-module with superfluid liquid helium at 1.8 K. A schematic diagram of a cryostat with the niobium cavities is shown in Fig. 3.1. Each cavity is driven by a 10 kW klystron amplifier. The maximum accelerating gradient is 15 MV/m.

Parameters of the ELBE accelerator used for experiments with bremsstrahlung are presented in the following:

- Electron beam energy: 6 – 18 MeV
- Max. bunch charge: 77 pC
- Max. average beam current: 1 mA
- Micropulse duration: 2 ps
- Micropulse repetition rate: 26 MHz
- Macropulse duration: 0.1 – 40 ms / cw
- Macropulse repetition rate: 1 – 25 Hz

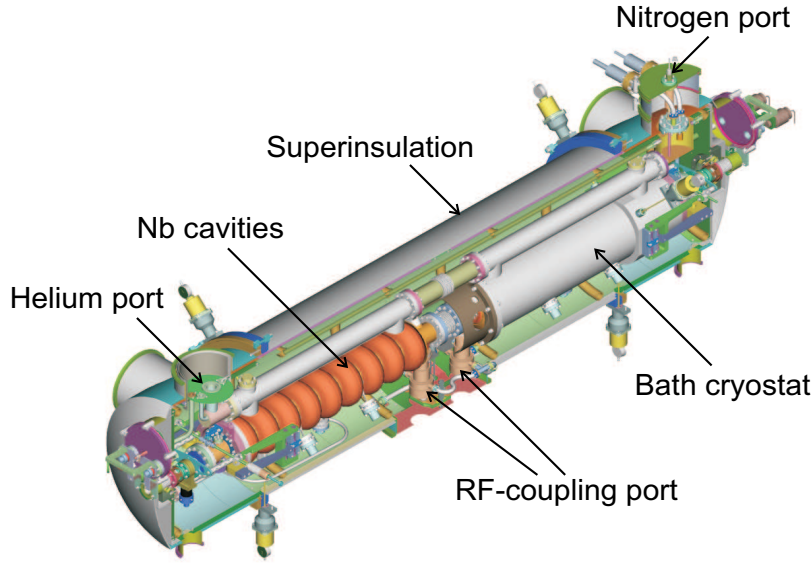


Figure 3.1: The ELBE cryogenic accelerator module.

### 3.2 The bremsstrahlung facility at the ELBE accelerator

The first module of the accelerator is used for production of photon beams with energies up to 18 MeV. A lay-out of the bremsstrahlung facility is shown in Fig. 3.2. The electron beam is deflected by  $45^\circ$  from the main beam line to the experimental area by a non-dispersive system of two dipole magnets and one quadrupole magnet. The bremsstrahlung is produced by a radiator [Wagn99] consisting of a thin niobium foil [Schi03a] which converts only a small fraction of the electron beam. The remaining fraction of the beam is deflected by a  $45^\circ$  purging magnet [Schi03c] to an electron-beam dump (cf. Fig. 3.2). The bremsstrahlung cone is collimated to a narrow photon beam by a collimator [Schi02a] made of pure aluminum (99.5 % Al). A hardener [Schi02b] placed in front of the collimator modifies the bremsstrahlung spectrum. The photon beam irradiates an NRF target and is finally absorbed in a photon-beam dump [Wagn01a]. The photon flux is monitored by NaI detector [Wagn02] placed at  $25^\circ$  relative to the beam. The detector setup [Schw03] shown in Fig. 3.2 is used for NRF experiments and is described in the next section.

The facility allows the production of polarized photon beams [Wagn01b] using off-axis bremsstrahlung. Two steerer magnets [Schi03b] are installed in front of the radiator to tilt the bremsstrahlung cone

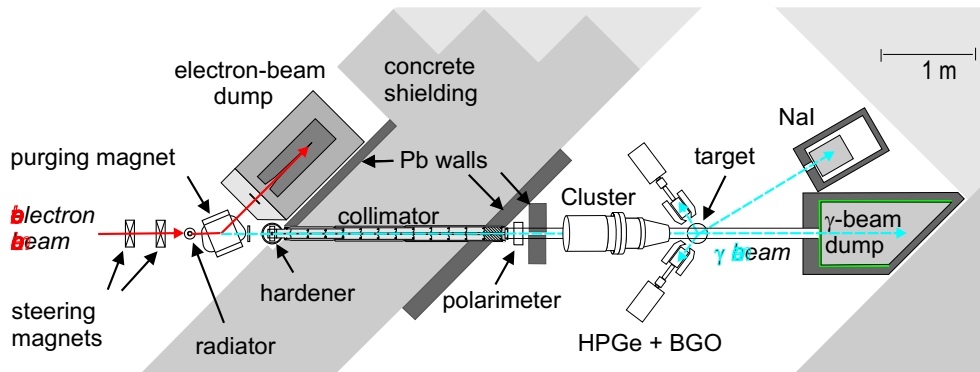


Figure 3.2: The bremsstrahlung facility at the ELBE accelerator.

under a certain angle relative to the collimator axis thus selecting a fraction of the bremsstrahlung cone with a defined polarization (cf. Fig. 2.3). The degree of polarization is measured by a polarization monitor [Schw02] placed behind the collimator (cf. Fig. 3.2).

The bremsstrahlung facility at the ELBE accelerator is presented in Refs. [Ruse04a], [Schw05] and [Wagn05a].

In this section the radiator, beam hardener, the beam collimator and the photon-beam dump will be described in more details. A possible application of the NaI detector [Ruse04b] for reconstruction of the bremsstrahlung spectrum and determination of its end-point energy is reported.

### 3.2.1 Radiator and bremsstrahlung production

The bremsstrahlung target (radiator) has a key position in the bremsstrahlung facility at the ELBE accelerator. It converts the kinetic energy of the electrons into electromagnetic radiation. Because of the possibility to produce polarized off-axis bremsstrahlung it has to be a thin foil, preventing multiple scattering of the electrons inside the radiator which reduces the degree of polarization. The smaller photon-beam intensity as compared with a thick radiator can be compensated by the high electron current offered by the accelerator. Simulations regarding the choice of optimum radiator materials have been performed [Wagn01a]. The used radiator thickness range is from  $3 \times 10^{-4}$  to  $10^{-3}$  times the radiation length  $X_0$  for radiators made of niobium. The metallic radiator foil is embedded in a water-cooled holder [Schi02b] with six radiator positions. A video camera for continuous observation of the electron-beam spot on the radiator and a pyrometer for measurement of the temperature of the radiator are installed.

#### Production of bremsstrahlung

According to the electrodynamics, an electron is in general deflected if it passes through the field of a nucleus (or atom). Since this deflection always causes a certain acceleration, radiation has to be emitted. The cross section for bremsstrahlung is proportional to  $Z^2$  [Heit84]. It makes high  $Z$  materials preferential for bremsstrahlung targets.

The dependence of the bremsstrahlung intensity on the radiator thickness was investigated in the present work performing Monte Carlo simulations. The program package GEANT4 contains all processes of electron interactions with matter. Results of the simulations for an electron beam en-

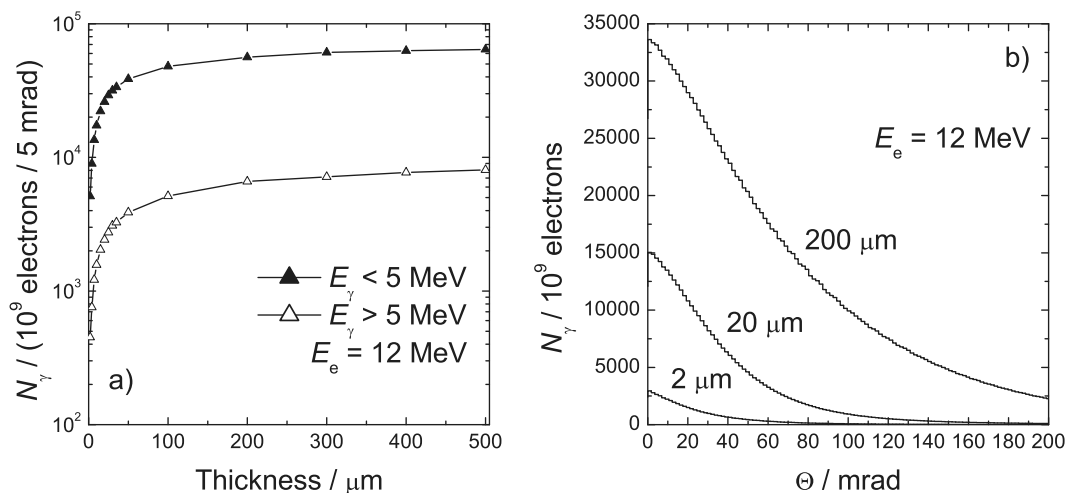


Figure 3.3: Simulations for the bremsstrahlung production a) and the angular distribution b) in dependence on the thickness of Nb radiators for a kinetic electron energy of 12 MeV.

ergy of 12 MeV and niobium radiators are presented in Fig. 3.3. Fig. 3.3 a) shows the number of bremsstrahlung photons in an opening angle of 5 mrad, the opening angle of the photon-beam collimator, for different radiator thicknesses. It can be seen that the intensity saturates at a certain radiator thickness. Two orders of magnitude change in radiator thickness lead to one order of magnitude higher intensity. A quasi-saturation occurs above 100  $\mu\text{m}$  thickness. The curves corresponding to low-energy photons ( $< 5$  MeV) and to the high energy photons ( $> 5$  MeV) are parallel. The bremsstrahlung spectrum is not modified by the radiator thickness in the considered thickness range. An effect of hardening of low energy photons which could make the thick radiator more preferential is insignificant.

The angular distribution of the produced bremsstrahlung photons is presented in Fig. 3.3 b) for three radiator thicknesses of 2, 20 and 200  $\mu\text{m}$ . The bremsstrahlung quanta are spread over a large angle range for a thick radiator in comparison with a thin one. From a background-reduction point of view the thin radiator is more favorable because the produced radiation is concentrated at forward angles and smaller amount of radiation has to be attenuated in the concrete wall and the collimator in comparison with a thick radiator.

### Production of polarized photons

The bremsstrahlung produced from electrons with kinetic energy  $E_e$  is partially polarized with a maximum degree of polarization at an angle of  $\mu/E_e$  where  $\mu$  is the rest energy of the electron. The most favored direction of polarization is perpendicular to the plane of observation defined from the incident electron and emitted photon [Heit84]. M. May and G. Wick [May51] have derived an expression for the bremsstrahlung cross section based on Weizsäcker's analysis [Weiz34] of the radiative collision between an electron and a nucleus. The cross section [May51] for production of photons polarized at an angle  $\phi$  to the plane of observation can be simplified to:

$$d\sigma = A[B + \sin^2 \theta \cos^2 \phi] \sin \theta d\theta, \quad (3.1)$$

where  $\theta$  is the angle between the electron and the emitted photon and  $A$  and  $B$  are constants depending on  $E_e$ ,  $Z$  and  $\theta$ .

The kinematics of electron scattering given by GEANT3 was combined with the cross section (3.1) in order to obtain the degree of polarization taking into account the thickness of the radiator, the electron-beam structure and the opening angle of the photon-beam collimator. A random generator

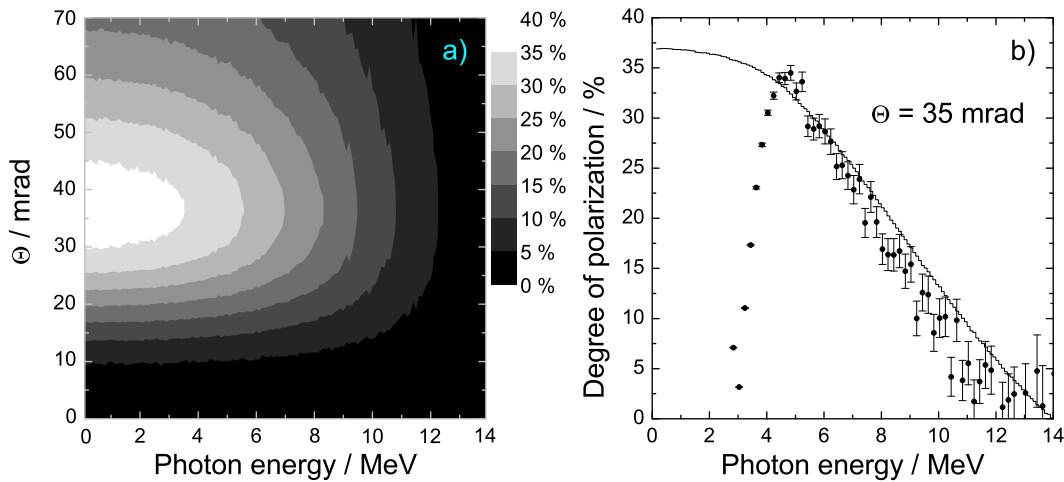


Figure 3.4: Results from simulations a) for the degree of polarization for 14 MeV electron beam and b) a cut at an angle of  $\theta = 35$  mrad. The data points are determined from analyzed proton spectra (see subsection 3.2.4) measured at  $E_e = 14$  MeV.

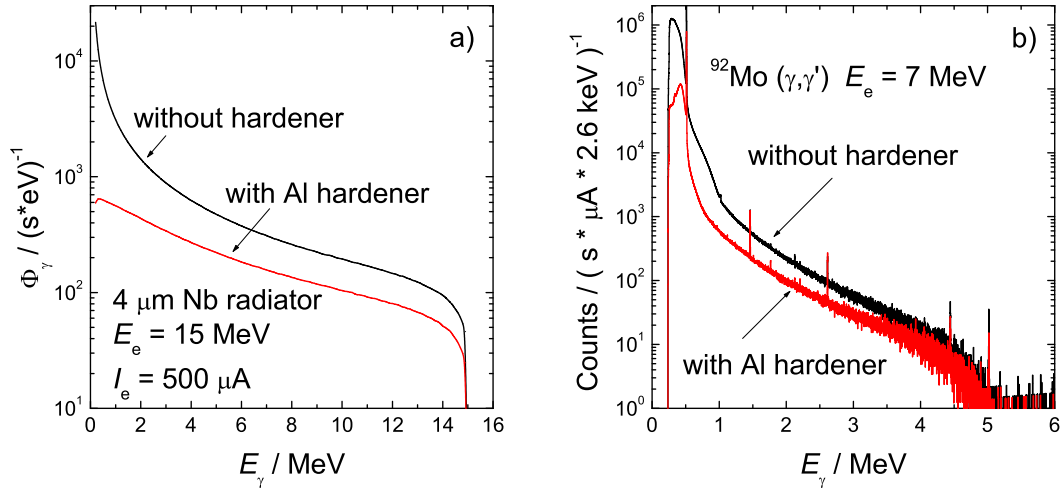


Figure 3.5: Simulations of the energy distribution of the incident photon-beam flux a) at the NRF-target position. The electron beam is considered with an energy of 15 MeV and a current of 500  $\mu\text{A}$ . The radiator is a Nb foil with a thickness of 4  $\mu\text{m}$ . Comparison of  $\gamma$ -ray spectra b) corresponding to measurements with and without used hardener.

based on Eq. (3.1) was used to assign an angle of polarization  $\phi$  to the individual bremsstrahlung quanta generated from GEANT. Results for the degree of polarization of bremsstrahlung produced from 15 MeV electrons in a 4  $\mu\text{m}$  thick Nb radiator in a 5 mrad opening angle are presented in Fig. 3.4. A cut at  $\theta = 35$  mrad is shown in Fig. 3.4 b). The simulations were performed for  $10^{10}$  incident electrons for every angle  $\theta$  varied in steps of 5 mrad.

### 3.2.2 Beam hardener

The bremsstrahlung has a continuum spectrum with an end-point energy equal to the kinetic energy of the incident electrons. At low energy it has a high intensity, which leads to a huge background in the measured spectra and limits the counting rates of the HPGe detectors. The shape of the bremsstrahlung spectrum can be modified by using a spectrum hardener, a cylindrical absorber made of aluminum with a length of 10 cm. Placed into the photon beam, it absorbs mainly low energy photons. Results of GEANT3 simulations for the photon flux at the NRF target position are shown in Fig. 3.5 a) for a 4  $\mu\text{m}$  thick Nb radiator and an electron current of 500  $\mu\text{A}$  without and with using the aluminum hardener. The influence of the Al hardener on the measured spectra can be seen in the comparison presented in Fig. 3.5 b). The spectra were measured for about 7 hours, they are efficiency corrected and normalized to the measuring time and the electron-beam current.

The hardener device [Schi02b] contains three cylinders of 10 cm length and 10 cm diameter which can be placed separately in the beam. One of them consists of TRIAMET<sup>1</sup>, a composite material with a density of 18 g/cm<sup>3</sup> made of 95 % W and 5 % Ni and Cu. It is used as a beam shutter and prevents the experimental cave from radiation inside the accelerator hall. The other two ones are aluminum hardeners. One of those hardeners is made entirely from Al while the other one consists of a 0.9 cm diameter Al cylinder surrounded by a 10 cm diameter TRIAMET.

### 3.2.3 Beam collimator

The bremsstrahlung produced by the radiator is collimated to a narrow beam by a collimator of 2.6 m length and an opening angle of 5 mrad [Schi02a]. It is made of pure Al (99.5 %) because of its high neutron separation energy ( $S_n = 13$  MeV). The aluminum has a photon attenuation effect similar to

<sup>1</sup>Bayerische Metallwerke GmbH, Leitenweg 5, 85221 Dachau, Germany

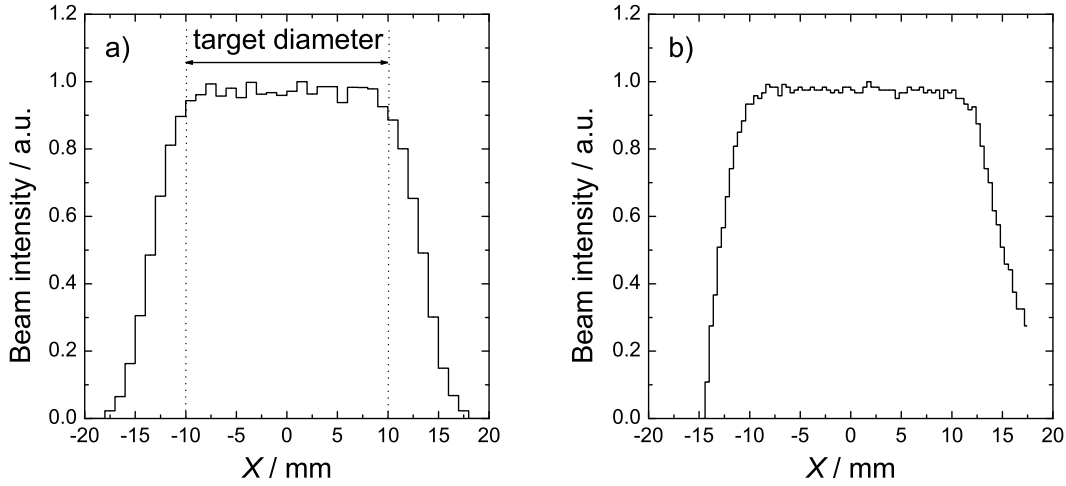


Figure 3.6: Cross section of the photon-beam spot along the horizontal axis obtained a) from GEANT3 simulations and b) from scanned X-ray film.

the surrounding concrete walls. Monte-Carlo simulations were performed in order to investigate the properties of the collimator and the structure of the photon-beam spot at the NRF target position. Photons were emitted from the place of radiator with an energy [Schi51] and an angular [Lanz51] distribution corresponding to the real bremsstrahlung. A screen was defined at the place of the NRF target perpendicular to the photon beam. The position of the photons on the screen was recorded. The result of the simulations is shown in Fig. 3.6 a). The photon-beam spot shows a homogeneous distribution over a circle with a diameter of 2 cm. A target diameter of 2 cm (cf. Fig. 3.6 a) was selected in order to use optimally the intensity of the photon beam.

X-ray films are used for monitoring the photon-beam position. The beam-intensity distribution can be extracted by scanning an irradiated and developed film with a He-Ne laser and a photo diode. The beam intensity along the horizontal axis is shown in Fig. 3.6 b). The comparison between the simulated and measured results for the structure of the beam spot shows good agreement.

### 3.2.4 Polarization monitor

Usage of polarized beams requires a monitor of the degree of polarization of the photons. A polarization monitor was developed using the process of photodisintegration of the deuteron. Because of the predominant  $E1$  absorption in this process the protons and neutrons are emitted preferentially in the direction of the electric field vector of the polarized bremsstrahlung. The degree of polarization can be deduced by measuring the azimuthal asymmetries of the protons.

The polarization monitoring setup [Schw02] consists of four silicon detectors positioned perpendicular to the photon beam at azimuthal angles of  $0^\circ$ ,  $90^\circ$ ,  $180^\circ$  and  $270^\circ$  in a cylindrical reaction chamber. The detectors have a thickness of  $300 \mu\text{m}$  and an area of  $600 \text{ mm}^2$ . A  $\text{CD}_2$  foil of  $40 \mu\text{m}$  thickness is used as a target. The distance between the detectors and the target is 11 cm. Example proton spectra measured with the silicon detectors at different electron-beam energies are shown in Fig. 3.7 a). A spectrum of a mixed  $^{239}\text{Pu}$ - $^{241}\text{Am}$ - $^{244}\text{Cm}$   $\alpha$ -particle source used for energy calibration is presented in Fig. 3.7 b).

Because the energies of the incident photons correlate with the measured proton energies the proton spectra can be used for determination of the bremsstrahlung end-point energy. The spectral distribution of the incident photon beam can also be extracted from the proton spectra. An analysis of the proton spectra is presented in Section 4.4.



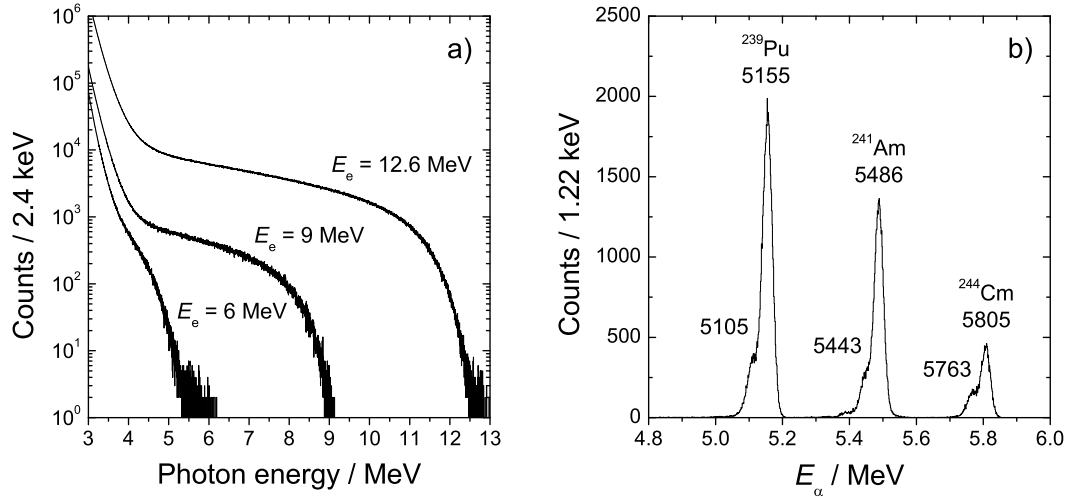


Figure 3.7: Measured proton spectra a) at different electron-beam energies. A spectrum b) of a mixed  $^{239}\text{Pu}$ - $^{241}\text{Am}$ - $^{244}\text{Cm}$   $\alpha$ -particle source.

### 3.2.5 Photon-beam dump

In order to minimize the background from scattered photons the photon beam has to be dumped after passing the NRF target. A photon-beam dump was developed [Wagn01a] made of polyethylene (PE) and shielded with 2 mm thick cadmium foil and 10 cm thick lead walls. The front lead wall has a thickness of 20 cm.

The beam dump has an entrance hole of 11 cm in diameter. Because of the Compton back-scattering and the rather big entrance hole the beam dump does not absorb fully the photon beam. A hole in the PE block was suggested in order to reduce the back-scattered radiation. The hole moves away the beginning of the PE block and the scattering process starts deep inside the beam dump. From geometrical considerations the beginning of the PE block sees the entrance of the beam dump under a small opening angle (see the drawing in Fig. 3.8) and thus reduces the intensity of the radiation outgoing from the beam dump. Monte Carlo simulations were performed to investigate the influence

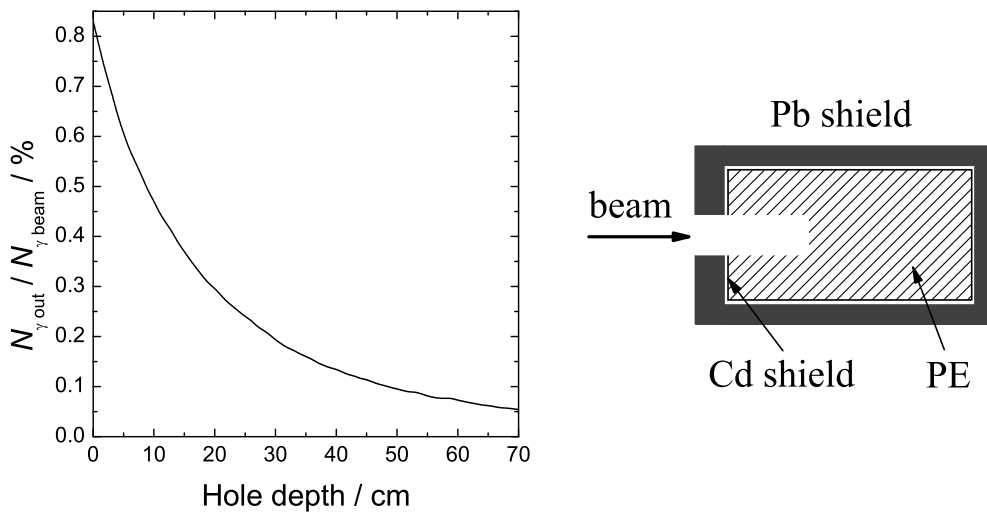


Figure 3.8: Simulations for the dependence of back scattered photons through the entrance hole of the photon-beam dump on the depth of the hole in the polyethylene block.

of the depth of the hole on the properties of the beam dump. Monoenergetic photon beams were assumed with energies of 5, 10, 15 and 20 MeV and the number of the photons back-scattered and penetrating the beam dump was counted. Results of the simulations for the fraction of the beam intensity of the scattered back from the photon-beam dump are shown in Fig. 3.8. A hole of 15 cm depth was drilled into the PE block.

### 3.2.6 Reconstruction of the bremsstrahlung spectrum using an NaI detector

At the bremsstrahlung facility of the ELBE accelerator a large NaI detector [Rick88] is used for photon-beam-flux monitoring. The NaI crystal has a size of  $10'' \times 10''$ . The detector is placed at  $25^\circ$  relative to the beam and shielded with a 10 cm thick lead housing with a collimator hole of 4 cm in diameter (cf. Fig. 3.2). A spectrum measured with the NaI detector was analyzed in order to reconstruct the spectral distribution of the incident photon beam using simulations for the response of the detector. Monte-Carlo simulations including the experimental setup of a photon-scattering experiment on  $^{98}\text{Mo}$  at  $E_e = 8.5$  MeV were performed for a photon beam with uniform energy distribution. The beam energy range from 0 to 10 MeV was divided into 40 bins with a width of 250 keV. The simulations were performed for  $10^9$  photons/bin using the code GEANT3. A response spectrum  $S_i$  of the deposited energy in the NaI crystal includes the probability for  $\gamma$ -scattering from the target and the response of the detector. Fig. 3.9 b) shows an example response spectrum of the detector from a quasi-monoenergetic photon beam with energies (cf. Fig. 3.9 a) between 9.75 and 10 MeV. The measured NaI-spectrum  $S_{\text{exp}}$  is approximated with a linear combination of such simulated response spectra  $S_i$ :

$$S_{\text{exp}} = \sum_i a_i S_i, \quad (3.2)$$

where the coefficients  $a_i$  are free positive definite parameters of the fit, which correspond to the intensity of the incident photon beam in the energy range of bin  $i$ .

Applying the method, an NaI spectrum measured for 2 hours from the photon-scattering experiment on  $^{98}\text{Mo}$  at an electron energy of about 8.5 MeV is used. The initial bremsstrahlung spectrum reconstructed from the measured NaI spectrum is shown in Fig. 3.10 a). It is compared with GEANT3 simulations of the photon flux including the radiator and the beam hardener (cf. e.g. Fig. 3.5). Fig. 3.10 a) shows that the unfolded spectrum reproduces well the slope of the beam-intensity distribution. The presented simulations are used in the inverse way in order to obtain the end-point energy of the bremsstrahlung spectrum more precisely. The measured NaI spectrum is compared with

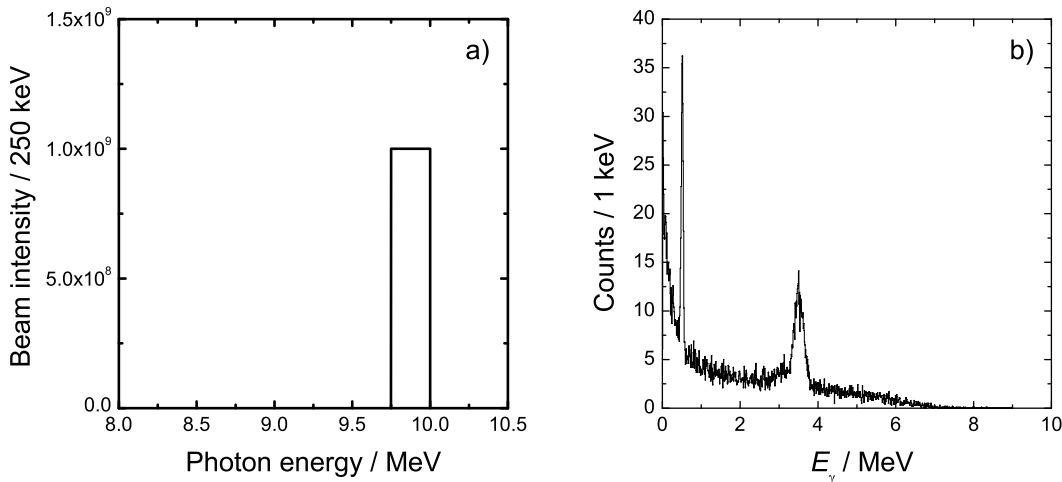


Figure 3.9: Simulations for the response of the NaI detector b) at a photon beam with uniform energy distribution a) between 9.75 and 10 MeV.

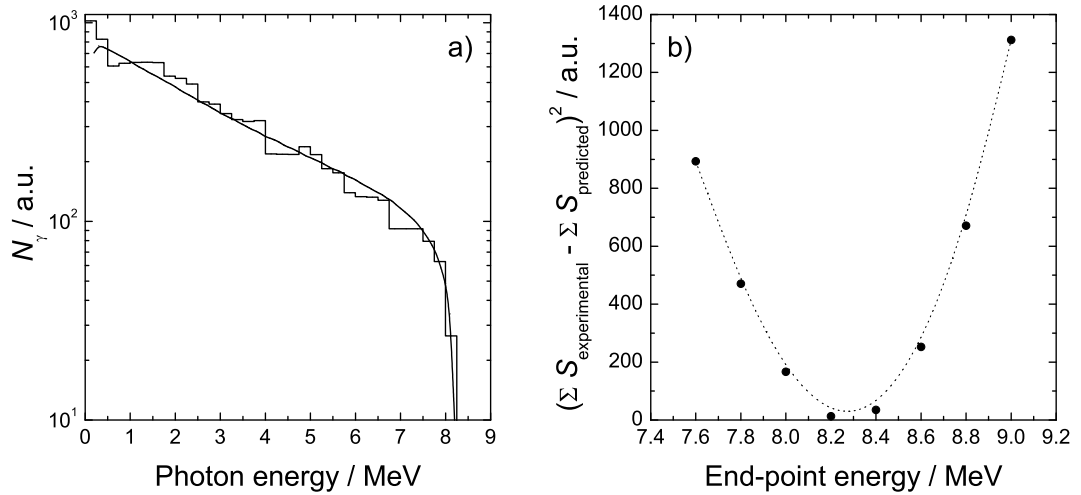


Figure 3.10: a) results for the reconstructed bremsstrahlung spectrum used in the  $^{98}\text{Mo}(\gamma, \gamma')$  experiment presented with a histogram and compared with simulations of the photon flux; b) determination of the bremsstrahlung end-point energy (see text);

simulated spectra corresponding to different electron-beam energies. The spectra were normalized in the energy range from 1 to 2 MeV. The squared difference between measured and predicted spectra for the NaI detector is plotted in Fig. 3.10 b). The minimum in Fig. 3.10 b) gives the end-point energy located at about 8.3 MeV. Of crucial importance for precise end-point energy determination is the energy calibration of the NaI detector and the knowledge of the angle of the detector relative to the beam.

The presented method reproduces rather well the spectral distribution of the incident beam spectrum. The end-point energy of the bremsstrahlung distribution can be determined. The method can be applied for on-line monitoring of the incident beam using a high efficient NaI detector and spectra measured for a short time.

### 3.3 Detector setup for NRF experiments at ELBE

Nuclear-structure investigations using the nuclear-resonance-fluorescence technique require an efficient setup of high-purity germanium (HPGe) detectors [Schw03]. The setup of HPGe detectors for NRF experiments is shown in Fig. 3.2. It consists of four n-type HPGe detectors with 100 % efficiency relative to a 3"  $\times$  3" NaI detector. Specifications of the used HPGe detectors are presented in Table 3.1. Two of them are fourfold segmented detectors, placed vertically at  $90^\circ$  relative to the beam. The other two HPGe detectors are placed horizontally at an angular range from  $90^\circ$  to  $127^\circ$  relative to the beam. This flexibility allows a measurement of the angular distributions of the  $\gamma$  rays scattered from

Table 3.1: Specifications of the HPGe detectors.

detector	crystal diameter / mm	crystal length / mm	operating bias / V	polar angle	distance to target / mm
#1 Ortec 41-N31587A	79.1	90	-4500	$127^\circ/90^\circ$	320/280
#2 EurisyS 73615	76.5	86.9	+4500	$90^\circ$	280
#3 Ortec 41-N31569A	78.2	93.1	-4800	$127^\circ/90^\circ$	320/280
#4 EurisyS 73633	76.7	86.9	+5000	$90^\circ$	280

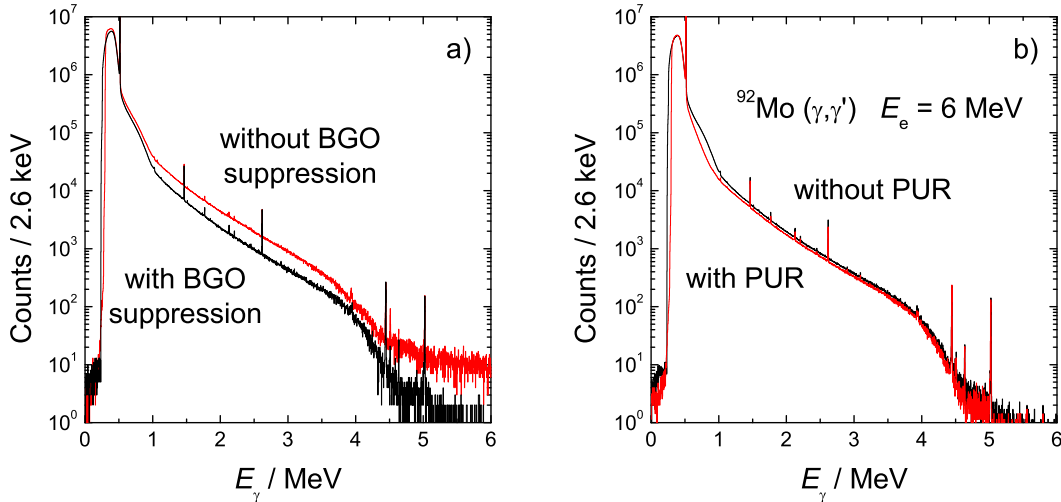


Figure 3.11: Normalized spectra to the photon flux deduced from the 5020 keV  $^{11}\text{B}$  line measured at  $90^\circ$  from the  $^{92}\text{Mo}(\gamma, \gamma')$  experiment at  $E_e = 6$  MeV. The spectra are measured with and without BGO suppression a) and with and without pile-up rejection b) but with BGO suppression.

even-even nuclei at  $90^\circ$  and  $127^\circ$  and the parity determination using polarized beams when all four detectors are placed on  $90^\circ$ . In addition, a Euroball cluster detector has been installed at  $145^\circ$  relative to the beam and at 480 mm distance to the target to increase the efficiency of the detector setup. The HPGe detectors are shielded with escape-suppression shields of bismuth germanate (BGO) scintillation detectors in order to reduce the background in the measured spectra. A comparison between measured spectra from the detectors at  $90^\circ$  with and without BGO suppression is shown in Fig. 3.11 a). The spectra are normalized to the photon flux deduced from the 5020 keV  $^{11}\text{B}$  line. Additional reduction of the background is performed by including a pile-up rejection (PUR). The PUR allows a work of the detectors at high count rates (10 – 15 kHz) without a significant influence to the background. Normalized spectra measured with and without PUR are compared in Fig. 3.11 b).

The active BGO shields have to be protected from the direct radiation from the target by using lead

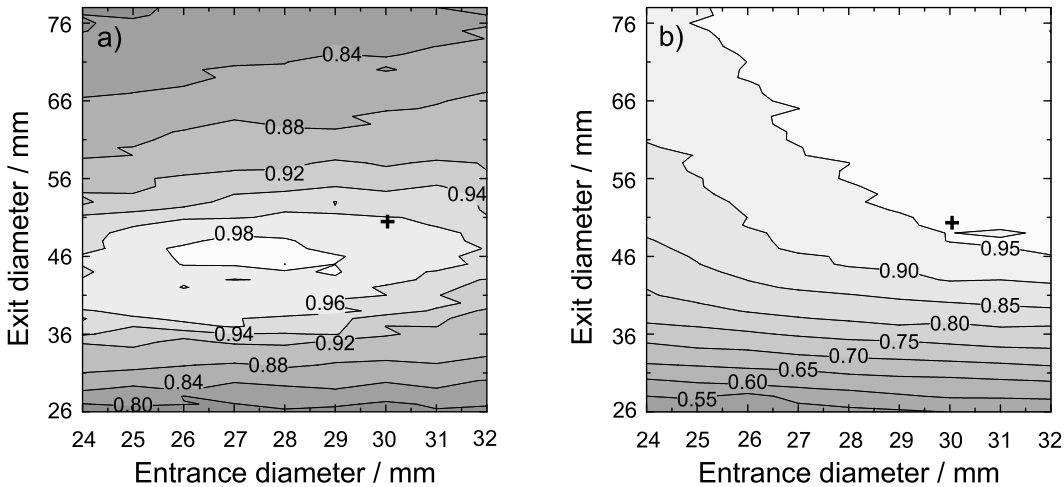


Figure 3.12: Normalized ratio of photo-peak to background a) and photo peak area b) versus the entrance (abscissa) and the exit diameter (ordinate) of the lead collimator. The cross marks the chosen diameters.

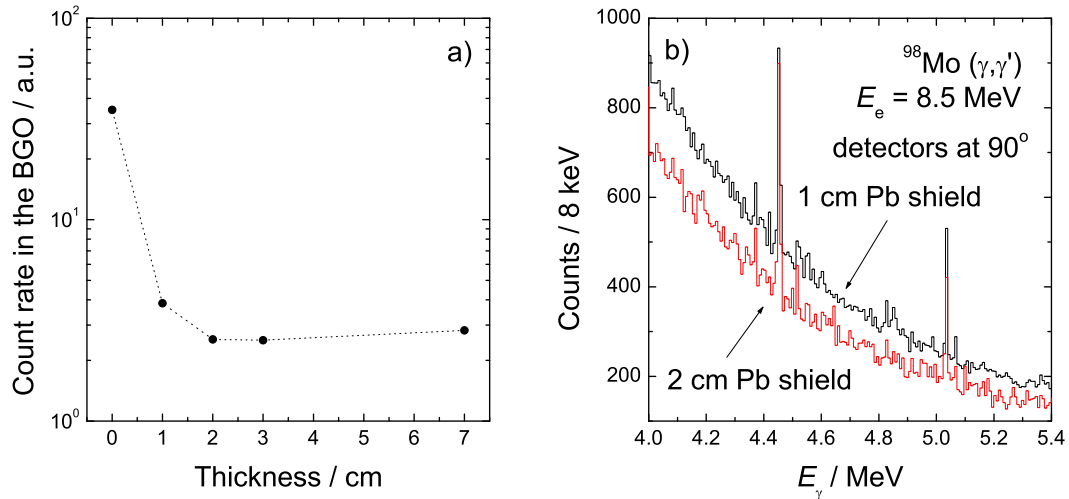


Figure 3.13: Dependence of the count rates in the BGO shield a) on the lead shield thickness. The absence of a shield is denoted with a thickness of 0 cm. Comparison b) between spectra measured with different Pb shield thicknesses. The spectra are normalized to the photon flux deduced from the 5020 keV transition in  $^{11}\text{B}$ .

collimator and from the background radiation by using lead shields. The lead collimator [Ruse03] and the lead shield were designed by performing GEANT3 simulations described in the follow paragraphs.

### Pb collimators

In order to optimize the collimators of the detectors, GEANT3 simulations were performed within the present work. A realistic geometry of the HPGe detector and the BGO shield has been implemented in the simulations. Monoenergetic  $\gamma$ -rays with energies of 7, 10, 13 and 16 MeV were generated from the surface of the NRF target. A histogram of the energy deposited in the HPGe crystal was collected when there is no energy deposition in the BGO shield for varying entrance and exit diameters of the lead collimator. Two competing criteria were used in order to obtain the optimum geometry of the collimator. The first criterion is to maximize the ratio of full-energy peak to total background (FE-to-Total). Fig. 3.12 a) shows this ratio versus the entrance and exit diameters of the collimator cone. The ratio shows a flat distribution with a maximum at small diameters. The second criterion is to get a large full-energy-peak (FE-peak) area. Fig. 3.12 b) shows the FE-peak area versus the two collimator diameters. This quantity increases with increasing opening angle of the collimator. A good compromise is a point in the flat part of the ratio FE-to-Total for which the FE-peak area is as big as possible. The entrance and exit diameters of the collimator were selected to 30 mm and 50 mm, respectively. This point is marked with a cross in Fig. 3.12.

### Pb shields

A lead shield surrounding the BGO detector is used to reduce the background radiation from outside. The probability for the scattering of direct radiation from the NRF target inside the shield increases with the volume of the shield, since the shield itself acts as a secondary source of radiation. Therefore the usage of a thick shield is not desired. Monte Carlo simulations were performed in order to optimize the thickness of the lead shield with respect to minimum count rates in the BGO shield. In the simulations monoenergetic photon beams irradiate a lead target with a mass of 3 g. The photons scattered from the target may scatter again in the beam-pipe back to the detector or scatter in the lead

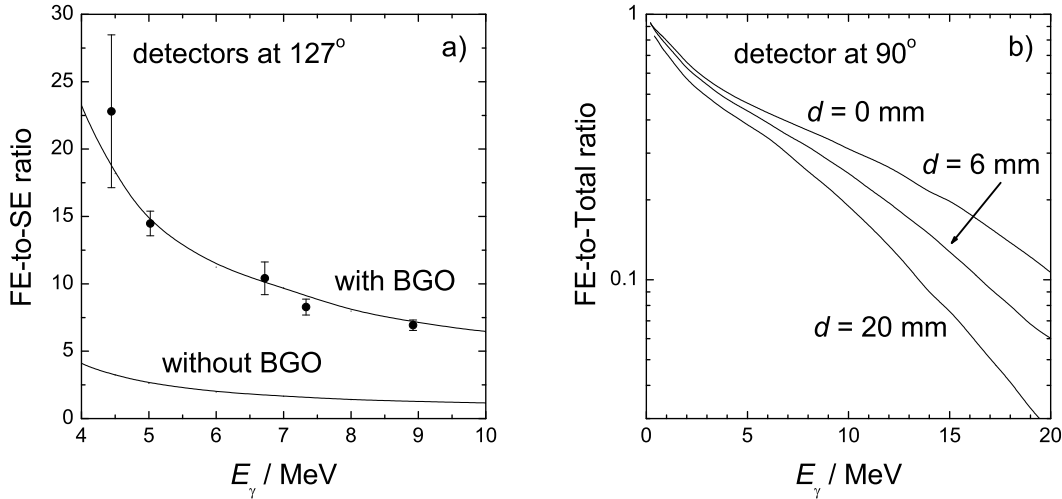


Figure 3.14: Simulations a) for the ratio of the full energy peak to the single escape one (FE-to-SE) and b) the ratio of the FE peak to the total counts in the spectrum (FE-to-Total) for different absorber thicknesses  $d$ .

shield. The simulations were performed for four beam energies of 5, 10, 15, and 20 MeV, respectively. The results of averaging over the different beam energies for the count rates of the BGO detector are presented in Fig. 3.13 a) for several thicknesses of the lead shield. The count rates show a minimum at 2 cm and slowly grow up with increasing thickness of the shield. A comparison between HPGe spectra with 1 cm and 2 cm lead shields is shown in Fig. 3.13 b). The spectra are normalized to the same photon flux deduced from the 5020 keV transition in  $^{11}\text{B}$ . Lead shields with thickness of 2 cm were installed at all four HPGe detectors according to the presented results.

### 3.4 Investigation of background in the measured spectra

The background in the measured spectra can be divided into three parts with respect to the origin of the background particles. The photons which are non resonantly scattered from the NRF target lead to a continuous background in the measured spectra called here a “target background”. Part of them may scatter again in structure material close to the detector. The background events from outside-photons is called “room background”. The background due to incomplete absorption of photons in the detector is called “detector background”. In this Section the three contributions to the background in the measured spectra are discussed. Simulations are compared with results of measurements. The Section ends with a summary of achieved results for the reduction of the background.

#### 3.4.1 “Detector background”

In nuclear spectroscopy high-purity germanium detectors (HPGe) are used for high-resolution  $\gamma$ -ray detection. The HPGe detectors have a rather small detection efficiency at high  $\gamma$ -ray energies because of the strong energy dependence of the photo effect. The processes of pair creation and Compton scattering play a dominant role at high energies and produce a background in the measured spectra called “detector background”. An escape-suppression shield of bismuth germanate (BGO) scintillation detectors is used in order to reduce the background events (cf. Fig. 3.11 a). Within the present work GEANT3 simulations were performed in order to investigate the influence of the escape-suppression shield to the background in the spectrum and for a verification of the detector-setup performance. The real HPGe detector and BGO shield geometry was implemented in the present simulations. Monoenergetic  $\gamma$ -rays with varying energies from 0 to 20 MeV were generated at the place of the NRF

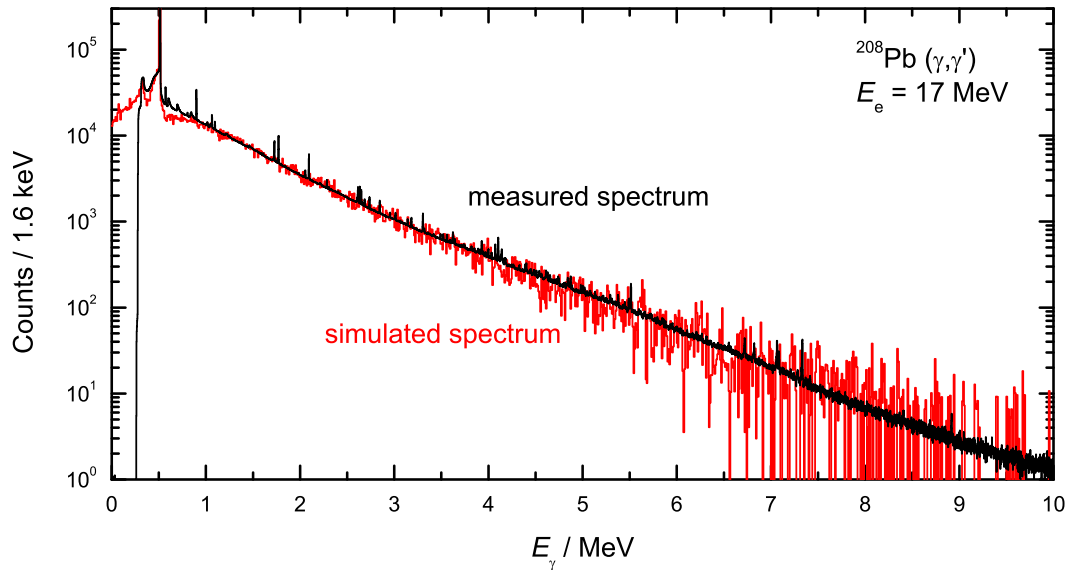


Figure 3.15: Comparison between a measured spectrum at  $90^\circ$  from the  $^{208}\text{Pb}(\gamma, \gamma')$  experiment at  $E_e = 17$  MeV and a simulated one for the same experimental conditions.

target. The ratio of the full-energy peak (FE) to the single escape one (SE) was extracted from the simulated spectra. Fig. 3.14 a) shows a comparison between the experimentally deduced FE-to-SE ratio and the one obtained from the simulations (the solid lines) with and without including a veto from the BGO shield. From the comparison a significant reduction of the background by usage of an active escape-suppression shield is visible.

A lead absorber is placed in front of the HPGe detector in order to reduce the amount of detected low-energy photons scattered from the NRF target. The usage of absorbers is necessary because the low-energy photons produce high count rates in the detector and limit its work. The simulations mentioned above were performed for different absorbers and with active BGO shield. Results for the ratio of full-energy peak to the total background in the simulated spectrum (FE-to-Total) are presented in Fig. 3.14 b). The results show that the usage of thick absorber has two negative features: (i) a reduction of the detector efficiency and (ii) an increase of the background in the spectra due to scattering inside the absorber which result in a reduction of the FE-to-Total ratio at high energy.

### 3.4.2 “Target background”

The scattering processes of photons in the NRF target are investigated in the present work with Monte Carlo simulations using the program package GEANT3. The complete geometry of the detector setup was implemented in the simulations including the HPGe detectors, BGO shields, the detector lead shields and collimators and the beam pipe. The NRF target and absorbers correspond to ones used in performed NRF measurements. A photon beam was generated with uniform energy distribution from 0 to 20 MeV. The energy of the incident photon and the deposited energies in the HPGe crystals and the BGO shields were recorded in an event by event file. The uniform energy distribution of the incident photons was folded with a bremsstrahlung spectrum and spectra were sorted for all detectors with BGO-veto in an off-line analysis. This kind of simulations provides enough statistics at high energy in the simulated spectra and gives a possibility for a sort of spectra at different conditions as bremsstrahlung end-point energy, for instance. An example of the comparison between simulated and measured spectra at  $90^\circ$  is shown in Fig. 3.15 for the case of 2 g  $^{208}\text{Pb}$  target and  $E_e = 17$  MeV. The simulations were performed for  $10^{11}$  incident photons. The NRF spectra are characterized by two features: (i) a huge 511 keV peak and (ii) a continuous background extended up to  $E_e$ . Simulations

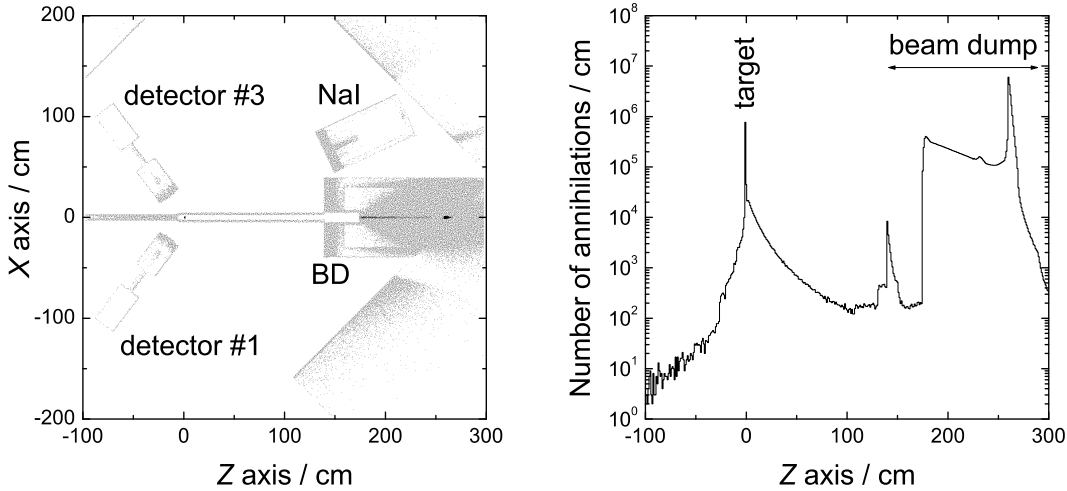


Figure 3.16: Places of annihilation at a plane along the photon-beam axis a). The vertical  $Y$  range is taken from  $-2.5$  cm to  $2.5$  cm. A projection of figure a) on the  $Z$ -axis is presented on the right panel b).

showing the places where annihilation happens were performed in order to localize the source of 511 keV rays. The complete geometry of the experimental cave (cf. Fig. 3.2) was implemented in the GEANT3 simulations including the detector setup, the NaI detector, the photon-beam dump and the concrete walls. Results of the simulations for a 2 g Pb target and a 10 MeV monoenergetic photon beam are presented in Fig. 3.16. Fig. 3.16 a) shows the places where an annihilation happens at a horizontal plane along the photon beam. A quantitative estimate of the annihilation is presented in Fig. 3.16 b) where only the  $z$ -component of the position is counted. Two main sources of 511 keV rays can be localized as result of the simulations - the NRF target and the photon-beam dump. Because the PE block of the photon-beam dump is shielded with a thick lead wall and the HPGc detectors are well shielded against the backscattered radiation from the photon-beam dump the observed 511 keV in the measured spectra is mainly due to the positron annihilation in the NRF target.

The second characteristic of the NRF spectra, the extended background, was investigated on the base of decomposition of the background to different scattering processes which take place in the NRF target. Simulations were performed for  $10^{10}$  incident photons and 3 g <sup>nat</sup>Mo target according to the procedure described above. A histogram called “All processes” contains the detected photons without applied restrictions to the process of interaction of the beam photons with the target matter. The other two histograms called “Compton scattering” and “Pair creation” were collected when the first process of photon interaction with the target is a Compton scattering or a pair creation, respectively. These histograms also do not contain events with subsequent bremsstrahlung from produced charged particles. The comparison in Fig. 3.18 shows that the contribution of the “pure” Compton scattering or pair creation is negligible. The way of selecting a process does not exclude combinations between Compton scattering and pair creation. The high-energy background in the histogram “Compton scattering” can, however, be explained by subsequent pair creation and the low-energy background in the histogram “Pair creation” can be explained by subsequent Compton scattering. The histogram called “Bremsstrahlung” contains events with subsequent bremsstrahlung produced in the target. Fig. 3.18 shows that “All processes” and “Bremsstrahlung” are almost identical. The bremsstrahlung production from the electrons and positrons from Compton scattering or pair creation cause the high-energy background in the measured spectra. Additional simulations were performed to show the energy and angular distribution of electrons and positrons produced in the target. The same <sup>nat</sup>Mo target has been defined and the beam was monoenergetic with energy of 10 MeV. Fig. 3.17 shows the number of electrons (Fig. 3.17 a) and positrons (Fig. 3.17 b) with respect of their energy and



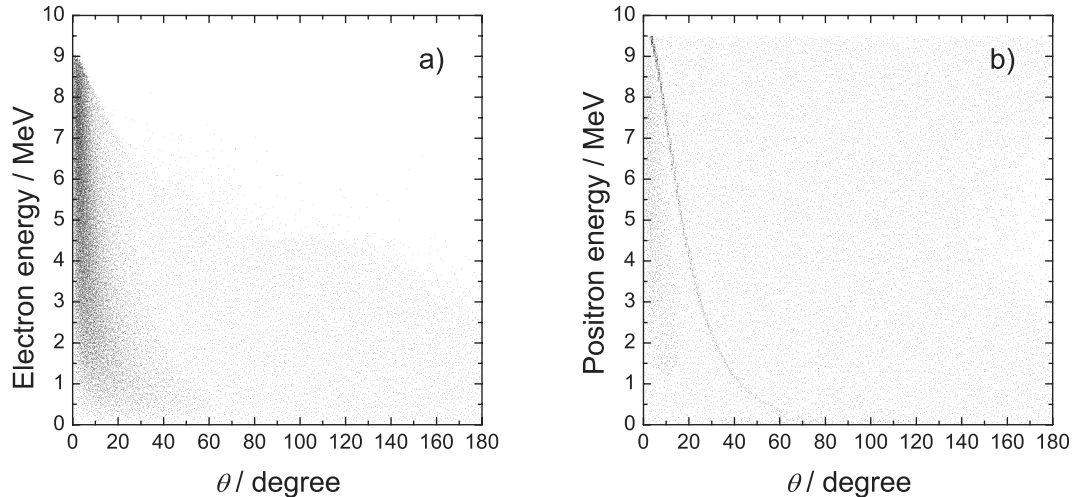


Figure 3.17: Results from GEANT3 simulations for the energy and angular distribution of produced electrons a) and positrons b) in 3 g  $^{\text{nat}}\text{Mo}$  target from monoenergetic photon beam with energy of 10 MeV.

momentum direction with respect of the photon beam. It is visible that electrons or positrons exist with energies close to the beam energy emitted even under  $90^\circ$ . From the bremsstrahlung angular distribution (cf. Fig. 3.3 b) it is clear that background photons can be observed even under  $127^\circ$ .

Knowing that the background in the spectra is a result of bremsstrahlung in the target and that its cross section is proportional to  $Z^2$  one can expect that the background does not depend linearly of the mass of the target. Measurements and simulations were performed for  $E_e = 12$  MeV and  $^{\text{nat}}\text{Mo}$  targets with different masses 1 g and 3 g, respectively. The spectra are normalized to the mass, i.e. the spectrum of 3 g  $^{\text{nat}}\text{Mo}$  target is multiplied to the ratio 1/3. The results of the measurement and the simulations are presented in Fig. 3.19 a) and Fig. 3.19 b), respectively.

An other effect of the bremsstrahlung produced in the target is that the background in the spectra depends on the orientation of the target. In order to reduce the self absorption the target is tilted under  $45^\circ$  with respect to the beam. That leads to bigger background in the spectra collected from detector #4 against #2. The reason for this is that the electrons or positrons emitted downward cross more target matter with respect to ones which move upward. In Fig. 3.20 a comparison is shown between measured and simulated spectra for  $^{208}\text{Pb}$  experiment at  $E_e = 17$  MeV from detectors #2 and #4 and a given orientation of the target. The opposite effect is observed if the target is tilted to the other direction. In this case detector #2 exhibits large background.

### 3.4.3 “Room background”

As “room background” the radiation from outside of the detector is considered. The “room background” can be divided to three parts with respect to the sources of radiation: (i) the electron-beam dump and radiator, (ii) the photon-beam dump and (iii) the photons scattered from the NRF target. A source for such “room background” radiation is the bremsstrahlung produced by the radiator. Part of the bremsstrahlung is collimated to a narrow photon beam and the rest has to be attenuated in the collimator and the concrete wall. Another source of radiation is the electron beam dump where the electron beam is stopped completely. The detector setup is shielded with a 1.6 m thick heavy concrete wall against the radiation from the accelerator hall. In addition one lead wall with thickness of 10 cm was installed in the accelerator hall between the electron beam dump and the concrete wall and another two walls with thicknesses of 20 cm each in the experimental cave (cf. Fig. 3.2). The last segment of the aluminum photon-beam collimator was exchanged with one made of TRIAMET.

A second source of “room background” is the photon-beam dump providing photons scattered back

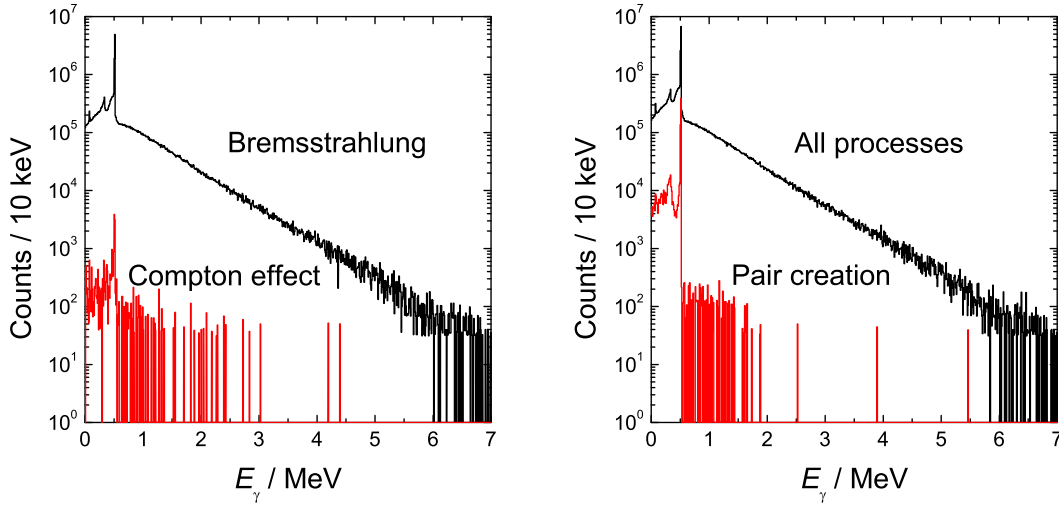


Figure 3.18: Simulations of the energy deposited in a HPGe detector for 3 g  $^{\text{nat}}\text{Mo}$  target and photon beam with end-point energy of 12 MeV. The spectra labeled with “Compton effect” and “Pair creation” contain events where the first scattering process of a beam photon in the target is a Compton scattering or a pair creation, respectively, but bremsstrahlung from the secondary electrons or positrons does not occur. The spectrum “Bremsstrahlung” is collected when the scattering of the beam photon in the target is followed by bremsstrahlung production. The spectrum “All processes” is simulated without any conditions. All spectra correspond to  $10^{10}$  incident photons.

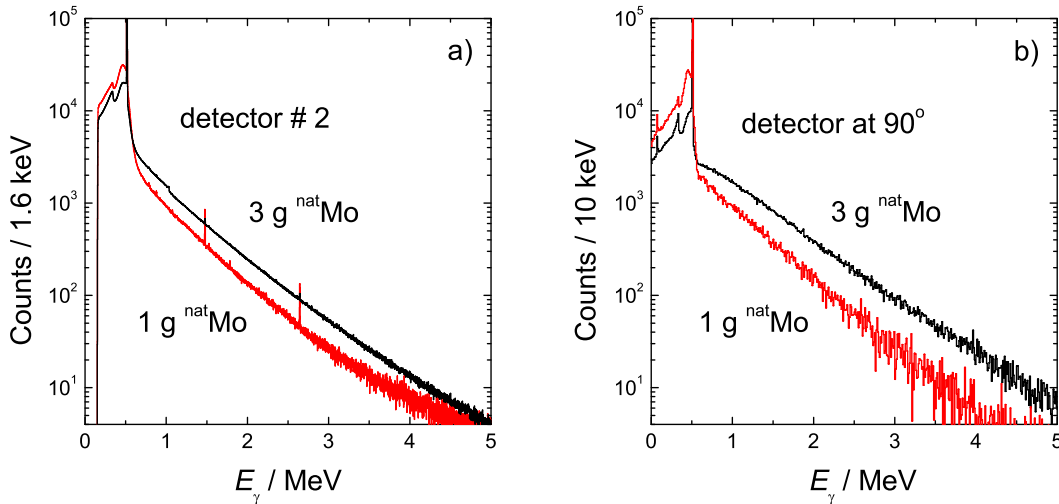


Figure 3.19: Comparison between a) spectra measured at different masses of  $^{\text{nat}}\text{Mo}$  target at  $E_e = 12$  MeV and b) spectra simulated for the same experimental conditions. The measured and simulated spectra for the 3 g  $^{\text{nat}}\text{Mo}$  target are divided by 3.

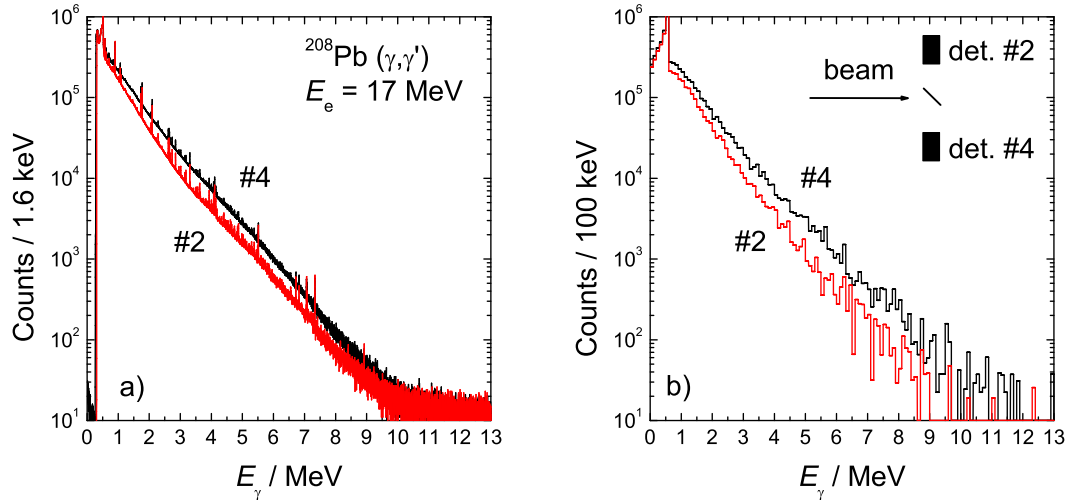


Figure 3.20: Comparison between spectra a) measured at  $90^\circ$  up (#2) and down (#4) in the  $^{208}\text{Pb}$  ( $\gamma, \gamma'$ )  $E_e = 17$  MeV experiment and simulated ones b) at the same conditions. The orientation of the target is shown in the upper right corner of b).

to the detector setup (cf. Fig. 3.8). The shields of lead walls and the heavy concrete wall and the optimized photon-beam dump should provide conditions with low background. A measurement with a photon beam but without NRF target was performed to prove the quality of the experimental setup. A spectrum collected at  $90^\circ$  for 8 hours at  $E_e = 9$  MeV is shown in Fig. 3.21 a). A background spectrum without beam is presented in Fig. 3.21 b) for comparison. The two spectra are normalized to the measuring time. The comparison shows that the background with beam is about two times bigger than the natural background and extended to about 6 MeV. A third source of “room background” are the photons scattered from the NRF target which may scatter in the surrounding material back to the detectors. The contributions to the background from photons scattered from different parts of the setup were investigated by performing Monte-Carlo simulations with GEANT3 program package. Elements of the setup were the aluminum beam pipe, the front wall of the photon-beam dump, the photon-beam dump and the concrete walls. The simulations were performed for monoenergetic photon beams with three different energies of 5, 10 and 15 MeV and the number of the photons which hit the detector setup was counted. An example for the results at 10 MeV photon-beam energy is shown on Fig. 3.22 a). The arrows show the possible tracks and the relative amount of scattered photons to the detectors. The biggest contribution to the background is given by the beam pipe. The radiation scattered from the beam pipe can be reduced by using a tube made of a low  $Z$  material. The same simulations were performed for a polyethylene (PE) beam pipe which produces by a factor of two less background compared with the aluminum one. According to these results the Al pipe was exchanged with a PE one. A comparison of experimental spectra from  $^{100}\text{Mo}$  at  $E_e = 9$  MeV with PE and Al beam tube is given in Fig. 3.22 b). The spectra are normalized the the same photon-flux. The exchange of the Al beam tube with a PE one yielded to about 25 – 30 % background reduction in the measured spectra.

The achieved results for reduction of the background in the measured spectra are summarized in the following:

- The radiation from the accelerator-hall side has to be minimized. A heavy concrete wall with a thickness of 1.6 m and three lead walls with a total thickness of 50 cm are used to absorb the photons from the electron-beam dump and the radiator which do not pass the hole of the photon-beam collimator. The last segment of the photon-beam collimator was replaced with one made of tungsten composite to prevent the not absorbed photons in the collimator from reaching the Si and HPGe detectors [Schi04].

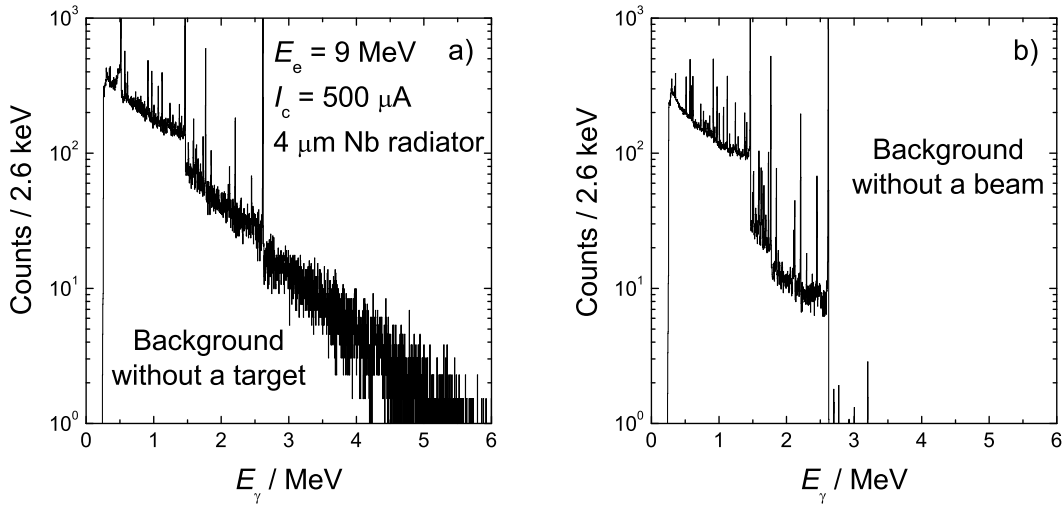


Figure 3.21: Comparison between a background spectrum measured without a target a) with photon beam and a spectrum measured without a beam. The spectra are measured at  $90^\circ$  and normalized to the measuring time.

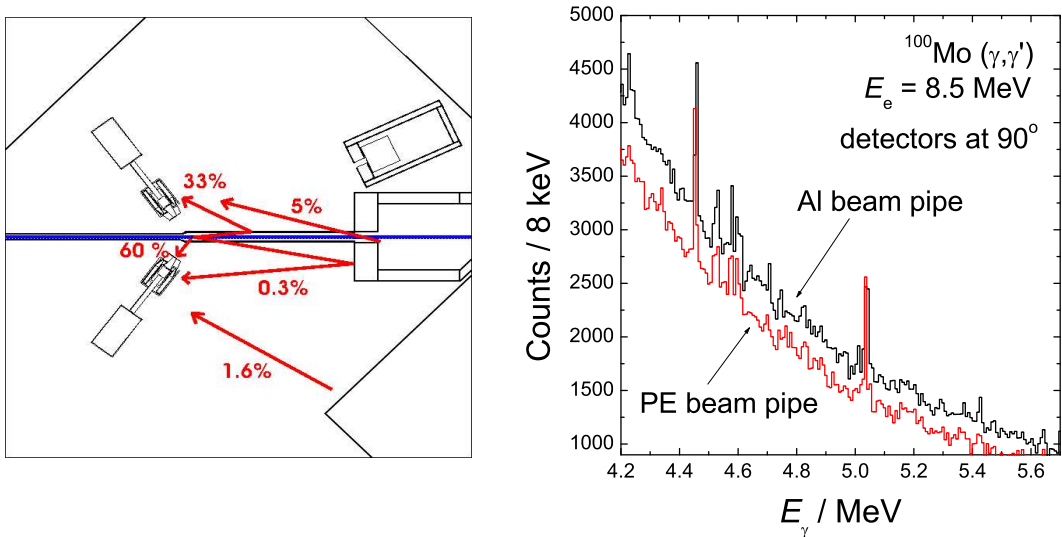


Figure 3.22: Schematic picture of the experimental cave. The photon beam goes from the left to the right. The results from the GEANT3 simulations at 10 MeV photon beam energy for the contributions to the background are shown with arrows. The amount of all  $\gamma$ -rays which cross the volume of the detectors is 100 %.

- The photon-beam dump was designed [Wagn01a] to remove the photons after passing the NRF target. It was additionally optimized to reduce the back-scattered photons (cf. Fig. 3.8).
- All materials surrounding the NRF target have to be made of low  $Z$  elements because they become secondary sources of radiation (cf. Fig. 3.22 a). The exchange of the aluminum beam pipe by a polyethylene one yielded about 25-30 % reduction of the background in the measured spectra (cf. Fig. 3.22 b). In a related subject the photon-beam dump has to be placed as far as possible from the detector setup.
- According to the previous point the thickness of the lead shield of the detectors was optimized in order to not generate extra radiation (cf. Fig. 3.13).
- The usage of thin absorber increase the efficiency of the detector and the ratio FE-to-Total in the measured spectrum (cf. Fig. 3.14 b). The high count rates of the detector can be reduced by using a thick hardener or one made of high  $Z$  material.
- To be efficient, the BGO shield has to be protected from the photons scattered from the NRF target. A lead collimator was designed for this purpose with a conical hole optimized to provide a high ratio FE-to-Total (cf. Fig. 3.12 a) and a high FE-peak area (cf. Fig. 3.12 b) in the measured spectra.
- As was shown the background radiation in the spectra depends strongly on the thickness of the NRF target (cf. Fig. 3.19). The background can be reduced by selecting a thin target and increasing the duration of the NRF experiment.

### 3.5 Data acquisition

The NRF setup used in experiments presented in this work consists of four 100 % HPGe detectors with BGO escape-suppression shields, four Si detectors and one cylindrical NaI detector of 25.4 cm diameter and 25.4 cm length (10"  $\times$  10"). A schematic diagram of the data acquisition system is presented in Fig. 3.23. In the following the separate electronics channels, marked with dashed lines in Fig. 3.23, are briefly described. The signals from the HPGe detector are amplified by a preamplifier mounted close to the Ge crystal. The first stage of the preamplifier is cooled by liquid nitrogen together with the Ge crystal for reduction of electronic noise. The electric signal is transported through a 40 m long shielded coaxial cable (RS223) to a separate air conditioned room (electronics room). The signal is amplified by a Main Amplifier (MA, Ortec<sup>2</sup> 671) and digitized by a 14 bit Analog to Digital Converter (ACD, Silena<sup>3</sup> 7423 UHS-S). The digital number corresponds to an address in a 24 bit memory buffer (Swistec<sup>4</sup> L&S) with length of 16 K in which the value of addressed memory cell is incremented.

The time signals are amplified by the Timing Filter Amplifier (TFA, Ortec 474). The Constant Fraction Discriminator (CFD, Ortec 584) converts the signals from the TFA's into a logic pulse. The logic pulses from all detectors are sent to a coincidence scheme (LeCroy<sup>5</sup> 4516) which generates gates to the memory buffers if a veto from the corresponding BGO is absent. The anti-coincidence with the BGO signal is with resolution of 15 ns for high-rate capability of the veto and low suppression due to false coincidences.

Each BGO shield consists of 8 crystals with individual photo-multiplier tubes (PMT) and preamplifier. The analog signals from the crystals of one BGO shield are summed up and transported to the electronics room by shielded 50  $\Omega$  cables. The logical signal is produced by Leading Edge Discriminator (LeCroy 4608C) and sent to the coincidence unit.

The signals from the 7 PMT of the NaI detector are also summed and transported to the electronics room. They are digitized by 13 bit ADC (Ortec AD413A).

The signals from the Si detectors are preamplified (Canberra<sup>6</sup> 2003BT) and transported to the electronics room. There they are amplified (Silena 761F) and digitized (Ortec AD413A). All Ortec AD413A

<sup>2</sup>Ortec, 801 South Illinois Avenue, Oak Ridge, TN 37839, U.S.A.

<sup>3</sup>SILENA, Via Firenze 3-20063 Cernusco s/Naviglio, Italy.

<sup>4</sup>Swistec GmbH, Graue Burg Straße 24-26, 53332 Bornheim, Germany.

<sup>5</sup>LeCroy, 700 Chestnut Ridge Road, Chestnut Ridge, NY 10977-6499 U.S.A.

<sup>6</sup>Canberra Industries Inc., 800 Research Parkway, Meriden, Connecticut, 06450 U.S.A.

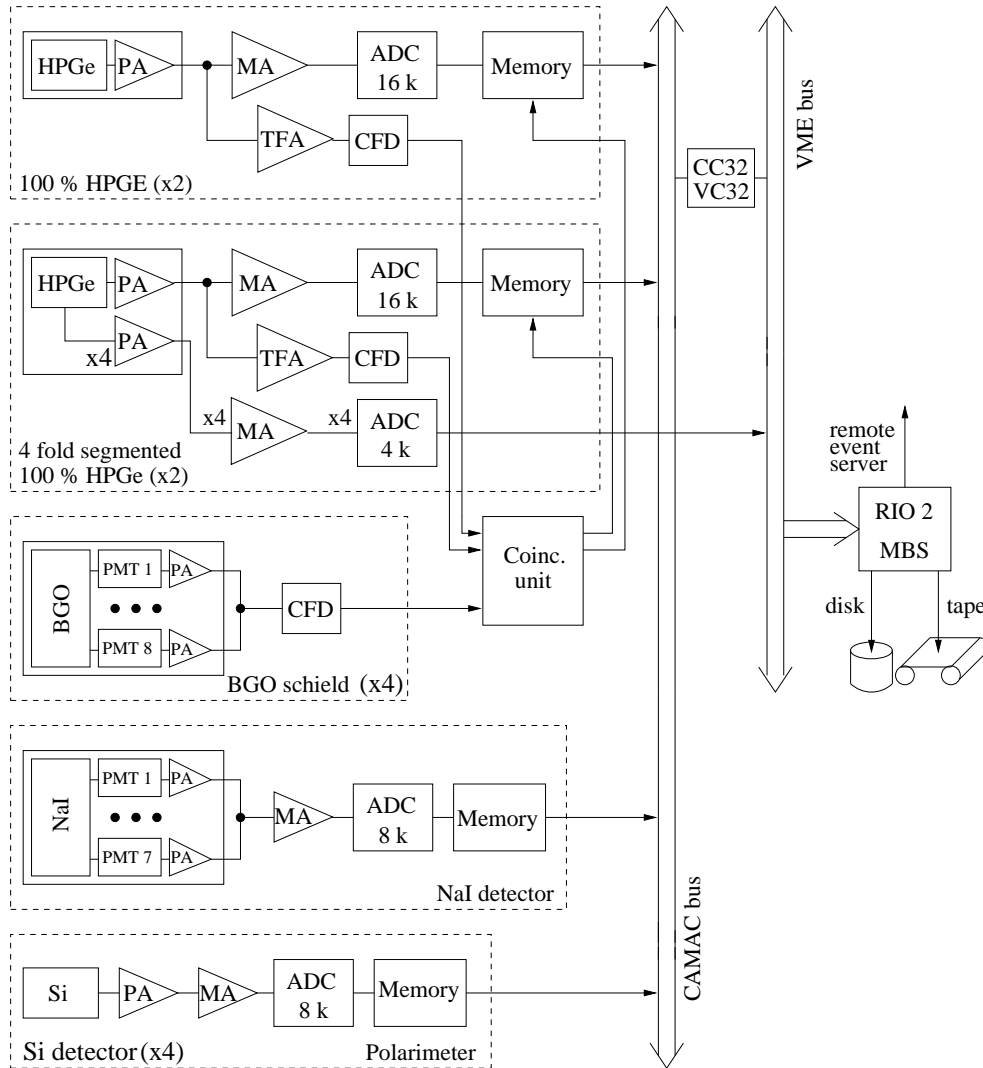


Figure 3.23: The data acquisition used in the photon-scattering experiments.

ADC's increment a memory buffer (Ortec HM413). Information from the AD413A are stored into a memory buffer by FERA bus.

The high voltage for the HPGe detectors and the PMT's is supplied by a multichannel power supply system (CAEN SY527). A 4-fold supply (Ortec 710) provides the bias of 25 V for the 300  $\mu\text{m}$  thick Si detectors.

The information stored in the memory cards is read by a front-end computer CES<sup>7</sup> RIO2 (Power PC CPU, 200 MHz, 64 MB RAM) using the real-time operation system Lynx OS. A data acquisition program MBS (Multi Branch System) [Bart00] controls the read-out and stores the information to tape or disk and sends it to a remote events server via the net. The read-out of the CAMAC modules is performed by VME-CAMAC interface (Wiener<sup>8</sup> VC32-CC32)

The on-line control to the acquisition is done on a separate computer, where the events are collected in individual histograms using the program LEA (Lean Easy Analysis) [Esse02] which takes the information transferred from the front-end computer.

For on-line and off-line monitoring purpose of slow control parameters a data exchange path based on an OPC (open connectivity) client-server model has been installed [Wagn05b]. Data from the accelera-

<sup>7</sup>CES, CH-1212 Grand-Lancy 1, Switzerland.

<sup>8</sup>W-IE-NE-R, Plein & Baus GmbH, Müllersbaum 20, 51399 Burscheid, Germany.

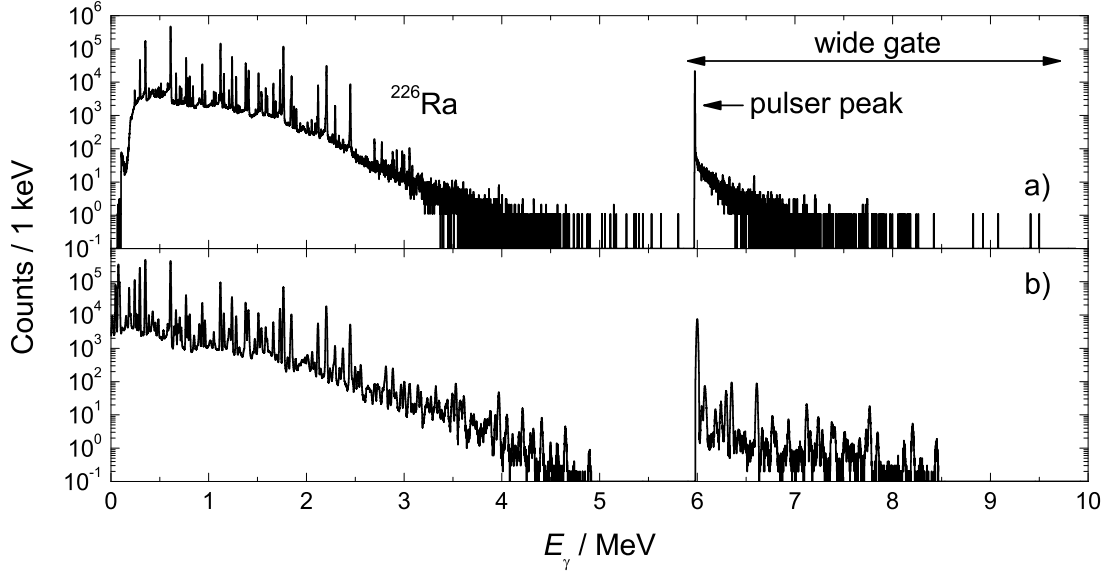


Figure 3.24: Comparison of measured spectrum with  $^{226}\text{Ra}$  source and pulser a) with simulated spectrum with included pile-up effect b). The measured and the simulated spectra were at 10 kHz rate of the  $^{226}\text{Ra}$  source and 50 Hz rate of the pulser. The simulated spectrum is folded with the experimental resolution given in Fig.4.1 b).

tor control are inserted into the data stream with a frequency of 10 Hz. The monitored parameters are:

- Electric field gradient of accelerator
- Micropulse and macropulse duration
- Beam-position-monitor information
- Currents of steerer and purging magnets
- Electron current in the e-gun
- Electric current in the dump
- Radiator and hardener position
- Count rates of the HPGe and BGO detectors

The measured spectra are modified by the effect of pile-up which happens in the preamplifier or the main amplifier. It is a pure effect of the electronics of summing of two pulses which come in a short time interval. An estimate of the pile-up can be obtained in a source measurement with included a pulser signal to the “test” input of the detector. An example spectrum of a  $^{226}\text{Ra}$  source with pulser is presented in Fig. 3.24 a). The superposition of the pulser signal and the signal from the detector gives a signal at energy higher than the amplitude of the pulser. In this work the quantity pile-up (PU) is used in sense of relative amount of the counts removed from the peak due to the pile-up effect:

$$\text{PU} = \frac{A_{\text{w.g.}} - A_{\text{pulser}}}{A_{\text{w.g.}}}, \quad \left( \frac{\Delta\text{PU}}{\text{PU}} \right)^2 = \frac{1}{A_{\text{w.g.}}} + \frac{A_{\text{w.g.}} + A_{\text{pulser}}}{(A_{\text{w.g.}} - A_{\text{pulser}})^2}, \quad (3.3)$$

where  $A_{\text{w.g.}}$  is the area of a wide gate including the pulser peak and  $A_{\text{pulser}}$  is the area of the pulser peak. Measurements of the pile-up for various rates of the  $^{226}\text{Ra}$  source and various amplitudes of the pulser are presented in Fig. 3.25 a) and b), respectively. The main amplifier provides a veto signal when pile-up occurs. Measurements with and without pile-up rejection (PUR) are presented in Fig. 3.25. The usage of PUR rejection brings a reductions of 1.8 times the pile-up events. The experiments included in this work were performed with PUR.

A simple model of the pile-up is applied in order to reproduce the redistribution of the counts in the spectrum caused by the pile-up effect. The time-interval distribution between two signals is given by:

$$f(\Delta t) = \lambda \exp(-\lambda \Delta t), \quad (3.4)$$

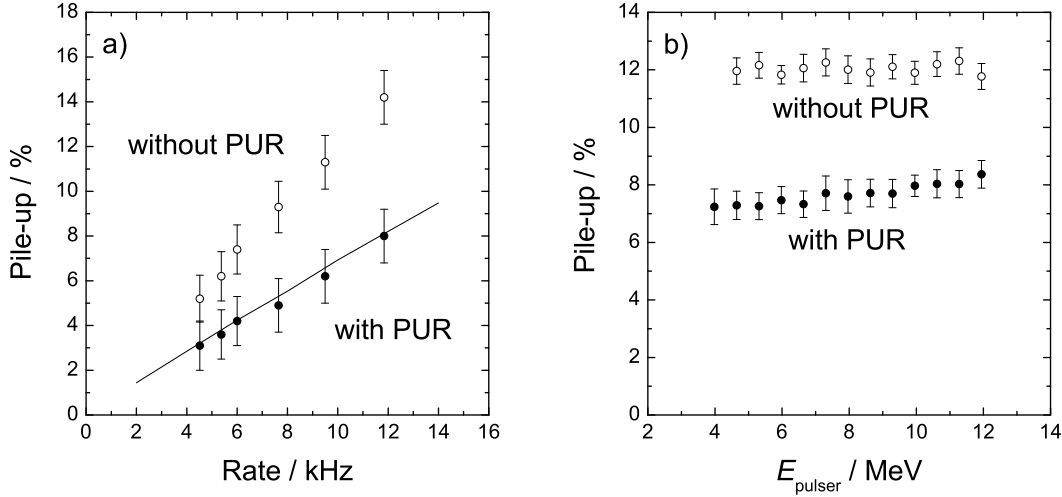


Figure 3.25: Dependence of the pile-up effect on the counting rate a) and on the amplitude of the pulser b) for 10 kHz rate of the source presented as data points. Results of simulations are shown as solid line.

where  $\lambda$  is the counting rate of the detector and  $\Delta t$  is the time interval. A pile-up is supposed to happen when the time interval  $\Delta t$  is smaller than some maximum time  $t_{\text{max}}$ . An information about the typical counting rates of the HPGe, BGO and the Si detectors is presented in Table 3.2.

GEANT3 simulations were performed in order to determine the time  $t_{\text{max}}$ . The geometry of the HPGe detector, the BGO shield and the lead collimator were implemented in the simulations. Gamma rays with energy and intensity distributions corresponding to the  $^{226}\text{Ra}$  source were emitted from the place of the target. A spectrum of energy deposited in the HPGe was collected when there was no veto from the BGO detector. A time interval  $\Delta t$  was assigned after every event in the simulations. If  $\Delta t$  was smaller than  $t_{\text{max}}$  the deposited energy in the HPGe from the present event and the previous one are added. The appearance of the pulser signal was included as a random generator after every event which satisfies the ratio of the rates of the pulser to the source. The time  $t_{\text{max}}$  was varied till the simulated pile-up reproduces the measurement. Results for  $t_{\text{max}} = 10.5 \mu\text{s}$  are presented in Fig. 3.25 a) as a line. An example spectrum from the simulations is shown in Fig. 3.24 b). It is additionally folded with the experimental resolution (cf. Fig. 4.1 b). The pulse shape of the main amplifier has to be included in the simulations for better agreement with the measured spectrum.

Table 3.2: Typical counting rates of the HPGe, BGO and the Si detectors.

experiment	HPGe (1000*s) <sup>-1</sup>	BGO (1000*s) <sup>-1</sup>	Si (1000*s) <sup>-1</sup>
$^{92}\text{Mo}$ at $E_e = 13.2$ MeV	9.3	18.3	3.6
$^{92}\text{Mo}$ at $E_e = 6$ MeV	5.0	7.6	0.4
$^{98}\text{Mo}$ at $E_e = 13.2$ MeV	10.4	17.6	3.9
$^{100}\text{Mo}$ at $E_e = 13.2$ MeV	11.2	19.7	3.5
$^{100}\text{Mo}$ at $E_e = 8.0$ MeV	1.6	2.9	0.3



# Chapter 4

## Data analysis

In this Chapter, the analysis of the measured spectra and the determination of the experimental observables are described. The determination of the efficiency function of the HPGe detectors at higher energies than the one provided from the transitions of the calibration sources is discussed in the frame of performed Monte-Carlo simulations. An analysis of the measured proton spectra is performed in order to determine precisely the spectral distribution of the beam photons as well as the bremsstrahlung end-point energy and the energy spread of the electron beam. A method for determination of the resonant continuum based on GEANT3 simulations for the detector response and for the distribution of the photons scattered from the target is described. A Monte Carlo code for  $\gamma$ -ray cascade simulations was developed as a tool in the analysis of the continuum and corrections for branching and feedings.

### 4.1 Determination of peak energy

The small cross sections for the  $(\gamma, \gamma')$ -reaction required measurements with long durations separated into several runs. Spectra of different runs were energy calibrated and then added up in order to prevent possible shifts in the positions of the peaks caused by instabilities in the electronic measuring chain. The known transitions of  $^{11}\text{B}$  and of  $^{13}\text{C}$  and  $^{27}\text{Al}$  (see Appendix A) were used for energy calibration in the experiments. Since the  $\gamma$ -rays are emitted from a recoiling nucleus their energy is shifted with respect to the transition energy due to the recoil energy and the Doppler shift. Expressions for Doppler shift and recoil energy are derived from the momentum and energy conservation laws. Considering the decay of a nucleus of mass  $M$  at rest, from an initial excited state  $E_i$  to a final state  $E_f$ ,  $E_x = E_i - E_f$ , then the recoil corrected  $\gamma$ -ray energy  $E_\gamma$  is given by the expression:

$$E_\gamma \cong E_x - \frac{(E_x)^2}{2Mc^2} \quad (4.1)$$

If the  $\gamma$ -rays are emitted under angles different than  $90^\circ$  then their energies change due to the Doppler shift:

$$E'_\gamma = E_\gamma \left(1 + \frac{E_\gamma}{Mc^2} \cos \theta\right) \quad (4.2)$$

where  $\theta$  is the angle of the detector relative to the beam. The calibration-transition energy is transformed to  $\gamma$ -ray energy according to Eqs. (4.1) and (4.2) and used for energy calibration of the measured spectra.

The used ADCs (SILENA 7423/UHS-S) have high differential linearity and an integral non-linearity less than 0.02 %. Therefore a polynomial of first degree is used for the fit of the experimental points:

$$E(x) = A_0 + A_1 \cdot x, \quad (4.3)$$

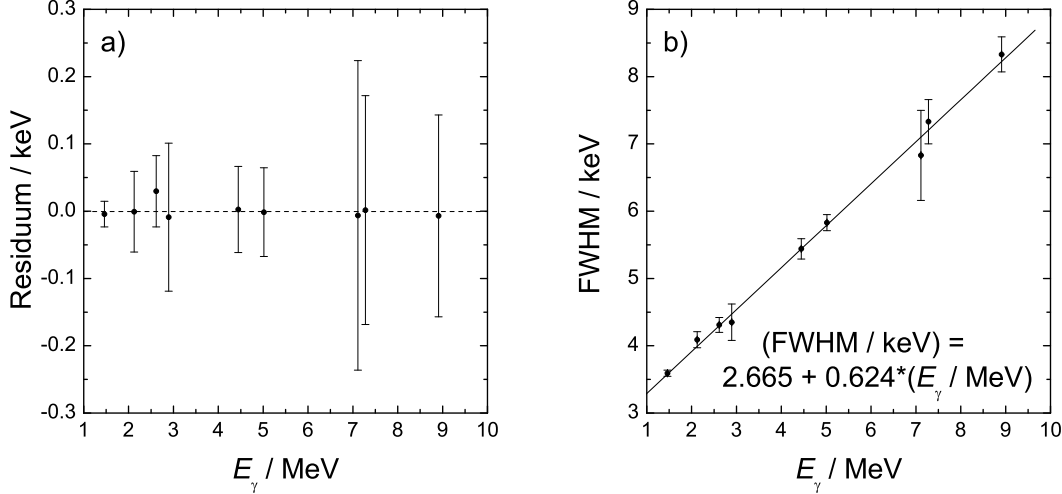


Figure 4.1: Residuum plot a) between linear energy calibration and peak energies for one of the detectors (#1) used in NRF setup at the ELBE accelerator and dependence b) of FWHM (Full Width at a Half Maximum) on the energy (solid line) for the sum spectrum of the two detectors at 127° (#1 and #3).

where  $x$  is the channel number and  $E(x)$  is the corresponding energy. A residuum plot between the linear fit and the centroid of the calibration peaks for one of the used detectors (#1) in the NRF setup at ELBE accelerator is shown in Fig. 4.1 a). The energy resolution of the detector is presented in Fig. 4.1 b). It is worse than in the laboratory measured of 2.75 keV at 1.33 MeV and binning of 0.2 keV/channel because of the used high compression of 1.3 keV/channel which is used to obtain a dynamic range from 0-20 MeV.

The obtained energies of the observed peaks have to be transformed back to the transition energy via the reverse to the relations (4.1) and (4.2):

$$E'_\gamma = E_\gamma \left(1 - \frac{E_\gamma}{Mc^2} \cos \theta\right), \quad (4.4)$$

$$E_x = E'_\gamma + \frac{E'^2_\gamma}{2Mc^2} \quad (4.5)$$

The NRF spectra are measured at different angles for spin assignment purpose. A weighted average  $\overline{E_x}$  over all detectors is calculated in order to be reduced the systematic uncertainty of determination of the transition energy:

$$\overline{E_x} = \left( \sum_{i=1}^2 \frac{E_{x,i}}{\Delta E_{x,i}^2} \right) \cdot \left( \sum_{i=1}^2 \frac{1}{\Delta E_{x,i}^2} \right)^{-1}, \quad \overline{\Delta E_x} = \left( \sum_{i=1}^2 \frac{1}{\Delta E_{x,i}^2} \right)^{-1}, \quad (4.6)$$

where the sum is over the number of detectors at different angles.

The programs “tv” [Theu90] and “gf3” [Radf95] were used for the analysis of the measured spectra.

## 4.2 Detector efficiency

The photo-peak efficiency function  $\epsilon(E_\gamma, \theta)$  depends on the solid angle of a detector placed at an angle  $\theta$  with respect to the beam axis and on the probability for detection of  $\gamma$ -rays with energy  $E_\gamma$  with photo-effect. The efficiency  $\epsilon(E_\gamma, \theta)$  of each detector can be obtained from the measurement of transitions of a standard source with known activities. The absolute efficiency for a given source

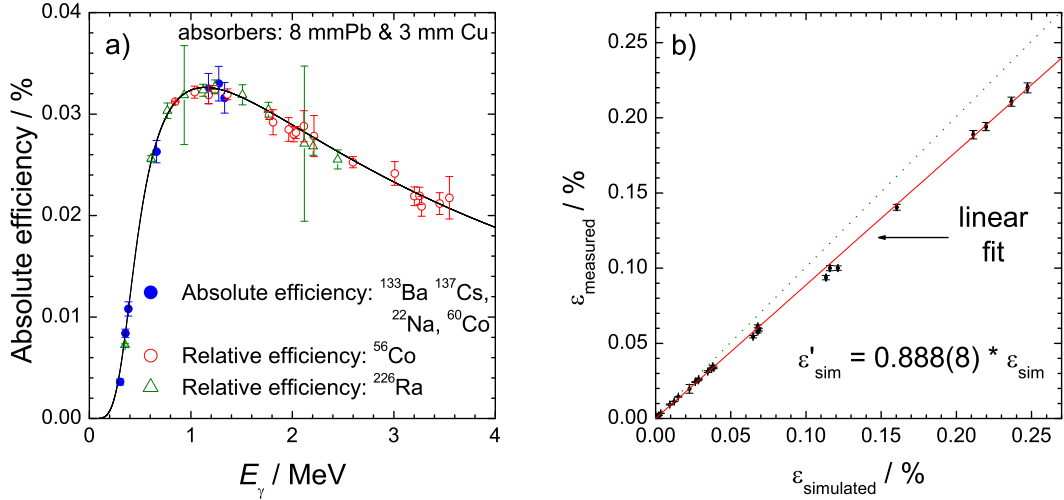


Figure 4.2: Comparison a) between measured and simulated (the solid line) absolute efficiency for detector # 1 and one particular set of absorbers. Correlation b) between measured and simulated efficiency for detector #2 obtained using different sets of absorbers. The solid line is a linear fit of the obtained points while the dotted line represents  $\epsilon_{\text{measured}} = \epsilon_{\text{simulated}}$ .

transition with energy  $E_\gamma$  and intensity  $\dot{N}_\gamma(E_\gamma)$  is deduced from the expression:

$$\epsilon(E_\gamma, \theta) = \frac{A/t_{\text{live}}}{\dot{N}_\gamma(E_\gamma)}, \quad \left(\frac{\Delta\epsilon}{\epsilon}\right)^2 = \left(\frac{1}{A}\right)^2 + \left(\frac{\Delta\dot{N}_\gamma}{\dot{N}_\gamma}\right)^2 \quad (4.7)$$

where  $A$  is the full-energy-peak area collected during the time  $t_{\text{live}}$ . The  $\gamma$ -ray intensity  $\dot{N}_\gamma(E_\gamma)$  is defined as the number of  $\gamma$ -rays with energy  $E_\gamma$  emitted isotropically from the source per unit of time. A set of sources from Amersham<sup>1</sup> was used for absolute efficiency calibration of the HPGe detector setup at Rossendorf. The set consists of  $^{133}\text{Ba}$ ,  $^{137}\text{Cs}$ ,  $^{22}\text{Na}$  and  $^{60}\text{Co}$  sources with certified activities with uncertainty of 4 % ( $3\sigma$ ). The highest available  $\gamma$ -ray energy is the 1332.5 keV transition in  $^{60}\text{Co}$ . A relative efficiency deduced from  $^{56}\text{Co}$  and  $^{226}\text{Ra}$  sources is used for the extension of the efficiency function up to 3.5 MeV. The  $^{56}\text{Co}$  source has been produced by the  $^{56}\text{Fe}(p,n)$  reaction at the Rossendorf cyclotron “CYCLONE 18/9” [Preu05]. Since the efficiency function can not be determined for energies higher than 3.5 MeV from source measurements a simulated efficiency was used in the analysis of the experiments performed at the ELBE accelerator. A realistic detector geometry including the HPGe crystal, the aluminum end-cup, the lead and copper absorbers and the polyethylene beam pipe was implemented in the GEANT3 simulations. Monoenergetic  $\gamma$ -rays were generated isotropically from the place of NRF target. The  $\gamma$ -ray energy was varied from 0 to 20 MeV and spectra of the deposited energy in the HPGe crystal collected for  $10^8$  generated  $\gamma$ -rays. The absolute efficiency is calculated as photo-peak area over  $10^8$ . The program “effit” from the RadWare package [Radf95] has been used for interpolation of the simulated efficiency points. The program fits the low- and high-energy range separately using the follow formula:

$$\ln(\epsilon(E_\gamma, \theta)) = [(A + B \cdot x + C \cdot x^2)^{-G} + [(D + E \cdot y + F \cdot y^2)^{-G}]^{-\frac{1}{G}} \quad (4.8)$$

where  $A - G$  are parameters of the fit,  $x = \ln(E_\gamma/100)$  and  $y = \ln(E_\gamma/1000)$  and the  $\gamma$ -ray energy is in keV. Fig. 4.2 a) shows a comparison between the simulated absolute efficiency, depicted with a solid line, and the measured one (bullets) for detector #1 used in the NRF setup at the ELBE accelerator. The relative efficiency obtained from  $^{56}\text{Co}$  and  $^{226}\text{Ra}$  sources shows that the simulations represent the

<sup>1</sup>AEA Technology QSA GmbH, Gieselweg 1, 38110 Braunschweig, Germany

shape of the efficiency function correctly. Because of the detector performance and the geometry of the HPGe crystal the simulated and the measured efficiency differ slightly by a constant factor. A sequence of source measurements was performed to obtain the normalization factor for the simulated efficiency. The detector efficiency was changed from almost zero to its maximal value by selecting different absorbers and by measurements without absorbers. Simulations were performed for every absorber set and compared with the measured values. Results of this investigation for detector #2 are presented in Fig. 4.2 b). The points are approximated with a linear fit depicted with a solid line. Assuming that the dependence between the simulated and measured efficiency will keep the same at high energies such procedure of correcting the results from simulations allows determination of the absolute efficiency over the energy range of observed transitions.

### 4.3 Spin assignment

It was shown in Section 2.2 that the resonantly scattered  $\gamma$ -rays have a certain angular distribution depending on the transition multipole order (see Eq. (2.16)). The transition multipole order can be obtained from a comparison of the efficiency and dead-time corrected  $\gamma$ -ray intensities  $I_\gamma$  at two different scattering angles,  $90^\circ$  and  $127^\circ$ :

$$\frac{I_\gamma(90^\circ)}{I_\gamma(127^\circ)} = \frac{A(90^\circ)/(\epsilon(90^\circ) \cdot t_{\text{live}}(90^\circ))}{A(127^\circ)/(\epsilon(127^\circ) \cdot t_{\text{live}}(127^\circ))} \quad (4.9)$$

A normalization factor  $C$  can be introduced in Eq. (4.9) such that the ratio of the expected angular-distribution ratio and the measured  $I_\gamma(90^\circ)/I_\gamma(127^\circ)$  one for known transitions of the calibration standard  $^{11}\text{B}$  is equal to unity. Such normalization factor removes the dependence of measuring time and a possible asymmetry in the detector setup. Then the Eq. (4.9) can be rewritten as:

$$R = \frac{I_\gamma(90^\circ)}{I_\gamma(127^\circ)} = \frac{A(90^\circ)/\epsilon(90^\circ)}{A(127^\circ)/\epsilon(127^\circ)} \cdot C, \quad (4.10)$$

$$C = \left( \frac{W(90^\circ)/W(127^\circ)}{\frac{A(90^\circ)/\epsilon(90^\circ)}{A(127^\circ)/\epsilon(127^\circ)}} \right)^{\text{cal.transition}}$$

The uncertainty of the ratio Eq. (4.10) assuming statistical independence is given by:

$$\left( \frac{R}{\Delta R} \right)^2 = \left( \frac{A(90^\circ)}{\Delta A(90^\circ)} \right)^2 + \left( \frac{A(127^\circ)}{\Delta A(127^\circ)} \right)^2 + \left( \frac{\epsilon(90^\circ)}{\Delta \epsilon(90^\circ)} \right)^2 + \left( \frac{\epsilon(127^\circ)}{\Delta \epsilon(127^\circ)} \right)^2 + \left( \frac{C}{\Delta C} \right)^2 \quad (4.11)$$

An assignment of the multipole order of the transition is made when one theoretical angular distribution ratio was within two standard deviations of the measured value and the other theoretical ratio was excluded by at least three standard deviations. If one of these two criteria was violated, the spin assignment is assigned tentatively.

### 4.4 Photon flux

The nuclear resonance fluorescence represents the resonant absorption of a real photon exciting a nuclear level and its subsequent decay by reemission of a photon. The photon scattering cross section can be obtained from the general definition for reaction cross section [Kran88]:

$$\sigma = \frac{R_\gamma(E_\gamma)}{\Phi_\gamma(E_\gamma)N_T}, \quad (4.12)$$

where  $\Phi_\gamma(E_\gamma)$  is the number of incident photons with energy  $E_\gamma$  per unit time,  $N_T$  is the number of target nuclei per area unit and  $R_\gamma(E_\gamma)$  is the rate of outgoing  $\gamma$ -rays. The number of  $\gamma$ -rays scattered

at an angle  $\theta$  in a solid angle  $\Omega$  is  $R'_\gamma(E_\gamma, \Omega) = R_\gamma(E_\gamma)W(\theta)\frac{\Omega}{4\pi}$ , where  $W_T(\theta)$  is the angular correlation function. If a detector with a solid angle  $\Omega$  is placed at angle  $\theta$  then the number of  $\gamma$ -rays  $C_T(E, \theta, t_{\text{live}})$  detected at an energy  $E_\gamma$ , a scattering angle  $\theta$  and a detector live time  $t_{\text{live}}$  is related to  $R'_\gamma(E_\gamma, \Omega)$ :

$$C_T(E_\gamma, \theta, t_{\text{live}}) = R_\gamma(E_\gamma)\frac{\epsilon(E, \theta)}{\frac{\Omega}{4\pi}}W_T(\theta)\frac{\Omega}{4\pi}t_{\text{live}}, \quad (4.13)$$

where  $\epsilon(E_\gamma, \theta)$  is the detector efficiency, defined in Section 4.2. The counts  $C_T(E_\gamma, \theta, t_{\text{live}})$  corresponding to an energy interval  $dE$  can be obtained from Eqs. (4.12) and (4.13) and assuming a Doppler shape of the absorption cross section  $\sigma_{D,T}(E_\gamma)$  (see Section 2.1):

$$C_T(E_\gamma, \theta, t_{\text{live}})dE = \Phi_\gamma(E_\gamma)\epsilon(E_\gamma, \theta)N_T\sigma_{D,T}(E_\gamma)W(\theta)t_{\text{live}}dE \quad (4.14)$$

The detector resolution (cf. Fig. 4.1 b) is in order of  $10^6$  times larger than the typical width of a narrow resonance (in the order of meV). Only the total peak area  $A_T(\theta, t_{\text{live}})$  can be obtained by energy integrating Eq. (4.14) over a single resonance:

$$A_T(\theta, t_{\text{live}}) = \int_0^{+\infty} C_T(E_\gamma, \theta, t_{\text{live}})dE = \Phi_\gamma(E_\gamma)\epsilon(E_\gamma, \theta)N_T I_{S,T}W(\theta)t_{\text{live}} \quad (4.15)$$

where  $I_{S,T}$  is the integrated scattering cross section.

The NRF target is combined with an additional target of an isotope with known transition energy and strengths for  $\gamma$  scattering (see Appendix A) for photon flux calibration. The spectral distribution of the incident photon beam can be obtained from Eq. (4.15) by using the known quantities of the calibration target labeled with “cal”:

$$\Phi_\gamma^{\text{cal}}(E_\gamma) = \frac{A_T^{\text{cal}}(\theta, t_{\text{live}})}{\epsilon(E_\gamma, \theta)N_T^{\text{cal}}I_{S,T}^{\text{cal}}W(\theta)t_{\text{live}}S} \frac{1}{s \cdot \text{eV} \cdot \text{cm}^2} \quad (4.16)$$

The number of target nuclei is given by:

$$N_T^{\text{cal}} = \frac{M^{\text{cal}}}{m_{\text{mol}}^{\text{cal}}} \cdot \frac{N_A}{S} = 0.6022 \cdot \frac{M^{\text{cal}}}{m_{\text{mol}}^{\text{cal}}} \cdot \frac{1}{S} \frac{1}{\text{cm}^2} \quad (4.17)$$

where  $M^{\text{cal}}$  and  $m^{\text{cal}}$  are the mass and the molar mass of the calibration target, respectively. The projected area of the target in  $\text{cm}^2$  on a plane perpendicular to the beam is marked with  $S$ , note that the beam diameter is bigger than the diameter of the target and has a homogeneous intensity distribution over a circle with diameter of 2 cm (cf. Fig. 3.6). At the NRF setup at the ELBE accelerator the target is a disk with diameter of 2 cm tilted under  $45^\circ$  relative to the beam.

#### 4.4.1 Approximation of the bremsstrahlung spectrum

The first relativistic calculation of the bremsstrahlung spectrum has been performed by H. A. Bethe and W. Heitler (BH) [Heit84] in 1934 based on quantum electro-dynamics. L. Schiff has integrated the cross section for bremsstrahlung given by BH over the azimuthal angle and derived an analytical expression [Schi51] known as “Schiff formula”. In general the Schiff formula overestimates the bremsstrahlung end-point energy. This discrepancy becomes significant at electron energies lower than 10 MeV. Several approximations were derived from the BH theory including different corrections. Some of them are compared in Fig. 4.3 a) for an electron kinetic energy of 10 MeV. Realistic calculations including corrections for the screening effect and for the Coulomb effect were performed by S. M. Seltzer and M. J. Berger (SB) [Selt85]. The correction for the screening effect takes in to account the screening of the charge of the nucleus by the electron cloud of the atom which leads to a reduction of the cross section for bremsstrahlung at lower photon energies. The correction for the Coulomb effect result in a rise of the cross section at high photon energies close to the end-point energy.

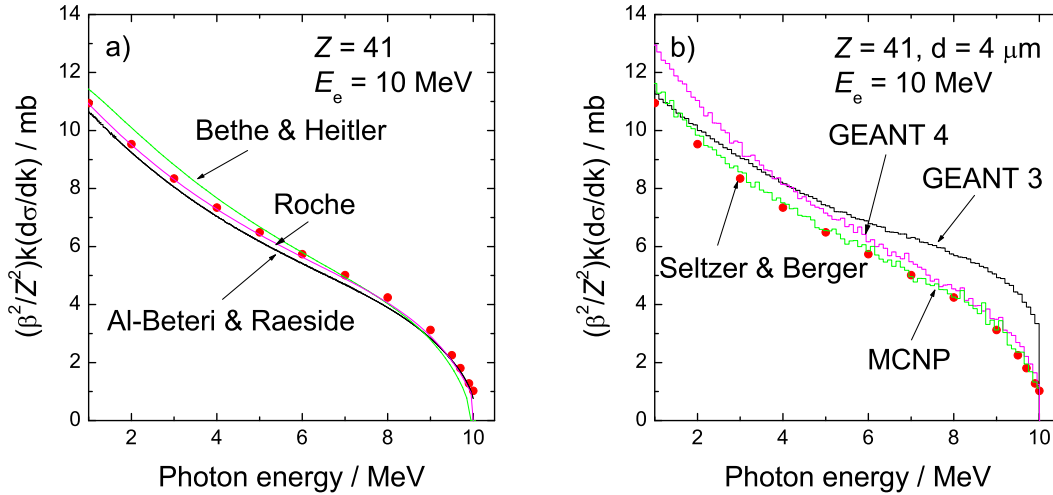


Figure 4.3: Comparison between the calculations for the bremsstrahlung spectrum from electrons with  $E_e = 10 \text{ MeV}$  in a thin radiator with  $Z = 41$  performed by Seltzer and Berger [Selt85] shown as points in both figures with a) the analytical approximations given by Bethe and Heitler [Heit84], Al-Beteri and Raeside [AlBe89] and Roche [Roch72] and with b) the results from performed simulations for  $4 \mu\text{m}$  thin Nb radiator using GEANT3, GEANT4 and MCNP.

A comparison between the cross sections given by HB and SB is presented in Fig. 4.3 a). An analytic expression of the spectral distribution of the bremsstrahlung quanta is given by A. A. Al-Beteri and D.E. Raeside [AlBe89]. They implement correction functions to the BH cross section and achieve good agreement to the shape of SB points and to the end-point energy, but in an absolute scale it underestimates the bremsstrahlung cross section (cf. Fig. 4.3 a). Nevertheless the Al-Beteri formula gives a good opportunity for implementation in a Monte Carlo code. Another approximation for the bremsstrahlung spectrum has been developed by G. Roche *et al.* [Roch72]. It includes corrections for the screening and for the Coulomb effect and agrees well with the SB calculations (cf. Fig. 4.3 a). The Monte Carlo programs as GEANT3, GEANT4 and MCNP use a fit to the SB data for generation of bremsstrahlung quanta. A comparison between SB data and performed simulations<sup>2</sup> for  $4 \mu\text{m}$  thick Nb radiator and  $E_e = 10 \text{ MeV}$  is shown in Fig. 4.3 b). The MCNP code shows good agreement with the SB calculations while the GEANT3 and GEANT4 (version 4.4.0) disagree in the beginning of the spectrum and at the end, respectively. The reason for the big disagreement between GEANT3 and SB calculations may be that the fit of the SB data is the optimized for high electron energies ( $\sim \text{GeV}$ ). The random generator which defines the spectral distribution of the bremsstrahlung quanta in GEANT3 was exchanged with another one based on the Al-Beteri formula. The reason for that was to use the fast transport mechanism of GEANT3 and to have a correct approximation of the bremsstrahlung spectrum. The modified GEANT3 was used for simulation of the photon flux for the experiments performed at Stuttgart Dynamitron accelerator. There the photon beam is produced from a  $4 \text{ mm}$  thick Au radiator and the theoretical approximations can not be applied directly neglecting the other processes of interaction of the electrons with the radiator matter. The results of the simulations are compared in Fig. 4.4 a) with the photon flux deduced from transitions in  $^{13}\text{C}$  and  $^{27}\text{Al}$  and with a fit of the experimental points with the Schiff formula. From the comparison in Fig. 4.4 a) it is visible that the Schiff formula gives a good approximation of the bremsstrahlung spectrum from thick radiator in the range above  $1.5 \text{ MeV}$ . Fits of the data points with Schiff formula were used in the analysis of the experiments performed in Stuttgart. In the fit the end-point energy was a free parameter. A thin Nb radiator is used at ELBE and the bremsstrahlung spectrum is calculated from the approximation of Roche. A program written by Prof. E. Haug according to Ref. [Roch72] is used in calculations

<sup>2</sup>The simulations with the MCNP code were performed by Dr. J. Klug.

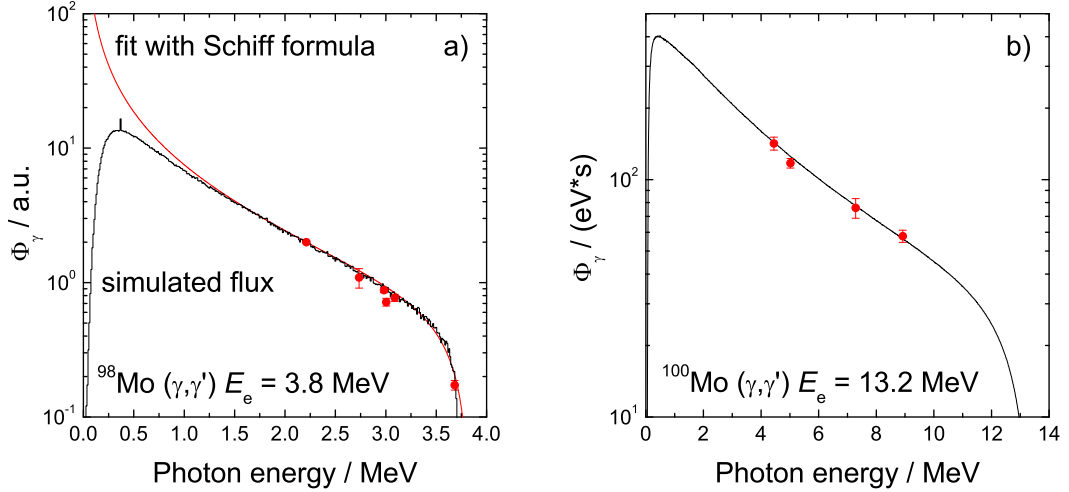


Figure 4.4: Comparison between a) the photon flux deduced from transitions from  $^{27}\text{Al}$  and  $^{13}\text{C}$  for 4 mm thick Au radiator with simulations with GEANT3 with included Al-Beteri formula (see text) and Schiff formula and b) between the photon flux deduced from transitions of  $^{11}\text{B}$  for 4  $\mu\text{m}$  thin Nb radiator with the approximation of Roche modified by the absorption in the Al hardener.

for the bremsstrahlung spectrum. The aluminum hardener modifies the bremsstrahlung spectrum. Simulations with GEANT3 are performed in order to obtain the spectral distribution of the photon beam radiating the NRF target. The geometry of the aluminum hardener and Al beam collimator were implemented in the simulation. A screen with a shape disk was placed at the NRF target position  $\gamma$ -rays are generated from the position of the radiator with energy distribution given from the approximation of Roche and a spectrum of them which hit the screen is collected. A comparison of the simulated photon flux with the flux deduced from the transitions in  $^{11}\text{B}$  is presented in Fig. 4.4 b).

#### 4.4.2 Determination of the electron-beam energy

The photo-disintegration of the deuteron is used as a tool for the determination of the degree of polarization of a polarized beam (see Section 3.2.4). The dependence of the proton energy on the photon energy  $E_e$  is also used for determination of the end-point energy of the bremsstrahlung spectrum. If  $\theta$  is the angle between the direction of the incident photon and the emitted proton, the conservation of momentum and energy determines the kinetic energy of the proton to:

$$E_p = \frac{1}{2} \left[ E_\gamma \left( 1 - \frac{E_\gamma}{2M_p c^2} \right) + E_\gamma \frac{V_p}{c} \cos \theta \right], \quad (4.18)$$

where  $M_p$  and  $V_p$  are the mass and velocity of the proton. The energy of the proton varies with  $\theta$  symmetrically around  $\theta = \pi/2$ . The energy distribution of protons is parabolic due to the finite solid angle of the Si detector. The angular distribution of the protons varies as  $\sin^2 \theta$  (see Refs. [Beth50, Fagg59]) for non-polarized photon beam. The width of the parabola depends on the solid angle of the detector and the size of the photon-beam spot on the PE foil. An example for the influence of the geometrical conditions to the shape of the spectrum is shown in Fig. 4.5 for the simplified case of photo-disintegration of deuteron from monoenergetic photons with  $E_\gamma = 10 \text{ MeV}$ . The geometry of the polarization chamber used in the setup in Rossendorf and the Si detectors were implemented in GEANT3 simulations. Protons were emitted with the described energy and angular distributions and a common spectrum of the deposited energy in the four Si detectors was collected. The simplest case of a point source is presented in Fig. 4.5 a), as was mentioned above the spectrum is a parabola with width depending on the solid angle of the Si detectors. The case of protons emitted from a rectangle surface, which correspond to the cross section of the photon beam and the PE foil, is presented in

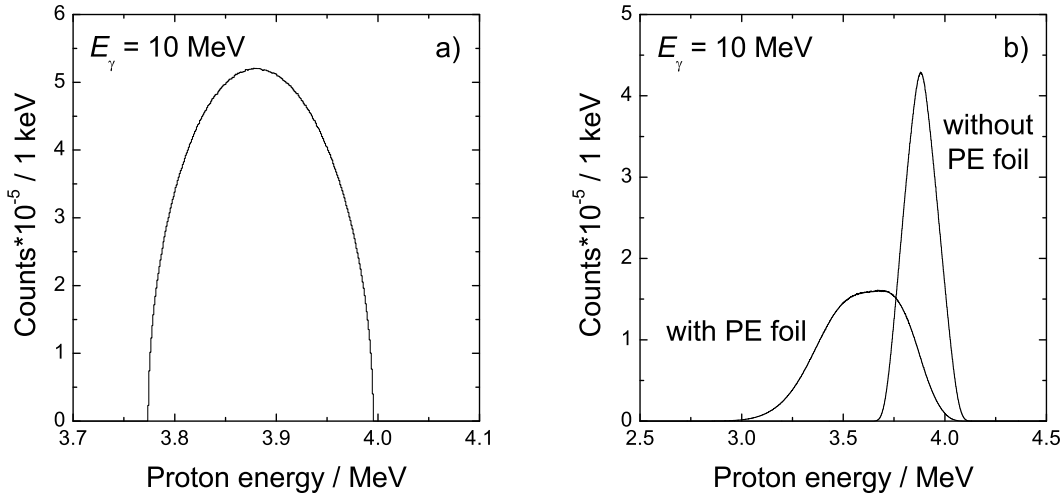


Figure 4.5: Simulated spectra of protons (see text) from photo-disintegration of the deuteron from monoenergetic photons with energy of 10 MeV. The protons are emitted a) from point source and b) from the photon-beam spot on the deuterized PE target without and with defined PE foil.

Fig. 4.5 b) the histogram “without PE foil”. The spectrum becomes broader in comparison with the point source due to the increased effective solid angle of the Si detectors. The realistic case of protons emitted inside the PE foil with space distribution corresponding to the overlap of the photon beam and the PE foil is presented in Fig. 4.5 b) the histogram “with PE foil”. The spectrum is much broader than the spectrum from the previous case because the protons scatter inside the foil. The measured proton spectrum is a convolution of the bremsstrahlung spectrum from electrons with Gaussian energy distribution with dispersion  $\sigma_e$  modified by the aluminum hardener and such predicted proton spectra (cf. Fig. 4.5 b) corresponding to photo-disintegration of the deuteron from monoenergetic photons. Three predicted proton spectra corresponding to different approximations of the bremsstrahlung spectrum are compared with a measured one for  $E_e = 13.2$  MeV and  $\sigma_e = 60$  keV in Fig. 4.6 a). The comparison shows that the approximations given by G. Roche *et al.* [Roch72] represent correctly the bremsstrahlung spectrum.

A procedure for fitting the measured proton spectrum with predicted ones is used to determine the electron-beam energy  $E_e$  as well as the electron-beam spread  $\sigma_e$ . The simulations described above were performed for uniform energy distribution of the photons and the results were recorded in an event-by-event file containing the photon energy and the deposited energy in the Si detector. Additional simulations were performed for the attenuation of the photons in the Al hardener. Photons with uniform energy distribution were emitted from the radiator and those which penetrate the hardener and reach the PE foil were counted. The results of the simulations were recorded in a spectrum containing the ratio of the penetrated-to-incident photons. Predicted proton spectra are prepared for various  $E_e$  and  $\sigma_e$  and compared with the measured spectrum in the following procedure:

- 1) Select an electron energy  $E_e$  and electron beam spread  $\sigma_e$ ;
- 2) Calculate the bremsstrahlung spectrum using the approximation of Roche and fold with Gaussian distribution with  $\sigma_e$ ;
- 3) Fold the bremsstrahlung spectrum with the attenuation of the hardener and thus obtaining the spectral distribution of the photon beam  $\Phi_\gamma$ ;
- 4) Calculate the proton flux as a product of  $\Phi_\gamma$  and the cross section for photo-disintegration of the deuteron [Beth50];
- 5) Calculate a predicted proton spectrum using the simulations described above. The spectrum is normalized to the measured one to minimize  $\chi^2$ .

The values of  $\chi^2$  are plotted in the plane  $(E_e, \sigma_e)$  in Fig. 4.6 b). The minimal  $\chi^2$  correspond to the



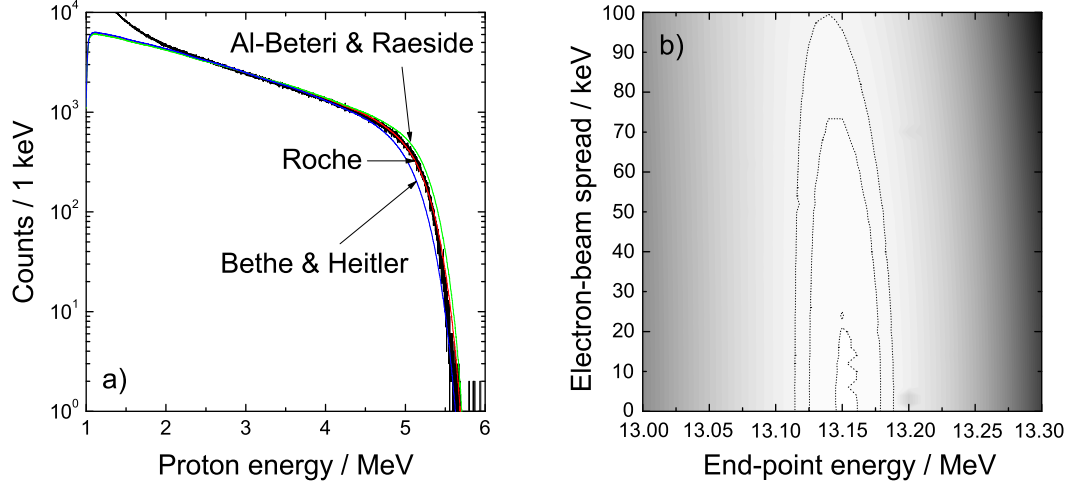


Figure 4.6: Comparison between measured proton spectrum for  $E_e = 13.2$  MeV and  $\sigma_e = 60$  keV with a) predicted proton spectra using the approximations of Bethe and Heitler, Al-Beteri and Raeside and Roche and b) predicted proton spectra using the Roche approximation for various  $E_e$  and  $\sigma_e$ , the darkness correspond to the minimized  $\chi^2$ .

end-point energy. The method is not sensitive to determine the electron-beam spread because of the dominant effect of the kinematics of the photo-disintegration which requires further reduction of the solid angle of the Si detectors.

## 4.5 Energy-integrated scattering cross section $I_S$

The energy-integrated-scattering cross section  $I_S$  can be deduced directly from Eq. (4.15) knowing the absolute values of the detector efficiency and photon flux. This requires a precise measurement of the live time of the data acquisition and efficiency calibration. Another possibility is to determine  $I_S$  relatively to the known cross section of a transition from a calibration standard (see Appendix A). For this purpose the Eq. (4.15) is applied for the calibration transition and for the one from the investigating target, labeled “cal” and “target”, respectively.

$$\left( \frac{A(\theta)}{n\Phi_\gamma\epsilon(E,\theta)W(\theta)I_S} \right)^{\text{target}} = \left( \frac{A(\theta)}{n\Phi_\gamma\epsilon(E,\theta)W(\theta)I_S} \right)^{\text{cal}} \quad (4.19)$$

which leads to:

$$I_S = \frac{n_{\text{cal}}}{n_{\text{target}}} \cdot \left( \frac{\Phi_\gamma\epsilon(E,\theta)W(\theta)I_S}{A(\theta)} \right)^{\text{cal}} \cdot \left( \frac{A(\theta)}{\Phi_\gamma\epsilon(E,\theta)W(\theta)I_S} \right)^{\text{target}} \quad (4.20)$$

The uncertainty is calculated as:

$$\begin{aligned} \left( \frac{\Delta I_S}{I_S} \right)^2 = & \left( \frac{\Delta A_T}{A_T} \right)^2 + \left( \frac{\Delta A_{\text{cal}}}{A_{\text{cal}}} \right)^2 + \left( \frac{\Delta \epsilon_T}{\epsilon_T} \right)^2 + \left( \frac{\Delta \epsilon_{\text{cal}}}{\epsilon_{\text{cal}}} \right)^2 + \\ & \left( \frac{\Delta N_{\gamma,T}}{N_{\gamma,T}} \right)^2 + \left( \frac{\Delta N_{\gamma,\text{cal}}}{N_{\gamma,\text{cal}}} \right)^2 + \left( \frac{\Delta I_{S,\text{cal}}}{I_{S,\text{cal}}} \right)^2 \end{aligned} \quad (4.21)$$

The scattered  $\gamma$ -rays are measured at different angles for spin assignment purpose. The total scattering cross section can be deduced independently for every angle. A weighted average cross section  $\overline{I_S}$  over all scattering angles is used in order to reduce the systematic uncertainty.

$$\overline{I_S} = \frac{\sum_{i=1}^2 \frac{I_{S,i}}{\Delta I_{S,i}^2}}{\sum_{i=1}^2 \frac{1}{\Delta I_{S,i}^2}} \quad \overline{\Delta I_S} = \frac{1}{\sum_{i=1}^2 \frac{1}{\Delta I_{S,i}^2}} \quad (4.22)$$

The level widths and the reduced transition probabilities are calculated from Eqs. (2.15) and (2.26). A level can decay to the ground state or to an intermediate state. The branching ratio for a given transition deexciting a level is defined in this work as a fraction of the intensity of the ground-state transition from the total deexcitation intensity:

$$B_0 = \frac{\Gamma_0}{\Gamma} = \frac{\Gamma_0}{\sum_{i=1}^n \Gamma_i} = \frac{I_0}{\sum_{i=1}^n I_i} = \frac{A_0/(\epsilon_0 W_0)}{\sum_{i=1}^n A_i/(\epsilon_i W_i)} \quad (4.23)$$

The branching ratios for the not ground-state transitions are calculated according to the definition:

$$B_f = \frac{\Gamma_f}{\sum_{i=1}^n \Gamma_i} = \frac{\Gamma_f}{\Gamma} \quad (4.24)$$

## 4.6 Detection limits

In the investigation of the total dipole strength and its fragmentation, the detection limits are of crucial importance. The detection limits for a peak are defined by setting a threshold that the counts in the peak must exceed to claim detection. Analysis of the detection limits defining a confidence limit of 95 % is followed in this work according to the derivation given in Ref. [Jenk95]. A region of interest of width  $\eta_P$  is marked on Fig. 4.7 a). The total integrated area  $N_T$  of that region is a superposition of the background counts  $B$  and the net peak counts  $P$ :

$$N_T = P + B \quad (4.25)$$

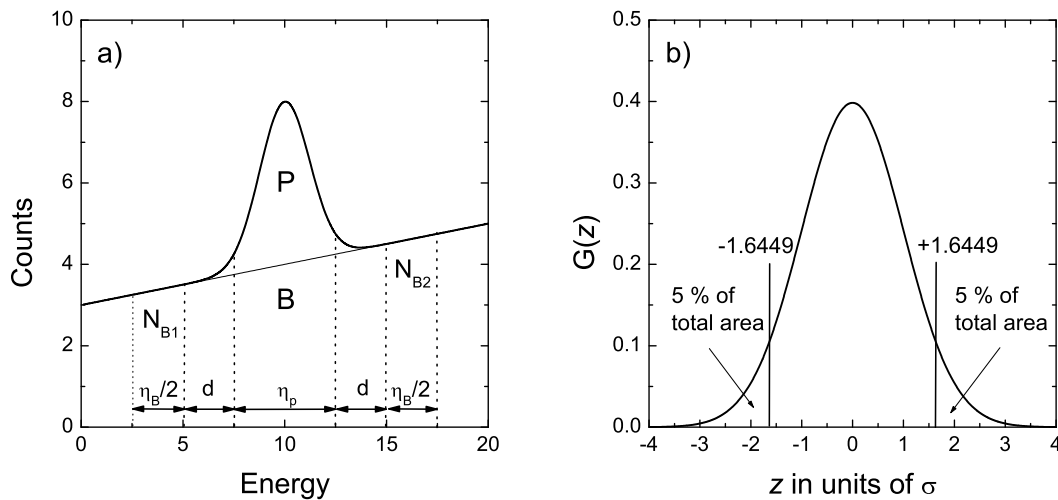


Figure 4.7: Definitions a) for the used quantities and b) the used detection limits.

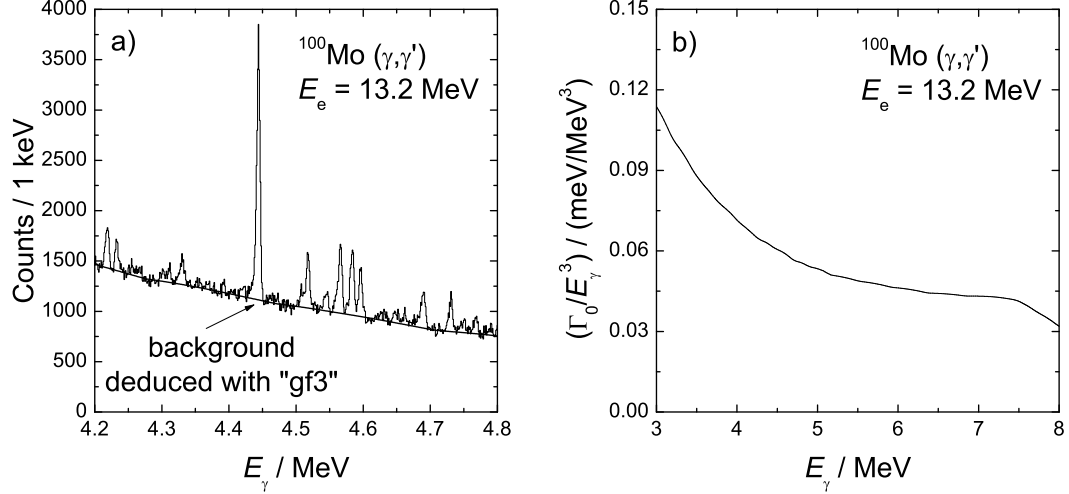


Figure 4.8: Determination of the background below the peaks a) and the derived determination limits b) expressed in terms of reduced widths.

The background counts can be estimated by the integrated counts  $N_{B_1}$  and  $N_{B_2}$  of two regions of width  $\eta_B/2$  one from left and the other from right of the peak (cf. Fig. 4.7 a). The background counts under the peak of interest become:

$$M_B = \frac{\eta_P}{\eta_B}(N_{B_1} + N_{B_2}) \approx B \quad (4.26)$$

with a standard deviation:

$$\sigma_{M_B} \approx \frac{\eta_P}{\eta_B} \sqrt{N_{B_1} + N_{B_2}} \approx \frac{\eta_P}{\eta_B} \sqrt{\frac{\eta_P}{\eta_B} B} \quad (4.27)$$

The net peak counts can be estimated by subtracting the background counts:

$$P = N_T - B \quad (4.28)$$

with a standard deviation:

$$\sigma_P = \sqrt{\sigma_{N_T}^2 + \sigma_{M_B}^2} \approx \sqrt{P + \left(1 + \frac{\eta_P}{\eta_B}\right) B} \quad (4.29)$$

Determination of the detection limits in the presence of background requires to use statistical confidence limits. A Gaussian probability distribution with 5 % and 95 % confidence limits are shown in Fig. 4.7 b), where  $z = (N - \mu)/\sigma$  and  $\mu$  is the mean value of the distribution. The 5 % confidence limit occurs at  $z = -1.6449$  because the area of the Gaussian to the left of this value is 5 % of the total area. Similarly, the 95 % confidence limit occurs at  $z = 1.6449$ . In terms of  $N$ , the 5 % and 95 % confidence limits are:

$$N_{5\%} = \mu - 1.6449\sigma \quad (4.30)$$

$$N_{95\%} = \mu + 1.6449\sigma \quad (4.31)$$

To claim detection, the net peak counts must exceed a threshold value set at  $N_D$ . The convention is to set this threshold high enough that there is only a 5 % probability of the background counts exceeding the threshold if the peak truly is not present. From Eq. (4.29), the standard deviation in the net peak counts when the backgrounds are zero is:

$$\sigma_0 = \sqrt{P + \left(1 + \frac{\eta_P}{\eta_B}\right) B} \quad (4.32)$$

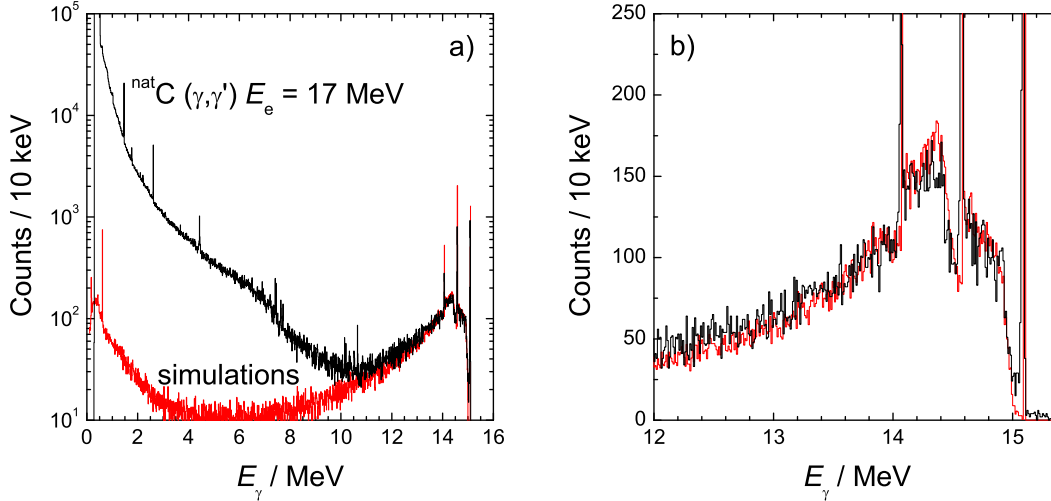


Figure 4.9: a) Comparison between measured spectrum from  $^{\text{nat}}\text{C}$  at  $127^\circ$  with a simulated spectrum for  $E_\gamma = 15.1$  MeV. The simulated spectrum is normalized to the area of the peak at 15.1 MeV. b) The same comparison showing the Compton background from 15.1 MeV peak.

Therefore, the threshold for 5 % false positive detection is obtained from Eq. (4.30):

$$N_D = 0 + 1.6449 \sqrt{P + \left(1 + \frac{\eta_P}{\eta_B}\right)B} \quad (4.33)$$

When the peak is present at the detection limit,  $P_{DL}$ , the conventional definition of the detection limit requires a 95 % probability of claiming a true positive. For this case the detection threshold  $N_D$  is:

$$N_D = P_{DL} - 1.6449 \sqrt{P + \left(1 + \frac{\eta_P}{\eta_B}\right)B} \quad (4.34)$$

Setting the detection thresholds equal between Eqs. (4.33) and (4.34) and using the fact that  $P_{DL} \ll B$  to eliminate  $P_{DL}$  from the square root leads to the detection limit:

$$P_{DL} = 1.6449 \sqrt{\left(1 + \frac{\eta_P}{\eta_B}\right)B} \quad (4.35)$$

In order to deduce detection limits for an energy range of resonance peaks the background in the whole measured spectrum is extracted by the program “gf3” from the RadWare [?] package. An example of the deduced background is shown in Fig. 4.8 a). The area  $B$  is calculated from the background spectrum using the dependence of FWHM on the  $\gamma$ -ray energy (cf. Fig. 4.1 b).

## 4.7 Determination of the resonant continuum

The measured photon-scattering spectra do not contain information on all excitations as narrow peaks. Because of the high level density above  $E_x = 4$  MeV and the Porter-Thomas fluctuations of the decay widths many of the excitations are so weak that they only can be observed as a continuum. The continuum can be extracted from the measured spectrum if there is a knowledge about the detector response and the fraction of the non-resonant background in the experimental spectrum. In this work, GEANT3 simulations are performed in order to correct the measured spectrum for the detector response and to determine the non-resonant background.

It was shown that the simulations with GEANT3 for the detector efficiency and for the ratio of the full-energy peak to the single escape (FE-to-SE) (cf. Fig. 3.14 a) agree well with the measurement.

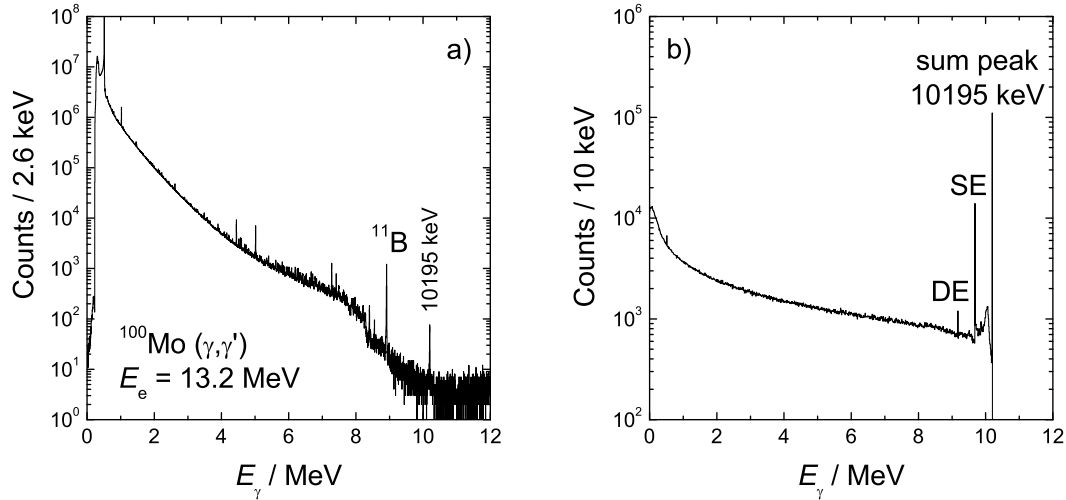


Figure 4.10: Photon-scattering spectrum from  $^{100}\text{Mo}$  with a) the observed peak at 10195 keV and b) the simulated spectrum from the decay of this level (see text).

An important ingredient in the simulations of the detector response is the BGO escape-suppression shield which cancels an event if there is an energy deposition in the BGO crystal. The threshold of the constant-fraction discriminator (CFD) of the BGO detector was measured to be 75 keV. The CFD threshold was included in the simulations for the ratio of FE-to-SE presented in Fig. 3.14 a) (the curve “with BGO”) which agree with the measured ratio of FE-to-SE from the  $^{11}\text{B}$  transitions. If the CFD threshold is set to infinity, i.e. no veto from the BGO detector, the ratio of FE-to-SE drops down (cf. the curve “without BGO” in Fig. 3.14 a). Therefore the CFD threshold has a big influence to the detector response and the good agreement shown in Fig. 3.14 a) proves the consistency of the simulations and the measurement. Another comparison showing the quality of the simulations is presented in Fig. 4.9. A measurement on 2765.5 mg  $^{\text{nat}}\text{C}$  (graphite) was performed with bremsstrahlung of an end-point energy of 17 MeV. The natural carbon contains 98.90 % of  $^{12}\text{C}$  which exhibit only a few strong excitations (see Appendix A). The spectrum measured for 8 hours is compared in Fig. 4.9 with a simulated detector-response spectrum for 15.1 MeV  $\gamma$ -rays emitted from the target. The full-energy peak in the simulated spectrum is normalized to the area of the peak at 15.1 MeV in the experimental spectrum. Two conclusions can be drawn from the comparison in Fig. 4.9: (i) the non-resonant background ends at 12 MeV (cf. Fig. 4.9 a), note, it depends also on the target material, and (ii) the Compton background from the transition at 15.1 MeV is well approximated by the simulations (cf. Fig. 4.9 b).

The second type of simulations are done to estimate the non-resonant background in the experimental spectrum. Such simulations are presented in Fig. 3.15 for the measurement on  $^{208}\text{Pb}$  at  $E_e = 17$  MeV. The GEANT3 simulations with modified distribution of the bremsstrahlung (see Subsection 4.4.1) reproduce correctly the slope of the background in the measured spectrum.

The determination of the resonant continuum is presented in two steps (i) the measured spectrum is corrected for the detector response and for the detector efficiency and (ii) compared with the simulated non-resonant background. The procedure of determination of the resonant continuum is performed in the following:

1) At an electron-beam energy higher than the neutron separation energy the production of neutrons from the target or from the surrounding materials is possible. The neutrons can be thermalised by inelastic scattering in the experimental hall and capture in the crystal of the HPGe detector. Indications for this process are observed as peaks corresponding to thermal neutron capture in different stable germanium isotopes in measurements with photon beams and neutron sources. A list of the most prominent peaks due to neutron capture in the Ge isotopes is presented in Table 4.1. The populated

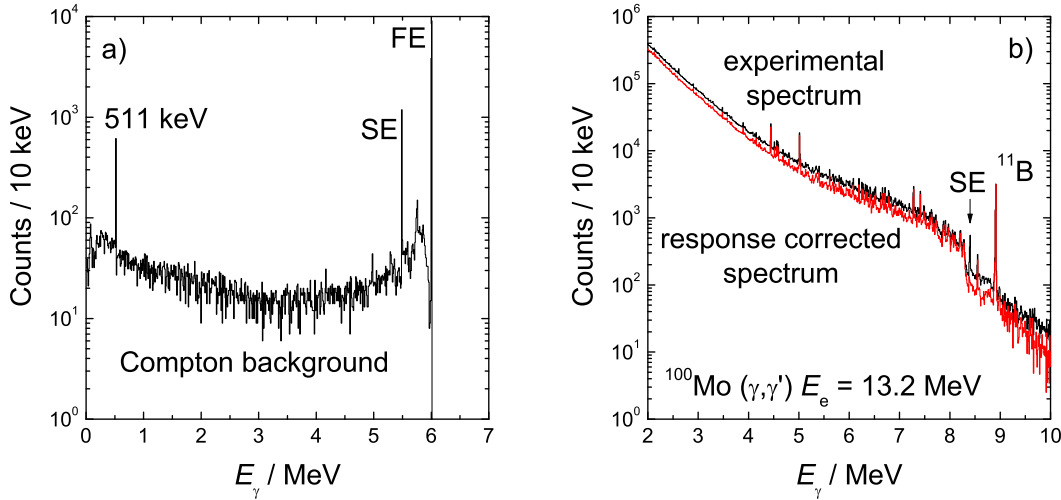


Figure 4.11: Simulated response of the HPGe detector a) for monoenergetic  $\gamma$ -rays with energy of 6 MeV and comparison b) between the measured and response corrected spectra.

levels in the  $^{A+1}\text{Ge}$  nucleus by neutron capture mainly decay via  $\gamma$ -ray cascades and with small probability for decay to the ground state. The observed prominent peaks are results of summing of the cascade  $\gamma$ -rays since the germanium crystal plays the role of a target and a detector simultaneously. An example for such a summed peak is the decay of the 10195 keV level in  $^{74}\text{Ge}$  for which no ground-state transition is known. Due to summing a strong peak is observed at 10195 keV (see Fig. 4.10 a). Since the neutron capture can happen randomly in the volume of the crystal the efficiency of the detector is reduced and high Compton background is produced. GEANT3 simulations were performed in order to obtain a response spectrum from the decay of a level populated by neutron capture. The geometry of the HPGe detector and the BGO shield were defined. A point in the Ge crystal was randomly selected and  $\gamma$ -rays were emitted corresponding to two step cascade to the ground state with random energy of the intermediate level and isotropic directions of the two  $\gamma$ -rays. A spectrum of the energy deposited in the Ge crystal was collected when there is no veto from the BGO detector. A simulated spectrum for the level at 10195 keV in  $^{74}\text{Ge}$  is presented in Fig. 4.10 b). The simulated spectrum was normalized to the sum peak in the measured spectrum and subtracted from it. The same simulations were performed for all germanium isotopes listed in Table 4.1.

The thermal-neutron capture in the materials surrounding the detectors produce individual peaks in the spectrum. These peaks are removed from the spectrum without the need of additional simulations. The natural background also counts in the photon-scattering spectra. Separate measurements without beam were performed after every experiment in order to collect a spectrum of the natural background at the same experimental conditions (see e.g. Fig. 3.21). The natural background was subtracted from the experimental spectrum after normalization to the live time of the corresponding detector.

The counts from neutron-capture  $\gamma$ -rays and from the natural background in the measured spectrum form  $1.4 \cdot 10^{-3} \%$  and  $6.1 \cdot 10^{-2} \%$ , respectively, from all counts in the spectrum.

2) The measured spectrum contains a background due to incomplete absorption of photons in the HPGe crystal, the so called “detector background”, discussed in Section 3.4. Simulations for the response of the detector were performed in order to remove the “detector background”. The simulations are the same as those for the detector efficiency (see Section 4.2) but for a uniform energy distribution of the emitted  $\gamma$ -rays in intervals of 10 keV to cover the range of the measured spectrum. An example of a simulated detector-response spectrum is given in Fig. 4.11 a). The full-energy peak of every simulated spectrum is normalized to the counts at the same energy in the measured one and the background counts are subtracted. The procedure of removal of the “detector background” starts from the end of the measured spectrum and continues to the beginning. A comparison of the measured and the

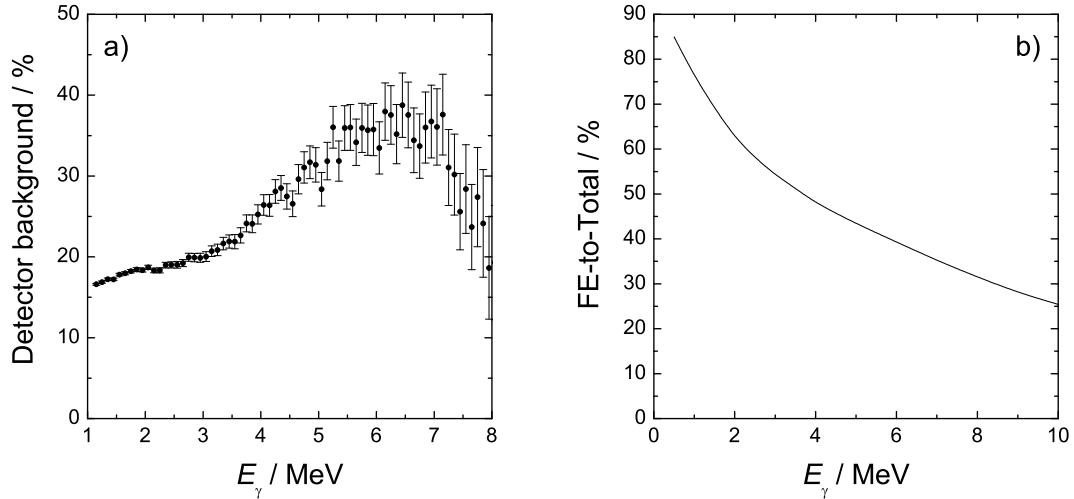


Figure 4.12: Detector background a) calculated as a ratio of the residuum spectrum from the experimental and response corrected spectrum (cf. Fig. 4.11b) to the response corrected spectrum. b) ratio of the FE peak to the total counts in the spectrum (FE-to-Total) from GEANT3 simulations for a detector at  $127^\circ$ .

detector-response corrected spectrum is shown in Fig 4.11 b).

Because of the high efficiency of the HPGe detectors and as result of the good escape suppression by the BGO shields the response correction could be performed without introducing large statistical uncertainties. The ratio of the not fully absorbed  $\gamma$ -rays to the  $\gamma$ -rays detected with full energy is presented in Fig. 4.12a). It is in strong dependence on the ratio of the FE-to-total shown in Fig. 4.12b) for detector at  $127^\circ$  and identical absorbers as in the experiments.

3) The measured spectrum contains several peaks from the resonant scattering from  $^{11}\text{B}$  used for calibration of the photon flux. The areas of the  $^{11}\text{B}$  peaks are subtracted from the spectrum.

4) After the corrections 1, 2 and 3 the spectrum contains only resonantly and non-resonantly scattered photons from the target detected with photo-effect. The spectrum is divided by the absolute full-energy peak efficiency in order to determine the spectrum of photons scattered in the solid angle of the detector. The spectrum is corrected for the live time to obtain a more convenient quantity: photons/(10 keV\*s\*sr).

5) A spectrum of non-resonantly scattered photons was simulated with GEANT3. Only the target was implemented in the simulations. Four screens were defined with a shape of a disk such that the solid angles of the screens and the detectors are the same. Photons with uniform distribution in the energy interval from 0 to 15 MeV were emitted in a parallel beam with a profile of an ellipse such that all photons hit the target. This is of importance for further normalization to the absolute photon

Table 4.1: Energies of the levels populated in thermal neutron capture experimentally observed in the photon-scattering experiments at  $E_e = 13.2$  MeV.

$E_\gamma$ / keV	reaction	$E_\gamma$ / keV	reaction
6505	$^{74}\text{Ge}(n,\gamma)^{75}\text{Ge}$	7630	$^{56}\text{Fe}(n,\gamma)^{57}\text{Fe}$
6683	$^{72}\text{Ge}(n,\gamma)^{73}\text{Ge}$	7646	$^{56}\text{Fe}(n,\gamma)^{57}\text{Fe}$
7366	$^{73}\text{Ge}(n,\gamma)^{74}\text{Ge}$	7723	$^{27}\text{Al}(n,\gamma)^{28}\text{Al}$
7415	$^{70}\text{Ge}(n,\gamma)^{71}\text{Ge}$	7915	$^{63}\text{Cu}(n,\gamma)^{64}\text{Cu}$
10195	$^{73}\text{Ge}(n,\gamma)^{74}\text{Ge}$		

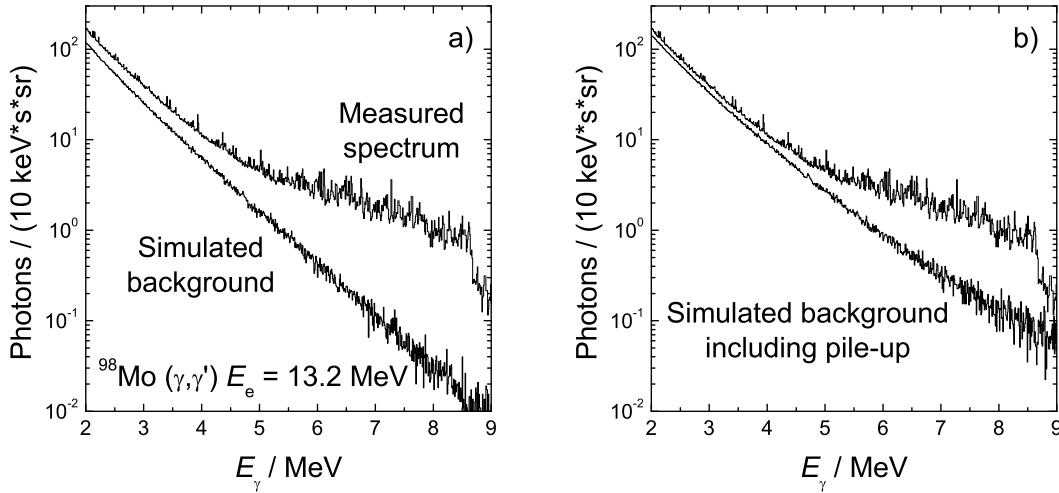


Figure 4.13: Comparison of the measured spectrum from  $^{98}\text{Mo}$  at  $E_e = 13.2$  MeV with a) the simulated background and b) with the background with included pile-up effect.

flux. The energies of the incident photons and those scattered from the target to the screen were recorded in an event-by-event file for every screen (detector). The uniform distribution of the incident photons was folded with the absolute flux (see Section 4.4) in an off-line analysis and a spectrum of non-resonantly scattered photons from the target produced for every detector. This spectrum still can not be compared with the experimental one because the measured spectrum contains counts resulting from the pile-up effect. The Monte Carlo program for simulations of the pile-up effect (see Section 3.5) was used to modify the simulated background spectrum. A comparison between the experimental spectrum from  $^{98}\text{Mo}$  at  $E_e = 13.2$  MeV with the simulated non-resonant background is shown in Fig. 4.13 a). The effect of the correction for pile-up is presented in Fig. 4.13 b).

The resonant continuum is determined by subtraction of the simulated non-resonant background from the measured spectrum.

## 4.8 A Monte Carlo code for $\gamma$ -ray cascade simulations in photon-induced reactions

Photon-induced reactions are considered to proceed through a compound nucleus with a cross section proportional to the product of the excitation width  $\Gamma_0$  and the decay width  $\Gamma_f$ . Once excited by an absorption of a real photon, the level can decay by emission of a  $\gamma$ -ray or a particle (proton or neutron). The total absorption cross section for a level  $E_x$  becomes a superposition of the cross sections of all possible channels of the reaction:

$$\sigma_\gamma = \frac{\pi}{2} \cdot \frac{\hbar^2 c^2}{E_x^2} \sum_f \frac{\Gamma_0 \Gamma_f}{(E_\gamma - E_0)^2 + \frac{1}{4} \Gamma^2} + \sum_{p=p,n,\alpha} \frac{\sigma_p \Gamma_0 \Gamma_p}{(E_p - E_0)^2 + \frac{1}{4} \Gamma^2} \quad (4.36)$$

Since the probability for the deexcitation of a given level by a  $\gamma$ -ray transition to the ground state, to an intermediate level, or by emission of a particle may be analogous a Monte Carlo code for simulations of  $\gamma$ -ray cascades was developed [Ruse06] in this work as a tool in the analysis of photon-scattering and photon-dissociation experiments.

The program is based on the nuclear statistical model. The assumed approximations are presented in the following:



1) The level density is given by the back-shifted Fermi gas model:

$$\rho(E_x, J) = f(J)e^{2\sqrt{a(E_x - E_1)}} / (12\sqrt{2}\sigma a^{1/4}(E_x - E_1)^{5/4}) \quad (4.37)$$

$$f(J) = e^{-J^2/2\sigma^2} - e^{-(J+1)^2/2\sigma^2} \quad (4.38)$$

$$\sigma = \sqrt{0.0146A^{5/3} \frac{1 + \sqrt{1 + 4a(E_x - E_1)}}{2a}} \quad (4.39)$$

where the functions  $f(J)$  and  $\sigma$  determine the spin dependence of the level density. The level-density parameter  $a$  and the back-shift energy  $E_1$  are taken from a recent systematics performed by T. von Egidy and D. Bucurescu [Egid05].

2) The densities of levels with positive parity and with negative parity are assumed to be equal (see Ref. [AlQu03]).

3) The Wigner distribution (Eq. (4.40)) is used for the fluctuations of the nearest-neighbour spacings of levels with the same spin. Optionally in the program, the distribution can be changed to the Poisson distribution (Eq. (4.41))

$$P(x) = \frac{1}{2}\pi x e^{-(\pi/4)x^2} \quad (\text{Wigner distribution}) \quad (4.40)$$

$$P(x) = e^{-x} \quad (\text{Poisson distribution}) \quad (4.41)$$

4) It is assumed the validity of the Brink-Axel hypothesis [Axel62] and that the excitation and the deexcitation strength functions can be described with the same Lorentzian function.

A priori known strength functions  $f_\gamma^{XL}(E_\gamma)$  for  $E1$ ,  $M1$  and  $E2$  transitions are used to calculate the average decay widths of the levels:

$$\overline{\Gamma}_{\text{if}} = (E_i - E_f)^{2L+1} \frac{f_\gamma^{XL}(E_\gamma)}{\rho(E_x, J_x^\pi)} \quad (4.42)$$

The strength functions for  $M1$  and  $E2$  transitions are derived from a standard Lorentzian:

$$f_\gamma^{XL}(E_\gamma) = \frac{2J_0 + 1}{2J_f + 1} \cdot \frac{1}{(\pi\hbar c)^2} \cdot \frac{1}{E_\gamma^{(2L-1)}} \cdot \frac{\sigma_0 E_\gamma^2 \Gamma_0^2}{(E_\gamma^2 - E_0^2)^2 + E_\gamma^2 \Gamma_0^2} \quad (4.43)$$

The parameters  $\sigma_0$ ,  $E_0$  and  $\Gamma_0$  are taken from the global parameterization of the  $M1$  spin-flip giant resonance and the  $E2$  isoscalar giant resonance provided by the ‘‘Reference Parameter Input Library’’ RIPL-2 [RIPL-2]. The parameterization of the  $M1$  giant resonance is:

$$\begin{aligned} E_0 &= 41A^{-1/3} \text{ MeV} \\ \Gamma_0 &= 4 \text{ MeV} \end{aligned} \quad (4.44)$$

$$\sigma_0 \text{ in mb, adjusted to } \frac{f_\gamma^{E1}}{f_\gamma^{M1}} = 0.0588A^{0.878} \text{ at 7 MeV,}$$

and the parameters for the  $E2$  giant resonance are:

$$\begin{aligned} E_0 &= 63A^{-1/3} \text{ MeV} \\ \Gamma_0 &= 6.11 - 0.021A \text{ MeV} \\ \sigma_0 &= \frac{0.00014Z^2 E_0}{A^{1/3}\Gamma_0} \text{ mb} \end{aligned} \quad (4.45)$$

The strength function for  $E1$  transitions is derived from a Lorentzian fit to the photo-absorption cross section [Beil74] after subtraction of  $f_\gamma^{M1}(E_\gamma)$  and  $f_\gamma^{E2}(E_\gamma)$ .

5)The Porter-Thomas distribution [Port56] is used for the fluctuations of the decay widths of the

levels. The widths of the individual levels are assigned according to  $\Gamma_{if} = y_{if}\overline{\Gamma}_{if}$ , where  $y_{if}$  follows the  $\chi^2$  distribution with zero degrees of freedom:

$$P(y) = \frac{1}{\sqrt{2\pi y}} e^{-y/2} \quad (4.46)$$

6) Calculated cross sections for  $(\gamma, p)$  and  $(\gamma, \alpha)$  reactions by T. Rauscher and F.-K. Thielemann [Raus04] are used for the simulation of the particle emission.

A block diagram of the algorithm of the program is presented in Fig. 4.14. The simulations start with the creation of level schemes containing levels with spin  $J = 0, 1$  and  $2$  according to the assumed level density and level-spacings distribution. Levels with spin higher than  $J = 2$  are not considered of importance for the photon-induced reactions with bremsstrahlung. The parity of the levels is assigned randomly such to keep the same density of the levels with positive and negative parity. The three level schemes are merged to one common scheme according to the energy of the levels. Since it is impossible to store the information of all partial decay widths a pseudo-random-generator [Becv98] is used. The idea of the method is to assign precursors to all levels of the scheme. The precursors are used to set the seed of the random generator of the Porter-Thomas distribution such that every time when a given level  $E_i$  is populated the same sequence of  $y_{if}$  values is generated to determine always the same partial decay widths. The created level scheme with assigned spins and parities to the levels together with the assigned partial decay widths for every level is called in this work “nuclear realization”. Every event of the simulations starts with the excitation of a level  $E_i$  with spin  $J = 1$  according to the photoabsorption cross section which is proportional to  $\Gamma_0/E_x^2$ . The emission of a particle is selected randomly such to keep the ratio of a radiative decay of a level  $E_i$  to a decay via emission of a particle the same as the ratio of the corresponding cross sections. If a particle is emitted the event is terminated and the simulations continue with a selection of a new excited level. The radiative deexcitation is selected according to the partial decay widths. If the decay is not to the ground state then the populated level is considered as an excited level and a new decay is performed till the ground state is reached.

The program provides the energy, the spin and the parity of the initial and final levels as well as the multipole order of the transition. The angular distribution of the transitions is calculated according to Eq. (2.21) for pure dipole or quadrupole transition<sup>3</sup>. Since one nuclear realization does not represent completely the properties of the nucleus, but is only a guess, the cascade simulations have to be run for many nuclear realizations. The mean value of a given quantity within the deviation is representable for the real nucleus. The mean value  $\bar{x}$  and the deviation  $\sigma$  are calculated according to [Bevi03]:

$$\begin{aligned} \bar{x} &= \frac{1}{N} \sum x_i \\ \sigma^2 &= \frac{1}{N} \sum (x_i - \bar{x})^2 \end{aligned} \quad (4.47)$$

Some tests of the program are presented in Figs. 4.15 and 4.16 for the case of  $^{98}\text{Mo}$ . Simulations for 1000 nuclear realizations were performed. Fig. 4.15 shows the result from the analysis of the created level schemes for the level density (Fig. 4.15 a) of levels with  $J = 1$  and the nearest neighbor spacings (Fig. 4.15 b), the histograms are compared with the defined distributions (solid lines).

---

<sup>3</sup>A program written by Dr. R. Schwengner for calculation of the angular distribution of cascade transitions was implemented in the code.

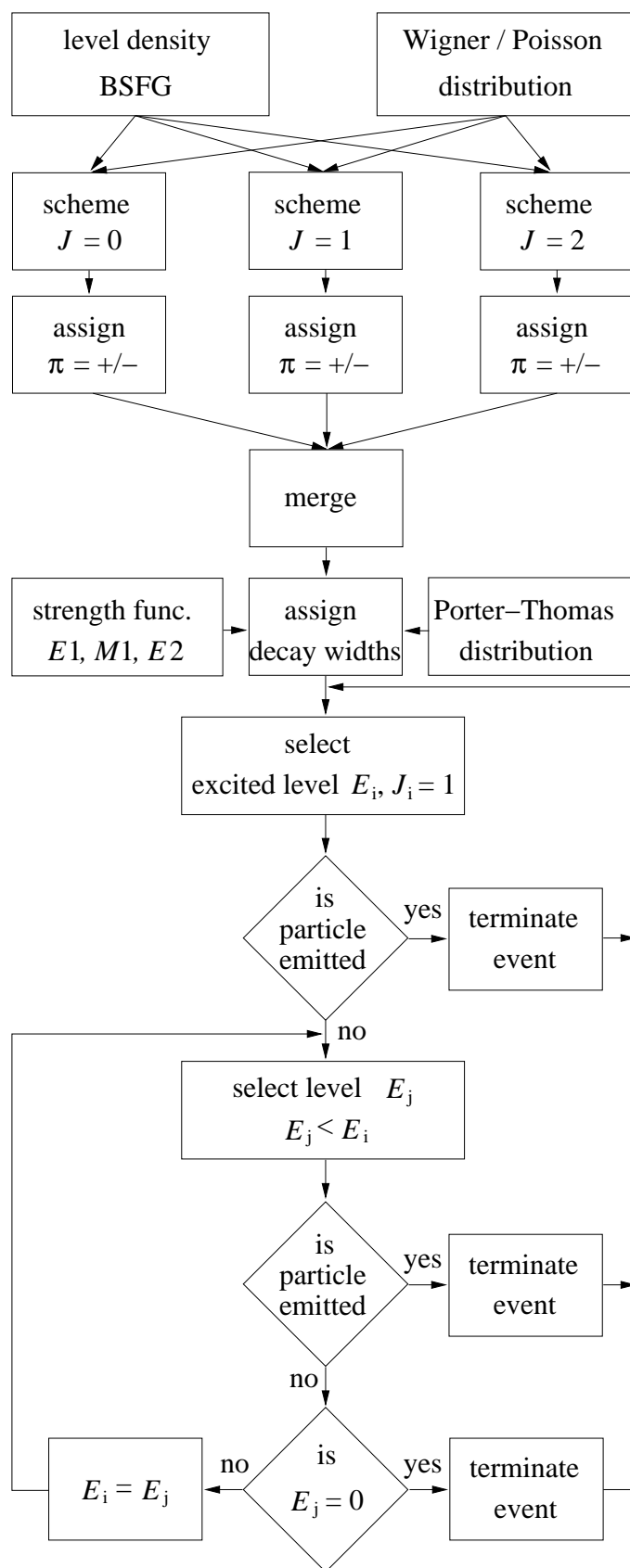


Figure 4.14: A block diagram of the algorithm used in the Monte Carlo code for  $\gamma$ -ray cascade simulations in photon-induced reactions.

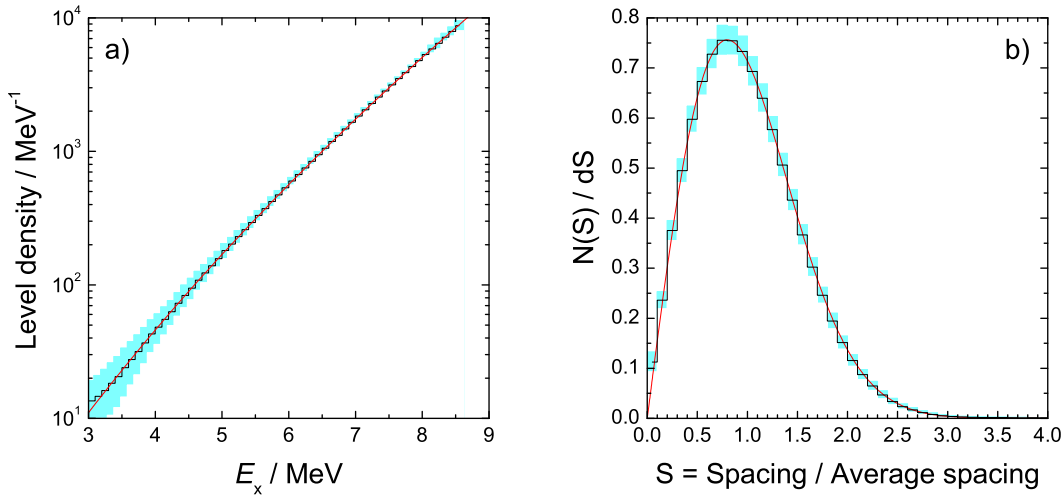


Figure 4.15: Comparisons between the distributions included in the program (solid lines) and the mean values of the results of simulations (histograms) for a) the level density and b) the spacing distribution of levels with spin  $J = 1$  in  $^{98}\text{Mo}$ . Hatched areas show the  $1\sigma$ -variation of the mean values due to the fluctuations in the level spacings.

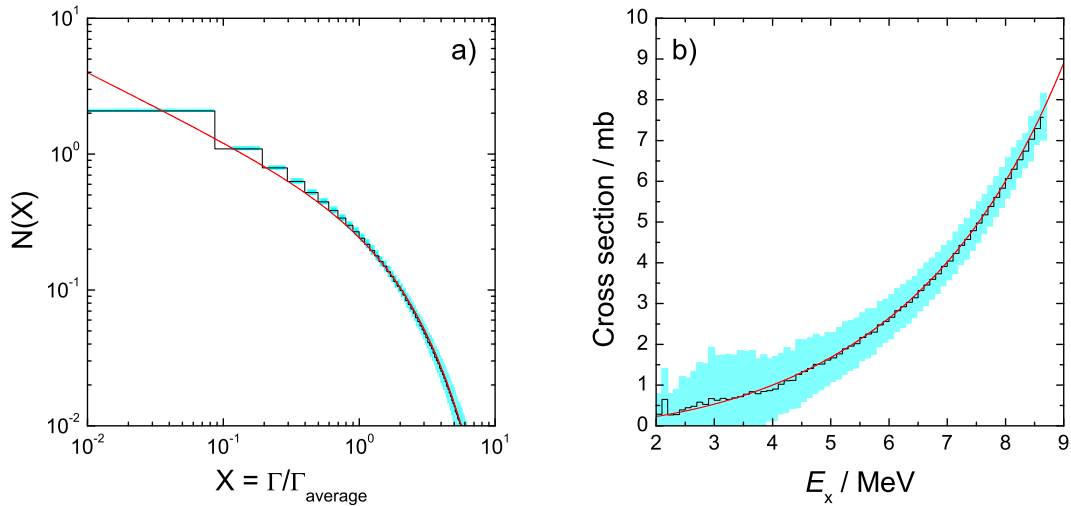


Figure 4.16: Comparisons between the distributions included in the program (solid lines) and the mean values of the results of simulations (histograms) for a) the width distribution and b) the absorption cross section for  $^{98}\text{Mo}$ . Hatched areas show the  $1\sigma$ -variation of the mean values due to the fluctuations in the level spacings and widths.

# Chapter 5

## Experimental results

In this Chapter, the experimental results of eleven photon-scattering experiments on  $^{92}\text{Mo}$ ,  $^{98}\text{Mo}$  and  $^{100}\text{Mo}$  are presented. The measurements were carried out at the bremsstrahlung facilities at the Dynamitron accelerator of the Universität Stuttgart and the superconducting electron accelerator ELBE of Forschungszentrum Rossendorf, Dresden. The Chapter is divided into two sections according to the energy range of excitation of the nuclear states. Branching transitions observed in the measurements on  $^{98}\text{Mo}$  and  $^{100}\text{Mo}$  at  $E_e = 3.8$  MeV were resolved by performing experiments at lower energies. A discussion on the problem with the inelastic photon scattering in the experiments at  $E_e = 13.2$  MeV is given by means of performed simulations of  $\gamma$ -cascade decay of the nuclear levels. A method for reconstruction of the measured strength distribution is presented. It allows a determination of the total radiative strength below the neutron separations energy  $S_n$ . The results for the absorption cross section obtained from the photon-scattering experiments at  $E_e = 13.2$  MeV are compared with the cross section for  $(\gamma, n)$  reaction above  $S_n$  [Beil74].

### 5.1 Low-lying dipole excitations in $^{92}\text{Mo}$ , $^{98}\text{Mo}$ and $^{100}\text{Mo}$

The low-lying excitations in  $^{92}\text{Mo}$  were investigated with bremsstrahlung of an end-point energy of 6 MeV. The photon-scattering experiment was carried out at the superconducting electron accelerator ELBE at Rossendorf. The bremsstrahlung was produced by irradiating a 4  $\mu\text{m}$  thick niobium radiator with a continuous-wave electron beam of a kinetic energy of  $E_e = 6$  MeV and an average beam current of 300  $\mu\text{A}$ . A hardener was not used in the measurement. The target consisted of 2035.7 mg  $^{92}\text{Mo}$  with an enrichment of 97.31 %. The molybdenum target was combined with  $^{11}\text{B}$  enriched to 99.52 % with a mass of 455.5 mg for the calibration of the photon flux. The relative photon flux determined from  $^{11}\text{B}$  was interpolated by using the approximation of the bremsstrahlung spectrum given by G. Roche [Roch72] (cf. Fig. 4.3 a). Gamma rays scattered from the target were detected with four 100 % HPGe detectors two of them placed at  $90^\circ$  and the other two at  $127^\circ$  relative to the photon beam. All detectors were equipped with escape-suppression shields made of BGO scintillation detectors (cf. Fig. 3.2). The detector efficiency has been simulated with GEANT3 as was described in Section 4.2. Spectra of scattered photons measured at  $90^\circ$  and  $127^\circ$  for 72 hours are shown in Fig. 5.1. Six transitions were observed in  $^{92}\text{Mo}$  which are listed in Appendix B. The results of the levels at 3091.4, 3925.8, 3944.0 and 4633.7 keV are consistent with the ones obtained in previous work [Metz77]. In addition, a transition at 4494.7 keV was observed in the spectrum at  $90^\circ$  (cf. Fig. 5.1) and  $J = (2)$  was tentively assigned to the corresponding level. A level at 4493.9 keV had also been observed in electron-scattering experiments [Bagl00] with an assignment of  $J^\pi = 2^+$ . For the additional levels proposed on the basis of previous photon-scattering experiments at  $E_e = 8$  and 10 MeV [Bagl00, Bauw00], we assume that the corresponding  $\gamma$  rays are transitions from levels with energies greater than 6 MeV to low-lying levels.

The ratios  $I_\gamma(E_\gamma, 90^\circ)/I_\gamma(E_\gamma, 127^\circ)$  and the level scheme of  $^{92}\text{Mo}$  deduced in the present photon-

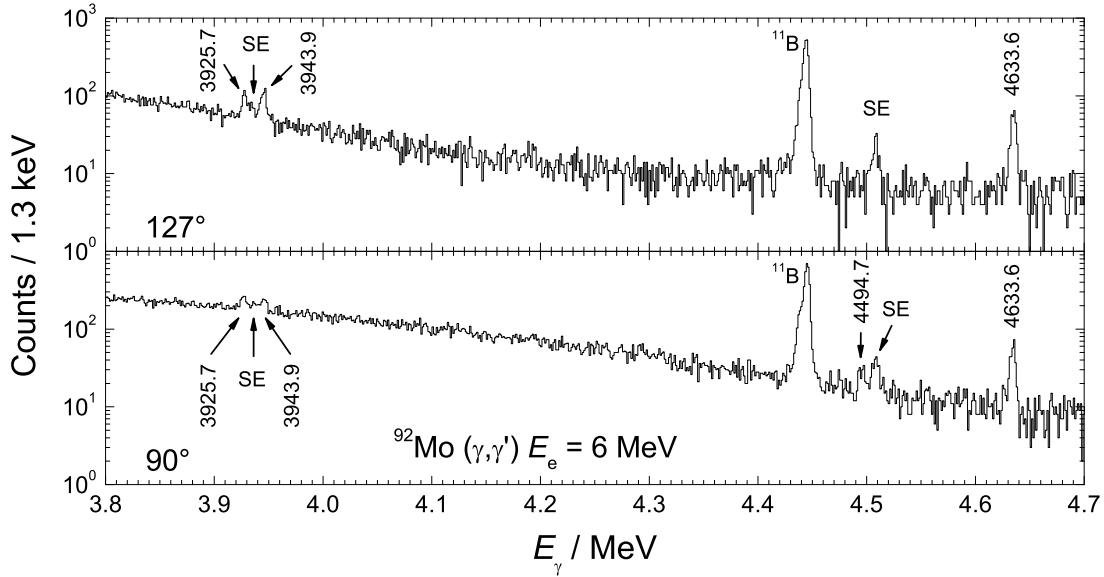


Figure 5.1: Parts of spectra of photons scattered from  $^{92}\text{Mo}$ , measured at  $127^\circ$  (top) and  $90^\circ$  (bottom) relative to the beam at  $E_e = 6$  MeV. The transitions assigned to  $^{92}\text{Mo}$  are labeled with their energies in keV. SE marks single-escape peaks.

scattering experiment are shown in Fig. 5.2.

Excited levels in  $^{98}\text{Mo}$  and  $^{100}\text{Mo}$  were investigated up to 3.8 MeV in nuclear resonance fluorescence experiments performed at the Dynamitron accelerator of the Universität Stuttgart [Knei96]. The experiments were carried out at electron-beam energies of 3.3 and 3.8 MeV for  $^{98}\text{Mo}$  and of 3.2, 3.4 and 3.8 MeV for  $^{100}\text{Mo}$  and an average electron current of  $250 \mu\text{A}$ . Samples of highly enriched  $^{98}\text{Mo}$  and  $^{100}\text{Mo}$  were used as targets in the experiments. The targets were combined with  $^{27}\text{Al}$  and  $^{13}\text{C}$  for photon flux calibration. Information about the targets and electron beam energies used in the measurements is summarized in Table 5.1.

Gamma rays scattered from the target were detected with three 100 % HPGe detectors placed at  $90^\circ$ ,  $127^\circ$  and  $150^\circ$  relative to the incident photon beam, respectively. The detectors were shielded with lead against background radiation. In addition the detector at  $127^\circ$  was surrounded by an escape-suppression shield consisting of four BGO detectors. Spectra from the individual detectors were recorded for 90 hours in the experiments at  $E_e = 3.8$  MeV and for 60 hours in the measurements at smaller electron-beam energies. Experimental spectra measured at  $150^\circ$  are shown in Fig. 5.3 for  $^{98}\text{Mo}$  and in Fig. 5.4 for  $^{100}\text{Mo}$ .

The relative photon flux was deduced from the transitions in  $^{27}\text{Al}$  with known cross section for photon scattering. The used NRF standards are given in Appendix A. An additional  $^{13}\text{C}$  target was used in the experiments at 3.8 MeV in order to extend the experimentally deduced flux closer to the bremsstrahlung end-point energy. The obtained points for the photon flux from  $^{27}\text{Al}$  and  $^{13}\text{C}$  were normalized to the number of nuclei in the calibration targets and to measurement time and averaged over all detectors. As was discussed in Section 4.4 the Schiff formula gives a good approximation of the photon flux from a thick radiator in the range of the observed transitions (cf. Fig. 4.4 a). A fit with the Schiff formula was used for a spectral distribution of the bremsstrahlung photons. The bremsstrahlung end-point energy was a free parameter of the fit.

Six transitions were observed in  $^{98}\text{Mo}$  for the first time in the experiment at  $E_e = 3.8$  MeV. The spectrum measured at  $150^\circ$  is shown in Fig. 5.3. The newly observed transitions are labeled with their energies. The angular distribution indicates dipole character for the transitions in  $^{98}\text{Mo}$ . The ratio  $I_\gamma(E_\gamma, 90^\circ)/I_\gamma(E_\gamma, 127^\circ)$  is presented in Fig. 5.5. The transition at 2816.9 keV fits well the energy spacing between the dipole state at 3551.2 keV and the second  $0^+$  state. An additional measurement



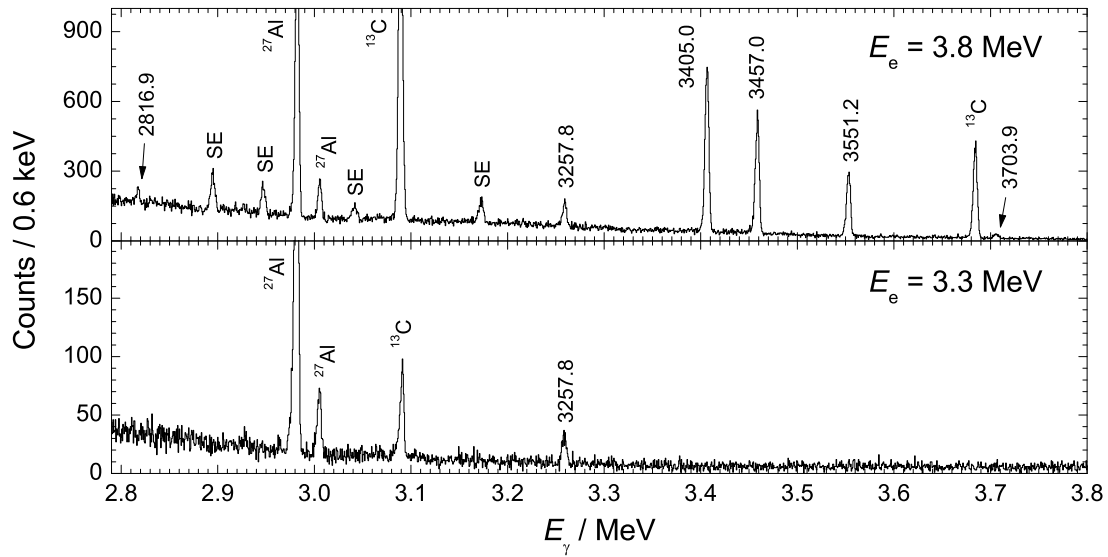


Figure 5.3: Parts of spectra of photons scattered from  $^{98}\text{Mo}$ , measured at  $150^\circ$  relative to the beam and at  $E_e = 3.8$  MeV (top) and  $E_e = 3.3$  MeV (bottom). The peaks labeled with their energies in keV correspond to dipole transitions assigned to  $^{98}\text{Mo}$ . SE marks the single-escape peaks.

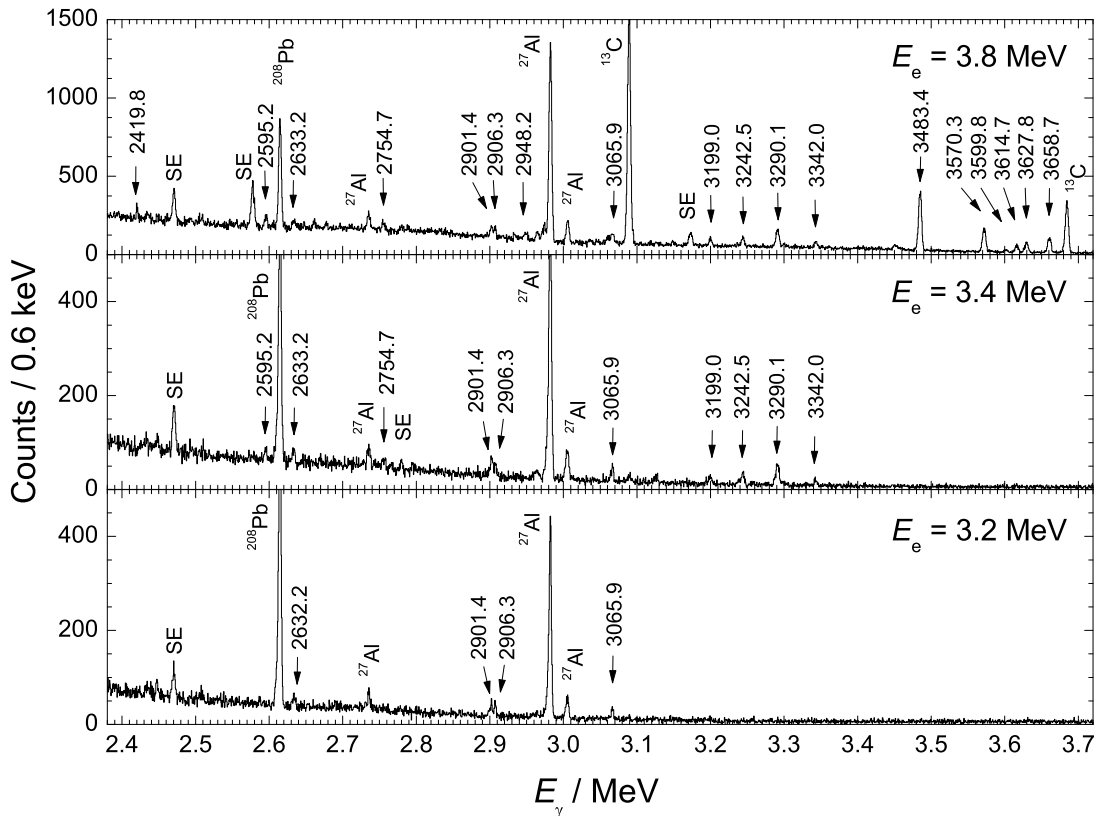


Figure 5.4: Comparison of partial spectra of photons scattered from  $^{100}\text{Mo}$  at  $150^\circ$  relative to the beam axis for different electron energies. The peaks labeled with their energies in keV correspond to dipole transitions assigned to  $^{100}\text{Mo}$ . SE marks the single-escape peaks.



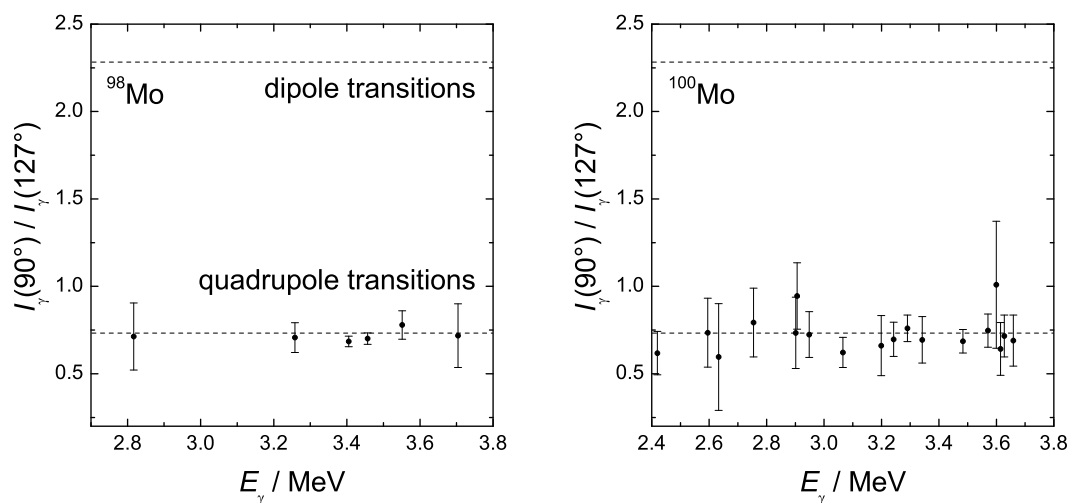


Figure 5.5: Ratio of  $\gamma$ -ray intensities observed at  $90^{\circ}$  and  $127^{\circ}$  relative to the beam for the transitions in  $^{98}\text{Mo}$  and  $^{100}\text{Mo}$ . The expected values for pure dipole (0.74) and quadrupole (2.28) transitions in even-even nuclei are shown with dashed lines.

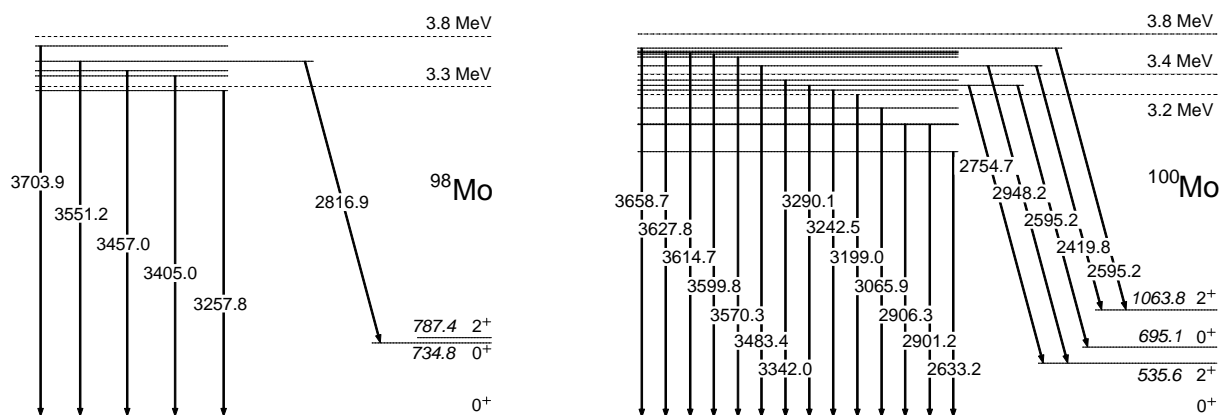


Figure 5.6: Level schemes of  $^{98}\text{Mo}$  (left panel) and  $^{100}\text{Mo}$  (right panel) including the dipole states found in this work (left) and the known low-lying levels (right). The used electron-beam energies are indicated by dashed lines.

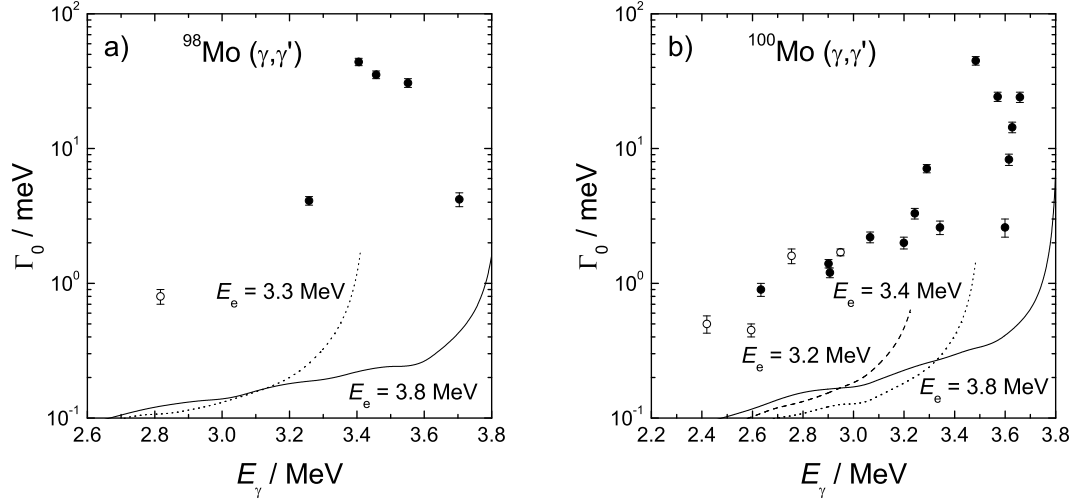


Figure 5.7: Comparison of the partial widths  $\Gamma_0$  of ground-state transitions (filled circles) and branching transitions (open circles), see text, with the detection limits obtained from the spectra measured at  $150^\circ$  and for all used electron-beam energies.

level and the  $0_2^+$  state at 695.1 keV and the  $2_1^+$  state at 535.6 keV, respectively, known from previous work [Sing97]. These transitions were not observed in the measurement at  $E_e = 3.2$  MeV (cf. Fig. 5.4). If the transitions at 2595.2 keV and 2754.7 keV were ground-state transitions they should occur in the spectrum at  $E_e = 3.2$  MeV as peaks with areas of about 140 and 330 counts, respectively, which is 8 and 12 times more than the respective detection limits (cf. Fig. 5.7). Therefore, they are considered as branches from the 3290.1 keV level to the  $0_2^+$  and  $2_1^+$  states. Positive parity is proposed for this state on the basis of the Alaga rules (cf. Eq. (2.44)).

The 3483.4 keV level: The transitions at 2948.2 and 2419.8 keV are neither observed in the measurement at  $E_e = 3.4$  MeV nor in the one at  $E_e = 3.2$  MeV. Assuming that these transitions are ground-state transitions and using the scattering cross section determined from the spectrum at  $E_e = 3.8$  MeV they should occur in the spectra measured at  $E_e = 3.2$  MeV as peaks with areas of 190 and 240 counts, respectively, and at  $E_e = 3.4$  MeV as peaks with 350 and 340 counts, respectively, which is not the case. These areas are 6 and 10 times higher than the respective detection limits for the spectrum at  $E_e = 3.2$  MeV, and 8 and 15 times higher than the respective detection limits in the spectrum at  $E_e = 3.4$  MeV. As the 2948.2 and 2419.8 keV transitions fit the respective energy spacings between the 3483.4 keV level and the  $2_1^+$  and  $2_2^+$  states they are assigned as branches to these states. Tentatively positive parity is assigned to this state based on the Alaga rules.

The 3658.8 keV level: The transition at 2595.2 keV fits the energy spacing between this level and the  $2_2^+$  state. However, it was also assigned as a branch from the level at 3290.1 keV to the  $0_2^+$  state. In the measurement at  $E_e = 3.8$  MeV the peak at 2595.2 keV is observed with about twice the intensity observed at  $E_e = 3.4$  MeV, where the level at 3658.8 keV is not excited. This proves that the two transitions depopulating the 3290.1 and 3658.8 keV levels, respectively, exist with nearly equal intensities. Thus, the 2595.2 keV transition is also assigned as populating the 3658.8 keV level to the  $2_2^+$  state. Positive parity is tentatively assigned to this state on the basis of the Alaga rules.

The level scheme of  $^{100}\text{Mo}$  deduced from the present experiments is shown in Fig. 5.6.

Table 5.2: Targets, electron-beam energies and measurement times used in the experiments at the bremsstrahlung facility at the ELBE accelerator.

nucleus	mass / mg	$^{11}\text{B}$ / mg	$E_e$ / MeV	$t_{\text{meas}}$ / hours
$^{92}\text{Mo}$	2036 (97.31 %)	340 (99.52 %)	13.2	57
$^{98}\text{Mo}$	2953 (98.55 %)	340 (99.52 %)	13.2	64
$^{98}\text{Mo}$	2953 (98.55 %)	321 (99.52 %)	8.5	114
$^{100}\text{Mo}$	2917 (99.27 %)	340 (99.52 %)	13.2	64
$^{100}\text{Mo}$	2917 (99.27 %)	340 (99.52 %)	8.0	80

## 5.2 Dipole excitations in $^{92}\text{Mo}$ , $^{98}\text{Mo}$ and $^{100}\text{Mo}$ up to the $(\gamma, n)$ threshold

The investigation of  $^{92}\text{Mo}$ ,  $^{98}\text{Mo}$  and  $^{100}\text{Mo}$  presented in the previous Section was extended up to the neutron separation energy in experiments at the bremsstrahlung facility at the Rossendorf ELBE accelerator. Photon-scattering experiments were performed on the three molybdenum isotopes at an electron-beam energy of 13.2 MeV above the neutron separation energies of  $^{92}\text{Mo}$  ( $S_n = 12.67$  MeV),  $^{98}\text{Mo}$  ( $S_n = 8.64$  MeV) and  $^{100}\text{Mo}$  ( $S_n = 8.29$  MeV). Because of possible observation of transitions in the neighboring nuclei produced via  $(\gamma, n)$  reaction additional measurements at  $E_e = 8.4$  MeV and  $E_e = 7.8$  MeV were performed on  $^{98}\text{Mo}$  and  $^{100}\text{Mo}$ , respectively. The bremsstrahlung was produced by irradiating a  $7\ \mu\text{m}$  thick niobium foil with continuous-wave electron beams with average currents of  $600\ \mu\text{A}$ . The low-energy tail of the bremsstrahlung spectrum was suppressed by usage of an aluminum hardener. The photon beam irradiates the target placed in an evacuated pipe. Isotopically enriched materials were used as targets in the experiments. The molybdenum targets were pressed into a form of a pill with diameter of 2 cm and packed in a thin polyethylene foil (PE). The targets were combined with elementary  $^{11}\text{B}$  for photon flux calibration. The  $^{11}\text{B}$  powder was “glued” to a PE foil in a shape of a pill with diameter of 2 cm using poly-vinyl alcohol. Photographs of used targets are shown in Fig. 5.8. Information about the beam energies, weights of the targets and times of measurement is summarized in Table 5.2.

The  $\gamma$ -rays scattered from the target were detected with four 100 % HPGe detectors (see Section 3.3), two of them placed at  $90^\circ$  and the other two at  $127^\circ$  relative to the incident photon beam. All detectors were equipped with BGO escape-suppression shields. Stacks of absorbers consisting of slices of copper with thicknesses of 3 mm and lead with thicknesses of 15 mm and 8 mm were placed in front of the

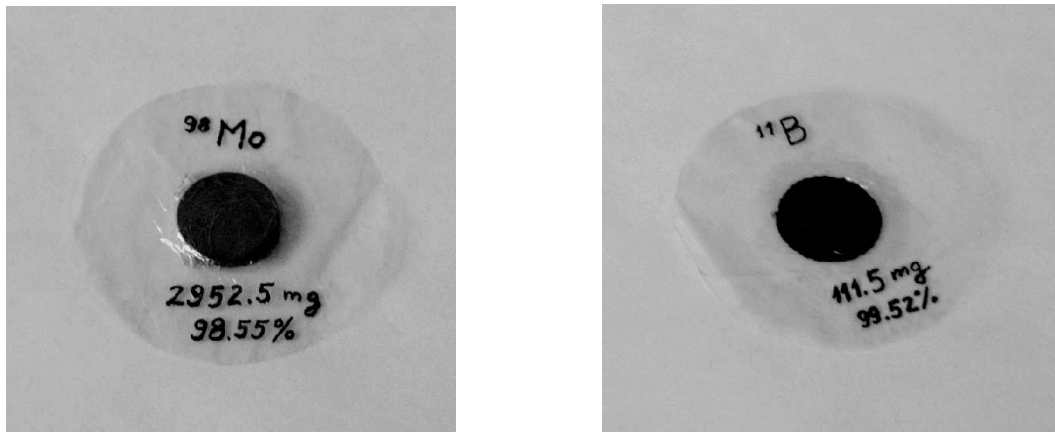


Figure 5.8: Photographs of used targets in the photon-scattering experiments at the ELBE accelerator.

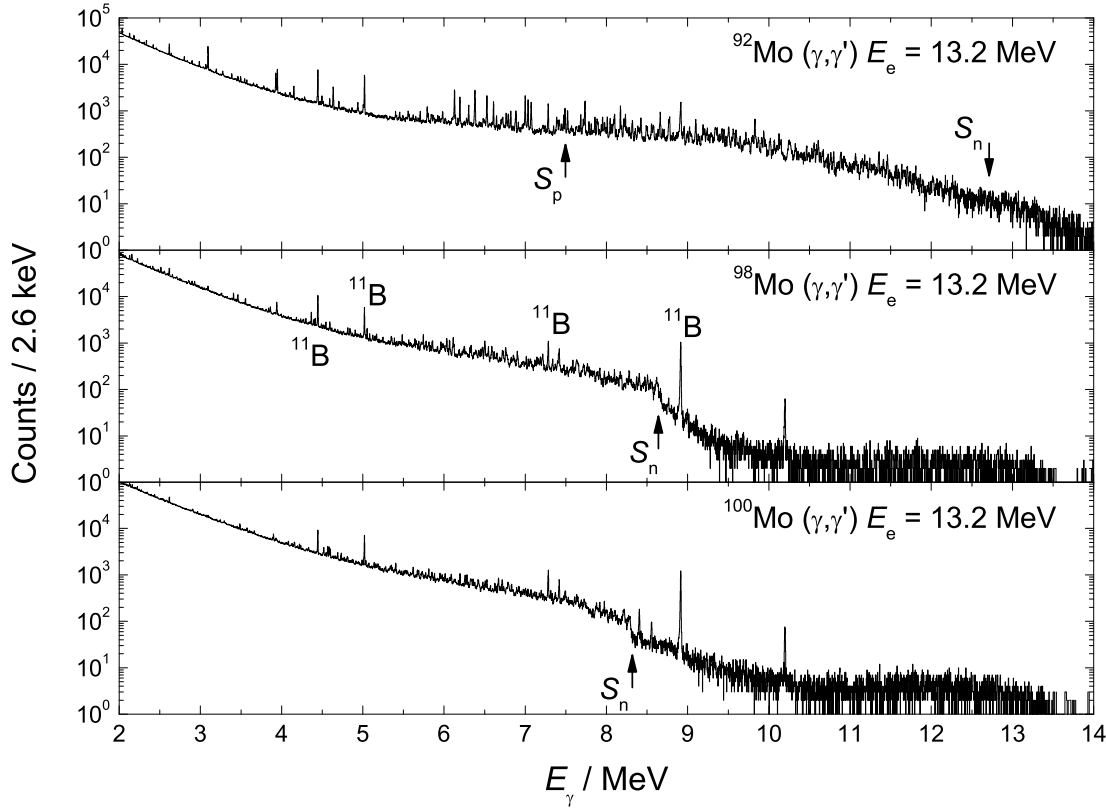


Figure 5.9: Comparison of spectra measured at  $127^\circ$  relative to the photon beam for  $^{92}\text{Mo}$ ,  $^{98}\text{Mo}$  and  $^{100}\text{Mo}$  for the electron-beam energy of 13.2 MeV.

detectors at  $90^\circ$  and  $127^\circ$ , respectively. Spectra of  $\gamma$ -rays scattered at  $127^\circ$  from the three molybdenum isotopes are presented in Fig. 5.9. The spectra are collected in experiments with the same electron-beam energy of 13.2 MeV. The spectrum from  $^{92}\text{Mo}$  contains prominent peaks while the other isotopes show a large number of weak excitations. The spectra are characterized with a decrease of intensity at the neutron separation energy. Since the  $(\gamma, p)$  channel in  $^{92}\text{Mo}$  opens at  $S_p = 7.46$  MeV the intensity decreases more smoothly. Peaks corresponding to transitions in the neighboring nuclei produced via  $(\gamma, n)$ ,  $(\gamma, p)$  or  $(n, \gamma)$  reactions were discarded from the analysis. Transitions which do not belong to the investigated molybdenum isotopes were identified by comparison with spectra measured at electron-beam energy lower than the neutron separation energy and using the information from NNDC. The number of transitions assigned to  $^{92}\text{Mo}$ ,  $^{98}\text{Mo}$  and  $^{100}\text{Mo}$  is 340, 485 and 499, respectively. The results of the analysis of the experiments at  $E_e = 13.2$  MeV are given in Appendix C. The multipole order of the observed transitions was obtained by comparing the ratios of the  $\gamma$ -ray intensities at  $90^\circ$  and  $127^\circ$  with the expected values of 0.73 and 2.28 for dipole and quadrupole radiation, respectively. The results for the ratio  $I_\gamma(E_\gamma, 90^\circ)/I_\gamma(E_\gamma, 127^\circ)$  are presented in Fig. 5.10. The spin assignment is performed as described in Section 4.3. From the comparison in Fig. 5.10 it is visible that most of the transitions have dipole character. Detection limits were determined from the spectra measured at  $127^\circ$  in order to prove whether a peak can be accepted as a transition. Decay widths  $\Gamma_0$  were calculated under the assumption that the observed transitions are deexcitations to the ground state. They are compared with the detection limits corresponding to 95 % confidence limits ( $2\sigma$ ) in Fig. 5.11. The results given in Appendix C contain only the transitions above the detection limits.

Part of the observed transitions are deexcitations to intermediate levels. An indication for branching transitions is the large number of observed peaks in the spectra at  $E_e = 13.2$  MeV in the range below 4 MeV in strong contrast to the low-energy experiments discussed in the previous Section. A possible

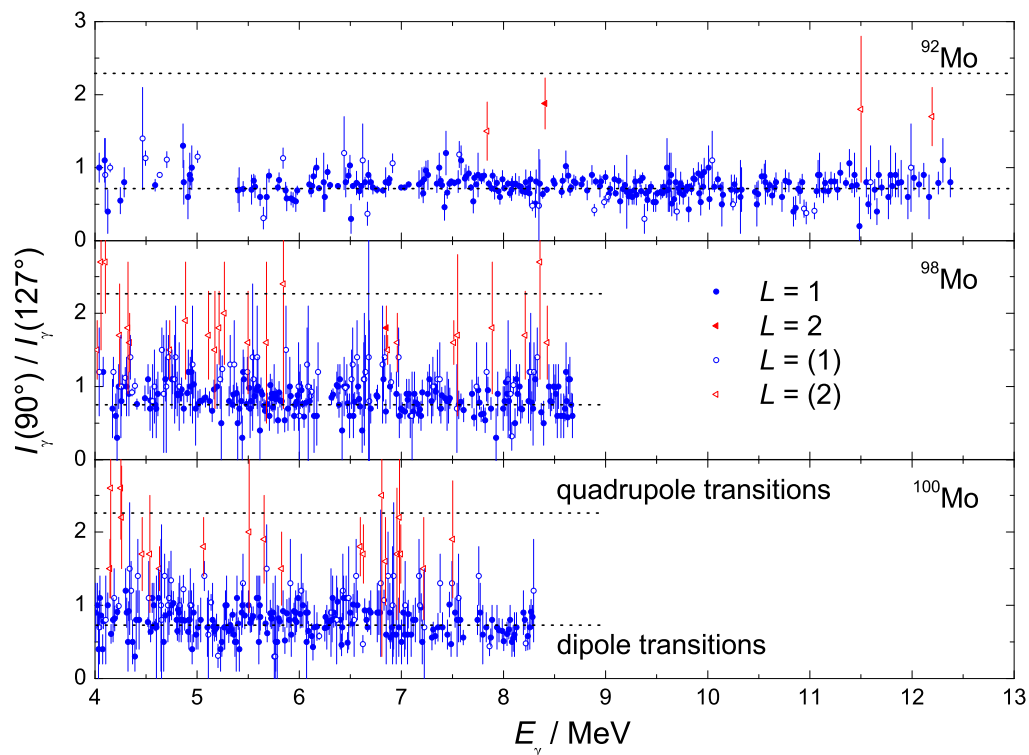


Figure 5.10: Ratio of  $\gamma$ -ray intensities at  $90^\circ$  and  $127^\circ$  determined from the experiments at an electron-beam energy of 13.2 MeV.

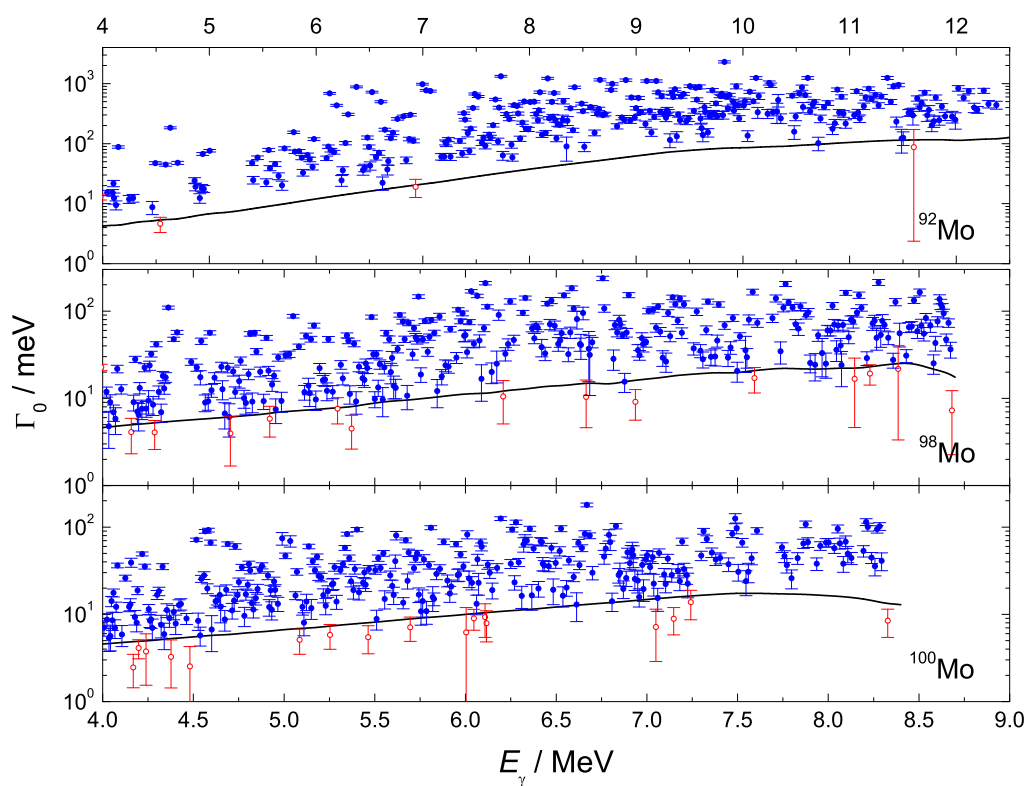


Figure 5.11: Comparison of the decay widths, deduced under the assumption that all transitions are ground-state transitions, with the determined detection limits. The points marked with open circles are considered below the detection limits.

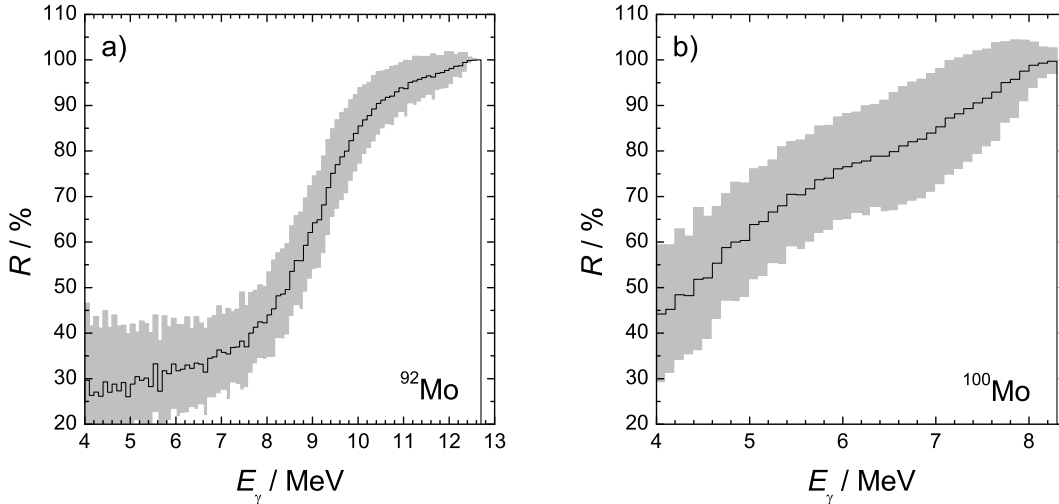


Figure 5.12: Ratio of the intensity of the ground-state transitions versus the intensity of all transitions (including branching) with the same energy in bins of 100 keV for the cases of a)  $^{92}\text{Mo}$  and b)  $^{100}\text{Mo}$ .

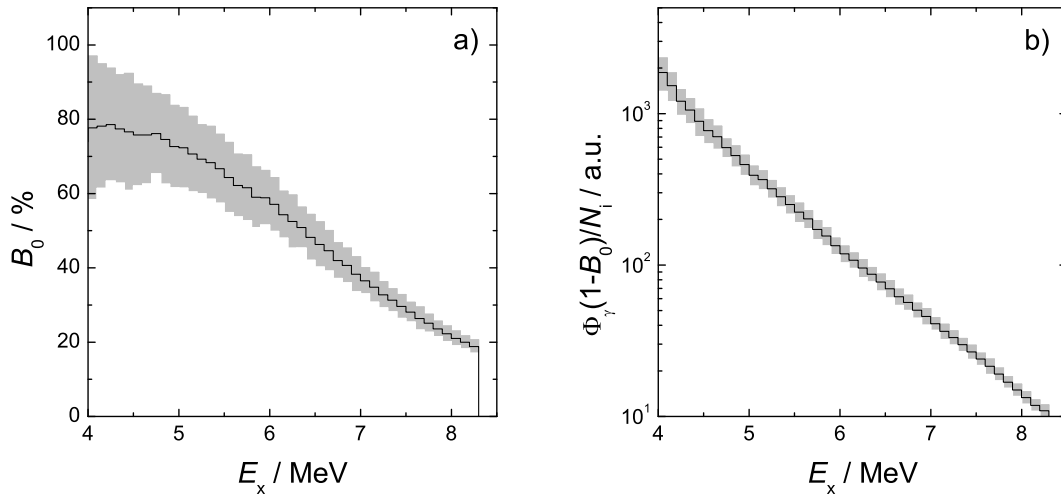


Figure 5.13: Results from the  $\gamma$ -ray cascade simulations for  $^{100}\text{Mo}$  for a) branching ratios for ground-state transitions and b) the average relative intensity of a branching transition deexciting a level with energy  $E_x$ .

way to resolve the branchings is to apply the Ritz principle and select combinations of transitions which satisfy two, three or more step cascades. Such attempts lead to thousands of combinations assuming two step cascades where the major part of them are random combinations due to the limited energy resolution of the experimental data. Other ways to find the possible branchings are measurements at many different electron energies analogous to the investigation of  $^{98}\text{Mo}$  and  $^{100}\text{Mo}$  at the Dynamitron accelerator. Here, it is practically impossible to resolve the branchings because the high level density above 4 MeV requires measurements with small step in the electron-beam energy and long duration to gain sufficient statistical accuracy. In this work the problem of the branchings is discussed in the frame of  $\gamma$ -ray cascade simulations. The Monte Carlo code for  $\gamma$ -ray cascade simulations (see Section 4.8) was used to obtain an estimate for the ratio  $R$  of the intensity of the ground-state transitions with a given energy  $E_\gamma$  to the intensity of all transitions with the same energy  $E_\gamma$ . The simulations were performed using the photon-flux spectrum from the experiment (cf. Fig. 4.4 b). Two spectra of  $\gamma$ -ray transitions to the ground state and of all transitions were collected with a binning of 100 keV.

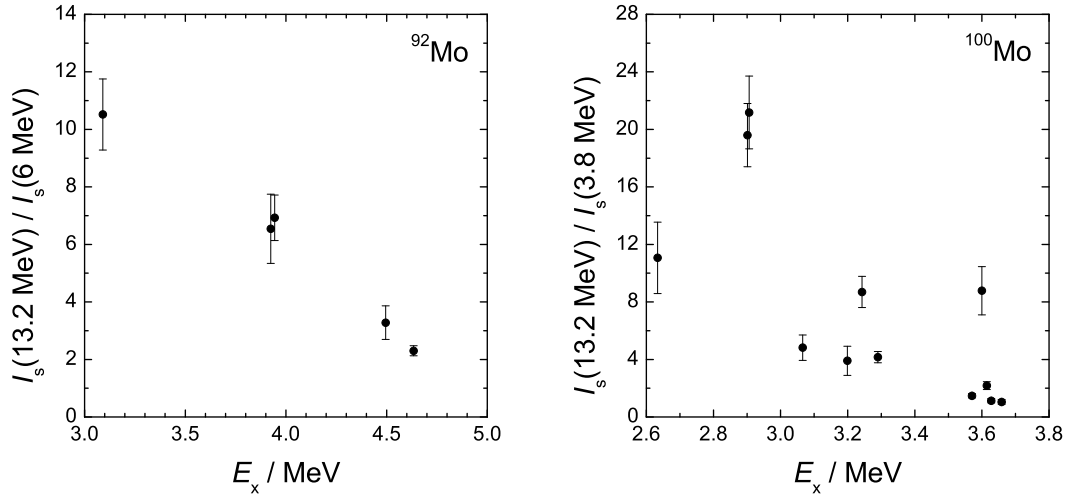


Figure 5.14: Ratio of the integrated cross section determined from the experiments at  $E_e = 13.2$  MeV versus the cross section from the measurements at  $E_e = 6$  MeV and  $E_e = 3.8$  MeV on  $^{92}\text{Mo}$  and  $^{100}\text{Mo}$ , respectively.

The deexcitations of fed levels to the ground state are also considered as ground-state transitions which reflects the situation in a real photon-scattering experiment. The ratio  $R$  gives an estimate of the fraction of the intensity of the ground-state transitions relative to the total  $\gamma$ -ray intensity in a given energy bin. Examples of the dependence of this ratio on the transition energy are presented in Fig. 5.12 a) and b) for the cases of  $^{92}\text{Mo}$  and  $^{100}\text{Mo}$ , respectively. Apparently, the observed peaks close to the neutron separation energy correspond only to deexcitations to the ground state. In the comparison, many branchings are expected at  $\gamma$ -ray energies around 2–4 MeV and the ratio presented in Fig. 5.12 is small.

An important question is the origin of the branching transitions around 2–4 MeV since in the experiments at  $E_e = 13.2$  MeV hundreds transitions were observed in this energy range. The branching ratios for decay to the ground state  $B_0$  can be determined from the same cascade simulations. The dependence of  $B_0$  on the excitation energy is presented in Fig. 5.13 for the case of  $^{100}\text{Mo}$ . The ratios  $B_0$  define an average probability for the decay of levels to the ground state. The average probability for decay to an intermediate transition then is  $(1 - B_0)/N_i$ , where  $N_i = \int_0^{E_x} \rho(E)dE$  is the number of intermediate levels with energy from 0 to  $E_x$ . The area of the peaks corresponding to the branching transitions depend on the product of the photon flux at  $E_x$  and the average probability  $(1 - B_0)/N_i$ . An estimate for the intensity of the branching transitions in dependence on the energy of the excited level  $E_x$  is presented in Fig. 5.13 b) for the case of  $^{100}\text{Mo}$ . From Fig. 5.13 b) it is visible that the levels close to the neutron threshold “produce” many but weak branchings while the levels around 4–5 MeV can decay to the intermediate levels via few but strong branching transitions. Note, that the cascade simulations do not include nuclear structure effects and consider the nucleus in terms of the random matrix theory.

According to these estimates the transitions observed as peaks can be divided to three groups according to the transition energy  $E_\gamma$ :

- 1)  $0 \text{ MeV} < E_\gamma < 4 \text{ MeV}$  - these transitions are mainly branching transitions from excited levels around 4–6 MeV to low-lying levels.
- 2)  $3 \text{ MeV} < E_\gamma < 6 \text{ MeV}$  - are deexcitations with mixed origin - ground state transitions and branchings.
- 3)  $5 \text{ MeV} < E_\gamma < S_n \text{ MeV}$  - are mainly ground-state transitions.

Such division of the  $\gamma$ -ray spectrum nevertheless can not be made with precise limits.

A branching to an intermediate level means that this level is fed and the measured intensity of the

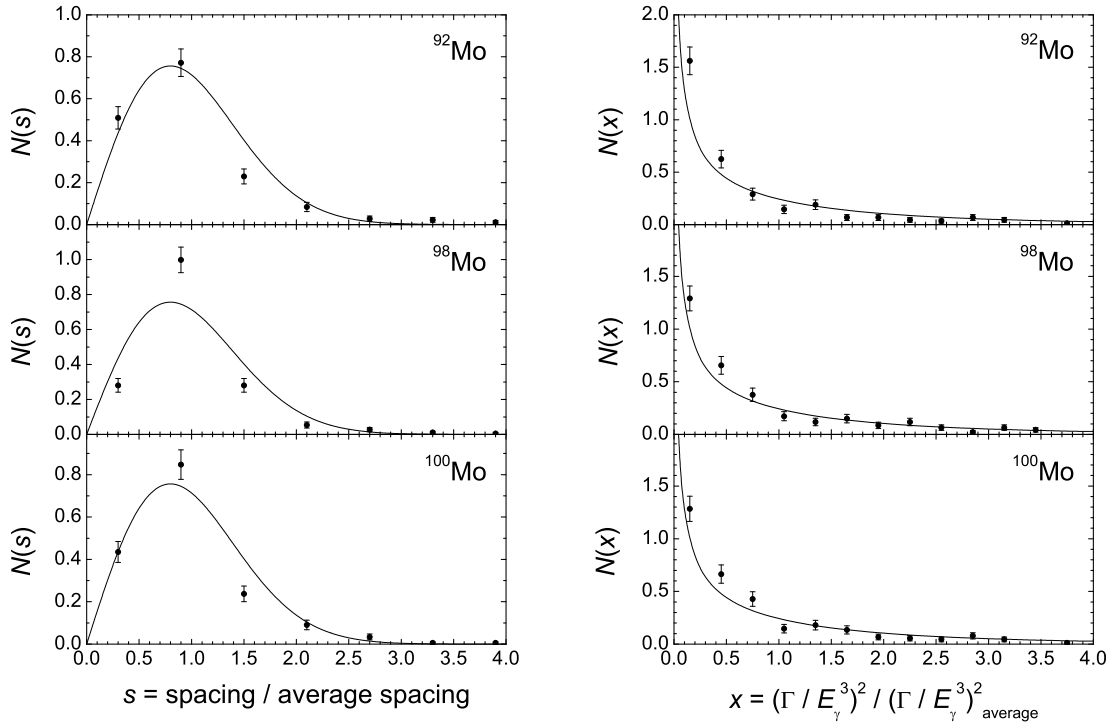


Figure 5.15: Left panel: the nearest-neighbor-spacings distributions of isolated narrow resonances above 5 MeV in  $^{92}\text{Mo}$ ,  $^{98}\text{Mo}$  and  $^{100}\text{Mo}$ . The drawn line represent the Wigner distribution. Right panel: distribution of the transition widths for the isolated narrow resonances above 5 MeV in  $^{92}\text{Mo}$ ,  $^{98}\text{Mo}$  and  $^{100}\text{Mo}$ . The solid lines represent the Porter-Thomas distribution.

deexciting ground-state transition is much stronger than if this level was populated only via photon absorption. The determined photon-scattering cross sections of such fed levels is bigger than if they were not fed. The influence of the feedings is shown in Fig. 5.14 where the integrated photon-scattering cross section of the low-lying levels in  $^{92}\text{Mo}$  and  $^{100}\text{Mo}$  are compared with the cross sections determined from the experiments at  $E_e = 13.2$  MeV. The cascade simulations can be used to determine the average enhancement of the photon-scattering cross section due to the feedings. Since the feedings means a transfer of intensity from an excited level to some intermediate one the cascade simulations have to be performed with included photon flux determined from the experiments at  $E_e = 13.2$  MeV.

### 5.2.1 Statistical properties of the observed resonances

The random-matrix-theory treatment of the nucleus as a system of interacting fermions predicts distributions of the level spacings and of the level widths. The level-spacings distribution is a measure for the fluctuations of the level distances around a uniform (equidistant) level scheme. This distribution has two extremes of no level repulsion - the Poisson distribution (Eq. (4.41)) and of strong repulsion - the Wigner one (Eq. (4.40)). The level widths show fluctuations around an average value  $\overline{\Gamma}_0$  as well. If the amplitudes of the transition matrix elements are assumed to form Gaussian ensemble, then the width distribution is well described by a  $\chi^2$  distribution with zero degree of freedom, known as Porter-Thomas distribution [Port56] (Eq. (4.46)).

These distributions are evident of thermal neutron-scattering experiments right at the neutron separation energy and by results of  $\beta$ -decay spectroscopy in the range close to the ground state. The photon-scattering experiments performed with continuum bremsstrahlung allow a simultaneous excitation of all levels with spin  $J = 1$  and they are a good tool to investigate the statistical properties of the nuclear levels in the intermediate excitation range. The analysis suffers from unresolved branch-



ings which appear at the low energy part of the spectrum and, moreover, by the insufficient detector resolution to resolve all resonances at high energy close to the neutron threshold.

The results from the photon-scattering experiments on  $^{92}\text{Mo}$ ,  $^{98}\text{Mo}$  and  $^{100}\text{Mo}$  at  $E_e = 13.2$  MeV are used to derive the distributions of the nearest neighbor spacings and of the transition widths. According to the discussion above for the origin of the observed resonances, only the transitions with energies larger than 5 MeV are included in the analysis of the statistical properties of the isolated resonances. The resonances were collected in groups of 50 transitions each according to their energy. An average spacing and average width was determined for each group and a histogram was created. The histograms of the individual groups were averaged and normalized to unity. The obtained distributions for the nearest neighbor spacings and for the transition widths are presented in Fig. 5.15.

The comparisons in Fig. 5.15 show that the Mo data do closely resemble Wigner and Porter-Thomas distributions indicating a quantum chaotic behavior as predicted for Gaussian orthogonal ensemble.

### 5.2.2 Determination of the total strength

The high level density and the Porter-Thomas fluctuations of the decay widths yield to many weak transitions which can not be observed as isolated peaks. In addition, as it was discussed above every level can decay to many intermediate levels via weak transitions. Therefore not all of the information is contained in peaks. Many of the transitions are so weak that their superposition is observed as a continuum of unresolved strength. An estimate for the intensity of resonant scattering “hidden” in the continuum can be obtained from a comparison of spectra of  $\gamma$ -rays scattered from different isotopes measured at the same conditions. The spectra measured at  $127^\circ$  from the photon-scattering experiments on  $^{98}\text{Mo}$  and  $^{100}\text{Mo}$  at  $E_e = 13.2$  MeV are shown in Fig. 5.16 a). The spectrum of  $^{100}\text{Mo}$  is normalized to the photon flux and to the target mass relative to  $^{98}\text{Mo}$ . The spectra were collected at identical experimental conditions. The two spectra are characterized by a decrease of intensity beyond the neutron separation energy caused by the dominant emission of neutrons. Above  $S_n$  the spectrum contains non-resonant background (see Section 3.4) because the deexcitation of the levels is dominated by emission of neutrons. Using the different neutron separation energies in  $^{98}\text{Mo}$  ( $S_n = 8.64$  MeV) and  $^{100}\text{Mo}$  ( $S_n = 8.3$  MeV) one finds a range between 8.3 and 8.6 MeV in the spectrum of  $^{98}\text{Mo}$  for which the non-resonant background is defined from the spectrum from  $^{100}\text{Mo}$ . The residuum spectrum will contain the intensity of the resonant  $\gamma$ -rays of  $^{98}\text{Mo}$ . The ratio of the integrated area in the mentioned range to the area of the identified peaks is about three which shows that only 30 % of the intensity are obtained from analysis of the peaks. This ratio depends on the resolution of the detectors and the number of levels with sufficient high widths  $\Gamma_0$ . The level density of states with  $J=1$  is shown in Fig. 5.17a) for the three Mo isotopes. The ratio  $D/\Gamma_0$  of the average level spacings to the average widths  $\Gamma_0$  is an estimate for the overlap of the levels. The ratio  $D/\Gamma_0$  is presented in Fig. 5.17b), here the average widths  $\Gamma_0$  are calculated from the photoabsorption cross section  $\sigma_\gamma$  (cf. Eq. 5.1 and Fig. 5.23).

It is desired to extend the estimate of the non-resonant background (cf. Fig. 5.16 a) in the measured spectrum at lower energies. In this work, GEANT3 simulations were performed in order to determine the non-resonant background in the measured spectra. An example for a comparison of simulated non-resonant background and the spectra of photons scattered from  $^{98}\text{Mo}$  and  $^{100}\text{Mo}$  is presented in Fig. 5.16 b). The determination of the non-resonant background and the performed simulations are discussed in detail in Section 4.7.

The continuum is defined as the residuum of the measured spectrum after subtraction of the non-resonant background. Comparisons between the measured spectra and the simulated non-resonant backgrounds are shown in the left panel of Fig. 5.18 for  $^{92}\text{Mo}$ ,  $^{98}\text{Mo}$  and  $^{100}\text{Mo}$ . The continuum contains the ground-state transitions (elastic scattering) and in addition, transitions to low-lying excited states (branching transitions) as well as transitions from these states to the ground state (cascade transitions) which cannot be clearly distinguished. The first step of the analysis of the continuum is a removal of all branching and cascade transitions. This removal is performed in a similar way as the

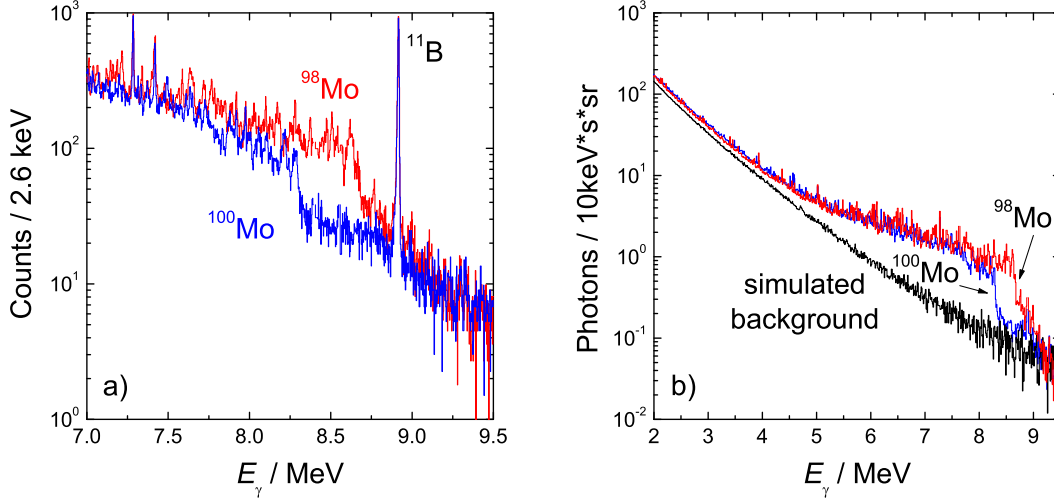


Figure 5.16: Comparison a) of the experimental spectra from  $^{98}\text{Mo}$  and  $^{100}\text{Mo}$  measured at  $E_e = 13.2$  MeV and b) the simulated non-resonant background with the efficiency corrected spectra.

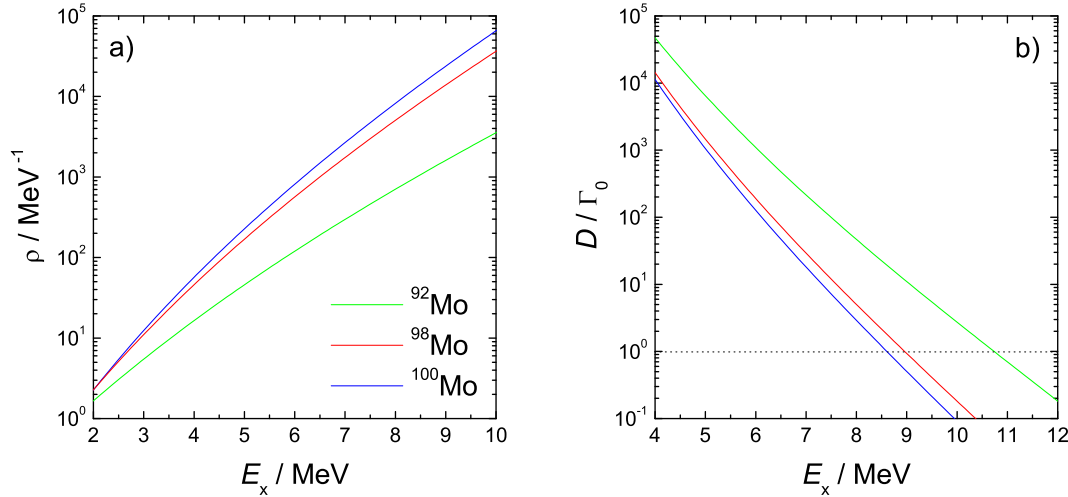


Figure 5.17: Dependence of the level density a) of states with  $J=1$  and the ratio of the averaged level spacing to the averaged width b) on the excitation energy for the investigated molybdenum isotopes.

removal of the “detector background” described in Section 4.7. Cascade simulations were performed for the investigated molybdenum isotopes. Spectra of deexcitation  $\gamma$ -rays were collected for every bin of 100 keV range of excited levels. Example of such deexcitation spectrum from levels located at 9.7 MeV in  $^{92}\text{Mo}$  is presented in Fig. 5.19. The intensity of the ground-state transitions in the simulated spectrum is normalized to the intensity of the continuum in the considered energy bin and the counts of the branching transitions are subtracted from the continuum. The procedure of correction for branching and feedings starts at the highest energy bin close to the neutron threshold and continues to lower energies. As a result of this correction the continuum contains only the intensity of the ground-state transitions which corresponds to elastic photon scattering. Comparison between the continuum and the distribution of the ground-state transitions is shown in the right panel of Fig. 5.18 for all investigated Mo isotopes. The cross section for elastic scattering can be determined from the corrected continuum and the photon flux for every bin individually according to Eq. (4.20). According to Eq. (2.5) the photoabsorption cross section is related to the cross section for elastic scattering:  $\sigma_\gamma = \sigma_{\gamma\gamma}/B_0$ . The branching ratios for transition to the ground state are determined from

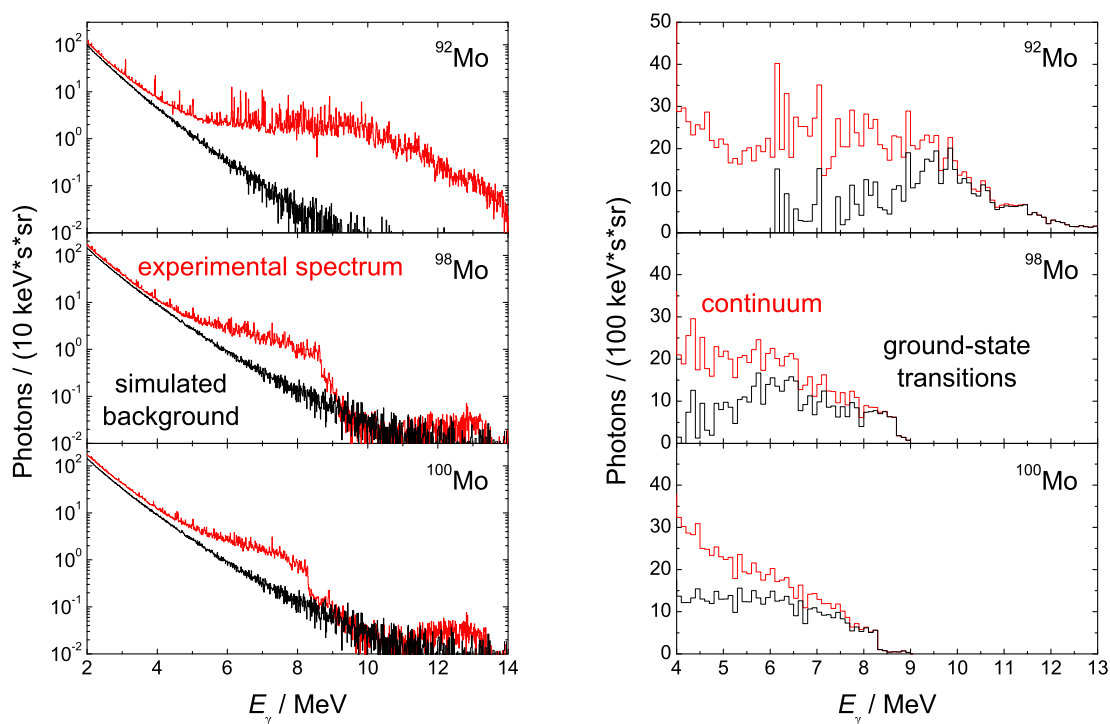


Figure 5.18: Comparisons between: left - the experimental spectrum and the simulated non-resonant background; right - the resonant continuum and the corrected one for branchings and feedings.

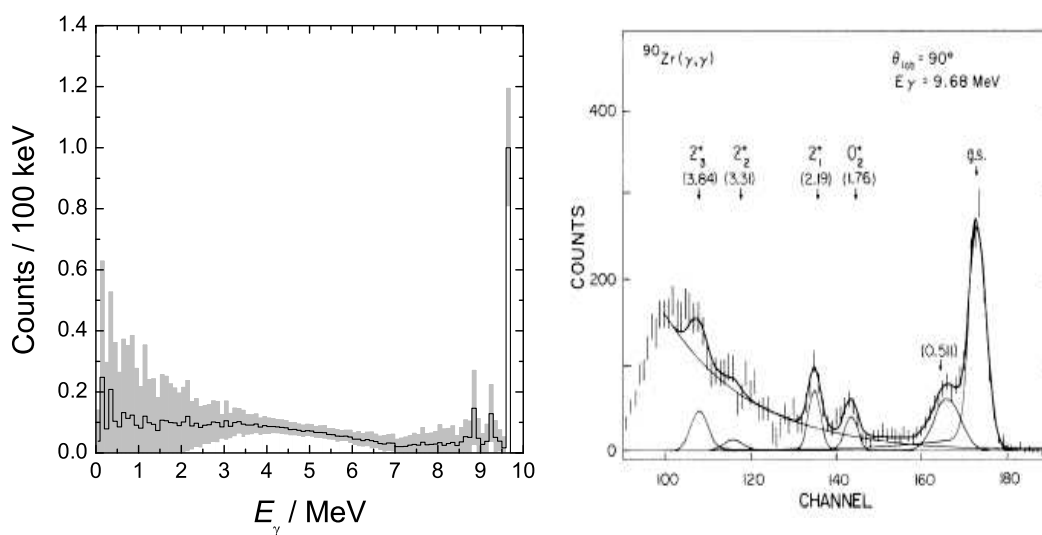


Figure 5.19: Left: simulated spectrum of transitions deexciting levels in  $^{92}\text{Mo}$  located at 9.7 MeV. Right: a spectrum of  $\gamma$ -rays scattered from  $^{90}\text{Zr}$  irradiated with tagged photons with energy of  $E_\gamma=9.68 \text{ MeV}$ , the figure is taken from [Alar87].

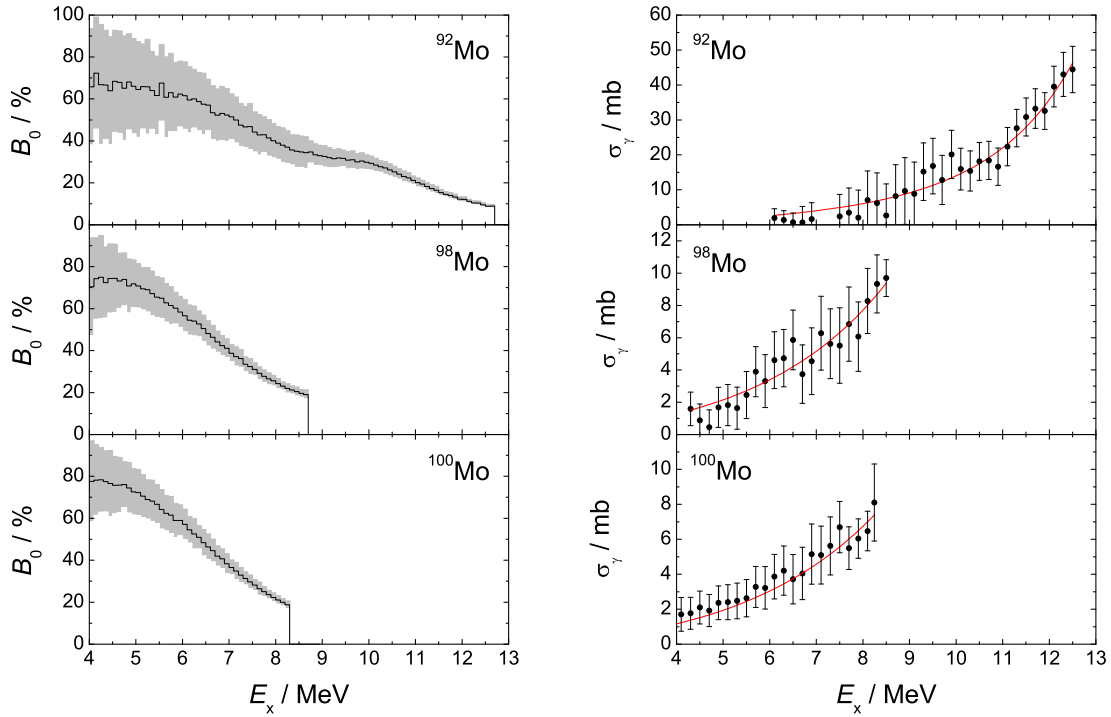


Figure 5.20: Left panel: simulated branching ratios  $B_0$  for ground-state transitions. Right panel: deduced photoabsorption cross section  $\sigma_\gamma$  compared with the included in the simulations cross section.

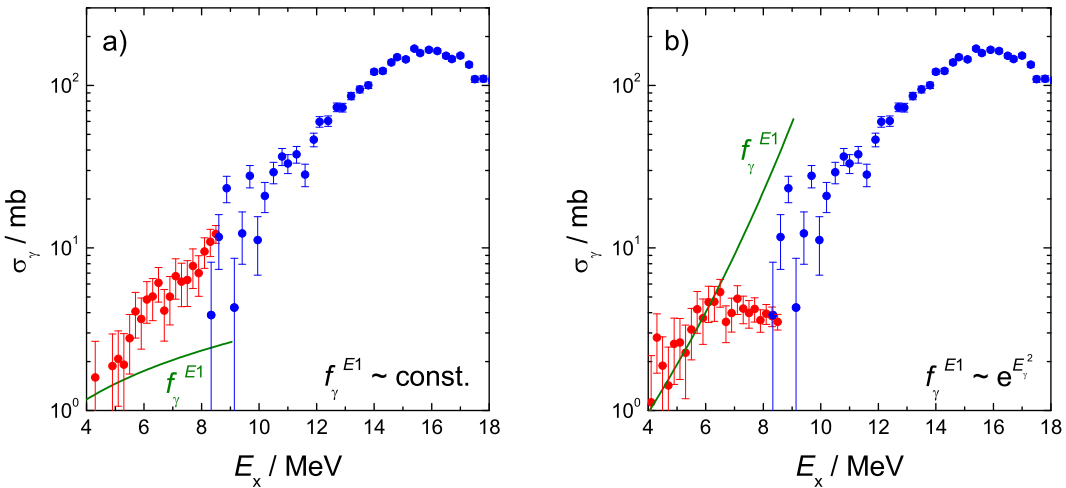


Figure 5.21: Analysis of the results from the photon-scattering experiment on  $^{98}\text{Mo}$  with a constant strength function a) and with a Gaussian strength function b) included in the simulations of  $\gamma$ -cascades.

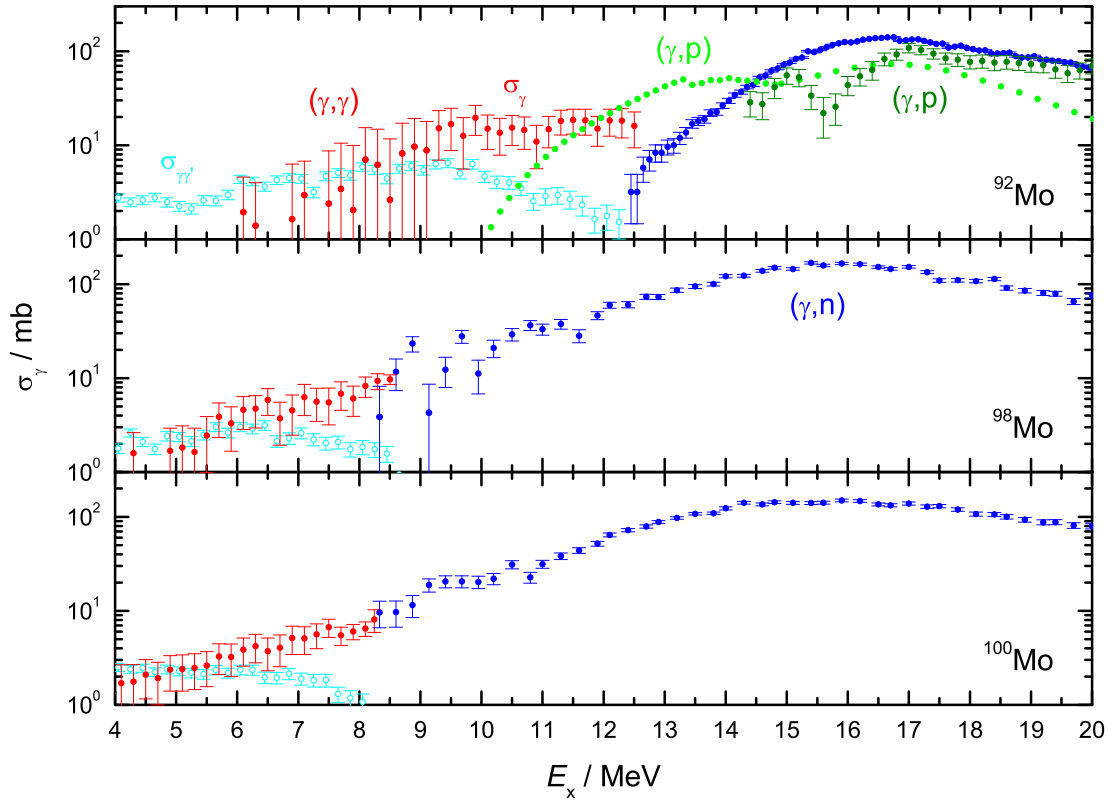


Figure 5.22: Comparison of determined photoabsorption cross section from the photon-scattering experiments on  $^{92}\text{Mo}$ ,  $^{98}\text{Mo}$ ,  $^{100}\text{Mo}$  at  $E_e = 13.2$  MeV with the measured cross section for  $(\gamma, n)$  reaction [Beil74]. In the case of  $^{92}\text{Mo}$ , the calculated [Raus04] and measured [Shod75] cross sections for  $(\gamma, p)$  reaction are depicted with light green and dark green points, respectively. The cross section deduced from the continuum without any corrections is presented with opened circles.

the same cascade simulations according Eq. 4.23, they are presented in the left panel of Fig. 5.20. The values for the ratios  $B_0$  are listed in Appendix D for the three investigated molybdenum isotopes. The determined photoabsorption cross sections  $\sigma_\gamma$  are presented in the right panel of Fig. 5.20. They are compared with absorption cross section used in the cascade simulations. Since the result of the analysis determines the absorption cross section, which defines the strength function, and the input of the cascade simulations is the same strength function then the simulations have to be performed for various input strength function till it converges with the result of the analysis. This procedure was applied only to the analysis of the  $^{92}\text{Mo}$  experiment, in the case of  $^{98}\text{Mo}$  and  $^{100}\text{Mo}$  the input strength function is bigger by a constant factor of 1.5 and 2.7, respectively, than the result of the analysis. An example of analysis of the  $^{98}\text{Mo}$  experiment with two extreme strength functions is presented in Fig. 5.21. The usage of a constant strength function (cf. Fig. 5.21 a) leads to small branching ratios for ground-state transitions  $B_0$  and over correction for the photoabsorption cross section. In contrast, the usage of rapidly increasing strength function (Gaussian function) leads to big ratios  $B_0$  and under-correction for  $\sigma_\gamma$  (cf. Fig. 5.21 b). The comparisons in Fig. 5.21 show that there is no agreements between the strength function included in the cascade simulations, expressed as cross section, and the result of the analysis.

The results for the photoabsorption cross section for  $^{92}\text{Mo}$ ,  $^{98}\text{Mo}$ ,  $^{100}\text{Mo}$  from the present experiments at  $E_e = 13.2$  MeV are compared with the measurement of the  $(\gamma, n)$  cross sections [Beil74] in Fig. 5.22. In the case of  $^{92}\text{Mo}$ , the calculated [Raus04] and the measured [Shod75] cross sections for the  $(\gamma, p)$  reaction are additionally depicted in Fig. 5.22. Since the calculated  $(\gamma, p)$  cross sections end at 14.8 MeV, they are extended with calculations using the Monte Carlo code “TALYS” [Koni04] up

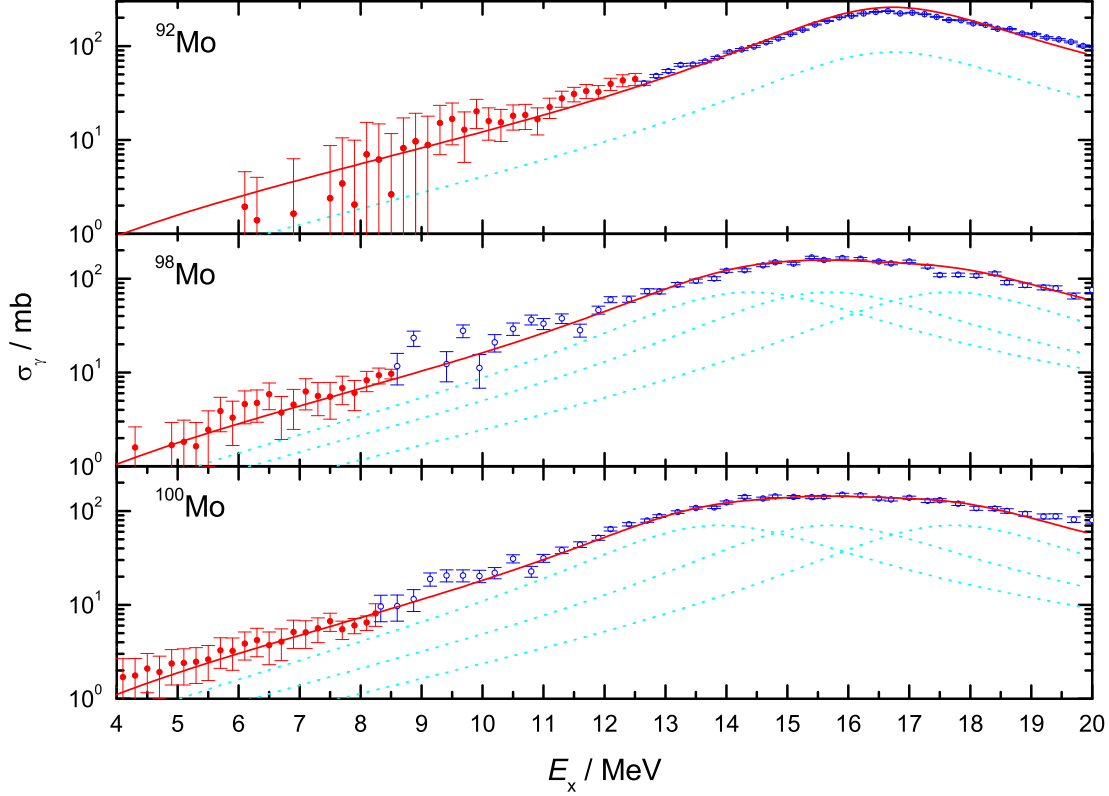


Figure 5.23: Comparison of determined photoabsorption cross section from the photon-scattering experiments on  $^{92}\text{Mo}$ ,  $^{98}\text{Mo}$ ,  $^{100}\text{Mo}$  at  $E_e = 13.2$  MeV (filled circles) and the measured cross section for  $(\gamma, n)$  reaction [Beil74] (open circles) with the fit of the Giant Dipole Resonance (solid line). In the case of  $^{92}\text{Mo}$ , the calculated cross sections for  $(\gamma, p)$  reaction are summed up. The fit is a superposition of three Lorentzian functions depicted with dash lines.

to 20 MeV. The cross section  $\sigma_{\gamma\gamma'}$  deduced from the continuum is presented in Fig. 5.22 with open circles to show the effect of the applied corrections.

It is of importance to have a parameterization of the GDR connecting the peak area of the GDR with the tail. The phenomenological interpretation of the GDR represents it as a result of vibrations of the neutron system against the proton system. The GDR of axially deformed nuclei is understood as superposition of independent vibrations along every axis of the ellipsoid such that the strength of this vibrations is conserved. A parameterization of the GDR, proposed by Prof. E. Grosse and presented in Eq. (5.1), is used for the interpolation of the data points obtained from the photon-scattering experiments and the measurements of  $(\gamma, n)$  cross sections. The photoabsorption cross section is represented as a superposition of three Lorentzian functions with integrated cross sections equal to  $1/3$  of the  $E1$  sum rule  $S_{\text{TRK}} = \int_0^\infty \sigma_\gamma(E) dE = 60NZ/A$  mb MeV [Ring80], known as Thomas-Reiche-Kuhn sum rule:

$$\sum_{i=1}^3 \sigma_{\gamma i} = \frac{2\alpha \cdot S_{\text{TRK}}}{3\pi} \sum_{i=1}^3 \frac{E_x^2 \Gamma_i(E_x)}{(E_x^2 - E_i^2)^2 + E_x^2 \Gamma_i^2(E_x)} \quad (5.1)$$

The width of the Lorentzian function is assumed to depend on the energy:  $\Gamma_i = \Gamma_0 (E_x/E_i)^\delta$ , where  $\Gamma_0$  is set to 4.0 MeV according to the systematics of the GDR widths [Carl74]. The energies  $E_i$  are

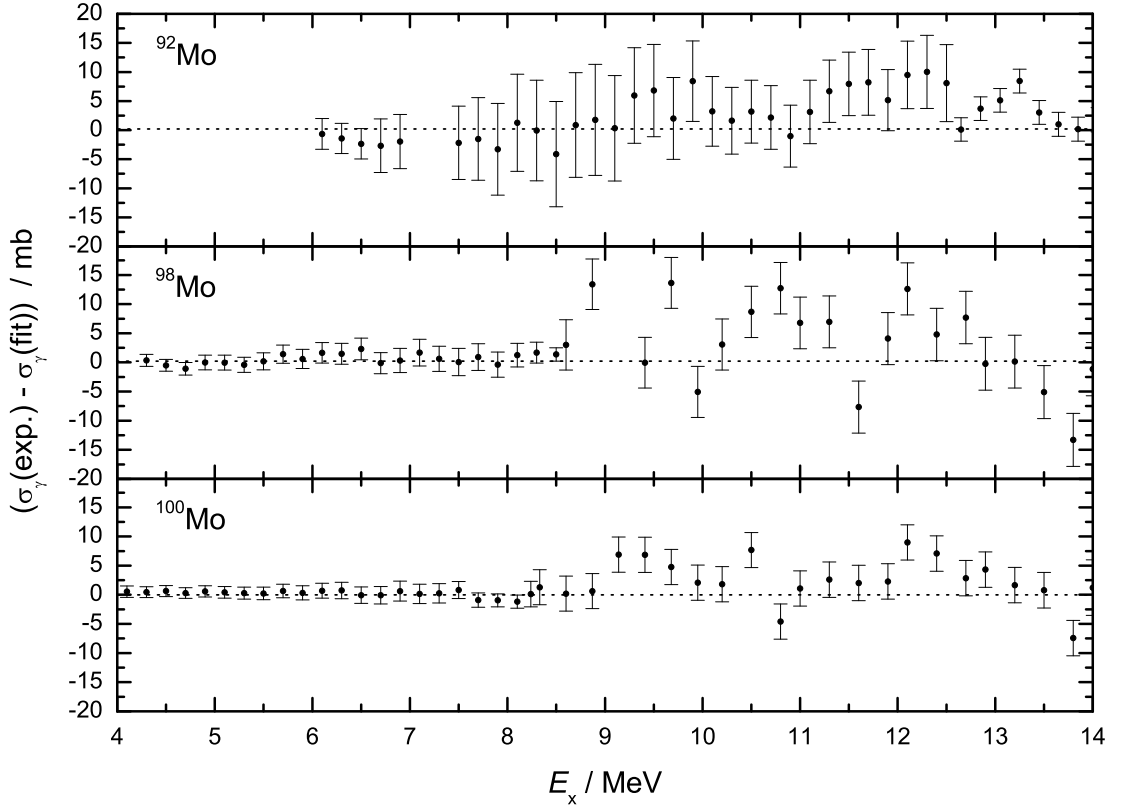


Figure 5.24: Residuum plot of the experimentally determined photoabsorption cross section  $\sigma_\gamma$  and the fit of the Giant Dipole Resonance presented in Fig. 5.23.

obtained from the deformation parameters  $\varepsilon$  and  $\gamma$  according to the Nilsson model [Nils95]:

$$\begin{aligned}
 E_1 &= E_0 \left[ 1 - \frac{2}{3} \varepsilon \cos \left( \gamma + \frac{2\pi}{3} \right) \right], \\
 E_2 &= E_0 \left[ 1 - \frac{2}{3} \varepsilon \cos \left( \gamma - \frac{2\pi}{3} \right) \right], \\
 E_3 &= E_0 \left[ 1 - \frac{2}{3} \varepsilon \cos \gamma \right].
 \end{aligned} \tag{5.2}$$

The deformation parameters  $\varepsilon$  and  $\gamma$  are calculated using the Nilsson-Strutinsky method [Nils95] and are presented in Table 6.1. The results of the best fit are presented in Table 5.3 and Fig. 5.23. The parameter  $\delta$  was obtained to be  $\delta = 0.0(3)$ , i.e. the GDR in the investigated Mo isotopes can be parameterized with a Lorentzian shape properly adjusted to the ground-state deformation with energy independent width.

Table 5.3: Results of the best fit of the Giant Dipole Resonance in  $^{92}\text{Mo}$ ,  $^{98}\text{Mo}$  and  $^{100}\text{Mo}$  according to the expression presented in Eq. (5.1).

nucleus	$E_0$ / MeV	$\alpha$	$\delta$
$^{92}\text{Mo}$	16.7(3)	1.19(12)	0.0(3)
$^{98}\text{Mo}$	15.92(13)	0.94(13)	0.0(2)
$^{100}\text{Mo}$	15.8(3)	0.91(4)	0.0(2)

The comparison of the photoabsorption cross section and the fit of the GDR (cf. Fig. 5.23) shows a slight enhancement of the strength at about 9 MeV. A residuum plot, presented in Fig. 5.24, of the experimental cross section and the fit shows irregularities despite large statistical uncertainties. Similar structures in the photoabsorption data are frequently assigned as “pygmy” resonances, see e.g. Refs. [Bart72] and [Adri05].



# Chapter 6

## Discussion

In this Chapter, the determined dipole-strength distributions are compared with predictions of the quasiparticle-random-phase approximation (QRPA). An QRPA code for deformed nuclei was developed by F. Dönau based on Nilsson-like single-particle wave functions and separable interaction terms [Doen05a]. The present version of the QRPA code is using the quasiparticle wave functions as obtained from the Rossendorf Tilted-Axis-Cranking (TAC) code [Frau93, Jenk01] which allows the treatment of quadrupole-deformed shapes, a monopole-pair potential as well as a rotational cranking term. The available TAC code enables the selfconsistent calculation of the equilibrium shapes by means of the shell-correction method. Using the strength-function method [Nest02] the code yields the strength distribution of transitions,  $E1$  or  $M1$ , between the ground state and the vibrational states.

The observed de-excitations in  $^{98}\text{Mo}$  and  $^{100}\text{Mo}$  of states with spin  $J = 1$  to both the  $0^+$  ground state and to the first excited  $0^+$  state is quantitatively discussed. A model based on one-particle-one-hole excitations has been developed by F. Dönau and S. Frauendorf which estimates the mixing of the two  $0^+$  shape isomers from the experimental transition strength.

### 6.1 Systematics of magnetic dipole strength in the stable even-mass Mo isotopes

In the following, the systematic behavior of the  $M1$  strength in the chain of even-mass Mo isotopes from  $^{92}\text{Mo}$  ( $N = 50$ ) to  $^{100}\text{Mo}$  ( $N = 58$ ) will be discussed in comparison with predictions of the standard quasiparticle-random-phase approximation (QRPA) [Ring80, Solo97] and, in addition, with predictions of the shell model. The results of the present experiments (see Section 5.1) are complemented by the ones of previous work on  $^{94}\text{Mo}$  [Piet99, Fran03] and  $^{96}\text{Mo}$  [Fran04]. In  $^{94}\text{Mo}$  and  $^{96}\text{Mo}$  also one and two  $1^-$  states, respectively, were identified, which are considered as the  $1^-$  members of the  $2^+ \otimes 3^-$  quintuplet and include about 13% and 30%, respectively, of the total dipole strength in the considered energy region [Fran03, Fran04]. In the following discussion, positive parity is assumed for all  $J = 1$  states up to 4 MeV in  $^{98}\text{Mo}$  and  $^{100}\text{Mo}$  but it should be kept in mind that a few of the observed states may have negative parity as well. The systematics of the low-lying  $1^+$  excitations as well as the cumulative  $M1$  strengths in the chain of Mo isotopes are presented in Fig. 6.2.

#### 6.1.1 QRPA calculations

The structure of the ground states is known to change from a spherical shape at  $A = 92$  to a deformed one at  $A = 100$  (cf. Ref. [Moel86]) which is expected to influence the strength distribution of the dipole excitations in the Mo isotopic chain with  $A = 92 - 100$ . As a necessary ingredient of the QRPA calculations the equilibrium shapes of the ground states have been determined by using the Nilsson-Strutinsky method [Nils95] including pairing properties with the gap parameters given in Ref. [Mant01]. The resulting potential-energy surfaces (PES) are shown in Fig. 6.2. They reflect the shape change from the nearly spherical nuclei  $^{92,94}\text{Mo}$  to relatively soft PES with triaxial minima in

<sup>98,100</sup>Mo. The deformation parameters of the minima are given in Table 6.1.

It should be mentioned that the exact location and strength of the dipole transitions cannot be predicted in detail, because for deformed nuclei an advanced QRPA code, in which all input quantities could be calculated fully selfconsistently with realistic residual interactions, is hitherto not available. The empirical Nilsson model and phenomenological residual interactions were used in order to make the QRPA approach applicable for deformed nuclei. Another problem is that in the standard QRPA aiming at the calculation of dipole states the coupling with states of other multiplicities is neglected. These missing couplings lead to shifts of the states and redistributions of the strengths. Their approximate treatment in terms of a phonon-phonon approach [Solo97, LoIu01] may improve the description but in detail the discrepancy to the individual data remains. In spite of the above simplifications the QRPA is the appropriate tool to describe the gross features of  $M1$ -strength distributions such as the summed strength and its dependence on nucleon numbers and on the shapes of the nuclei. The following questions will be discussed :

(i) Is the QRPA, which includes the change of the deformation in the series  $A = 92 - 100$ , able to describe the observed *summed* dipole strength in the energy range of  $E \approx 2.5 - 4$  MeV and what  $M1$  strength is predicted at higher energy?

(ii) What can be learned about the structure of the excitation modes and the residual interaction?

The QRPA calculations use a mixture of separable multipole-multipole residual interactions with the strength parameters described below. As a helpful tool for analyzing the calculated QRPA spectra the method of mode suppression [Doen05] is applied which enables the complete elimination of spurious modes and, moreover, can be used to characterize the types of the excitations in terms of the different interactions.

The following discussion will be restricted only on  $M1$  excitations because the QRPA gives practically no strength for the electric-dipole states below 4 MeV (see Fig. 6.5). States with  $J^\pi = 1^-$  in the range up to 4 MeV as found in <sup>94</sup>Mo [Fran03] and <sup>96</sup>Mo [Fran04] are likely to be two-phonon states formed by a coupling of collective octupole and quadrupole phonons, which are outside the QRPA description. Generally, the QRPA calculations predict substantial  $E1$  strength above 6 MeV which is the average shell gap between the shells of different parities in nuclei around  $A = 100$ .

The QRPA calculations for the  $1^+$  excitations shall be described in more detail. The following Hamiltonian was used in the QRPA calculations:

$$H_{M1}^{\text{QRPA}} = h_{\text{MF}} - \frac{1}{2} \sum_{t=0,1} \kappa_j^t \mathbf{J}^t \cdot \mathbf{J}^t - \frac{1}{2} \sum_{t=0,1} \kappa_s^t \mathbf{S}^t \cdot \mathbf{S}^t. \quad (6.1)$$

The term  $h_{\text{MF}}$  in Eq. (6.1) includes the Nilsson mean field plus monopole pairing using the equilibrium deformation derived before. The following terms  $\mathbf{J}^t \cdot \mathbf{J}^t$  ( $jj$ ) and  $\mathbf{S}^t \cdot \mathbf{S}^t$  ( $ss$ ) are interaction terms composed of the isoscalar ( $t = 0$ ) and isovector ( $t = 1$ ) parts of the total angular momentum operator  $\mathbf{J} = \mathbf{L} + \mathbf{S}$  and the spin operator  $\mathbf{S}$ , i.e.  $\mathbf{J}^{t=0,1} = \mathbf{J}^\pi + (-1)^t \mathbf{J}^\nu$  and  $\mathbf{S}^{t=0,1} = \mathbf{S}^\pi + (-1)^t \mathbf{S}^\nu$  where  $\pi$  and  $\nu$  stand for proton and neutron, respectively. The actual strength of the interaction terms is tuned by the values of the parameters  $\kappa_j^t$  and  $\kappa_s^t$  in Eq. (6.1). A quadrupole-quadrupole interaction term turned out to be not important for the dipole states under study.

The suppression method [Doen05] for the removal of the spurious oscillations of the total angular momentum  $\mathbf{J}$  is considered below. The quadratic term  $\kappa_j \mathbf{J} \cdot \mathbf{J}$  in the QRPA Hamiltonian (Eq. (6.1)) acts like an oscillator spring force for the angular momentum  $\mathbf{J}$  with the tunable stiffness parameter  $\kappa_j$ . Hence, by choosing the stiffness parameter  $\kappa_j$  rather large the frequency of the unwanted oscillations of  $\mathbf{J}$  contributing to the QRPA spectrum can be shifted up to any high energy such that this spurious motion becomes frozen, i.e., this mode gets too “hard” to be excited within the considered energy range. With the same method the oscillatory motion of any other selected operator can be eliminated. This technique is used to analyze the structure of the phonon excitations.

The  $M1$  transition operator can be expressed by the same operators  $\mathbf{J}^t$  and  $\mathbf{S}^t$  determining the

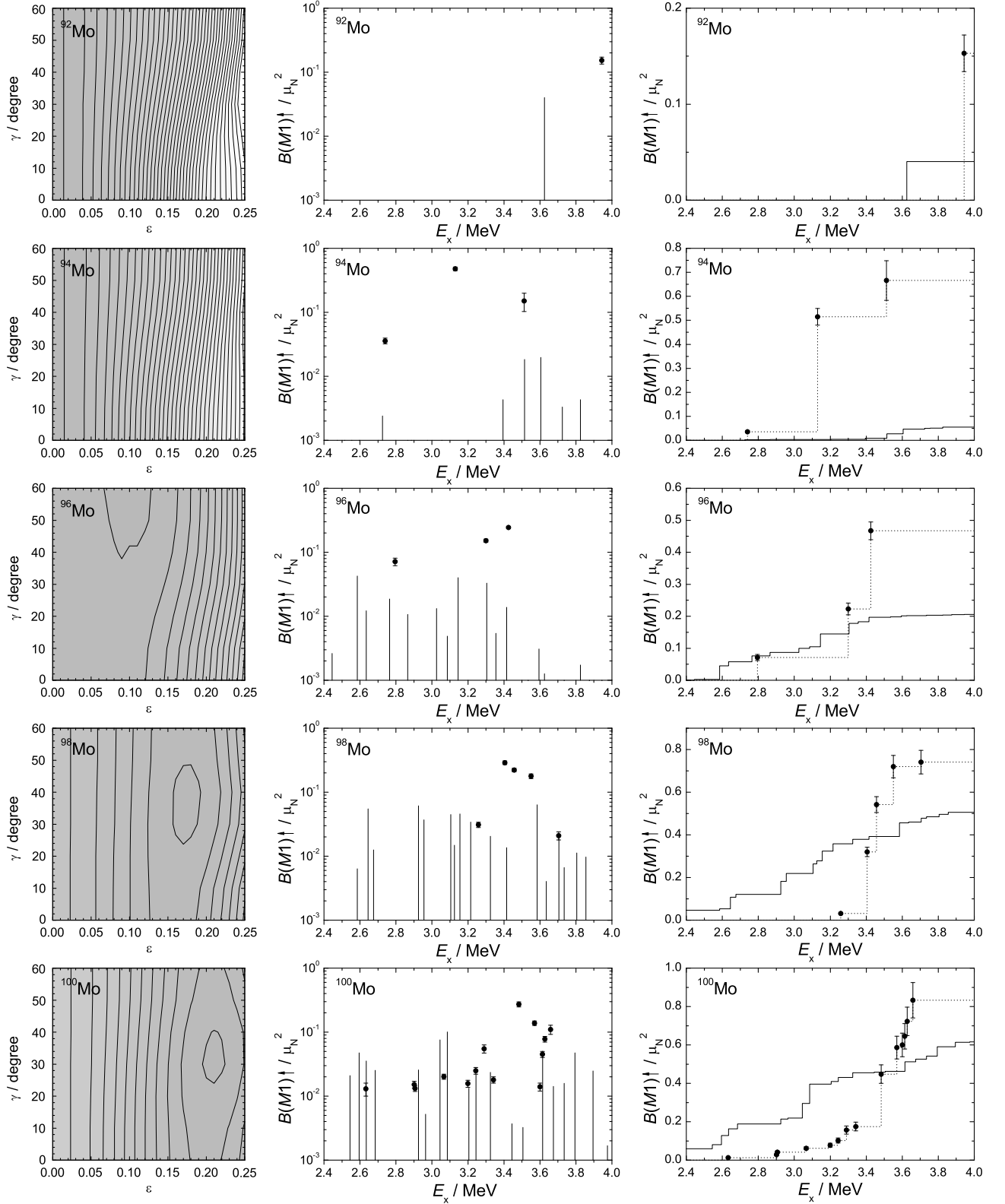


Figure 6.1: Potential energy surfaces (left) and  $M1$ -strength distributions in the even-mass Mo isotopes presented as individual-level plots (middle) and as a cumulative plot (right). Experimental values are given as data points. RPA calculations are presented as bars or solid lines. Note that the values for  $^{98}\text{Mo}$  and  $^{100}\text{Mo}$  are based on the assumption of positive parity for all  $J = 1$  states observed in the present experiments.

interaction terms in Eq. (6.1):

$$\widehat{\mathbf{M1}} = \sqrt{\frac{3}{4\pi}}(\mathbf{L}^\pi + g_s^\pi \mathbf{S}^\pi + g_s^\nu \mathbf{S}^\nu) = \sqrt{\frac{3}{4\pi}} \left( \frac{1}{2} \mathbf{J}^{t=0} + \frac{1}{2} \mathbf{J}^{t=1} + g_s^{t=0} \mathbf{S}^{t=0} + g_s^{t=1} \mathbf{S}^{t=1} \right). \quad (6.2)$$

With the usual gyromagnetic factors  $g_s^\pi$  and  $g_s^\nu$  and an attenuation factor of 0.7 one obtains the values  $g_s^{t=0} = 0.12 \mu_N$  and  $g_s^{t=1} = 2.79 \mu_N$  for the strengths of the isoscalar and isovector-spin parts, respectively, of the  $M1$  transition operator. From the above decomposition (6.2) the following general conclusions can be drawn for the  $M1$  transition matrix elements. The term proportional to the total angular momentum ( $\sim \mathbf{J}^{t=0} \equiv \mathbf{J}$ ) should not contribute at all, since for an exact calculation the relation  $\langle 1^+ | \mathbf{J} | 0 \rangle = 0$  holds automatically. However, the QRPA for the deformed case does not satisfy angular-momentum conservation. Therefore, it is a necessary requirement for an accurate QRPA treatment of deformed nuclei to make sure that the transition amplitudes  $\langle ph | \mathbf{J} | 0 \rangle$  vanish for all phonon excitations  $|ph\rangle$  to the QRPA ground state  $|0\rangle$ . This is achieved by the suppression of the spurious motion from  $\mathbf{J}$ .

The isovector-orbital term ( $\sim \mathbf{J}^{t=1} = \mathbf{J}^\pi - \mathbf{J}^\nu$ ) is known to generate proton-neutron contrarotational  $1^+$  states [LoIu78] which, in principle, can attract a large part of the available  $M1$  strength below 5 MeV [Rich95]. Such an isovector- $jj$  contribution is expected to be large when high- $j$  proton and neutron orbits get excited because of their sizeable angular-momentum content. The isoscalar-spin contribution ( $\sim \mathbf{S}^{t=0}$ ) is strongly quenched by the factor of 0.12, whereas the isovector-spin contribution ( $\sim \mathbf{S}^{t=1}$ ) is the largely favored term because of the factor of 2.79. Hence, the total  $M1$  transition strength is determined practically from the isovector- $jj$  term and the isovector- $ss$  term only. The particular distribution of the  $M1$  strength on the energy (i.e. the spectral distribution) depends, of course, also on the occupation and quantum numbers of the deformed orbits involved in the QRPA phonon excitations. As mentioned above the QRPA calculations started with the elimination of the spurious angular-momentum contributions. For this purpose the isoscalar- $jj$  interaction term is taken with a sufficiently large strength of  $\kappa_j^{t=0} \geq 10^2 \text{ MeV}/\hbar^2$  which is strong enough to achieve  $\langle ph | \mathbf{J} | 0 \rangle = 0$  [Doen05] for all resulting QRPA phonon states.

For the spin-spin interaction there is no unique choice for the isoscalar and isovector strength parameters to be directly applied. The compilation given in Ref. [Faes90] offers a whole set of values used in the literature. The parameter  $\kappa_s^{t=0} = 0$  was chosen since the  $M1$  strength is not sensitive against the isoscalar- $ss$  interaction. The constant  $\kappa_s^{t=1} = -1 \text{ MeV}/\hbar^2$  taken for the repulsive isovector- $ss$  interaction is a favorable value to move the main part of the spin-magnetic strength to about 8 MeV which is the suggested energy region of the isovector-spin contribution [Zawi90, Sarr93].

Contrary to the  $ss$  interaction the isovector- $jj$  term in Eq. (6.1) can not be derived from an effective two-body interaction. Therefore, this term was exclusively used to analyze the  $M1$  strength with respect to the isovector-orbital contribution. A zero value of  $\langle ph | \mathbf{J}^{t=0} | 0 \rangle$  is obtained by using a large constant  $\kappa_j^{t=1} \geq 10^2 \text{ MeV}/\hbar^2$  for the isovector- $jj$  term, i.e., the contribution of this mode to the calculated  $M1$  strength is suppressed. The comparison of the result with the transition strength without such a suppression allows us to estimate the contribution of the isovector-orbital mode. As expected there is practically no such contribution to the low-lying  $M1$  strength for the nearly spherical cases  $^{92,94,96}\text{Mo}$ , whereas in the deformed isotopes  $^{98}\text{Mo}$  and  $^{100}\text{Mo}$  the isovector-orbital mode exhausts 53 % and 56 %, respectively, of the summed  $M1$  strength. Similarly, the contributions from the isovector-spin amplitudes  $\langle ph | \mathbf{S}^{t=0,1} | 0 \rangle$  to the  $M1$  strength were determined by choosing large values of  $\kappa_s^{t=1} \geq 10^2 \text{ MeV}/\hbar^2$  such that this contribution is suppressed.

### 6.1.2 Shell-model calculations

Shell-model calculations<sup>1</sup> were performed using a model space including the active proton orbits  $\pi(0f_{5/2}, 1p_{3/2}, 1p_{1/2}, 0g_{9/2})$  and neutron orbits  $\nu(0g_{9/2}, 1d_{5/2}, 0g_{7/2})$  relative to a hypothetical  $^{68}\text{Ni}$  core. Since an empirical set of effective interactions for this model space is not available up to now, various

<sup>1</sup>The shell-model calculations were performed by Dr. R. Schwengner.

Table 6.1: Deformation parameters of the ground states and summed  $M1$  strengths up to 4 MeV for the even-even Mo isotopes. The experimental values (Exp) are compared with predictions from the shell model (SM) and the quasiparticle-random-phase approximation (QRPA).

$A$	$\varepsilon_2$	$\gamma$	$\sum B(M1) \uparrow / \mu_N^2$		
			Exp	SM	QRPA
92	0.0	–	0.15(2)	–	0.06
94	0.02	–	0.67(7)	1.01	0.06
96	0.10	60°	0.47(2)	0.50	0.19
98	0.18	37°	0.74(6)	0.39	0.45
100	0.21	32°	0.83(9)	0.81	0.54

empirical interactions have been combined with results of schematic nuclear interactions applying the surface delta interaction. Details of this procedure are described in Refs. [Wint93, Wint94]. The single-particle energies relative to the  $^{68}\text{Ni}$  core have been derived from the single-particle energies of the proton orbits given in Ref. [Ji88] with respect to the  $^{78}\text{Ni}$  core and from the neutron single-hole energies of the  $0g_{9/2}, 0g_{7/2}$  orbits [Gros76]. The transformation of these single-particle energies to those relative to the  $^{68}\text{Ni}$  core has been performed [Blom85] on the basis of the effective residual interactions given in, e.g., Refs. [Wint93, Wint94]. The obtained values are  $\epsilon_{0f_{5/2}}^\pi = -9.806$  MeV,  $\epsilon_{1p_{3/2}}^\pi = -9.733$  MeV,  $\epsilon_{1p_{1/2}}^\pi = -7.427$  MeV,  $\epsilon_{0g_{9/2}}^\pi = -1.227$  MeV,  $\epsilon_{0g_{9/2}}^\nu = -6.582$  MeV,  $\epsilon_{1d_{5/2}}^\nu = -4.395$  MeV,  $\epsilon_{0g_{7/2}}^\nu = -0.623$  MeV.  $M1$  transition strengths were calculated with effective  $g$  factors of  $g_s^{\text{eff}} = 0.7g_s^{\text{free}}$ . To make the calculations feasible a truncation of the occupation numbers was applied. Two protons were allowed to be lifted from the  $1p_{1/2}$  orbit to the  $0g_{9/2}$  orbit. One  $0g_{9/2}$  neutron could be lifted over the shell gap either to the  $1d_{5/2}$  or to the  $0g_{7/2}$  orbit. For  $^{98}\text{Mo}$  and  $^{100}\text{Mo}$  a maximum of two neutrons could be excited from the  $1d_{5/2}$  to the  $0g_{7/2}$  orbit. With these restrictions configuration spaces with dimensions of up to 3000 were obtained for the  $1^+$  states. The calculations were carried out with the code RITSSCHIL [Zwar85].

### 6.1.3 Comparison of experimental and calculated $M1$ strengths

The cumulative  $M1$  strengths versus the excitation energy obtained from the shell-model and QRPA calculations are shown in Fig. 6.2 together with the experimental values. There is no one-to-one correspondence between the calculated and the experimental  $M1$ -strength distributions.

The shell-model calculations predict an increase of the number of  $1^+$  states with increasing neutron number above the  $N = 50$  shell closure. While there is no  $1^+$  state in the considered energy range up to 4 MeV in  $^{92}\text{Mo}$ , there are three  $1^+$  states in  $^{94}\text{Mo}$  and  $^{96}\text{Mo}$ , 10 in  $^{98}\text{Mo}$  and 12 in  $^{100}\text{Mo}$ . The summed  $M1$  strengths predicted by the shell-model calculations are shown in Fig. 6.2 and Table 6.1. The large summed strength in  $^{94}\text{Mo}$  is dominated by one state with the main configuration  $\pi(0g_{9/2}^2)\nu(1d_{5/2}^2)$ , which has a strength of  $B(M1, 0^+ \rightarrow 1^+) = 0.90\mu_N^2$ . This special four-particle configuration corresponds to a two-phonon state, which cannot be described in the QRPA calculations. The calculated summed  $M1$  strengths in  $^{96}\text{Mo}$  and  $^{100}\text{Mo}$  agree with the experimental values, while the value predicted for  $^{98}\text{Mo}$  is too small. The calculated summed strength in  $^{100}\text{Mo}$  is dominated by the value of  $B(M1, 0^+ \rightarrow 1^+) = 0.36\mu_N^2$  of a state with the four-particle configuration  $\pi(0g_{9/2}^2)\nu(0g_{7/2}^2)$  that is analogous to the case of  $^{94}\text{Mo}$ .

The QRPA calculations reproduce the fact that the  $M1$  strength is distributed over only few states in the spherical nuclei  $^{92,94}\text{Mo}$  while there are many states with smaller individual  $B(M1)$  values in the deformed nuclei  $^{98,100}\text{Mo}$  (cf. Fig. 6.1). This tendency of an increasing spread of the strength is a direct consequence of the increasing splitting of the orbit energies with increasing deformation. As shown in Fig. 6.2 and Table 6.1 the summed  $M1$  strengths obtained from the QRPA calculations underestimate the experimental ones. However, the increase of the summed  $M1$  strengths with in-

creasing neutron number is reproduced. The discrepancy between the calculated and experimental summed  $M1$  strength in  $^{94}\text{Mo}$  is caused by the fact that the dominant  $M1$  strength is generated by a special four-particle configuration (see above). Summarizing, the results of the QRPA calculations show that the deformation causes a spread of the  $M1$ -strength distribution and an increase of the summed  $M1$  strength. The spread is a direct consequence of the energetical spread of the quasiparticle states for a deformed system. As a result of the QRPA calculations we found the  $M1$  strengths in the nearly spherical nuclei to be generated by isovector-spin vibrations only while the  $M1$  strengths in the deformed nuclei are a combination of isovector-orbital vibrations and isovector-spin vibrations. The absence of a pure isovector-orbital character of the  $1^+$  excitations is possibly due to the fact that there are no proton and neutron deformation-aligned high- $j$  orbits in the Mo isotopes with  $A = 92 - 100$  which create the favored situation for the isovector angle rotation.

#### 6.1.4 $M1$ strength predicted at high energy

In addition to the energy range covered by the present experiments we have performed QRPA calculations up to an excitation energy of 10 MeV. The predicted  $M1$ -strength distributions are shown in Fig. 6.3. The summed  $M1$  strengths in this extended energy range reach values of  $\sum B(M1) \uparrow \approx 3 - 4 \mu_N^2$  which is the maximum expected from particle-hole excitations for the  $N = 3, 4$  shell. In the QRPA calculations it turns out that practically all the transition strength of the isovector-orbital type ( $\approx 0.5 \mu_N^2$  in the deformed nuclei) is concentrated below 4 MeV excitation energy while the bump of  $M1$  transitions predicted above 4 MeV with a large summed strength of about  $\sum B(M1) \approx 3 \mu_N^2$  is exclusively caused by isovector-spin vibrations. The contributions of isovector-orbital vibrations to the total  $M1$  strengths in the spherical  $^{92}\text{Mo}$  and the deformed  $^{100}\text{Mo}$  are depicted in Fig. 6.3. In addition, the  $M1$  strength predicted for the neutron-rich isotope  $^{110}\text{Mo}$  is plotted. The equilibrium deformation parameters obtained for this nuclide are  $\varepsilon_2 = 0.23$  and  $\gamma = 60^\circ$ . Shell-model calculations carried out for the spherical  $^{92}\text{Mo}$  up to about 8.5 MeV predict a  $1^+$  state with a large strength of  $B(M1) \uparrow = 4.8 \mu_N^2$  at 8.2 MeV which is dominated by the spin-flip configuration  $\nu(0g_{9/2}^{-1}0g_{7/2}^1)$ .

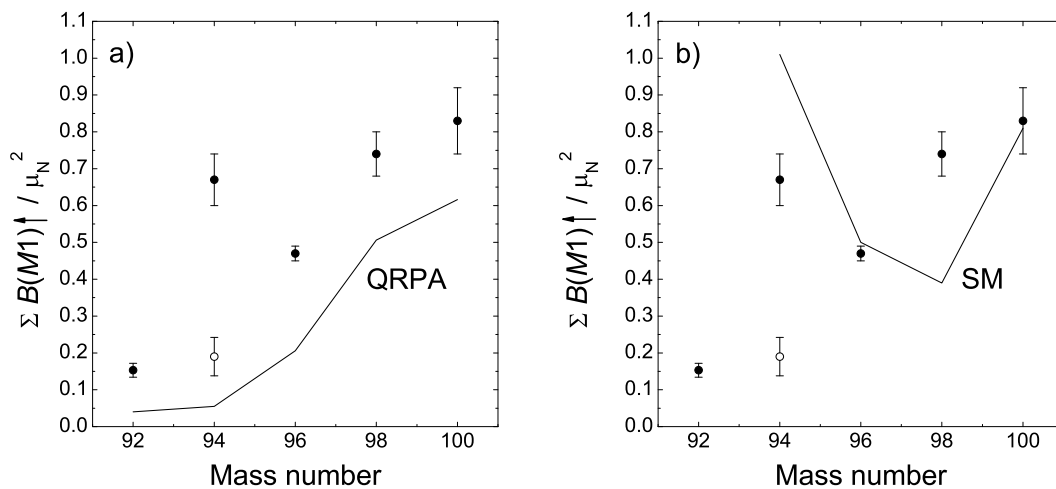


Figure 6.2: Comparison of the observed summed  $M1$  strengths up to 4 MeV (filled circles) with the predictions of QRPA calculations (a) and the shell-model calculations (b). The contribution of the mixed-symmetry state in  $^{94}\text{Mo}$ , which is not described in the present calculations, to the summed  $M1$  strength is  $0.48(3) \mu_N^2$ . The open circle represents the value without this contribution.

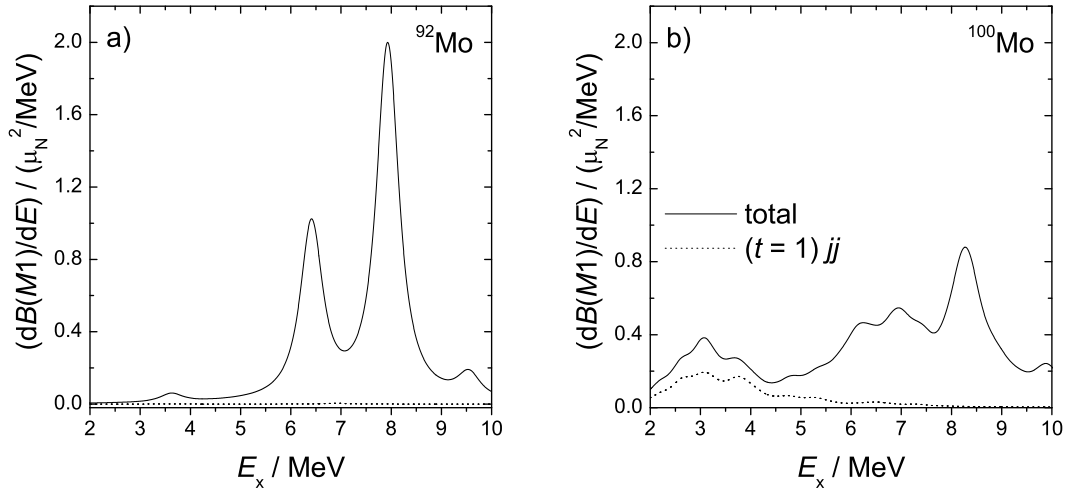


Figure 6.3: Contributions of different types of vibrations to the  $M1$ -strength distributions in  $^{92}\text{Mo}$  (a) and  $^{100}\text{Mo}$  (b). The solid lines represent the total strength while the dashed lines show the isovector-orbital contributions.

## 6.2 Shape coexistence in $^{98}\text{Mo}$ and $^{100}\text{Mo}$

The appearance of low-lying  $0^+$  states in even-even nuclei is interpreted as the manifestation of the coexistence of different shapes in nuclei [Wood92, Andr00]. The shape of the coexisting configurations can be studied by analyzing  $E2$  transition strength via, e.g. Coulomb excitations. More information on the shape coexistence can be obtained by measuring the electric monopole ( $E0$ ) transition strength between low-lying  $0^+$  states [Wood99]. The nuclides  $^{98}\text{Mo}$  and  $^{100}\text{Mo}$ , studied in photon-scattering experiments with bremsstrahlung up to  $E_e = 3.8$  MeV (see Section 5.1), show a specific feature - de-excitation of one state with spin  $J = 1$  to both the  $0^+$  ground state and to excited  $0^+$  state. Transitions from  $J = 1$  states to excited  $0^+$  states were previously observed in  $^{70,72}\text{Ge}$  [Jung95],  $^{92}\text{Zr}$  [Wern02],  $^{94}\text{Mo}$  [Fran03], and  $^{108}\text{Cd}$  [Gade03]. Such peculiar transitions from  $J = 1$  to excited  $0^+$  states have not been quantitatively discussed so far because common interpretation like two-phonon mixed-symmetry states in terms of Interacting Boson Approximation (IBA) or the interpretation in terms of the Random Phase Approximation (RPA) do not take shape coexistence into account. A model based on one-particle-one-hole (1p1h) excitations has been developed which allows to determine the mixing of the two intrinsic configurations of the  $0^+$  states from the experimental transition strengths. The present experiments do not allow parity assignments for the observed  $J = 1$  states found in  $^{98}\text{Mo}$  and  $^{100}\text{Mo}$ . Based on systematics of the neighboring nuclei  $^{92}\text{Zr}$  [Wern02, Fran04] and  $^{94}\text{Mo}$  [Fran03] positive parity is assumed. However, the model developed in the following applies for  $1^-$  states in an analogous way.

The total energy as a function of the quadrupole deformation parameter  $\varepsilon_2$  and of the triaxiality parameter  $\gamma$  was calculated by means of the shell-correction method (for details see Ref. [Frau00]) without BCS pairing field in order to search for coexisting shapes in  $^{98,100}\text{Mo}$  and to identify their single-particle configurations. The pairing interaction will be taken into account explicitly in our derivation for the mixing coefficients (see discussion below). The resulting energy surface for  $^{98}\text{Mo}$  is shown in Fig. 6.4. The lowest minimum (a) corresponds to  $\varepsilon_2 = 0.19$  and  $\gamma = 16^\circ$  and the second minimum (b) to  $\varepsilon_2 = 0.22$  and  $\gamma = 0^\circ$ . A similar energy surface is obtained for  $^{100}\text{Mo}$ . The reason for the shape coexistence can be understood from the plot of the proton single-particle energies along a deformation path between the two minima as shown in Fig. 6.4. The shape change is caused by the reoccupation of the last pair of protons from an ( $fp$ ) orbital to a  $g_{9/2}$  orbital, which drives into the second minimum at a larger  $\varepsilon_2$  and a smaller  $\gamma$ . These findings are consistent with the results of a recent Coulomb-excitation study [Ziel02].

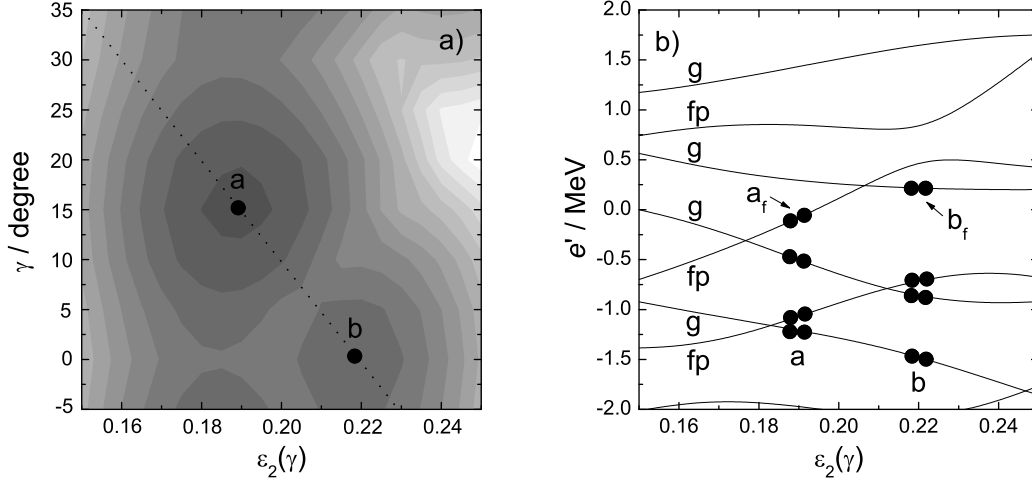


Figure 6.4: Total energy  $E(\epsilon, \gamma)$  for  $^{98}\text{Mo}$  a) as a function of the deformation parameters  $\epsilon_2$  and  $\gamma$ . The triaxial and prolate equilibrium shapes are marked by  $a$  and  $b$ , respectively. Deformed single-particle energies b) of the proton orbitals along the dashed path in the  $E(\epsilon, \gamma)$  surface. The circles illustrate the occupation of the relevant configurations  $a$  and  $b$ , respectively. The possible pair transfer between the crossing orbitals  $a_f$  and  $b_f$ , respectively, is responsible for the configuration mixing.

The pairing interaction scatters the last proton pair between the crossing orbitals  $a_f$  and  $b_f$  (cf. bottom part of Fig. 6.4) which leads to a mixing of the two configurations signaled by the decay to the second  $0^+$  state. In order to study this mixing in connection with the  $M1$  excitations the mixed states  $0_{1,2}^+$  are written in terms of the pure configurations  $a$  and  $b$  according to the frequently used two-level model [Wood92, Wood99]:

$$\begin{aligned} |0_1^+\rangle &= \cos \alpha |a\rangle + \sin \alpha |b\rangle \\ |0_2^+\rangle &= -\sin \alpha |a\rangle + \cos \alpha |b\rangle \end{aligned} \quad (6.3)$$

The slight modification of the individual orbitals with the deformation change  $a \rightarrow b$  can be neglected. Their occupation plays the decisive role. Furthermore, it is known from RPA studies [Hama84, Zaw91, Noja90] that the low-lying magnetic-dipole excitations are not very collective. In fact, the lowest RPA states contain usually more than 75% of one of the lowest 1p1h proton excitations. Based on this experience it is assumed that the  $1^+$  states can be approximated by a simple 1p1h excitation from the ground state.

The majority of the  $1^+$  states is generated by 1p1h excitations involving any empty proton or neutron orbitals,  $p$  and any filled ones,  $h$ , *except* one of the crossing levels  $a_f$  or  $b_f$ . The  $M1$  transition strength is then given by

$$\langle 1^+ | \mathcal{M}(M1) | 0_{1,2}^+ \rangle \approx \langle p | \mathcal{M}(M1) | h \rangle \langle 0_1^+ | 0_{1,2}^+ \rangle \quad (6.4)$$

which means that it is essentially determined by the single-particle transition  $h \rightarrow p$  which is not very much influenced by the 2p2h configuration change  $a \leftrightarrow b$ . Apparently, the transition  $1^+ \rightarrow 0_2^+$  becomes suppressed in this “spectator” case due to the orthogonality  $\langle 0_1^+ | 0_2^+ \rangle = 0$ . A branching to the excited state  $0_2^+$  is possible for the minor group of  $1^+$  states which involve one of the crossing proton orbitals in the 1p1h excitation. For example, an excitation that lifts a proton from  $a_f$  to some empty level  $p$  is only possible for the component in the ground state with the configuration  $a$ . Likewise, an excitation that lifts a proton from  $b_f$  to  $p$  is only possible for the component with the configuration  $b$ . These two  $1^+$  states remain pure. Pair scattering cannot mix them, because the Pauli principle does not allow a pair on  $a_f$  or  $b_f$  (blocking effect). The transition matrix element for the  $1^+$  state of  $a$ -type,



which is the lower one, is

$$\langle 1^+ | \mathcal{M}(M1) | 0_{1,2}^+ \rangle \approx \langle p | \mathcal{M}(M1) | a_f \rangle \langle a | 0_{1,2}^+ \rangle \quad (6.5)$$

An analogous argument holds for lifting a proton from a level  $h$  to  $a_f$  or  $b_f$ . Using Eqs. (6.3) and (6.5) the desired relation between the mixing coefficients and the  $B(M1)$  values becomes

$$\frac{B(M1, 1^+ \rightarrow 0_2^+)}{B(M1, 1^+ \rightarrow 0_1^+)} = \left[ \frac{\sin \alpha}{\cos \alpha} \right]^2 \quad (6.6)$$

Note that the unknown matrix elements  $\langle p | \mathcal{M}(M1) | a_f \rangle$  cancel in the ratio. Hence, the branching ratio is a direct measure of the relative contributions  $\sin^2 \alpha$  and  $\cos^2 \alpha$  to the configurations  $a$  and  $b$  in each of the two  $0^+$  states. In addition, the known relation

$$V_{ab} = [E(0_2^+) - E(0_1^+)] \sin \alpha \cos \alpha \quad (6.7)$$

enables us to estimate the interaction matrix element  $V_{ab}$  for the two-level mixing (Eq. (6.3)) from the experimental energy difference and the mixing coefficients determined above.

The experimental intensities of the 2816.9 and 3551.2 keV transitions in  $^{98}\text{Mo}$  result in 0.28(5) for the ratio in Eq. (6.6) which yields the mixing coefficients  $\sin^2 \alpha = 0.22(3)$  and  $\cos^2 \alpha = 0.78(3)$ . In the case of  $^{100}\text{Mo}$  the intensities of the 2595.2 and 3290.1 keV transitions lead to  $B(M1, 1_1^+ \rightarrow 0_2^+)/B(M1, 1_1^+ \rightarrow 0_1^+) = 0.45(13)$ . The obtained mixing coefficients are  $\sin^2 \alpha = 0.31(6)$  and  $\cos^2 \alpha = 0.69(6)$ . The interaction matrix elements obtained from Eq. (6.7) for  $^{98}\text{Mo}$  and  $^{100}\text{Mo}$  are 326 keV and 321 keV, respectively. Its constancy is expected since it is related to the same proton configuration in the two nuclides.

The  $E0$  transition strength between the  $0^+$  states is given by the quantity  $\rho^2 = [\sin \alpha \cos \alpha \Delta R_C^2]^2$  (cf. e.g. Ref. [Wood99]). The difference  $\Delta R_C^2$  between the squares of the charge radii (in units of  $(1.2 \text{ fm } A^{1/3})^2$ ) of the unmixed states  $a$  and  $b$  is determined by the difference between the radii of the  $pf$  and  $g$  orbitals and the difference between the deformations of  $a$  and  $b$ . The values  $\rho^2(^{98}\text{Mo}) = 0.033$  and  $\rho^2(^{100}\text{Mo}) = 0.075$  were obtained using the same estimates that lead in the case  $\sin^2 \alpha = 0.5$  to Eqs. (14) and (47) in Ref. [Wood99] and the mixing coefficients, which are to be compared with the experimental values of 0.027(2) and 0.042(6), respectively. The larger value for  $^{100}\text{Mo}$  reflects to some extent the larger mixing coefficient, but is mainly due to the larger deformation of the second minimum ( $\varepsilon_2 = 0.26, \gamma = 46^\circ$ ). The  $E0$  transition strength depends on both the mixing coefficients and  $(\Delta R_C^2)^2$ , which is sensitive to the deformation and the radial profile of the single-particle wave functions. Our method, which is based on the Pauli principle, gives the mixing coefficients directly. It only presumes that the two unmixed  $0^+$  states are related to the transfer of one nucleon pair between two Nilsson orbitals. It does not matter whether the two unmixed states have a different shape or not. For the considered cases of  $^{98,100}\text{Mo}$ , the calculations and the measurements [Ziel02] indicate a difference between the shapes. The present method cannot be used if the two unmixed states are related to the transfer of two or more pairs. However, this case should be a small effect of higher order.

### 6.3 Dipole-strength distributions in $^{92}\text{Mo}$ , $^{98}\text{Mo}$ and $^{100}\text{Mo}$

The method of analysis of the photon-scattering experiments, presented in Subsection 5.2.2, allowed us determination of the photoabsorption cross section below the neutron separation energy. The dipole-strength distributions in  $^{92}\text{Mo}$ ,  $^{98}\text{Mo}$  and  $^{100}\text{Mo}$  were obtained combining the results from the  $(\gamma, \gamma')$  and  $(\gamma, n)$  [Beil74] experiments (cf. Fig. 5.22). In order to examine the behavior of the dipole-strength distributions we apply QRPA calculations in a deformed basis. Analogous QRPA calculations and the used deformation parameters were given in the study of the magnetic-dipole strength up to 4 MeV in the even-mass Mo isotopes with  $A = 92 - 100$  (cf. Table 6.1). The QRPA calculations for the

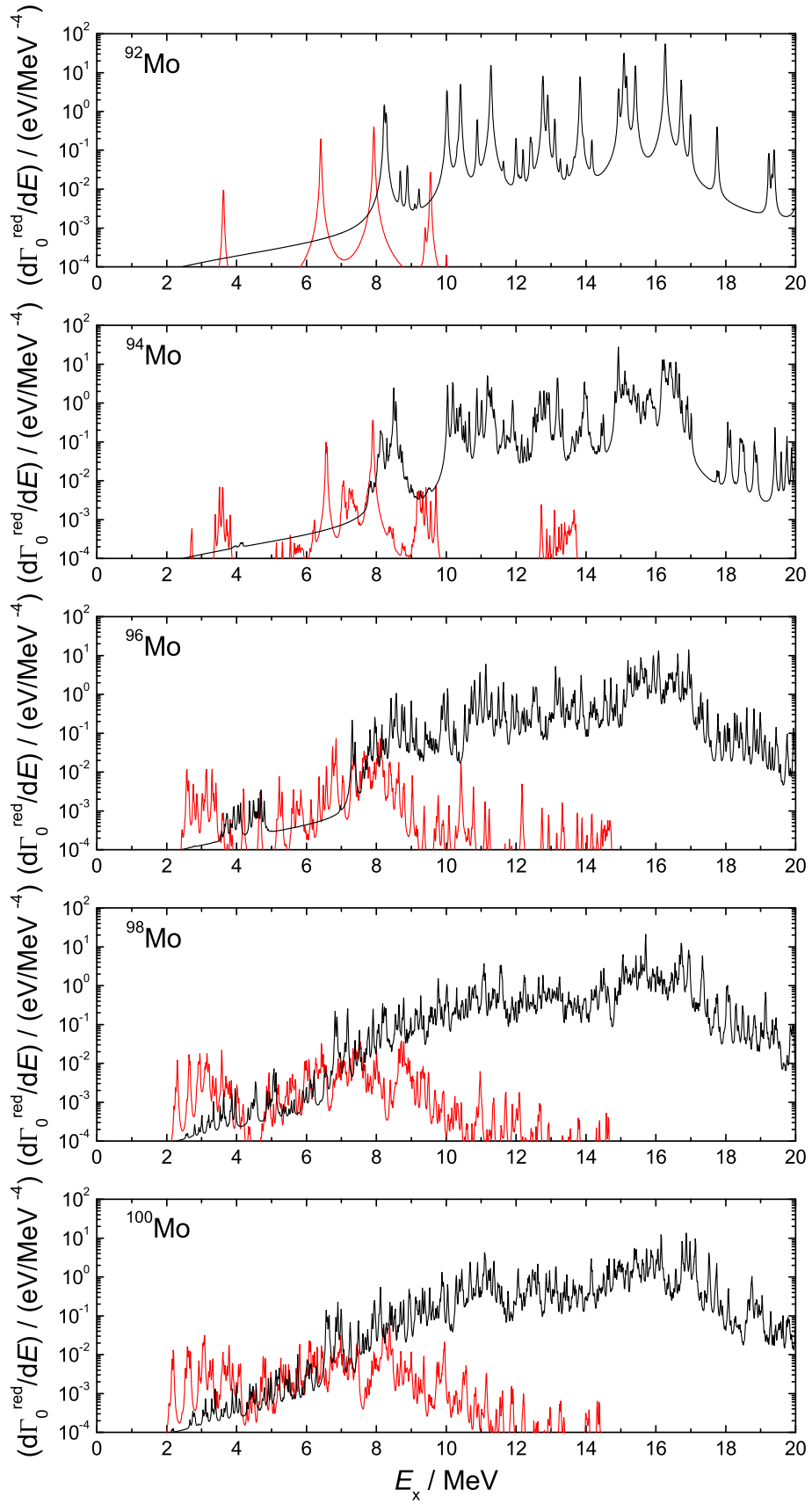


Figure 6.5: Calculated excitation strength of dipole states in the stable even-mass Mo isotopes. The distributions of the  $M1$  and  $E1$  transitions are depicted with red and black, respectively. The distributions are smeared with Lorentzian function with a width of 20 keV.

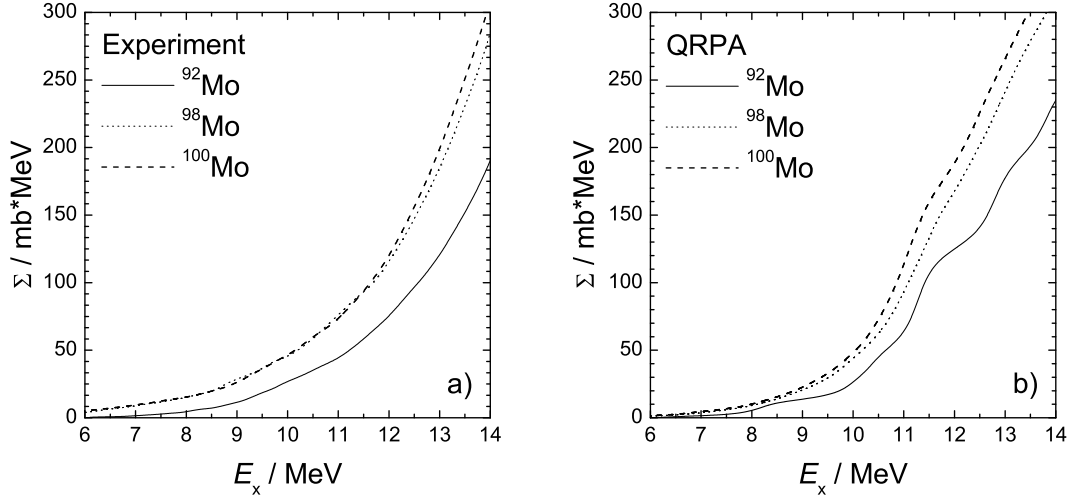


Figure 6.6: a) Cumulative plot of the integrated photoabsorption cross section for  $^{92}\text{Mo}$ ,  $^{98}\text{Mo}$  and  $^{100}\text{Mo}$  obtained from the photon-scattering experiments and the  $(\gamma, n)$  measurements [Beil74]. b) the same plot compared with predictions from the QRPA. The calculated strength is smeared with Lorentzian function with a width of 0.5 MeV.

$1^-$  excitations shall be described in more detail. The following Hamiltonian was used in the QRPA calculations:

$$H_{E1}^{\text{QRPA}} = h_{\text{MF}} - \frac{1}{2} \sum_{\mu=-1,+1}^{t=0,1} \kappa_{1\mu}^t Q_{1\mu}^t Q_{1-\mu}^t - \frac{1}{2} \sum_{\mu=-3,+3}^{t=0,1} \kappa_{3\mu}^t Q_{3\mu}^t Q_{3-\mu}^t. \quad (6.8)$$

The term  $h_{\text{MF}}$  in Eq. (6.8) includes the Nilsson mean field plus monopole pairing using the equilibrium deformation derived before (cf. Section 6.1). The following terms denote the isoscalar ( $t = 0$ ) and isovector ( $t = 1$ ) part of the dipole-dipole interaction ( $\lambda = 1$ ) and octupole-octupole interaction ( $\lambda = 3$ ) defining the multipole operators by  $Q_{\lambda\mu}^t = [r^\lambda Y_{\lambda\mu}]^\pi + (-)^t [r^\lambda Y_{\lambda\mu}]^\nu$ . The  $E1$  transition operator is given by:

$$\widehat{\mathbf{E1}} = e[rY_{1\mu}]^\pi. \quad (6.9)$$

The excitation energies and the  $E1$  transition strengths of  $J^\pi = 1^-$  states were calculated using the QRPA with doubly stretched coordinates [Saka89]. It is important to take the deformation degree of freedom in the QRPA calculations into account because the nuclear shape changes from the spherical isotope  $^{92}\text{Mo}_{50}$  to a triaxial shape in the isotopes  $^{98}\text{Mo}_{56}$  and  $^{100}\text{Mo}_{58}$  [Moel86]. The QRPA code is based on a Nilsson-like deformed basis which enables us to apply the nuclear selfconsistency approach [Saka89] and separable dipole-plus-octupole interactions. The isoscalar constants  $\kappa_{\lambda\mu}^{t=1}$  were chosen to be large enough to eliminate the spurious center of mass motion according to the suppression method [Doen05]. A comparison of calculated spectra for  $M1$  and  $E1$  excitations for all stable even-mass Mo isotopes is presented in Fig. 6.5. For calculating the  $E1$  strength the only strength parameter which is not determined by the selfconsistency condition is the relative strength of the isovector interaction term. This parameter has been adapted to the position of the maximum of the GDR. In order to examine the behavior of the dipole-strength distributions we calculated the cumulative integrated cross section  $\Sigma = \sum_0^{E_x} \sigma_\gamma(E) \Delta E$  with the QRPA. In Fig. 6.6 the cumulative integrated cross sections are displayed for the three studied isotopes and compared with the experimental data. One sees that  $\Sigma$  increases from  $^{92}\text{Mo}$  to  $^{98,100}\text{Mo}$  by about a factor of two at 8 MeV, close to the neutron thresholds of  $^{98,100}\text{Mo}$ .

The QRPA calculations reproduce in particular the relative increase of the  $\Sigma$  with increasing  $N/Z$ . An increase of the dipole strength with the neutron number  $N$  is usually attributed to the so called Pygmy Dipole Resonance (PDR)(cf. [Zilg02, Hart04]), a concentration of electric-dipole ( $E1$ ) strength

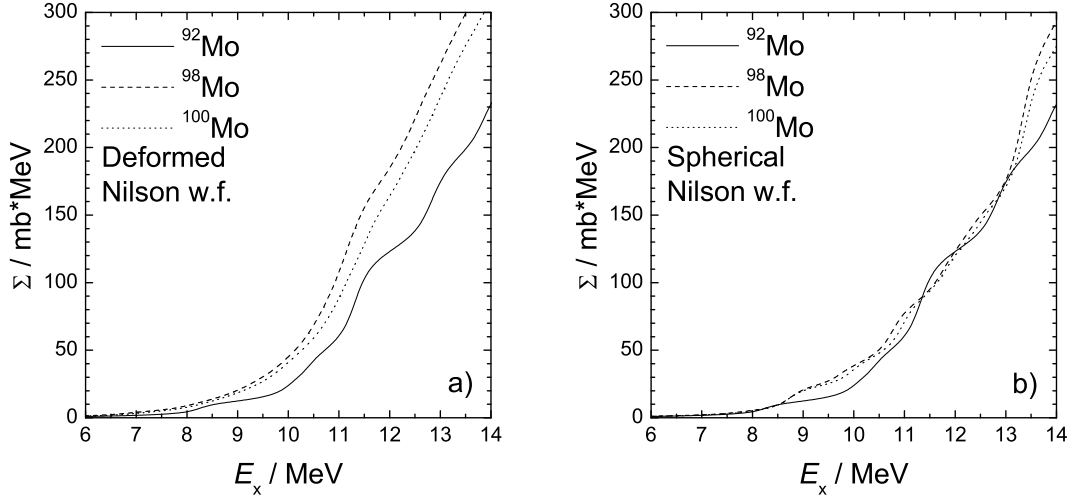


Figure 6.7: Comparison of the calculated cumulative integrated cross sections for  $^{92}\text{Mo}$ ,  $^{98}\text{Mo}$  and  $^{100}\text{Mo}$  for the case of a) deformed Nilson wave functions and b) spherical Nilson wave functions. The calculated strength is smeared with Lorentzian function with a width of 0.5 MeV.

in the energy range between 6 and 10 MeV, which is considered as an out-of-phase oscillation of a neutron skin against an inert core. The properties of the PDR are therefore expected to depend strongly on the ratio of neutron number to proton number  $N/Z$ . The distributions in Fig. 6.6 have a smooth energy dependence and do not indicate a strong PDR structure. The enlargement of  $\Sigma$  with increasing  $N/Z$  seems to be related to the influence of the increasing deformation. This has been proven by performing QRPA calculations with a spherical shape for  $^{98}\text{Mo}$  and  $^{100}\text{Mo}$ , shown in Fig. 6.7, that predict  $\Sigma$  resembling the one of the spherical  $^{92}\text{Mo}$  and, thus, being smaller than the one obtained with a deformed shape for  $^{98}\text{Mo}$  and  $^{100}\text{Mo}$ , respectively. In fact, the effect of the deformation as the reason of an enlargement of the photoabsorption cross section is plausible. It is well known that the width of GDR gets considerably broadened by deformation [Bohr75] which leads to a lift of strength in the tail because the total value of the photoabsorption cross section is limited by the energy-weighted sum rule.

## Chapter 7

# Summary and conclusions

The dipole-strength distributions in the nuclides  $^{92}\text{Mo}$ ,  $^{98}\text{Mo}$  and  $^{100}\text{Mo}$  were investigated in photon-scattering experiments with bremsstrahlung. The method of the nuclear resonance fluorescence was applied to determine the excitation energies, spins and widths of levels up to the neutron threshold. The photon-scattering experiments were carried out at the Dynamitron accelerator of the Universität Stuttgart and at the ELBE accelerator of the Forschungszentrum Rossendorf. The photons scattered from the target were measured with high purity germanium detectors with efficiencies of 100 % relative to a  $3'' \times 3''$  NaI scintillation detector.

Various electron-beam energies from 3.2 to 3.8 MeV were used in the low-energy experiments on  $^{98}\text{Mo}$  and  $^{100}\text{Mo}$  at the Dynamitron accelerator in order to resolve branching transitions. Five  $J = 1$  states up to  $E_x = 4$  MeV in  $^{98}\text{Mo}$  and 14 in  $^{100}\text{Mo}$  were observed for the first time. Five levels were observed in  $^{92}\text{Mo}$  in the experiment at the ELBE accelerator at  $E_e = 6$  MeV, one of them at  $E_x = 4498.4$  keV for the first time in photon-scattering experiment. The transition strengths deduced from the present low-energy experiments for  $^{92}\text{Mo}$ ,  $^{98}\text{Mo}$ , and  $^{100}\text{Mo}$  together with known values for  $^{94}\text{Mo}$  and  $^{96}\text{Mo}$  allowed us to study the systematics of the low-lying magnetic dipole excitations in the chain of stable even-even Mo isotopes.

The experimental results for the  $M1$  strength were compared with predictions of QRPA approximation in a deformed basis, and with predictions of the shell model. The QRPA calculations reproduce the growing and the spread of the  $M1$  strength with increasing neutron number. The substantial  $M1$  strength observed in the deformed isotopes  $^{98}\text{Mo}$  and  $^{100}\text{Mo}$  can be explained in the QRPA calculations by a combination of the isovector-spin and isovector-orbital vibrations. The shell-model calculations especially reproduce the large  $M1$  strength in  $^{94}\text{Mo}$  as caused by a special four-particle configuration that is outside the scope of the QRPA.

States with  $J = 1$  which decay to both the  $0^+$  ground state and the first excited  $0^+$  state were observed in  $^{98}\text{Mo}$  and  $^{100}\text{Mo}$ . The existence of decay branches from  $J = 1$  to the two  $0^+$  states indicates that the two coexisting configurations are mixed in the  $0^+$  states. Performed mean-field calculations suggest that the unmixed configurations are related to the transfer of a proton pair between two Nilsson states, which causes a moderate deformation change. Assuming that the decaying  $J=1$  state has a dominant  $1p1h$  component, it is shown that the ratio of the squared mixing coefficients is directly proportional to the measured branching ratio. The derived coefficients indicate strong mixing and are consistent with the measured strengths of  $E0$  decay. The observation of decay branches to excited  $0^+$  states combined with the present model provides a new means to investigate the structure of isomeric  $0^+$  states.

As part of this work, numerous GEANT simulations were performed in order to optimize the design of the components of the bremsstrahlung facility at the ELBE accelerator and to reduce background radiation. The lead collimators and the lead shields of the detectors were designed by performing GEANT simulations. The photon-beam dump and the material of the photon-beam pipe were optimized to provide less photons scattered to the detectors. A detection sensitivity of  $B(E1) \uparrow \approx 0.15 \times 10^{-3} e^2\text{fm}^2$  was achieved in the presented photon-scattering experiments. A discussion on the origin of the back-

ground in the measured spectrum is presented. Monte Carlo simulations are applied in the analysis of the data for determination of the detector efficiency, the bremsstrahlung spectrum modified by an aluminum hardener and the determination of its end-point energy from spectra of protons emitted during the photodisintegration of the deuteron or the spectra of scattered  $\gamma$ -rays from the target and detected with an NaI detector.

Dipole-strength distributions up to the neutron-separation energies in the nuclides  $^{92}\text{Mo}$ ,  $^{98}\text{Mo}$  and  $^{100}\text{Mo}$  have been investigated at the ELBE accelerator. The photon-scattering experiments were carried out at identical conditions and at an electron energy of 13.2 MeV such that the energy region around the neutron-separation energies in the three nuclides could be studied. Because of the possible observation of transitions in the neighboring nuclei produced via  $(\gamma, n)$  reaction, additional measurements at electron energies of 8.4 and 7.8 MeV, below the neutron-separation energy, were performed on  $^{98}\text{Mo}$  and  $^{100}\text{Mo}$ , respectively. The number of transitions assigned to  $^{92}\text{Mo}$ ,  $^{98}\text{Mo}$  and  $^{100}\text{Mo}$  is 340, 485 and 499, respectively, the main part of them being dipole transitions. Statistical properties of the observed transitions are obtained. The distributions of the nearest-neighbor spacings and the transition widths do closely resemble Wigner and Porter-Thomas distributions, respectively, indicating a quantum chaotic behavior as predicted for a Gaussian orthogonal ensemble.

Because of the Porter-Thomas fluctuations of the level widths the most of the levels do not appear as prominent peaks in the experimental spectra. Due to the high level density above 5 MeV and the finite resolution of the detectors these weakly populated levels produce a continuum of overlapping peaks. It is shown from a comparison of the spectra of  $^{98}\text{Mo}$  and  $^{100}\text{Mo}$  that close to the neutron-separation energy of  $^{98}\text{Mo}$  the strength in the continuum is two times higher than the strength in the peaks. GEANT simulations were applied to determine the non-resonant background in the measured spectra, i.e. the counts in the spectrum which do not result from deexcitation of nuclear levels, and thus to extract the continuum. The continuum contains the ground-state transitions as well as the branching transitions to the low-lying levels and the subsequent deexcitations of these levels. In this work, a Monte Carlo code for  $\gamma$ -ray cascade simulations was developed which allows us (i) to deconvolute the intensity distribution of the ground-state transitions from the continuum and thus to determine the cross section for elastic scattering and (ii) to calculate the branching ratios for deexcitations to the ground state and to obtain the photoabsorption cross section. Since the obtained photoabsorption cross sections for  $^{92}\text{Mo}$ ,  $^{98}\text{Mo}$  and  $^{100}\text{Mo}$  match with the measured cross sections for the  $(\gamma, n)$  reaction the method allows us to determine the tail of the Giant Dipole Resonance below the neutron-separation energy. The obtained dipole-strength distributions for  $^{92}\text{Mo}$ ,  $^{98}\text{Mo}$  and  $^{100}\text{Mo}$  show that the strength increases with the neutron number. The experimental results are discussed in the frame of QRPA calculations in a deformed basis which describe the increasing strength as a result of the increasing deformation.

# Appendix A

## NRF calibration standards

Properties of the levels in  $^{11}\text{B}$ ,  $^{13}\text{C}$  and  $^{27}\text{Al}$  used as calibration standards. The information about the level energy  $E_x$ , the angular momentum  $J_x^\pi$ , the level width  $\Gamma$  and the branching ratio for decay to the ground state  $B_0$  are taken from [Ajze90], [More93] and [Piet95].

$E_x$ keV	$J_x^\pi$	$\Gamma$ eV	$B_0$ %	$I_S$ eVb
$^{11}\text{B } J_0 = 3/2^-$				
2124.69(3)	1/2 <sup>-</sup>	0.120(9)	100	51(4)
4444.9(5)	5/2 <sup>-</sup>	0.56(2)	100	164(6)
5020.3(3)	3/2 <sup>-</sup>	1.68(6)	85.6(6)	219(8)
7285.5(4)	5/2 <sup>+</sup>	1.00(7)	87(2)	95(7)
8920(2)	5/2 <sup>-</sup>	4.2(2)	95(1)	286(14)
$^{13}\text{C } J_0 = 1/2^-$				
3089.44(2)	1/2 <sup>+</sup>	0.54(4)	100	216(17)
3684.507(19)	3/2 <sup>-</sup>	0.40(3)	99(4)	224(86)
$^{27}\text{Al } J_0 = 5/2^+$				
2212.01(10)	7/2 <sup>+</sup>	0.0172(3)	100	18.0(3)
2734.9(7)	5/2 <sup>+</sup>	0.051(7)	22.1(10)	1.3(2)
2982.00(5)	3/2 <sup>+</sup>	0.117(3)	97.4(5)	31.9(8)
3004.2(8)	9/2 <sup>+</sup>	0.0077(5)	88.6(11)	4.3(3)
3956.8(4)	3/2 <sup>+</sup>	0.177(11)	84.4(17)	21.1(17)

Properties of the calibrations transitions. The mixing ratio  $\delta$  is given in Krane-Steffen phase convention.

$E_\gamma(90^\circ)$ keV	$W(90^\circ)$	$E_\gamma(127^\circ)$ keV	$W(127^\circ)$	$\delta$	$\Pi L$
$^{11}\text{B}$					
2124.47(3)	1.000	2124.21(3)	1.000		$M1$
4443.9(5)	1.000	4442.8(5)	1.000	+0.19(3)	$M1 + E2$
5019.1(3)	0.938	5017.6(3)	1.005	-0.03(5)	$M1$
7282.9(4)	0.931	7279.8(4)	1.006		$E1$
8916(2)	0.987	8912(2)	1.001	+0.11(4)	$M1 + E2$
$^{13}\text{C}$					
3089.05(2)	1.000	3088.58(2)	1.000		$E1$
3683.951(19)	0.944	3083.281(19)	1.004	+0.094(9)	$M1 + E2$
$^{27}\text{Al}$					
2211.91(10)	0.895	2211.80(10)	1.004	+0.468(9)	$M1 + E2$
2734.8(7)	0.828	2734.6(7)	1.014	+0.19(3)	$M1 + E2$
2981.82(5)	0.996	2981.61(5)	1.000	-0.01(1)	$M1 + E2$
3004.0(8)	0.934	3003.8(8)	0.980	$\approx 0.0$	$E2 + M3$
3956.5(4)	1.000	3956.1(4)	1.000		



## Appendix B

# Low-lying excitations in $^{92}\text{Mo}$ , $^{98}\text{Mo}$ and $^{100}\text{Mo}$

Assigned low-lying excitations to  $^{92}\text{Mo}$ ,  $^{98}\text{Mo}$  and  $^{100}\text{Mo}$  from the photon-scattering experiments described in Section 5.1.

Table B.1: Excitations assigned to  $^{92}\text{Mo}$

$E_x$ keV	$J_x$	$J_f$	$B_f$ %	$\frac{I_\gamma(90^\circ)}{I_\gamma(127^\circ)}$	$I_s$ eVb	$\Gamma$ meV	$B(E1) \uparrow$ $10^{-3}e^2\text{fm}^2$	$B(M1) \uparrow$ $10^{-3}\mu_N^2$	$B(E2) \uparrow$ $e^2\text{fm}^4$
1509.8(1)	$2^+$	$0^+$							
3091.4(2)	$2^{+a}$	$0^+$	82(2) <sup>b</sup>	1.9(5)	27(3)	20(3)			362(44)
3925.8(2)	$2^{+a}$	$0^+$	65(5) <sup>b</sup>	1.9(7)	22(4)	42(8)			183(33)
3944.0(2)	1	$0^+$	100 <sup>b</sup>	1.0(2)	27(3)	36(5)	1.7(2)	153(19)	
4494.8(6)	$2^{+a}$	$0^+$	100 <sup>b</sup>		8.7(15)	8.2(14)			29(55)
4633.7(1)	$1^{(-)a}$	$0^+$	59(19) <sup>b</sup>	0.72(7)	43(3)	231(106)	3.93(13)	356(117)	

<sup>a</sup> Parity taken from Ref. [Bagl00].

<sup>b</sup> Branching ratio taken from Ref. [Metz77].

Table B.2: Excitations assigned to  $^{98}\text{Mo}$

$E_x$ keV	$E_\gamma$ keV	$J_x$	$J_f$	$B_f$ %	$\frac{I_\gamma(90^\circ)}{I_\gamma(127^\circ)}$	$I_s$ eVb	$\Gamma$ meV	$B(E1) \uparrow$ $10^{-3}e^2\text{fm}^2$	$B(M1) \uparrow$ $10^{-3}\mu_N^2$
3257.8(1)	3257.8(1)	1	$0^+$	100	0.71(8)	4.5(4)	4.1(3)	0.34(3)	31(3)
3405.0(1)	3405.0(1)	1	$0^+$	100	0.68(3)	44(3)	44(3)	3.2(2)	289(19)
3457.1(1)	3457.0(1)	1	$0^+$	100	0.70(3)	34(2)	35(2)	2.45(16)	222(15)
3551.2(1)	3551.2(1)	1	$0^+$	87.7(14)	0.78(8)	28(2)	35(2)	0.65(6) <sup>c</sup>	58(6) <sup>c</sup>
	2816.9(2)	1	$0_2^+$	12.3(14)	0.71(19)			0.18(4) <sup>c</sup>	17(3) <sup>c</sup>
3703.9(2)	3703.9(2)	1	$0^+$	100	0.72(18)	3.5(5)	4.2(6)	0.23(3)	21(3)

<sup>c</sup> Reduced transition strength  $B(E1) \downarrow$  or  $B(M1) \downarrow$ .

Table B.3: Excitations assigned to  $^{100}\text{Mo}$ 

$E_x$	$E_\gamma$	$J_x$	$J_f$	$B_f$	$\frac{I_\gamma(90^\circ)}{I_\gamma(127^\circ)}$	$I_s$	$\Gamma$	$B(E1) \uparrow$	$B(M1) \uparrow$
keV	keV			%		eVb	meV	$10^{-3}e^2\text{fm}^2$	$10^{-3}\mu_N^2$
2633.3(1)	2633.2(1)	1	$0^+$	100	0.6(3)	1.5(3)	0.90(18)	0.14(3)	13(3)
2901.2(1)	2901.2(1)	1	$0^+$	100	0.73(20)	2.0(2)	1.43(17)	0.17(2)	15.2(18)
2906.4(1)	2906.3(1)	1	$0^+$	100	0.95(19)	1.70(18)	1.25(13)	0.15(2)	13.2(14)
3065.9(1)	3065.9(1)	1	$0^+$	100	0.62(9)	2.8(3)	2.2(2)	0.22(2)	20.2(19)
3199.0(2)	3199.0(2)	1	$0^+$	100	0.66(17)	2.2(3)	2.0(3)	0.17(2)	15.7(20)
3242.5(1)	3242.5(1)	1	$0^+$	100	0.70(10)	3.6(4)	3.3(4)	0.28(3)	25(3)
3290.1(1)	3290.1(1)	$1^{(+)\text{d}}$	$0^+$	70(4)	0.72(7)	7.6(6)	10.7(15)	0.20(4) <sup>c</sup>	18(4) <sup>c</sup>
	2754.7(2)	$1^{(+)\text{d}}$	$2_1^+$	15(3)	0.79(19)			0.07(3) <sup>c</sup>	7(2) <sup>c</sup>
	2595.2(1)	$1^{(+)\text{d}}$	$0_2^+$	15(4)	0.74(20)			0.09(3) <sup>c</sup>	8(3) <sup>c</sup>
3342.1(1)	3342.0(1)	1	$0^+$	100	0.69(13)	2.7(3)	2.6(3)	0.20(2)	18(2)
3483.4(1)	3483.4(1)	$1^{(+)\text{d}}$	$0^+$	80.9(16)	0.68(7)	43(3)	55(5)	1.02(12) <sup>c</sup>	91(10) <sup>c</sup>
	2948.2(1)	$1^{(+)\text{d}}$	$2_1^+$	10(1)	0.72(13)			0.21(4) <sup>c</sup>	18(3) <sup>c</sup>
	2419.8(1)	$1^{(+)\text{d}}$	$2_2^+$	9(1)	0.62(12)			0.34(7) <sup>c</sup>	31(6) <sup>c</sup>
3570.3(1)	3570.3(1)	1	$0^+$	100	0.75(10)	21.9(18)	24.2(19)	1.52(12)	138(11)
3599.9(2)	3599.8(2)	1	$0^+$	100	1.0(4)	2.3(4)	2.5(4)	0.16(2)	14(2)
3614.8(1)	3614.7(1)	1	$0^+$	100	0.64(15)	7.3(7)	8.2(8)	0.50(5)	45(5)
3627.9(1)	3627.8(1)	1	$0^+$	100	0.71(12)	12.6(12)	14.4(14)	0.86(8)	78(8)
3658.8(1)	3658.7(1)	$1^{(+)\text{d}}$	$0^+$	83(4)	0.65(14)	20.7(19)	25(4)	0.41(8) <sup>c</sup>	36(7) <sup>c</sup>
	2595.2(1)	$1^{(+)\text{d}}$	$2_2^+$	17(4)	0.74(20)			0.23(9) <sup>c</sup>	20(8) <sup>c</sup>

<sup>c</sup> Reduced transition strength  $B(E1) \downarrow$  or  $B(M1) \downarrow$ .

<sup>d</sup> Parity assigned according to the Alaga rules.

## Appendix C

# Transitions in $^{92}\text{Mo}$ , $^{98}\text{Mo}$ and $^{100}\text{Mo}$ up to the $(\gamma, n)$ threshold

Properties of the observed transitions in the photon-scattering experiments on  $^{92}\text{Mo}$ ,  $^{98}\text{Mo}$  and  $^{100}\text{Mo}$  at  $E_e = 13.2$  MeV described in Section 5.2.

Table C.1: Observed transitions in  $^{92}\text{Mo}$

$E_\gamma$ keV	$L$	$\frac{I_\gamma(90^\circ)}{I_\gamma(127^\circ)}$	$I_s$ eVb	$\frac{\Gamma_0^2}{\Gamma}$ meV	$E_\gamma$ keV	$L$	$\frac{I_\gamma(90^\circ)}{I_\gamma(127^\circ)}$	$I_s$ eVb	$\frac{\Gamma_0^2}{\Gamma}$ meV
774.5(1)	(1)		251(18)	13.0(9)	3091.2(1)	(1)		284(19)	236(16)
1121.7(3)	(1)		28(5)	3.1(5)	3143.7(7)	(1)		4.8(12)	4.1(10)
1340.9(1)	(1)		184(13)	29(2)	3192.8(1)	(1)		26(2)	23(2)
1510.1(1)	(2)		2416(160)	478(32)	3249.5(8)	(1)		5.9(13)	5.4(12)
1764.2(1)	(1)		32(3)	8.7(7)	3262.8(11)	(1)		4.7(13)	4.4(12)
1848.8(5)	(1)		9(3)	2.7(9)	3281.1(5)	(1)		10.3(14)	9.6(13)
2113.2(3)	(1)		17(2)	6.6(7)	3383.5(1)	(1)		28(2)	28(2)
2179.5(1)	(1)		86(6)	35(2)	3427.6(12)	(1)		7(2)	8(2)
2209.8(10)	(1)		5.4(17)	2.3(7)	3440(2)	(1)		4(2)	4(2)
2221.6(5)	(1)		11.4(19)	4.9(8)	3493.2(1)	(1)	0.94(9)	31(2)	33(2)
2227.7(6)	(1)		10.1(19)	4.3(8)	3541.4(1)	(1)	0.96(10)	26.6(18)	29(2)
2305.1(1)	(1)		31(3)	14.1(11)	3567.3(1)	1	0.97(12)	23.1(16)	25.5(18)
2416.3(1)	(1)		57(4)	29(2)	3651.0(2)	(1)	1.12(18)	16.7(15)	19.3(18)
2453.6(2)	(1)		19(2)	10.1(10)	3818.7(2)	1	0.62(13)	11.8(13)	14.9(17)
2462.0(7)	(1)		6.1(15)	3.2(8)	3838.1(4)	(1)	0.43(14)	8.3(12)	10.6(16)
2467.4(6)	(1)		7.2(15)	3.8(8)	3890.3(3)	1	1.0(2)	12.0(12)	15.7(16)
2638.0(1)	(1)		27(2)	16.0(13)	3908.5(4)	(1)	1.4(3)	8.6(11)	11.4(15)
2797.6(1)	(1)		49(4)	33(2)	3925.6(1)	(1)	1.14(4)	140(7)	188(9)
2831.3(10)	(1)		8(3)	5(2)	3935.0(2)	(1)	1.11(16)	17.4(14)	23.4(19)
2835.1(6)	(1)		13(3)	9(2)	3944.0(1)	(1)	0.97(3)	184(9)	248(12)
2919.8(5)	(1)		9.1(15)	6.7(11)	3963.6(5)	1	0.4(3)	6.3(11)	8.6(15)
3063.3(11)	(1)		37(3)	30(2)	3980.4(4)	1	0.7(2)	9.5(11)	13.0(16)

Table C.1: Observed transitions in  $^{92}\text{Mo}$  (continued)

$E_\gamma$ keV	$L$	$\frac{I_\gamma(90^\circ)}{I_\gamma(127^\circ)}$	$I_s$ eVb	$\frac{\Gamma_0^2}{\Gamma}$ meV	$E_\gamma$ keV	$L$	$\frac{I_\gamma(90^\circ)}{I_\gamma(127^\circ)}$	$I_s$ eVb	$\frac{\Gamma_0^2}{\Gamma}$ meV
4041.8(3)	1	1.0(2)	10.7(11)	15.2(16)	6300.7(1)	1	0.76(4)	90(5)	308(16)
4093.8(4)	1	1.1(3)	10.5(13)	15(2)	6377.9(1)	1	0.75(2)	251(12)	886(41)
4100.4(5)	(1)	0.9(5)	14.9(18)	22(3)	6439.6(9)	(1)	1.2(5)	10.2(18)	37(7)
4105.8(7)	(1)		8.5(18)	12(3)	6455.8(7)	1	0.8(2)	11.0(15)	40(6)
4124.1(6)	1	0.4(3)	6.4(11)	9.5(16)	6481.2(2)	1	0.89(9)	35(2)	127(9)
4147.2(1)	(1)	1.00(6)	59(3)	88(5)	6496.2(3)	1	1.03(14)	24(2)	89(7)
4247.9(4)	1	0.55(18)	7.6(11)	11.9(18)	6506.1(7)	1	0.3(2)	11.6(18)	43(7)
4285.5(4)	1	0.8(2)	7.8(11)	12.4(18)	6524.5(1)	1	0.75(3)	196(9)	723(35)
4464.9(9)	(1)	1.4(7)	5.1(12)	9(2)	6561.1(4)	1	0.79(16)	15.9(17)	59(6)
4493.6(1)	(1)	1.13(10)	27.3(17)	48(3)	6588.1(3)	1	0.68(12)	18.7(18)	71(7)
4589.3(2)	1	0.76(8)	24.6(16)	45(3)	6607.0(1)	1	0.75(3)	132(6)	499(24)
4633.2(1)	(1)	0.90(3)	99(5)	184(9)	6621.9(11)	(1)	1.1(5)	5.9(14)	22(6)
4702.2(1)	(1)	1.11(11)	25.2(16)	48(3)	6644.7(1)	1	0.80(7)	45(3)	172(11)
4861.9(4)	1	1.3(3)	11.9(14)	24(3)	6667.6(9)	(1)	0.37(16)	9.6(18)	37(7)
4868.9(6)	1	0.8(3)	9.3(13)	19(3)	6677.0(6)	1	0.9(2)	13.2(19)	51(8)
4910.0(6)	1	0.6(3)	5.9(10)	12(2)	6700.1(2)	1	0.80(9)	32(2)	124(9)
4928.0(5)	1	0.9(3)	8.7(12)	18(3)	6720.0(2)	1	0.73(9)	39(3)	153(12)
4936.3(1)	1	0.84(8)	32(2)	68(4)	6761.5(1)	1	0.70(5)	65(4)	259(15)
4946.8(5)	1	1.0(3)	8.4(11)	18(2)	6818.5(1)	1	0.69(4)	71(4)	286(16)
5003.5(1)	(1)	1.15(8)	35(2)	77(5)	6845.2(6)	1	0.8(2)	13.1(17)	53(7)
5401.0(3)	1	0.69(17)	18.7(17)	47(5)	6874.1(2)	1	0.79(10)	29(2)	120(9)
5411.1(7)	1	0.7(3)	9.8(14)	25(4)	6883.2(1)	1	0.84(5)	74(4)	304(17)
5450.2(2)	1	0.71(10)	22.7(17)	59(5)	6912.6(2)	(1)	1.06(13)	27(2)	112(9)
5533.0(6)	1	0.7(2)	8.5(12)	23(3)	6996.5(1)	1	0.73(2)	230(11)	979(46)
5554.8(2)	1	0.82(9)	29(2)	79(5)	7031.8(1)	1	0.73(2)	181(9)	777(37)
5566.7(4)	1	0.74(15)	14.6(14)	39(4)	7070.3(1)	1	0.77(3)	174(8)	752(36)
5616.1(3)	1	0.60(12)	16.7(15)	46(4)	7172.8(6)	1	0.77(19)	13.6(17)	61(8)
5648.8(5)	(1)	0.31(15)	10.3(14)	29(4)	7201.0(6)	1	0.8(2)	13.5(18)	61(8)
5680.3(8)	1	0.6(3)	7.2(12)	20(4)	7212.5(5)	1	0.65(13)	23(2)	105(11)
5704.1(2)	1	0.89(9)	30(2)	84(6)	7221.4(5)	1	0.84(17)	22(2)	100(11)
5789.4(1)	1	0.73(5)	53(3)	155(9)	7239.9(3)	1	0.96(13)	26(2)	117(10)
5801.8(2)	1	0.83(10)	25.3(19)	74(5)	7259.8(6)	1	0.9(2)	13.3(17)	61(8)
5840.6(2)	(1)	1.13(14)	25(2)	75(6)	7346.9(4)	1	0.78(12)	24(2)	112(10)
5865.8(3)	1	0.69(11)	19.7(16)	59(5)	7369.4(6)	1	1.0(2)	14.5(19)	68(9)
5876.8(5)	1	0.58(17)	11.0(14)	33(4)	7384.9(1)	1	0.82(6)	68(4)	322(18)
5919.3(2)	1	0.58(9)	21.1(17)	64(5)	7396.7(2)	1	0.76(6)	53(3)	251(16)
5939.3(3)	1	0.56(10)	17.7(16)	54(5)	7421.5(6)	1	0.46(18)	31(4)	149(21)
5966.4(4)	1	0.54(14)	13.2(15)	41(5)	7435.8(6)	1	1.2(3)	16(2)	76(10)
5979.9(1)	1	0.69(6)	38(2)	119(7)	7447.9(2)	1	0.66(8)	37(3)	178(13)
6098.4(3)	1	0.77(13)	17.8(16)	57(5)	7469.9(1)	1	0.78(5)	81(4)	394(21)
6115.5(2)	1	0.68(8)	27(2)	89(7)	7487.1(1)	1	0.81(3)	139(7)	674(33)
6126.1(1)	1	0.75(2)	211(10)	687(32)	7519.0(1)	1	0.79(4)	125(6)	611(31)
6138.8(2)	1	0.88(11)	23.9(18)	78(6)	7555.2(5)	1	0.81(15)	21(2)	104(11)
6168.1(2)	1	1.00(13)	22.0(17)	73(6)	7567.1(4)	(1)	1.18(18)	25(2)	126(12)
6192.0(1)	1	0.72(3)	131(6)	436(21)	7584.5(5)	1	1.1(2)	18(2)	92(10)
6238.5(11)	1	0.8(4)	7.3(15)	25(5)	7622.4(5)	1	0.85(14)	28(3)	141(14)
6250.0(7)	1	0.6(2)	10.6(15)	36(5)	7632.9(5)	1	0.88(16)	25(3)	126(13)
6275.9(2)	1	0.94(10)	30(2)	103(7)	7658.4(2)	1	0.92(10)	40(3)	203(15)

Table C.1: Observed transitions in  $^{92}\text{Mo}$  (continued)

$E_\gamma$ keV	$L$	$\frac{I_\gamma(90^\circ)}{I_\gamma(127^\circ)}$	$I_s$ eVb	$\frac{\Gamma_0^2}{\Gamma}$ meV	$E_\gamma$ keV	$L$	$\frac{I_\gamma(90^\circ)}{I_\gamma(127^\circ)}$	$I_s$ eVb	$\frac{\Gamma_0^2}{\Gamma}$ meV
7681.0(1)	1	0.73(4)	107(6)	547(29)	8660.7(1)	1	0.73(4)	178(9)	1155(60)
7703.8(7)	1	0.54(16)	21(3)	109(14)	8688.6(2)	1	0.81(9)	46(3)	300(23)
7713.7(2)	1	0.86(7)	77(5)	399(24)	8706.8(2)	1	0.79(9)	48(4)	313(23)
7732.0(1)	1	0.77(2)	256(12)	1328(63)	8764.2(1)	1	0.77(5)	118(7)	787(45)
7750.6(9)	1	0.9(3)	12(2)	64(11)	8774.8(1)	1	0.84(5)	149(8)	995(54)
7783.6(2)	1	0.85(7)	59(4)	312(19)	8819.3(4)	1	0.69(13)	29(3)	195(20)
7809.9(2)	1	0.89(9)	49(3)	258(17)	8865.5(4)	1	0.90(13)	40(4)	273(24)
7839.9(8)	(2)	1.5(4)	19(3)	59(9)	8888.2(4)	(1)	0.42(8)	36(3)	245(24)
7856.1(1)	1	0.78(5)	82(5)	440(25)	8903.2(1)	1	0.81(5)	166(9)	1142(62)
7881.7(1)	1	0.72(5)	79(5)	426(25)	8944.7(6)	1	0.75(15)	35(4)	244(28)
7892.4(2)	1	0.89(8)	59(4)	319(21)	8955.1(2)	1	0.81(7)	85(6)	588(39)
7912.3(5)	1	0.71(14)	22(2)	122(13)	8985.0(4)	(1)	0.53(8)	39(3)	270(24)
7933.8(2)	1	0.79(9)	41(3)	225(16)	8998.1(3)	1	0.87(9)	56(4)	391(28)
7950.4(1)	1	0.68(4)	92(5)	505(28)	9020.0(2)	(1)	0.60(6)	82(6)	575(39)
7965.0(5)	1	0.60(10)	32(3)	176(18)	9031.0(4)	1	0.64(11)	47(4)	334(30)
7989.2(3)	1	0.84(12)	31(3)	173(15)	9044.0(3)	1	0.71(9)	48(4)	338(26)
8006.9(1)	1	0.72(4)	89(5)	496(27)	9086.7(7)	1	0.84(19)	30(4)	213(26)
8043.1(1)	1	0.78(5)	89(5)	501(28)	9097.6(1)	1	0.65(4)	154(8)	1106(61)
8062.9(2)	1	0.65(6)	55(4)	310(20)	9126.8(3)	1	0.82(10)	49(4)	352(27)
8078.0(4)	1	0.70(15)	43(4)	245(25)	9141.9(7)	1	0.54(16)	21(3)	153(22)
8086.3(4)	1	0.78(10)	64(5)	362(28)	9168.2(5)	1	0.71(12)	38(4)	280(27)
8096.8(1)	1	0.77(4)	127(7)	720(39)	9187.6(1)	1	0.76(4)	151(8)	1106(59)
8117.6(4)	1	0.78(14)	25(3)	141(14)	9206.1(2)	1	0.67(5)	97(6)	716(43)
8151.0(4)	1	0.75(13)	26(3)	151(15)	9226.5(6)	1	0.61(12)	46(5)	339(35)
8169.0(1)	1	0.74(3)	212(10)	1225(59)	9238.7(3)	1	0.67(8)	83(6)	611(44)
8184.2(2)	1	0.68(7)	46(3)	266(19)	9259.4(5)	1	0.60(10)	42(4)	313(29)
8210.2(2)	1	0.67(9)	85(6)	496(37)	9277.8(10)	1	0.69(19)	37(5)	272(39)
8217.8(4)	1	0.80(17)	48(5)	282(29)	9289.3(10)	1	0.81(16)	49(6)	364(41)
8229.8(1)	1	0.67(4)	119(6)	698(37)	9300.6(7)	1	0.63(14)	44(5)	332(39)
8242.3(3)	1	0.72(9)	42(3)	247(19)	9315.7(15)	(1)		15(4)	116(31)
8252.7(6)	1	0.65(17)	21(3)	123(16)	9335.9(3)	1	0.82(8)	94(6)	708(48)
8264.6(3)	1	0.84(11)	36(3)	211(17)	9346.7(4)	1	0.68(8)	79(6)	598(44)
8282.1(3)	(1)	0.48(7)	34(3)	203(17)	9362.1(2)	1	0.86(7)	106(6)	807(48)
8311.4(8)	1	0.51(19)	42(8)	250(50)	9379.0(11)	(1)	0.3(2)	17(3)	131(26)
8318.6(4)	1	0.81(16)	85(9)	512(55)	9393.4(5)	1	0.65(12)	40(4)	306(31)
8346(2)	(1)	0.5(8)	15(6)	90(39)	9409.8(8)	1	0.56(15)	32(5)	246(35)
8354.2(8)	1	0.8(3)	40(7)	241(42)	9420.1(3)	1	0.68(8)	80(6)	612(46)
8383.7(2)	1	0.64(6)	64(4)	388(26)	9443.4(2)	1	0.74(7)	87(6)	676(43)
8407.6(5)	2	1.9(4)	46(4)	168(14)	9468.3(6)	1	0.53(13)	30(4)	233(28)
8422.5(1)	1	0.70(4)	142(8)	871(47)	9490.3(6)	1	0.53(13)	34(4)	264(31)
8488.4(2)	1	0.82(7)	74(5)	464(29)	9503.4(2)	1	0.65(5)	116(7)	905(55)
8500.4(3)	1	0.78(8)	56(4)	349(25)	9539.2(4)	1	0.67(10)	45(4)	352(32)
8513.8(10)	1	0.49(19)	14(3)	89(16)	9558.2(2)	1	0.65(6)	108(7)	855(55)
8569.6(3)	1	0.67(8)	64(5)	405(31)	9569.0(4)	1	0.74(9)	68(5)	541(43)
8579.0(3)	1	0.82(10)	63(5)	402(31)	9592.6(3)	1	0.69(10)	111(9)	885(75)
8610.1(5)	1	1.0(2)	24(3)	152(18)	9601.5(15)	1	1.0(4)	33(6)	262(51)
8632.6(2)	1	0.89(10)	49(4)	316(23)	9612.1(16)	1	0.7(3)	23(5)	183(37)
8650.4(3)	1	0.70(8)	58(4)	379(28)	9623.8(15)	1	0.8(4)	18(4)	140(33)

Table C.1: Observed transitions in  $^{92}\text{Mo}$  (continued)

$E_\gamma$ keV	$L$	$\frac{I_\gamma(90^\circ)}{I_\gamma(127^\circ)}$	$I_s$ eVb	$\frac{\Gamma_0^2}{\Gamma}$ meV	$E_\gamma$ keV	$L$	$\frac{I_\gamma(90^\circ)}{I_\gamma(127^\circ)}$	$I_s$ eVb	$\frac{\Gamma_0^2}{\Gamma}$ meV
9638.9(8)	1	0.9(3)	50(8)	405(61)	10667.6(6)	1	0.80(13)	50(5)	498(47)
9646.5(8)	1	0.51(17)	42(8)	342(62)	10706(3)	(2)		17(4)	102(26)
9670.3(9)	1	0.57(19)	19(3)	154(25)	10726.6(8)	1	0.6(2)	26(4)	262(39)
9687.2(7)	1	0.80(19)	36(4)	291(36)	10760.6(6)	1	0.82(15)	41(4)	409(42)
9696.2(7)	(1)	0.40(12)	36(5)	293(37)	10794.8(5)	1	0.80(13)	47(4)	478(45)
9713.2(3)	1	0.72(8)	95(7)	776(57)	10839.9(15)	1	0.4(2)	17(3)	176(35)
9723.3(9)	1	0.66(16)	39(5)	318(41)	10860.7(12)	1	0.45(16)	21(3)	218(35)
9734.6(7)	1	0.78(16)	38(4)	315(34)	10884.7(4)	1	0.71(9)	77(6)	794(60)
9747.5(4)	1	0.73(10)	57(5)	468(39)	10902.0(10)	1	0.68(17)	32(4)	331(42)
9759.0(6)	1	0.63(13)	35(4)	286(33)	10923.9(5)	1	0.80(11)	58(5)	604(51)
9786.3(3)	1	0.69(8)	75(5)	624(44)	10941.7(10)	(1)	0.44(12)	30(4)	312(41)
9800.6(4)	1	0.74(9)	82(6)	680(52)	10962.7(12)	(1)	0.38(15)	21(3)	214(36)
9813.4(11)	1	0.43(17)	36(5)	298(45)	11042.8(7)	(1)	0.41(11)	28(4)	296(38)
9826.1(1)	1	0.74(4)	276(14)	2314(120)	11064.6(4)	1	0.68(9)	70(6)	747(62)
9840.3(4)	1	0.71(8)	72(5)	605(45)	11078.6(10)	1	0.9(2)	31(4)	330(44)
9858.4(6)	1	0.85(14)	46(4)	388(37)	11094.3(9)	1	0.9(3)	25(4)	263(38)
9871.2(3)	1	0.84(9)	77(6)	648(47)	11132.5(12)	1	0.69(17)	39(5)	423(55)
9907.7(4)	1	0.92(15)	59(6)	502(48)	11149.7(8)	1	0.79(15)	55(6)	588(61)
9916.4(7)	1	0.65(14)	42(5)	355(43)	11178.6(5)	1	0.68(8)	76(6)	825(62)
9929.8(8)	1	0.53(18)	52(9)	443(74)	11206.2(7)	1	0.81(13)	51(5)	559(52)
9937.0(4)	1	0.89(15)	105(10)	901(88)	11240.7(6)	1	0.81(11)	60(5)	653(56)
9952.9(4)	1	0.74(10)	51(4)	437(36)	11270.5(9)	1	0.70(14)	40(4)	435(48)
9964.7(6)	1	0.94(19)	31(4)	265(30)	11296.7(6)	1	0.93(14)	55(5)	612(54)
10007.4(8)	1	1.0(3)	50(7)	435(64)	11353.1(3)	1	0.79(7)	112(7)	1247(80)
10016.6(7)	1	0.57(14)	59(8)	512(66)	11385.6(8)	1	1.06(19)	44(5)	497(51)
10042.9(13)	(1)	1.1(4)	16(3)	136(28)	11410.6(5)	1	0.75(9)	80(6)	899(68)
10064.7(3)	1	0.74(7)	83(6)	733(48)	11436.5(19)	1	0.9(3)	21(4)	234(45)
10098.0(4)	1	0.84(10)	58(4)	511(40)	11458.1(5)	1	0.76(9)	84(6)	953(71)
10122.5(2)	1	0.73(5)	140(8)	1245(72)	11486(4)	1	0.2(4)	11(5)	121(52)
10138.1(15)	1	0.5(3)	37(8)	332(70)	11502(2)	(2)	1.8(10)	18(5)	125(32)
10147.6(7)	1	0.63(17)	70(9)	620(80)	11552.0(8)	1	0.8(2)	28(4)	328(44)
10229.9(16)	1	0.7(2)	35(6)	316(56)	11571.4(7)	1	0.50(13)	29(4)	335(45)
10246.0(9)	(1)	0.50(8)	112(10)	1017(90)	11593.2(18)	(1)	0.8(5)	26(8)	298(94)
10261.3(9)	1	0.77(13)	103(10)	945(87)	11633.5(6)	1	0.70(14)	48(5)	568(60)
10280.7(12)	1	0.69(17)	36(5)	334(44)	11655.4(10)	1	0.40(18)	34(5)	396(57)
10319(3)	1	0.6(5)	37(14)	344(127)	11672.8(9)	1	0.9(2)	41(5)	479(58)
10329.4(17)	1	0.7(3)	58(14)	535(129)	11701.9(5)	1	0.73(11)	60(5)	706(64)
10354(2)	(1)		29(5)	265(51)	11728.0(16)	(1)		25(5)	296(62)
10461.9(4)	1	0.67(9)	66(5)	630(51)	11743.1(12)	(1)		31(6)	366(68)
10480(2)	1	0.5(3)	17(4)	158(41)	11769.3(17)	1	0.6(3)	17(4)	203(45)
10493.1(10)	1	0.64(18)	30(4)	282(42)	11789.3(18)	1	0.9(4)	20(4)	237(50)
10528.4(3)	1	0.88(10)	72(5)	688(51)	11805.8(7)	1	0.75(14)	49(5)	590(62)
10553.4(6)	1	0.88(17)	90(9)	864(91)	11838.2(13)	1	0.9(3)	20(4)	246(44)
10563.5(12)	1	0.8(3)	42(8)	407(80)	11864.0(8)	1	0.79(19)	34(4)	416(52)
10585.3(4)	1	0.70(9)	66(5)	644(49)	11893.7(12)	1	0.8(3)	24(4)	288(45)
10606.0(2)	1	0.76(6)	128(8)	1244(74)	11960(3)	1	0.6(3)	23(5)	283(63)
10629.4(7)	1	0.62(13)	35(4)	345(38)	11990(5)	(1)	1.0(6)	20(6)	251(77)
10653.0(7)	1	0.73(13)	45(5)	447(46)	12017.8(14)	1	0.86(17)	67(7)	838(91)

Table C.1: Observed transitions in  $^{92}\text{Mo}$  (continued)

$E_\gamma$ keV	$L$	$\frac{I_\gamma(90^\circ)}{I_\gamma(127^\circ)}$	$I_s$ eVb	$\frac{\Gamma_0^2}{\Gamma}$ meV	$E_\gamma$ keV	$L$	$\frac{I_\gamma(90^\circ)}{I_\gamma(127^\circ)}$	$I_s$ eVb	$\frac{\Gamma_0^2}{\Gamma}$ meV
12067.8(15)	1	0.77(17)	46(5)	581(69)	12256.5(12)	1	0.79(15)	59(6)	763(79)
12114.8(12)	1	0.90(16)	59(6)	753(76)	12301(2)	1	1.1(3)	35(5)	458(66)
12166(3)	1	0.6(3)	31(6)	400(72)	12374(2)	1	0.8(2)	33(5)	442(69)
12195.9(19)	(2)	1.7(4)	48(6)	369(49)					

Table C.2: Observed transitions in  $^{98}\text{Mo}$ 

$E_\gamma$ keV	$L$	$\frac{I_\gamma(90^\circ)}{I_\gamma(127^\circ)}$	$I_s$ eVb	$\frac{\Gamma_0^2}{\Gamma}$ meV	$E_\gamma$ keV	$L$	$\frac{I_\gamma(90^\circ)}{I_\gamma(127^\circ)}$	$I_s$ eVb	$\frac{\Gamma_0^2}{\Gamma}$ meV
646.3(1)	(1)		404(26)	14.7(9)	1759.2(3)	(1)		34(4)	9.2(11)
838.5(1)	(1)		307(20)	18.7(12)	1774.2(1)	(1)		119(8)	33(2)
897.4(1)	(1)		132(9)	9.2(6)	1785.4(1)	(1)		90(6)	24.9(17)
971.2(1)	(1)		104(8)	8.5(6)	1823.4(1)	(1)		38(3)	11.0(9)
1102.6(2)	(1)		29(3)	3.0(3)	1832.6(1)	(1)		37(3)	10.7(9)
1143.5(2)	(1)		65(6)	7.3(6)	1856.2(1)	(1)		33(3)	9.7(8)
1162.5(4)	(1)		41(5)	4.8(5)	1870.1(2)	(1)		26(3)	7.7(8)
1175.7(1)	(1)		60(5)	7.2(5)	1875.0(2)	(1)		26(3)	8.0(8)
1230.7(1)	(1)		34(3)	4.5(4)	1889.2(1)	(1)		47(4)	14.5(11)
1301.3(2)	(1)		23(3)	3.3(4)	1912.4(1)	(1)		57(4)	18.1(13)
1306.1(1)	(1)		45(4)	6.6(5)	1932.1(1)	(1)		37(3)	12.0(10)
1317.9(1)	(1)		57(4)	8.5(6)	1944.7(1)	(1)		50(4)	16.5(12)
1367.7(1)	(1)		48(4)	7.8(6)	1972.1(2)	(1)		29(3)	9.7(9)
1379.2(5)	(1)		16(3)	2.7(4)	1979.6(6)	(1)		17(4)	5.9(12)
1388.8(2)	(1)		35(4)	5.8(6)	1983.9(5)	(1)		20(4)	6.7(12)
1419.7(1)	(1)		129(8)	22.5(14)	1991.7(8)	(1)		9(2)	3.0(7)
1432.5(1)	(1)		277(17)	49(3)	1998.0(5)	(1)		13(2)	4.6(7)
1448.7(2)	(1)		25(3)	4.6(5)	2016.6(1)	(1)		74(5)	26.1(17)
1471.5(4)	(1)		13(2)	2.4(4)	2024.2(1)	(1)		55(4)	19.5(13)
1491.4(1)	(1)		35(3)	6.8(6)	2043.5(2)	(1)		24(3)	8.7(9)
1524.1(2)	(1)		22(3)	4.4(5)	2073.0(1)	(1)		66(4)	24.5(16)
1546.3(1)	(1)		102(7)	21.1(14)	2081.6(2)	(1)		24(2)	9.1(9)
1551.3(1)	(1)		97(7)	20.3(13)	2139.2(3)	(1)		18(2)	7.0(8)
1558.6(2)	(1)		33(3)	7.0(6)	2160.8(2)	(1)		33(3)	13.1(11)
1573.8(6)	(1)		10(2)	2.2(5)	2166.7(3)	(1)		20(2)	7.9(9)
1594.4(1)	(1)		47(4)	10.3(8)	2222.2(1)	(1)		132(9)	57(4)
1608.6(3)	(1)		14(2)	3.2(5)	2228.6(3)	(1)		23(2)	9.8(10)
1615.1(3)	(1)		15(2)	3.4(5)	2254.1(4)	(1)		15(2)	6.8(10)
1646.5(8)	(1)		10(3)	2.2(6)	2259.5(3)	(1)		19(2)	8.5(10)
1652.6(2)	(1)		31(3)	7.3(7)	2287.0(7)	(1)		6.4(17)	2.9(8)
1659.4(4)	(1)		12(2)	3.0(5)	2303.0(2)	(1)		19(2)	8.6(9)
1679.6(1)	(1)		43(4)	10.5(8)	2315.9(4)	(1)		12.3(18)	5.7(8)
1686.5(2)	(1)		31(3)	7.7(7)	2338.0(2)	(1)		25(2)	11.9(11)
1693.8(1)	(1)		39(3)	9.7(8)	2350.6(7)	(1)		7.1(18)	3.4(8)
1740.6(1)	(1)		53(4)	13.9(10)	2358.8(2)	(1)		18(2)	8.8(10)
1748.5(6)	(1)		9(2)	2.3(5)	2371.2(4)	(1)		15(2)	7.1(11)

Table C.2: Observed transitions in  $^{98}\text{Mo}$  (continued)

$E_\gamma$ keV	$L$	$\frac{I_\gamma(90^\circ)}{I_\gamma(127^\circ)}$	$I_s$ eVb	$\frac{\Gamma_0^2}{\Gamma}$ meV	$E_\gamma$ keV	$L$	$\frac{I_\gamma(90^\circ)}{I_\gamma(127^\circ)}$	$I_s$ eVb	$\frac{\Gamma_0^2}{\Gamma}$ meV
2390.1(7)	(1)		7.2(18)	3.5(9)	3065.1(4)	(1)		10.0(16)	8.2(13)
2403.9(6)	(1)		10(2)	4.9(10)	3074.8(2)	(1)		16.3(18)	13.4(15)
2423.1(1)	(1)		37(3)	18.4(14)	3081.1(5)	(1)		8.2(15)	6.8(12)
2451.0(1)	(1)		29(3)	14.9(13)	3090.0(1)	(1)		53(4)	44(3)
2466.0(4)	(1)		11.6(18)	6.1(9)	3099.4(5)	(1)		8.5(15)	7.1(13)
2471.7(5)	(1)		11.9(19)	6.3(10)	3105.2(8)	(1)		7.0(17)	5.9(14)
2477.3(1)	(1)		43(3)	22.8(17)	3110.2(12)	(1)		4.5(17)	3.8(14)
2487.1(1)	(1)		23(2)	12.4(11)	3119.0(3)	(1)		12.2(16)	10.3(13)
2525.8(2)	(1)		32(3)	17.8(15)	3129.6(9)	(1)		4.3(14)	3.6(12)
2538.1(2)	(1)		45(3)	24.9(19)	3142.5(2)	(1)		15.7(18)	13.5(15)
2551.2(2)	(1)		73(5)	41(3)	3149.4(4)	(1)		11.5(16)	9.9(13)
2558.2(3)	(1)		41(4)	23(2)	3157.6(8)	(1)		5.4(14)	4.7(12)
2589.2(1)	(1)		34(3)	19.5(15)	3166.3(3)	(1)		12.0(17)	10.4(14)
2597.4(1)	(1)		25(2)	14.5(12)	3184.0(3)	(1)		11.4(16)	10.0(14)
2608.5(1)	(1)		53(4)	32(2)	3192.5(3)	(1)		11.2(15)	9.9(13)
2633.1(1)	(1)		13(2)	7.6(13)	3199.5(6)	(1)		6.2(14)	5.5(12)
2641.1(8)	(1)		11(2)	6.5(12)	3210.2(9)	(1)		4.4(14)	3.9(12)
2675.3(4)	(1)		19(2)	11.6(13)	3218.5(5)	(1)		6.8(14)	6.1(12)
2683.0(3)	(1)		23(2)	14.3(14)	3234.0(7)	(1)		7.5(15)	6.8(14)
2691.8(3)	(1)		21(2)	13.4(14)	3244.2(4)	(1)		19(2)	17(2)
2699.8(2)	(1)		39(3)	24.3(19)	3249.9(7)	(1)		11(2)	10.4(19)
2708.3(1)	(1)		45(3)	29(2)	3257.9(1)	(1)		32(3)	30(2)
2732.6(7)	(1)		23(6)	15(4)	3266.6(4)	(1)		11.1(15)	10.2(14)
2746.5(2)	(1)		32(3)	21(2)	3276.4(6)	(1)		9.8(17)	9.1(16)
2756.7(4)	(1)		16.2(19)	10.7(13)	3282.9(5)	(1)		11.1(17)	10.4(16)
2766.0(2)	(1)		31(3)	20.5(17)	3305.6(7)	(1)		10.2(19)	9.6(18)
2791.8(6)	(1)		14(5)	9(3)	3311.8(6)	(1)		12(2)	12(2)
2806.9(9)	(1)		4.9(15)	3.4(10)	3328.5(2)	(1)		20(2)	19(2)
2816.0(8)	(1)		14.5(18)	10.0(13)	3347.7(12)	(1)		4.2(15)	4.1(14)
2821.6(3)	(1)		18(2)	12.1(14)	3354.3(11)	(1)		4.8(14)	4.7(14)
2844.5(8)	(1)		21(3)	14.5(19)	3365.2(7)	(1)		5.8(14)	5.7(13)
2851.4(3)	(1)		51(4)	36(3)	3377.7(9)	(1)		5.5(14)	5.4(14)
2858.8(2)	(1)		41(3)	29(2)	3384.1(3)	(1)		14.1(19)	14.0(19)
2873.6(3)	(1)		20(2)	14.1(16)	3405.0(1)	(1)		67(4)	67(4)
2916.9(5)	(1)		8.2(15)	6.1(11)	3413.9(5)	(1)		9.1(14)	9.2(14)
2925.4(1)	(1)		54(4)	40(3)	3434.4(2)	(1)		14.5(15)	14.9(16)
2931.5(4)	(1)		15.3(19)	11.4(14)	3450.9(4)	(1)		9.0(14)	9.3(14)
2936.7(5)	(1)		11.3(18)	8.4(13)	3457.2(7)	(1)		57(4)	59(4)
2946.4(2)	(1)		19.1(19)	14.4(14)	3467.6(3)	(1)		9.2(13)	9.6(14)
2962.0(2)	(1)		17.8(19)	13.6(14)	3522.6(6)	(1)		11.9(18)	12.8(19)
2978.3(2)	(1)		18.9(19)	14.5(15)	3531.1(8)	(1)		10.7(19)	12(2)
2992.9(6)	(1)		12(3)	9(2)	3551.6(1)	(1)		42(3)	46(3)
3008.3(5)	(1)		7.8(15)	6.1(12)	3564.7(7)	(1)		4.8(12)	5.3(14)
3015.5(2)	(1)		21(2)	16.3(16)	3572.9(6)	(1)		6.0(13)	6.6(15)
3030.1(8)	(1)		5.2(15)	4.1(12)	3587.8(5)	(1)		11.4(16)	12.7(18)
3035.1(6)	(1)		6.9(15)	5.5(12)	3599.2(5)	(1)		13.6(19)	15(2)
3043.2(2)	(1)		16.8(18)	13.5(14)	3606.6(7)	(1)		11.4(18)	13(2)
3051.2(4)	(1)		7.9(14)	6.4(11)	3615.8(5)	(1)		12.3(17)	14.0(19)



Table C.2: Observed transitions in  $^{98}\text{Mo}$  (continued)

$E_\gamma$ keV	$L$	$\frac{I_\gamma(90^\circ)}{I_\gamma(127^\circ)}$	$I_s$ eVb	$\frac{\Gamma_0^2}{\Gamma}$ meV	$E_\gamma$ keV	$L$	$\frac{I_\gamma(90^\circ)}{I_\gamma(127^\circ)}$	$I_s$ eVb	$\frac{\Gamma_0^2}{\Gamma}$ meV
3625.5(17)	(1)		3.6(15)	4.1(17)	4410.1(1)	1	0.76(7)	34(2)	57(3)
3639.6(8)	(1)		7.3(16)	8.4(18)	4488.0(2)	1	0.84(17)	15.0(13)	26(2)
3653.0(7)	(1)		8.9(16)	10.3(19)	4518.8(2)	1	1.1(2)	12.8(12)	23(2)
3662.1(13)	(1)		4.9(14)	5.7(17)	4538.2(6)	1	0.7(3)	9.8(18)	18(3)
3678.5(5)	1	1.1(3)	9.5(14)	11.2(16)	4543.2(2)	1	0.81(14)	25(2)	46(4)
3703.8(2)	1	0.77(15)	18.2(16)	21.7(19)	4564.6(7)	(1)	0.8(5)	5.0(10)	9.0(19)
3714.9(9)	1	0.1(4)	4.8(13)	5.8(15)	4581.5(7)	(1)	1.0(5)	5.1(11)	9(2)
3752.5(5)	(1)	1.3(4)	9.6(13)	11.7(16)	4590.5(1)	1	0.75(9)	31(2)	57(4)
3762.9(3)	(1)	1.3(2)	16.3(15)	20.0(19)	4599.2(5)	1	0.7(4)	6.8(11)	12(2)
3806.0(2)	1	0.99(15)	20.2(16)	25(2)	4616.1(5)	1	0.9(3)	9.4(13)	17(3)
3816.0(7)	1	0.8(4)	7.5(13)	9.4(16)	4654.2(4)	(1)	1.5(3)	12.2(15)	23(3)
3836.9(1)	1	0.83(9)	31(2)	40(3)	4660.5(12)	(1)		6.8(16)	13(3)
3848.3(5)	1	1.0(3)	10.7(14)	13.8(18)	4673.3(14)	(1)	0.9(8)	3.5(11)	7(2)
3857.6(1)	1	0.89(7)	44(3)	57(3)	4688.8(5)	1	1.1(3)	11.8(15)	23(3)
3902.8(3)	1	1.2(3)	11.2(13)	14.8(17)	4697(2)	(1)	1.0(9)	3.2(13)	6(3)
3915.6(2)	1	1.0(2)	13.8(13)	18.3(18)	4719.2(4)	(1)	1.4(3)	10.6(13)	21(3)
3937.0(1)	1	0.81(4)	88(4)	118(6)	4731.0(5)	(2)	1.5(4)	10.1(15)	11.8(17)
3944.0(1)	(1)	1.07(11)	29.2(19)	39(3)	4752.6(7)	1	1.1(4)	8.1(13)	16(3)
3954.0(3)	1	0.9(3)	10.0(12)	13.5(17)	4760.7(4)	1	1.1(2)	13.7(15)	27(3)
3981.6(3)	(1)	1.4(3)	10.9(13)	15.0(17)	4779.2(10)	(1)	1.1(6)	5.1(11)	10(2)
3991.9(2)	1	0.90(16)	16.5(14)	23(2)	4788.6(10)	(1)	1.4(7)	4.5(11)	9(2)
4020.5(5)	(2)	1.5(4)	14.1(19)	11.9(16)	4804.1(5)	1	0.9(3)	9.5(13)	19(3)
4034.2(2)	(2)		6(3)	5(2)	4812.6(2)	1	0.88(10)	27.5(19)	55(4)
4041.5(9)	(1)	1.2(6)	6.4(14)	9.1(19)	4824.7(11)	(1)	1.0(6)	4.6(11)	9(2)
4059.4(10)	(2)	2.7(12)	8.1(17)	6.9(14)	4837.4(1)	1	0.90(10)	28(18)	57(4)
4069.9(17)	(2)		7(2)	6(2)	4847.7(3)	1	0.96(16)	17.0(14)	35(3)
4079.7(4)	1	1.2(2)	15.2(16)	22(2)	4868.4(4)	1	0.7(2)	9.8(12)	20(3)
4102.2(5)	(2)	2.7(7)	14.6(18)	12.7(16)	4887.0(6)	(2)	1.9(8)	7.5(15)	9.3(18)
4170.7(8)	1	0.7(4)	6.0(12)	9.0(19)	4902.7(1)	1	0.91(12)	23.9(17)	50(4)
4179.8(2)	(1)	1.2(2)	18.7(16)	28(2)	4914.3(4)	1	1.2(3)	10.0(12)	21(3)
4191.7(11)	(1)		4.7(12)	7.1(19)	4933.5(5)	1	1.0(4)	6.8(11)	15(2)
4198.1(17)	(2)		7(2)	7(2)	4944.5(4)	1	1.2(3)	8.6(12)	18(3)
4204.2(5)	1	0.6(3)	8.6(13)	13(2)	4953.8(10)	(1)	1.3(8)	3.5(11)	8(2)
4215.9(9)	1	0.3(7)	4.9(12)	7.9(19)	4967.4(3)	1	1.03(19)	13.8(13)	30(3)
4231.0(4)	1	1.0(3)	14.6(16)	23(3)	4985.2(9)	1	0.7(5)	4.3(11)	9(2)
4240.2(8)	(2)	1.7(7)	8.2(16)	7.6(15)	5008.5(3)	1	0.76(18)	14.4(14)	31(3)
4252.5(12)	(1)	1.0(7)	6.0(18)	9(3)	5028.5(2)	1	0.80(16)	14.7(13)	32(3)
4258.7(5)	1	0.8(2)	15.2(19)	24(3)	5050.2(1)	1	0.81(6)	40(2)	88(5)
4267.8(2)	1	1.00(16)	20.5(17)	32(3)	5081.6(2)	1	0.85(13)	17.5(14)	39(3)
4277.3(10)	(1)		5.3(13)	9(2)	5112.3(9)	(2)	1.7(6)	8.7(16)	12(2)
4295.3(1)	(1)	1.12(14)	26.4(19)	42(3)	5121.3(3)	1	0.80(13)	22.9(19)	52(4)
4309.0(6)	1	1.0(4)	7.4(12)	12(2)	5134.0(11)	(1)		6.1(13)	14(3)
4322.6(9)	(2)	1.8(9)	7.1(16)	6.9(16)	5141.5(13)	(2)		8(2)	12(3)
4332.4(4)	1	0.9(3)	11.2(14)	18(2)	5147.5(3)	1	0.67(15)	20.7(17)	48(4)
4339.3(6)	(2)	1.6(4)	13.2(18)	12.9(18)	5165.0(2)	1	0.96(13)	30(2)	69(5)
4346.9(4)	(1)	1.4(3)	10.7(14)	18(2)	5174.5(12)	(2)	1.5(8)	7(2)	10(2)
4361.7(1)	(1)	0.92(5)	67(3)	111(6)	5195.4(4)	1	1.0(3)	9.5(12)	22(3)
4391.1(1)	(1)	1.01(10)	28.8(18)	48(3)	5214.9(5)	(2)	1.8(5)	11.4(15)	16(2)

Table C.2: Observed transitions in  $^{98}\text{Mo}$  (continued)

$E_\gamma$	$L$	$\frac{I_\gamma(90^\circ)}{I_\gamma(127^\circ)}$	$I_s$	$\frac{\Gamma_0^2}{\Gamma}$	$E_\gamma$	$L$	$\frac{I_\gamma(90^\circ)}{I_\gamma(127^\circ)}$	$I_s$	$\frac{\Gamma_0^2}{\Gamma}$
keV			eVb	meV	keV			eVb	meV
5225.4(7)	(1)	1.1(4)	7.0(11)	17(3)	5844.4(15)	(2)	2.4(17)	7(2)	12(4)
5235.9(9)	1	0.5(5)	5.1(11)	12(3)	5856.7(3)	1	0.54(16)	29(3)	86(8)
5244.4(2)	(1)	1.24(18)	20.1(16)	48(4)	5869.1(8)	(1)	1.5(6)	6.0(12)	18(4)
5267.5(6)	(2)	2.0(7)	8.3(14)	12(2)	5889.2(6)	1	0.7(3)	7.9(12)	24(4)
5312.4(3)	1	0.8(2)	10.0(11)	24.4(3)	5906.4(7)	1	1.0(4)	7.7(12)	23(4)
5323.8(5)	(1)	1.3(4)	6.9(11)	17(3)	5916.8(2)	1	0.87(13)	20.5(16)	62(5)
5346.5(2)	1	0.75(11)	21.3(16)	53(4)	5949.7(7)	1	0.6(2)	9.5(14)	29(4)
5354.5(2)	1	0.89(13)	18.5(14)	46(4)	5959.6(2)	1	0.75(7)	34(2)	104(7)
5362.5(8)	(1)	1.3(6)	4.5(10)	11(3)	5972.6(2)	1	0.79(10)	24.8(18)	77(6)
5386.1(2)	1	0.91(14)	16.9(14)	43(4)	5983.9(2)	1	0.88(10)	31(2)	95(7)
5397.3(1)	1	0.5(5)	3.7(10)	9(3)	5992.8(8)	(1)	1.0(6)	17(3)	52(8)
5412.4(4)	1	0.7(2)	9.1(11)	23(3)	5999.5(8)	(1)	0.6(6)	17(3)	53(8)
5432.7(6)	1	0.8(3)	6.6(11)	17(3)	6008.4(7)	1	1.0(3)	10.8(15)	34(5)
5442.0(6)	1	0.3(3)	6.3(11)	16(3)	6021.9(2)	1	0.95(12)	24.0(17)	75(6)
5450.3(4)	1	1.2(3)	9.8(12)	25(3)	6031.7(1)	1	0.76(5)	54(3)	169(9)
5458.0(5)	1	1.1(3)	8.7(12)	22(3)	6046.1(4)	1	0.59(15)	13.3(14)	42(4)
5482.2(1)	1	0.76(7)	33(2)	86(5)	6065.5(1)	1	0.78(6)	47(3)	150(9)
5492.2(3)	(1)	1.2(2)	12.3(13)	32(3)	6076.5(7)	(1)	1.3(5)	14(2)	46(7)
5499.6(7)	(2)	1.6(7)	6.3(13)	10(2)	6088(2)	(1)	1.0(11)	5(2)	17(8)
5508.7(3)	1	0.98(19)	12.2(12)	32(3)	6101.4(4)	1	0.80(15)	19.8(18)	64(6)
5518.9(7)	1	0.7(4)	5.1(10)	13(3)	6110.0(1)	(1)	0.87(6)	65(3)	210(11)
5528.0(4)	1	0.8(2)	9.3(11)	25(3)	6120.3(2)	(1)	0.93(9)	35(2)	113(7)
5543.9(18)	(1)	1.4(10)	3.7(13)	10(4)	6144.9(18)	1	0.6(5)	6.1(16)	20(5)
5552.5(8)	(1)	1.1(4)	8.5(14)	23(4)	6172(3)	1	0.6(4)	8(3)	25(10)
5563.1(2)	1	0.87(13)	21.0(16)	56(5)	6183.0(8)	(1)	1.2(4)	27(4)	90(13)
5579.0(4)	1	0.95(17)	17.7(16)	48(5)	6219.9(11)	(1)		9.7(17)	33(6)
5588.2(15)	(1)	1.4(7)	7.4(19)	20(5)	6234.3(10)	(1)		12.4(19)	42(7)
5595.4(10)	1	1.0(4)	11(2)	29(5)	6246.9(3)	(1)		38(3)	129(11)
5603.8(15)	(1)		5.1(15)	14(4)	6265.8(7)	(1)		13.7(18)	47(6)
5615.1(12)	1	0.4(4)	4.8(12)	13(3)	6315.7(3)	1	0.85(10)	28(2)	96(7)
5625.9(4)	1	0.93(19)	13.5(14)	37(4)	6330.1(2)	1	0.89(8)	41(3)	143(9)
5637.9(1)	1	0.89(9)	33(2)	91(6)	6367.2(4)	1	1.02(18)	18.2(17)	64(6)
5654.2(2)	1	0.74(9)	27.4(19)	76(5)	6379.0(8)	1	1.0(3)	13.9(19)	49(7)
5664.4(3)	1	0.67(14)	17.1(15)	48(4)	6388.1(7)	1	0.75(17)	19(2)	69(7)
5678.6(14)	(2)	1.6(11)	6.4(19)	11(3)	6397.7(5)	1	1.1(2)	18(2)	65(7)
5686.7(2)	1	0.76(15)	26(2)	73(6)	6419.7(11)	1	0.4(4)	11(2)	39(9)
5708.0(6)	1	0.6(2)	11.3(16)	32(5)	6438.5(10)	1	1.0(4)	9.1(16)	33(6)
5715.9(4)	1	1.02(15)	22.6(19)	64(6)	6451.0(2)	(1)	0.98(10)	34(2)	123(8)
5725.4(5)	1	0.84(17)	17.7(19)	50(5)	6465.6(6)	1	1.0(3)	20(3)	71(10)
5732.7(6)	1	0.9(2)	16.6(19)	47(6)	6473.2(3)	1	0.77(13)	37(3)	133(12)
5741.3(1)	1	0.72(6)	51(3)	147(9)	6491.6(6)	1	0.6(3)	19(3)	68(9)
5753.9(9)	1	0.9(4)	6.6(12)	19(4)	6511.4(11)	(1)	1.1(4)	12(2)	42(8)
5764.5(3)	1	0.83(15)	16.5(15)	48(4)	6522.1(10)	(1)	1.3(5)	13(2)	46(8)
5775.8(2)	1	0.86(10)	26.7(18)	77(5)	6530.4(6)	1	0.6(3)	15.1(18)	56(7)
5791.6(5)	1	0.54(18)	11.7(14)	34(4)	6543.2(2)	1	0.79(13)	41(3)	152(11)
5801.2(3)	1	0.92(15)	17.4(15)	51(5)	6566.5(10)	(1)	1.4(5)	8.6(15)	32(6)
5811.2(2)	1	0.81(9)	27.2(18)	80(6)	6577.1(10)	1	1.0(3)	15(2)	57(9)
5828.4(2)	1	0.80(12)	19.2(15)	57(5)	6586.0(3)	1	0.83(9)	49(3)	184(13)

Table C.2: Observed transitions in  $^{98}\text{Mo}$  (continued)

$E_\gamma$ keV	$L$	$\frac{I_\gamma(90^\circ)}{I_\gamma(127^\circ)}$	$I_s$ eVb	$\frac{\Gamma_0^2}{\Gamma}$ meV	$E_\gamma$ keV	$L$	$\frac{I_\gamma(90^\circ)}{I_\gamma(127^\circ)}$	$I_s$ eVb	$\frac{\Gamma_0^2}{\Gamma}$ meV
6596.2(3)	1	0.73(11)	28(2)	107(8)	7395.8(3)	1	0.88(11)	25.2(19)	120(9)
6614.7(8)	1	0.4(3)	21(5)	81(19)	7428.0(4)	1	0.84(17)	14.4(15)	69(7)
6631.1(12)	(1)	1.1(5)	11.0(19)	42(7)	7446.7(9)	1	0.8(4)	6.1(13)	29(6)
6636.5(18)	(1)	1.1(9)	11(3)	41(13)	7461.0(7)	1	0.8(3)	7.9(13)	38(6)
6647.9(8)	(1)	1.2(5)	25(4)	95(16)	7473.4(3)	1	0.84(14)	17.3(16)	84(8)
6680(2)	(1)	1.4(18)	10(6)	37(21)	7497.7(13)	(2)		7.1(18)	21(5)
6685(3)	(1)	0.8(11)	8(5)	32(21)	7512.9(5)	(2)	1.6(3)	17.5(18)	52(5)
6698.5(7)	1	0.7(2)	11.3(15)	44(6)	7543(2)	(1)	0.7(6)	7(3)	36(16)
6756.1(2)	1	0.88(8)	60(4)	238(15)	7551.4(17)	(2)	1.7(11)	10(3)	30(8)
6765.4(7)	1	0.86(16)	27(3)	107(11)	7562.0(7)	1	0.75(19)	16(2)	80(11)
6815.6(13)	(1)	1.3(8)	7.1(18)	28(8)	7582.8(4)	1	0.79(11)	33(3)	166(14)
6823.9(6)	1	1.1(3)	17(2)	70(9)	7608.8(6)	1	0.68(16)	14.6(17)	73(9)
6836.3(6)	(1)	1.4(3)	14.0(15)	57(6)	7691.7(6)	1	0.90(19)	16.2(18)	83(9)
6847.1(6)	1	0.66(16)	20(2)	80(10)	7711.0(6)	1	0.58(12)	27(3)	139(14)
6853.4(4)	2	1.8(3)	29(3)	71(6)	7737(2)	(1)	1.0(6)	6.7(19)	35(10)
6865.7(4)	(2)	1.5(2)	21.7(19)	53(5)	7752.2(8)	1	0.95(18)	21(2)	109(12)
6877.3(14)	(2)	3.1(22)	6.3(15)	16(4)	7764.2(4)	1	0.78(9)	39(3)	205(15)
6888.3(5)	1	1.0(3)	13.9(16)	57(7)	7780.8(4)	1	0.62(10)	24(2)	126(11)
6900.0(3)	(1)	1.06(13)	37(3)	154(11)	7803.1(5)	1	0.63(12)	20.7(19)	109(10)
6950.5(8)	1	0.9(3)	8.5(13)	36(6)	7820.2(9)	1	0.54(17)	13.3(18)	70(10)
6959.0(6)	(2)	1.6(4)	12.4(16)	31(4)	7834.6(13)	(1)	1.2(4)	11.8(19)	63(10)
6971.7(8)	(1)	1.4(4)	11.6(18)	49(8)	7846.8(6)	1	0.95(18)	21(2)	113(12)
6979.3(8)	1	0.6(3)	9.9(18)	42(8)	7877.0(6)	1	0.70(15)	16.8(18)	91(10)
6994.8(5)	1	0.7(2)	10.5(13)	44(6)	7889.6(7)	1	0.70(16)	18(2)	97(11)
7008.5(2)	1	0.68(10)	23.5(18)	100(8)	7900.5(15)	(2)	1.8(9)	7.9(18)	26(6)
7035.1(3)	1	0.66(10)	24.2(19)	104(8)	7927(2)	1	0.3(4)	4.4(15)	24(8)
7050.5(6)	1	0.9(2)	15.0(17)	65(8)	7943.3(8)	1	0.9(3)	9.7(14)	53(8)
7061.5(4)	1	0.82(11)	26(2)	113(9)	7965(2)	(1)		6(3)	33(15)
7073.2(6)	1	0.9(2)	13.4(16)	58(7)	7986(2)	(2)		8(2)	25(8)
7087.0(11)	1	0.6(3)	6.7(13)	29(6)	7995.7(7)	1	0.7(3)	10.9(15)	60(9)
7104.8(13)	(1)	0.6(6)	6.1(15)	27(7)	8011.2(7)	1	0.8(2)	10.8(15)	60(8)
7116.9(4)	1	0.66(16)	22(2)	95(9)	8023.2(5)	1	1.06(18)	20.7(19)	115(11)
7127.7(7)	1	0.9(3)	11.7(16)	52(7)	8033.4(9)	1	0.9(3)	12.6(18)	70(10)
7142.1(2)	1	0.78(8)	33(2)	144(10)	8044.8(18)	(1)	1.1(8)	6.4(17)	36(10)
7156.5(3)	1	0.76(10)	27(2)	120(9)	8054.2(8)	1	0.8(4)	12.1(19)	68(11)
7169.3(5)	1	0.63(13)	17.4(17)	77(8)	8067.6(11)	(1)	0.9(6)	7.2(14)	40(8)
7181.8(3)	1	0.69(9)	31(2)	139(10)	8073(4)	(2)		7(3)	24(11)
7192.0(8)	1	0.6(2)	12.5(18)	56(8)	8080.7(6)	(1)	0.32(19)	12.1(16)	69(9)
7204.3(5)	1	0.92(17)	27(3)	120(12)	8095.9(2)	(1)	1.02(12)	29(2)	163(12)
7258.1(7)	1	0.9(3)	8.2(13)	37(6)	8112.4(8)	1	0.5(2)	8.8(14)	50(8)
7274.1(4)	1	1.1(2)	22(2)	99(10)	8124.1(6)	1	1.1(2)	13.9(15)	80(9)
7295.4(7)	1	0.8(3)	7.6(13)	35(6)	8137.1(10)	1	0.9(3)	13(2)	76(13)
7308.7(9)	(1)	1.0(4)	6.1(12)	28(6)	8158.0(6)	1	1.0(3)	17(2)	96(12)
7327.0(5)	1	1.0(2)	13.1(15)	61(7)	8168.4(4)	1	0.7(2)	26(2)	152(14)
7336.2(2)	1	0.93(11)	28(2)	129(9)	8182.4(4)	1	0.69(12)	18.8(17)	109(10)
7352.7(8)	(1)	1.1(4)	6.4(12)	30(6)	8212.9(10)	(2)	1.7(6)	8.3(15)	29(5)
7375.9(11)	(1)	1.1(5)	6.4(14)	30(7)	8244.2(10)	1	0.8(3)	12(2)	72(12)
7387.1(8)	1	0.7(2)	9.7(15)	46(7)	8255.1(11)	(1)	1.2(4)	13(2)	78(12)

Table C.2: Observed transitions in  $^{98}\text{Mo}$  (continued)

$E_\gamma$	$L$	$\frac{I_\gamma(90^\circ)}{I_\gamma(127^\circ)}$	$I_s$	$\frac{\Gamma_0^2}{\Gamma}$	$E_\gamma$	$L$	$\frac{I_\gamma(90^\circ)}{I_\gamma(127^\circ)}$	$I_s$	$\frac{\Gamma_0^2}{\Gamma}$
keV			eVb	meV	keV			eVb	meV
8265.8(19)	(1)	1.2(8)	8(2)	49(14)	8512.7(11)	1	0.9(4)	11(2)	68(13)
8276.6(4)	1	0.78(15)	36(3)	214(18)	8526.9(10)	1	0.6(3)	8.7(15)	55(10)
8289.1(21)	1	0.7(5)	9(3)	53(15)	8537.1(7)	1	1.0(3)	13.2(17)	84(11)
8298.0(13)	(1)	1.2(4)	13(2)	77(14)	8562.4(9)	1	0.6(3)	10.7(17)	68(11)
8309.7(9)	1	1.1(3)	11.6(17)	70(11)	8579.8(15)	(2)		6.6(16)	25(6)
8330.8(9)	(1)	1.4(4)	8.2(14)	50(8)	8589.7(9)	1	0.6(3)	6.7(13)	43(8)
8357.1(11)	(2)	2.7(16)	7.6(15)	28(5)	8601.9(6)	1	0.70(17)	11.9(15)	76(10)
8370.1(5)	1	0.65(12)	21(2)	127(13)	8612.7(5)	1	1.2(4)	21(3)	136(17)
8393(2)	1	0.5(3)	9(3)	56(17)	8619.8(7)	1	0.8(2)	19(3)	120(17)
8429.1(9)	(2)	1.6(5)	8.4(14)	31(5)	8627.4(7)	1	0.58(13)	17.0(19)	110(12)
8444.0(7)	1	1.0(3)	10.6(14)	66(9)	8636.1(5)	1	1.1(2)	14.6(17)	94(11)
8459.2(7)	1	0.8(2)	10.8(14)	67(9)	8649.9(6)	1	1.1(3)	7.3(11)	48(7)
8471.7(4)	1	0.79(12)	21.4(18)	133(12)	8662.3(5)	1	0.75(16)	11.3(12)	73(8)
8491.3(9)	1	1.0(3)	9.4(16)	59(10)	8673.9(10)	1	0.6(3)	5.6(11)	37(8)
8503.5(5)	1	0.99(17)	26(3)	165(16)					

Table C.3: Observed transitions in  $^{100}\text{Mo}$ 

$E_\gamma$	$L$	$\frac{I_\gamma(90^\circ)}{I_\gamma(127^\circ)}$	$I_s$	$\frac{\Gamma_0^2}{\Gamma}$	$E_\gamma$	$L$	$\frac{I_\gamma(90^\circ)}{I_\gamma(127^\circ)}$	$I_s$	$\frac{\Gamma_0^2}{\Gamma}$
keV			eVb	meV	keV			eVb	meV
537.2(1)	(1)		2770(168)	69(4)	1221.2(1)	(1)		86(6)	11.1(8)
696.1(1)	(1)		860(53)	36(2)	1226.4(4)	(1)		23(3)	3.0(4)
741.0(1)	(1)		457(28)	21.8(13)	1254.6(1)	(1)		142(9)	19.4(12)
769.9(1)	(1)		399(25)	20.5(12)	1266.6(13)	(1)		12(5)	1.6(6)
838.0(1)	(1)		256(17)	15.6(10)	1271.7(6)	(1)		32(5)	4.4(6)
928.8(1)	(1)		370(23)	27.6(17)	1277.6(3)	(1)		43(5)	6.1(6)
1000.9(2)	(1)		29(4)	2.5(3)	1285.2(1)	(1)		84(7)	12.0(9)
1004.4(2)	(1)		22(3)	1.9(2)	1294.4(6)	(1)		27(5)	3.9(7)
1042.1(1)	(1)		68(5)	6.4(5)	1299.7(3)	(1)		48(5)	7.1(7)
1047.8(1)	(1)		89(8)	8.4(7)	1306.9(2)	(1)		51(5)	7.6(6)
1051.7(5)	(1)		23(5)	2.2(5)	1317.7(2)	(1)		46(4)	6.9(6)
1064.1(1)	(1)		267(17)	26(2)	1326.6(1)	(1)		63(5)	9.6(7)
1070.8(1)	(1)		200(13)	19.9(12)	1359.4(1)	(1)		85(6)	13.6(9)
1081.1(1)	(1)		75(6)	7.6(6)	1396.1(3)	(1)		12(3)	2.0(4)
1092.4(1)	(1)		153(10)	15.8(10)	1435.5(1)	(1)		32(3)	5.8(5)
1119.1(4)	(1)		22(4)	2.4(4)	1442.8(1)	(1)		130(8)	23.5(15)
1135.0(3)	(1)		13(3)	1.5(3)	1449.0(1)	(1)		37(3)	6.8(6)
1138.7(1)	(1)		29(4)	3.3(3)	1488.0(3)	(1)		11(2)	2.1(4)
1160.2(1)	(1)		36(4)	4.2(4)	1492.1(2)	(1)		16(2)	3.0(4)
1182.1(1)	(1)		49(4)	5.9(5)	1502.7(1)	(1)		75(6)	14.6(10)
1185.5(1)	(1)		41(4)	5.1(4)	1507.8(1)	(1)		27(3)	5.4(6)
1195.8(1)	(1)		27(3)	3.4(4)	1518.6(3)	(1)		19(3)	3.8(5)
1206.2(3)	(1)		30(4)	3.7(5)	1523.9(8)	(1)		8(3)	1.6(5)
1210.8(3)	(1)		45(5)	5.7(5)	1532.4(1)	(1)		61(5)	12.3(9)
1215.6(1)	(1)		66(5)	8.5(6)	1541.7(3)	(1)		25(3)	5.2(6)

Table C.3: Observed transitions in  $^{100}\text{Mo}$  (continued)

$E_\gamma$ keV	$L$	$\frac{I_\gamma(90^\circ)}{I_\gamma(127^\circ)}$	$I_s$ eVb	$\frac{\Gamma_0^2}{\Gamma}$ meV	$E_\gamma$ keV	$L$	$\frac{I_\gamma(90^\circ)}{I_\gamma(127^\circ)}$	$I_s$ eVb	$\frac{\Gamma_0^2}{\Gamma}$ meV
1547.9(3)	(1)		29(3)	5.9(6)	2081.0(1)	(1)		48(4)	18.1(14)
1554.0(1)	(1)		62(5)	13.0(9)	2097.6(1)	(1)		41(3)	15.4(12)
1560.6(2)	(1)		35(3)	7.4(7)	2107.3(5)	(1)		12(2)	4.5(8)
1567.8(1)	(1)		73(5)	15.6(11)	2147.4(3)	(1)		15(2)	6.2(8)
1584.0(1)	(1)		66(5)	14.3(10)	2157.2(1)	(1)		95(6)	38(2)
1599.6(1)	(1)		73(5)	16.3(11)	2166.7(3)	(1)		14(2)	5.9(8)
1607.8(1)	(1)		71(5)	16.0(11)	2182.0(3)	(1)		50(6)	21(3)
1614.4(5)	(1)		23(3)	5.1(7)	2187.2(9)	(1)		16(5)	7(2)
1625.0(1)	(1)		66(5)	15.1(11)	2198.7(2)	(1)		35(3)	14.6(12)
1642.7(1)	(1)		66(5)	15.4(11)	2220.5(1)	(1)		101(7)	43(3)
1654.0(1)	(1)		93(6)	22.1(14)	2234.6(3)	(1)		12.3(19)	5.3(8)
1666.7(1)	(1)		90(6)	21.7(14)	2243.0(1)	(1)		41(3)	17.8(13)
1676.1(1)	(1)		86(6)	21.0(14)	2251.7(1)	(1)		25(2)	10.9(10)
1686.4(2)	(1)		27(3)	6.7(8)	2271.8(1)	(1)		59(4)	26.2(18)
1690.3(3)	(1)		24(3)	5.8(7)	2279.5(6)	(1)		10.3(19)	4.7(8)
1696.4(6)	(1)		8(2)	2.1(5)	2287.9(3)	(1)		18(2)	8.3(9)
1710.9(3)	(1)		36(4)	9.1(9)	2327.5(2)	(1)		38(3)	17.8(14)
1719.9(5)	(1)		23(3)	6.0(8)	2334.3(7)	(1)		10(2)	4.8(10)
1727.2(3)	(1)		30(3)	7.8(8)	2350.6(6)	(1)		12(2)	5.9(10)
1737.2(3)	(1)		11(2)	2.9(5)	2358.6(4)	(1)		16(2)	7.6(10)
1742.1(3)	(1)		13(2)	3.3(5)	2373.0(5)	(1)		25(4)	12.2(19)
1751.1(1)	(1)		64(5)	17.1(12)	2378.5(7)	(1)		20(4)	9.8(18)
1779.8(4)	(1)		27(4)	7.4(10)	2391.0(1)	(1)		49(4)	24.4(19)
1796.6(1)	(1)		48(4)	13.3(11)	2405.4(2)	(1)		23(2)	11.7(12)
1829.1(1)	(1)		62(4)	17.9(12)	2413.2(3)	(1)		19(2)	9.7(11)
1834.3(1)	(1)		28(3)	8.1(7)	2421.5(2)	(1)		30(3)	15.2(13)
1839.4(2)	(1)		18(2)	5.1(6)	2433.7(1)	(1)		64(4)	33(2)
1845.7(3)	(1)		13(2)	3.8(6)	2460.5(2)	(1)		25(3)	13.3(15)
1861.2(1)	(1)		84(6)	25.2(16)	2464.7(3)	(1)		19(3)	10.1(13)
1869(2)	(1)		7(7)	2(2)	2470.7(4)	(1)		16(3)	8.5(13)
1872.0(7)	(1)		20(7)	6(2)	2474.9(5)	(1)		12(2)	6.2(13)
1879.2(4)	(1)		17(2)	5.3(7)	2509.7(3)	(1)		17(2)	9.2(11)
1885.8(1)	(1)		113(7)	35(2)	2515.8(2)	(1)		21(2)	11.3(12)
1892.7(1)	(1)		42(3)	12.9(10)	2529.1(3)	(1)		22(2)	12.0(13)
1898.3(1)	(1)		83(6)	26.0(17)	2534.8(1)	(1)		39(3)	22.0(19)
1917.2(1)	(1)		114(7)	37(2)	2548.8(1)	(1)		24(3)	13.7(17)
1930.6(1)	(1)		80(5)	25.8(17)	2585.7(1)	(1)		40(3)	22.9(17)
1937.7(1)	(1)		40(3)	13.1(10)	2595.3(3)	(1)		20(2)	11.4(12)
1942.8(1)	(1)		53(4)	17.3(12)	2624.3(2)	(1)		19(2)	11.1(12)
1950.9(1)	(1)		115(7)	38(2)	2632.4(3)	(1)		16.6(19)	10.0(11)
1959.4(1)	(1)		45(3)	14.9(11)	2640.3(5)	(1)		11(2)	6.9(12)
1980.4(1)	(1)		38(3)	12.9(10)	2646.0(7)	(1)		9(2)	5.3(12)
1989.8(1)	(1)		76(5)	26.2(17)	2656.1(2)	(1)		14(2)	8.4(13)
2024.2(3)	(1)		16(2)	5.6(8)	2680.1(4)	(1)		23(5)	14(3)
2042.1(1)	(1)		40(3)	14.6(11)	2701.7(3)	(1)		7.6(18)	4.8(11)
2054.9(1)	(1)		32(3)	11.8(10)	2737.7(4)	(1)		7(2)	4.6(14)
2062.9(4)	(1)		16(2)	5.8(8)	2755.4(3)	(1)		4.9(14)	3.3(9)
2075.6(2)	(1)		36(3)	13.4(11)	2862.5(12)	(1)		7(2)	4.8(14)

Table C.3: Observed transitions in  $^{100}\text{Mo}$  (continued)

$E_\gamma$	$L$	$\frac{I_\gamma(90^\circ)}{I_\gamma(127^\circ)}$	$I_s$	$\frac{\Gamma_0^2}{\Gamma}$	$E_\gamma$	$L$	$\frac{I_\gamma(90^\circ)}{I_\gamma(127^\circ)}$	$I_s$	$\frac{\Gamma_0^2}{\Gamma}$
keV			eVb	meV	keV			eVb	meV
2872.1(4)	(1)		22(3)	15.6(18)	3600.3(2)	1	0.57(19)	20.1(19)	23(2)
2883.7(3)	1	0.8(2)	13.0(16)	9.4(11)	3615.5(2)	1	0.67(14)	15.9(15)	18.0(17)
2901.0(1)	(1)	1.22(12)	40(3)	28.9(19)	3627.2(3)	(1)	0.36(12)	13.8(15)	15.8(17)
2905.7(1)	(1)	1.19(12)	36(3)	26.6(18)	3653.2(7)	1	0.6(3)	6.8(14)	7.8(17)
2942.4(5)	(1)		10.8(18)	8.1(13)	3658.7(3)	1	0.8(2)	22(3)	25(3)
2947.1(3)	(1)		15(2)	10.9(15)	3662.8(4)	(1)	1.2(6)	15(3)	17(3)
2962.0(1)	(1)		40(3)	30(2)	3752.9(3)	(2)	2.0(5)	14.9(18)	10.9(13)
2970.6(6)	(1)		10.5(17)	8.0(13)	3759.0(8)	(1)	1.4(8)	4.3(11)	5.2(14)
2979.6(8)	(1)		6.6(16)	5.1(12)	3767.8(5)	(1)	1.4(5)	6.4(11)	7.9(14)
2990.1(3)	(1)		16.7(19)	13.0(14)	3788.2(3)	1	1.1(4)	6.5(10)	8.1(13)
3001.1(4)	(1)		13.8(18)	10.8(14)	3798.0(3)	1	1.1(4)	6.7(10)	8.3(13)
3010.8(7)	(1)		7.4(16)	5.9(13)	3819.5(3)	1	0.9(2)	14.3(15)	18.1(19)
3036.1(4)	(1)		13.6(19)	10.9(15)	3833.5(4)	(2)	1.5(4)	10.5(16)	8.0(12)
3045.2(5)	(1)		11.7(18)	9.4(14)	3848.3(4)	1	0.8(3)	9.8(13)	12.6(17)
3066.2(2)	(1)		14(2)	11.0(18)	3860.6(3)	1	0.7(2)	12.2(14)	15.8(18)
3079.3(3)	(1)		16.2(19)	13.3(16)	3870.2(6)	(1)	1.1(4)	6.7(12)	8.8(16)
3106.3(7)	(1)		7.0(16)	5.8(14)	3887.9(1)	1	0.91(12)	21.2(15)	28(2)
3112.9(5)	(1)		8.0(15)	6.7(12)	3896.6(1)	(1)	0.89(7)	46(3)	61(3)
3117.7(5)	(1)		6.9(14)	5.8(12)	3903.6(7)	1	0.8(4)	5.8(12)	7.7(16)
3124.9(4)	(1)		8.4(14)	7.1(12)	3915.2(4)	1	0.8(2)	10.5(12)	13.9(17)
3140.6(2)	(1)		4.8(11)	4.1(9)	3925.9(1)	(1)	1.12(13)	25.0(17)	34(2)
3175.6(3)	(1)		7.6(14)	6.7(13)	3941.3(4)	1	1.1(3)	11.4(14)	15.4(18)
3182.2(4)	(1)		6.0(13)	5.3(12)	3948.7(7)	1	0.7(4)	6.0(12)	8.2(16)
3194.0(3)	(1)		11(2)	9.7(19)	3963.1(12)	1	0.7(5)	4.9(16)	7(2)
3198.3(4)	(1)		9(2)	7.6(17)	3968.5(5)	(2)	1.6(5)	11.9(17)	9.8(14)
3220.3(8)	1	0.3(3)	7.3(15)	6.6(14)	3997.8(3)	1	1.0(4)	5.6(10)	7.8(14)
3228.8(5)	(1)	1.1(5)	19(3)	17(3)	4007.2(4)	1	0.9(4)	5.1(10)	7.0(14)
3233.1(8)	1	0.2(6)	12(3)	11(3)	4023.6(3)	1	1.0(3)	6.2(10)	8.7(15)
3242.7(1)	1	0.91(12)	32(2)	29(2)	4034.4(8)	1	0.4(5)	3.8(11)	5.3(15)
3290.1(1)	(1)	1.08(12)	32(2)	30(2)	4042.4(10)	(1)	0.7(5)	4.0(13)	5.7(18)
3297.7(3)	(1)	1.4(3)	12.9(14)	12.2(13)	4048.4(4)	1	1.1(3)	10.0(13)	14.2(19)
3311.7(4)	(1)	1.4(4)	10.1(13)	9.6(13)	4053.2(9)	(1)		6.0(14)	9(2)
3376.2(4)	(1)		18(2)	18(2)	4059.0(3)	1	0.86(19)	12.4(13)	17.7(19)
3399.9(4)	(1)		17(2)	17(2)	4066.9(7)	(1)		4.9(11)	7.0(17)
3417.1(11)	(1)		7.0(16)	7.1(17)	4074.0(4)	1	0.4(2)	8.4(11)	12.1(17)
3428.5(6)	(1)		11.6(18)	11.9(18)	4081.5(1)	1	0.78(10)	25.2(17)	37(3)
3445.2(5)	1	0.8(3)	9.9(16)	10.2(16)	4106.1(9)	(1)	0.8(6)	4.0(10)	5.9(16)
3450.6(2)	(1)	1.12(18)	19.6(18)	20.2(18)	4124.9(2)	1	1.00(17)	17.8(15)	26(2)
3483.9(1)	(1)	0.94(7)	55(3)	58(3)	4145.9(3)	(2)	1.5(4)	13.7(17)	12.3(15)
3465.2(3)	1	1.1(2)	17.2(17)	17.9(18)	4152.9(5)	(2)	2.6(15)	15(2)	13(2)
3512.3(3)	(1)	1.5(4)	10.9(13)	11.6(14)	4156.4(3)	1	0.61(13)	26(3)	39(5)
3520.1(5)	1	0.7(4)	6.3(12)	6.8(13)	4177.3(4)	1	0.8(3)	6.2(11)	9.3(17)
3545.1(5)	(1)	1.0(11)	7.8(14)	8.5(15)	4187.8(5)	(1)	1.1(4)	5.3(11)	8.0(17)
3551.2(11)	(2)	1.7(15)	6(2)	3.9(13)	4192.5(2)	1	0.82(17)	12.4(13)	19(2)
3563.5(7)	(1)	1.3(5)	6.7(13)	7.3(14)	4217.5(1)	1	0.91(9)	32(2)	50(3)
3570.7(1)	(1)	0.96(10)	33(2)	36(2)	4232.0(2)	(1)	0.99(12)	22.9(16)	36(2)
3578.1(3)	1	0.59(16)	13.5(14)	15.0(15)	4253.6(4)	(2)	2.6(7)	12.2(16)	11.5(15)
3591.4(5)	1	0.4(2)	8.2(13)	9.2(14)	4260.8(6)	(2)	2.2(7)	9.0(15)	8.5(14)

Table C.3: Observed transitions in  $^{100}\text{Mo}$  (continued)

$E_\gamma$ keV	$L$	$\frac{I_\gamma(90^\circ)}{I_\gamma(127^\circ)}$	$I_s$ eVb	$\frac{\Gamma_0^2}{\Gamma}$ meV	$E_\gamma$ keV	$L$	$\frac{I_\gamma(90^\circ)}{I_\gamma(127^\circ)}$	$I_s$ eVb	$\frac{\Gamma_0^2}{\Gamma}$ meV
4266.5(5)	(1)		5.5(11)	8.7(18)	4911.1(3)	1	0.64(14)	13.3(14)	28(3)
4273.8(12)	(2)		7.4(19)	7.0(18)	4918.4(9)	1	0.8(4)	5.8(12)	12(3)
4300.4(4)	1	1.2(3)	10.5(12)	17(2)	4925.9(6)	1	0.8(2)	9.0(13)	19(3)
4310.1(4)	1	0.9(2)	11.5(13)	19(2)	4932.3(9)	(1)	1.0(5)	5.4(12)	11(3)
4322.1(12)	1	0.5(4)	4.7(13)	8(2)	4944.4(4)	1	1.0(2)	11.3(14)	24(3)
4329.8(2)	1	0.92(13)	21.8(18)	36(3)	4951.1(5)	1	0.4(2)	8.9(13)	19(3)
4339.2(12)	(1)	1.5(9)	3.6(12)	6(2)	4965.7(6)	1	0.9(4)	6.2(11)	13(2)
4353.8(5)	(1)	1.2(4)	6.8(12)	11(2)	4989.5(2)	1	0.6(2)	34(6)	74(13)
4368.1(7)	1	0.5(3)	5.5(11)	9.0(19)	5007.2(2)	1	0.7(3)	21.6(18)	47(4)
4391.0(6)	1	0.3(2)	6.3(12)	11(2)	5034.4(2)	1	0.8(3)	32(5)	69(11)
4402.4(8)	1	0.8(4)	4.7(11)	7.8(19)	5062.8(3)	(2)	1.8(4)	12.3(13)	16.5(18)
4420.1(3)	(1)	1.4(5)	7.6(11)	12.9(19)	5071.1(2)	(1)	1.4(2)	13.9(12)	31(3)
4431.3(4)	1	0.8(4)	7.7(11)	13(2)	5101.2(6)	1	0.7(4)	5.4(10)	12(2)
4462.3(4)	(2)	1.7(5)	8.6(12)	9.0(13)	5109.2(9)	(1)	0.6(6)	3.6(10)	8(2)
4516.7(1)	1	0.77(6)	41(2)	72(4)	5123.7(9)	(1)		6.2(13)	14(3)
4526.0(7)	(1)	1.1(5)	4.8(10)	8.4(19)	5135.9(1)	(1)	1.04(11)	26.5(17)	61(4)
4537.7(8)	(2)	1.7(8)	5.4(13)	5.7(14)	5150.0(12)	1	0.8(5)	5.1(13)	12(3)
4544.2(3)	1	0.64(14)	14.3(13)	26(3)	5158.2(3)	1	0.71(12)	17.7(16)	41(4)
4559.4(3)	1	1.1(2)	15.5(16)	28(3)	5169.5(3)	1	0.65(14)	13.8(13)	32(3)
4565.4(1)	1	0.71(6)	50(3)	89(5)	5181.7(3)	1	0.68(11)	19.6(16)	46(4)
4576.9(4)	1	1.0(3)	10.9(14)	20(3)	5190.3(5)	1	0.70(18)	11.8(13)	28(3)
4583.0(1)	1	0.72(6)	51(3)	93(5)	5204.5(4)	(1)	0.31(16)	11.1(13)	26(3)
4594.8(1)	1	0.73(8)	36(3)	67(5)	5215.9(8)	(1)		7.0(13)	17(3)
4600.5(16)	(1)	0.7(7)	3.7(16)	7(3)	5229.6(9)	1	0.4(3)	5.3(11)	13(3)
4622.7(6)	1	1.1(4)	7.6(12)	14(2)	5241.2(6)	1	0.5(2)	7.7(12)	18(3)
4631.0(4)	(2)	1.5(3)	13.0(15)	14.5(17)	5264.2(6)	1	0.7(3)	9.2(14)	22(3)
4645.3(9)	(1)	1.0(9)	9(2)	17(4)	5271.1(6)	1	0.7(3)	9.4(14)	23(3)
4650.8(14)	(1)	0.8(13)	7(2)	12(4)	5277.5(3)	1	1.0(2)	14.4(14)	35(4)
4672.9(11)	1	0.5(4)	4.6(12)	9(2)	5289.0(6)	1	1.0(4)	5.8(10)	14(3)
4680.9(6)	(1)	1.4(3)	10.1(13)	19(3)	5310.3(4)	1	0.65(16)	13.1(13)	32(3)
4688.9(1)	1	0.86(9)	34(2)	64(4)	5324.0(3)	1	0.73(15)	15.3(14)	38(4)
4713.7(7)	(1)	1.0(5)	5.8(11)	11(2)	5335.5(2)	1	0.67(9)	23.4(17)	58(4)
4724.3(9)	(1)	1.1(5)	7.4(18)	14(4)	5347.7(1)	1	0.87(8)	34(2)	84(5)
4730.2(2)	1	0.89(12)	31(2)	60(5)	5359.6(3)	1	0.60(12)	17.6(15)	44(4)
4743.3(5)	(1)	1.3(4)	8.6(13)	17(3)	5369.4(6)	1	0.5(2)	9.6(13)	24(3)
4750.0(4)	1	1.0(2)	12.0(14)	24(3)	5382.3(10)	1	0.5(4)	7.5(16)	19(4)
4767.0(2)	1	1.03(16)	17.7(15)	35(3)	5390.1(6)	1	1.1(3)	13.2(16)	33(4)
4781.5(8)	(1)		4.9(12)	10(2)	5402.1(1)	1	0.75(8)	37(2)	94(6)
4789.3(4)	(1)		8.6(13)	17(3)	5412.4(8)	1	0.4(3)	7.0(13)	18(3)
4800.1(4)	1	0.8(2)	10.9(14)	22(3)	5435.3(6)	1	0.9(3)	9.0(13)	23(3)
4805.9(3)	1	0.65(13)	18.8(16)	38(3)	5442.7(6)	1	1.0(3)	11.8(15)	30(4)
4812.7(2)	1	0.94(17)	15.9(14)	32(3)	5449.4(6)	(1)	1.3(4)	8.5(14)	22(4)
4822.7(5)	1	0.9(4)	6.7(11)	14(2)	5467.0(3)	1	0.86(18)	12.8(13)	33(4)
4830.4(6)	(1)	1.0(4)	5.6(11)	11(2)	5502.5(4)	1	1.0(2)	12.3(13)	32(4)
4844.1(7)	1	0.8(3)	7.5(12)	15(3)	5510.3(13)	(2)	2.0(11)	5.6(14)	9(2)
4853.8(5)	1	0.8(2)	9.6(13)	20(3)	5519.2(4)	1	0.76(13)	16.7(15)	44(4)
4865.9(3)	(1)	1.22(19)	15.8(14)	33(3)	5532.0(5)	1	0.81(17)	12.8(13)	34(4)
4878.1(3)	1	0.79(13)	17.5(15)	36(3)	5547.7(3)	1	0.85(13)	18.8(15)	50(4)

Table C.3: Observed transitions in  $^{100}\text{Mo}$  (continued)

$E_\gamma$	$L$	$\frac{I_\gamma(90^\circ)}{I_\gamma(127^\circ)}$	$I_s$	$\frac{\Gamma_0^2}{\Gamma}$	$E_\gamma$	$L$	$\frac{I_\gamma(90^\circ)}{I_\gamma(127^\circ)}$	$I_s$	$\frac{\Gamma_0^2}{\Gamma}$
keV			eVb	meV	keV			eVb	meV
5554.2(11)	1	0.4(3)	5.6(13)	15(4)	6270.3(8)	1	0.7(3)	6.8(13)	23(4)
5584.7(4)	1	1.1(3)	10.4(12)	28(3)	6278.5(1)	1	0.79(7)	33(2)	114(7)
5596.6(7)	1	1.1(3)	7.8(13)	21(4)	6292.9(4)	1	0.77(17)	11.5(12)	40(4)
5604.5(12)	1	0.5(3)	6.1(13)	17(4)	6310.1(15)	(1)	0.9(6)	4.7(13)	16(5)
5612.5(1)	1	1.0(4)	15(3)	41(7)	6321.0(9)	1	0.8(3)	18(3)	64(12)
5618.4(3)	1	0.84(18)	29(3)	80(9)	6327.4(9)	1	1.1(3)	20(3)	70(12)
5656.3(5)	(2)	1.9(6)	8.2(12)	14(2)	6337.3(4)	1	0.9(2)	20.1(19)	70(7)
5670.5(1)	1	0.75(9)	25.3(18)	71(5)	6354.1(2)	1	0.82(10)	27(2)	96(7)
5680.7(7)	(1)	1.5(6)	8.7(17)	24(5)	6365.4(19)	(1)	0.8(6)	4.7(15)	17(5)
5686.3(5)	1	0.62(12)	18.2(18)	51(5)	6375.4(5)	1	1.05(19)	16.1(16)	57(6)
5715.7(3)	1	0.89(18)	12.0(12)	34(4)	6401.8(8)	1	0.8(4)	5.6(11)	20(4)
5725.1(3)	1	0.82(14)	15.3(14)	44(4)	6414.1(4)	1	0.46(15)	19(2)	68(8)
5732.7(3)	1	0.82(13)	17.6(15)	50(4)	6421.2(6)	1	0.70(19)	19(2)	68(7)
5742.4(7)	1	0.9(4)	5.9(11)	17(3)	6426.4(9)	(1)	1.2(5)	10.7(18)	38(7)
5754.9(12)	1	0.3(5)	3.8(11)	11(3)	6433.9(5)	1	1.1(3)	10.1(14)	36(5)
5763.8(15)	(1)	0.3(11)	4.9(17)	14(5)	6458.8(6)	1	1.1(3)	9.9(13)	36(5)
5770.2(4)	1	0.5(4)	15(2)	43(6)	6473.3(6)	1	0.49(14)	16(2)	58(7)
5784.5(10)	1	0.5(5)	3.7(11)	11(3)	6483(2)	(1)	1.1(7)	5.3(17)	19(6)
5798.0(3)	1	0.82(17)	12.6(12)	37(4)	6497.4(6)	1	0.9(2)	10.6(14)	39(5)
5808.8(1)	1	0.78(7)	34(2)	99(6)	6518.9(5)	1	0.75(17)	14.4(17)	53(7)
5819.5(15)	(1)		5.4(17)	16(5)	6526.4(3)	1	1.01(14)	26(2)	96(8)
5826.3(6)	(2)	1.5(5)	8.5(14)	15(3)	6537.3(12)	(1)	0.8(5)	4.4(11)	16(4)
5840.5(6)	1	0.92(28)	9.9(14)	29(4)	6556.6(8)	(1)	1.4(5)	5.4(11)	20(4)
5858.7(5)	1	0.52(18)	11.1(13)	33(4)	6570.0(4)	1	1.0(2)	11.1(12)	42(5)
5879.2(2)	1	0.89(19)	22.8(18)	68(6)	6596.8(4)	(2)	1.8(4)	11.9(14)	27(3)
5900.8(6)	1	0.8(3)	8.1(12)	25(4)	6612.3(17)	(1)		3.4(12)	13(5)
5913.5(10)	(1)	1.3(6)	5.7(12)	17(4)	6622.1(4)	(1)	0.47(12)	17.1(17)	65(7)
5920.9(8)	1	0.6(3)	6.9(12)	21(4)	6628.1(5)	(2)	1.7(4)	16.1(18)	37(4)
5947.6(2)	1	0.92(11)	20.9(15)	64(5)	6640.8(3)	1	0.93(16)	15.1(14)	58(6)
5957.0(6)	1	0.8(3)	9.2(15)	28(5)	6658.0(4)	1	0.80(13)	21.9(19)	84(7)
5963.8(6)	1	0.9(3)	9.3(15)	29(5)	6668.9(2)	1	0.70(6)	47(3)	180(11)
5972.8(2)	1	0.77(13)	15.6(13)	49(4)	6685.1(4)	1	0.93(13)	20.7(16)	80(7)
5988.7(4)	1	1.1(2)	11.4(13)	36(4)	6699.1(11)	1	0.9(3)	7.7(13)	30(5)
6009.4(4)	1	0.88(19)	26(3)	82(9)	6763.9(8)	1	0.9(4)	12(2)	46(8)
6019.3(11)	(1)	1.2(5)	8.2(17)	26(6)	6772.5(8)	1	0.9(3)	14(2)	57(8)
6035.3(8)	1	1.0(3)	7.3(12)	23(4)	6790.4(10)	1	0.9(3)	20(3)	81(13)
6061.1(9)	(2)	4(3)	6.9(17)	13(3)	6797.3(9)	(1)	1.3(10)	17(3)	67(14)
6065.7(7)	1	0.9(3)	13.4(19)	43(6)	6807.7(10)	(2)	2.5(22)	5.9(14)	14(3)
6071.9(12)	1	0.5(5)	7(2)	23(7)	6829.2(3)	(1)	1.07(14)	25.4(19)	103(8)
6082.7(3)	1	0.90(15)	21(2)	67(7)	6844.3(11)	(2)	1.6(6)	12(2)	28(5)
6089.1(4)	1	0.65(13)	18.5(19)	60(6)	6851.0(15)	1	0.6(4)	7(2)	30(9)
6122.3(5)	1	0.58(17)	11.4(13)	37(5)	6869.7(8)	(1)	1.4(6)	4.8(11)	20(5)
6133.4(7)	1	0.43(18)	9.2(13)	30(4)	6886.2(8)	1	0.9(4)	6.3(12)	26(5)
6146.9(9)	1	0.7(3)	5.8(12)	19(4)	6892.9(4)	1	0.56(15)	12.4(14)	51(6)
6173.8(5)	1	0.71(19)	10.3(13)	34(4)	6905.8(6)	1	0.7(2)	9.3(14)	39(6)
6194.3(1)	(1)	0.58(5)	37(2)	124(8)	6912.6(11)	(1)	1.0(8)	12(3)	50(11)
6249.2(5)	1	0.69(18)	11.2(13)	38(5)	6919.2(13)	1	0.6(3)	13(3)	55(12)
6257.4(2)	1	0.84(9)	27.7(19)	94(7)	6924.6(10)	(1)	1.4(10)	11(3)	48(13)



Table C.3: Observed transitions in  $^{100}\text{Mo}$  (continued)

$E_\gamma$ keV	$L$	$\frac{I_\gamma(90^\circ)}{I_\gamma(127^\circ)}$	$I_s$ eVb	$\frac{\Gamma_0^2}{\Gamma}$ meV	$E_\gamma$ keV	$L$	$\frac{I_\gamma(90^\circ)}{I_\gamma(127^\circ)}$	$I_s$ eVb	$\frac{\Gamma_0^2}{\Gamma}$ meV
6933.9(12)	(1)		6.1(16)	26(7)	7525.8(6)	1	0.9(2)	13.6(15)	66(8)
6949.6(11)	1	0.6(4)	5.8(16)	24(7)	7546(2)	1	0.8(5)	4.9(15)	24(8)
6957.4(11)	(2)	1.7(9)	6.3(14)	16(4)	7558.8(15)	(1)	1.1(6)	6.2(15)	31(8)
6973.9(8)	1	0.7(4)	8.7(19)	37(8)	7576.9(9)	1	0.8(3)	8.8(14)	44(7)
6980.8(12)	(2)	2.2(13)	8(2)	20(5)	7606.6(4)	1	0.56(10)	18.0(16)	91(8)
6994.2(5)	(2)	1.7(4)	17(2)	43(5)	7744.2(8)	1	0.8(2)	11.3(14)	59(8)
7000.9(5)	1	0.5(3)	11.2(15)	48(7)	7758.1(10)	(1)	1.4(4)	8.9(14)	46(7)
7018.0(6)	1	0.9(3)	8.2(12)	35(5)	7771.2(12)	1	0.9(4)	7.0(13)	37(7)
7031.8(5)	1	0.6(3)	10.6(16)	45(7)	7796.6(14)	1	0.6(4)	4.9(12)	26(6)
7037.5(10)	(1)	1.0(6)	5.2(14)	23(6)	7830.9(8)	1	0.7(2)	8.3(12)	44(7)
7059.9(11)	1	0.6(4)	3.6(10)	15(5)	7862.8(7)	(1)	0.44(13)	12.0(15)	64(8)
7067.8(3)	1	0.88(19)	11.7(13)	51(6)	7875.1(6)	1	0.56(12)	19.9(19)	107(10)
7095.1(5)	1	0.6(3)	6.6(11)	29(5)	7886.9(10)	1	0.8(2)	12.4(16)	67(9)
7103.2(7)	(1)	1.1(4)	5.1(10)	22(5)	7935.4(10)	1	0.7(3)	7.0(11)	38(6)
7115.0(3)	1	0.8(2)	9.9(12)	44(5)	7955.4(6)	1	0.66(16)	11.1(13)	61(7)
7136.3(5)	1	0.8(3)	6.4(11)	28(5)	7987.7(7)	1	0.65(16)	12.0(13)	66(8)
7171.4(7)	(1)	1.4(5)	7.1(12)	32(6)	8001.7(6)	1	0.51(13)	11.9(13)	66(8)
7181.2(9)	(1)	1.0(5)	5.4(12)	24(5)	8033.2(8)	1	0.61(16)	10.2(13)	57(8)
7194.1(3)	1	0.97(19)	15.3(15)	69(7)	8051.9(6)	1	0.67(13)	17.0(18)	96(10)
7203.7(7)	1	0.5(3)	7.3(12)	33(6)	8063.4(9)	1	0.8(2)	11.6(16)	65(10)
7219.1(9)	(2)	1.5(7)	10(2)	28(6)	8082.9(16)	1	0.5(2)	6.7(14)	38(8)
7225.1(13)	(1)	0.7(8)	5.0(15)	23(7)	8095.5(11)	1	0.55(18)	12(2)	68(11)
7299.3(5)	1	0.56(17)	10.2(13)	47(6)	8107.7(12)	1	0.6(3)	8.7(18)	50(11)
7312.0(3)	1	0.67(10)	19.3(15)	90(7)	8127.3(10)	1	0.7(2)	7.7(12)	44(7)
7330.5(3)	1	0.58(11)	15.6(14)	73(7)	8194.0(9)	1	0.9(3)	9.2(13)	53(8)
7357.4(6)	1	0.70(19)	10.9(14)	51(7)	8208.4(6)	1	0.80(13)	19.6(18)	115(11)
7380.0(7)	(1)	1.3(4)	9.0(13)	43(6)	8217.8(6)	(1)	0.48(10)	17.0(18)	100(11)
7403.0(8)	1	0.7(2)	9.3(13)	44(7)	8238.2(9)	1	0.58(19)	7.6(11)	45(7)
7450.3(10)	1	0.6(2)	7.8(14)	38(7)	8256.7(14)	1	0.7(3)	6.0(13)	36(8)
7470.7(4)	1	1.01(17)	17.3(16)	84(8)	8269.2(6)	1	0.91(17)	15.9(16)	95(10)
7486.9(7)	1	0.47(17)	26(4)	125(17)	8283.2(6)	1	0.84(16)	17.1(17)	102(11)
7494.5(11)	(1)	1.3(3)	20(3)	98(14)	8294.1(13)	(1)	1.2(7)	6.9(16)	41(10)
7503.2(12)	(2)	1.9(8)	11(2)	31(7)					



## Appendix D

# Photoabsorption cross sections up to the $(\gamma, n)$ threshold

Photoabsorption cross sections  $\sigma_\gamma$  up to the neutron-separation energy in  $^{92}\text{Mo}$ ,  $^{98}\text{Mo}$  and  $^{100}\text{Mo}$  obtained from the analysis described in Subsection 5.2.2 of the photon-scattering experiments at  $E_e = 13.2$  MeV.

$E_x$ MeV	$\sigma_\gamma(^{92}\text{Mo})$ mb	$\sigma_\gamma(^{98}\text{Mo})$ mb	$\sigma_\gamma(^{100}\text{Mo})$ mb	$E_x$ MeV	$\sigma_\gamma(^{92}\text{Mo})$ mb	$\sigma_\gamma(^{98}\text{Mo})$ mb	$\sigma_\gamma(^{100}\text{Mo})$ mb
4.1			1.7(10)	8.7	8(9)		
4.3		1.6(10)	1.8(9)	8.9	10(10)		
4.5		0.9(10)	2.1(9)	9.1	9(9)		
4.7		0.5(11)	1.9(9)	9.3	15(8)		
4.9		1.7(13)	2.4(10)	9.5	17(8)		
5.1		1.8(13)	2.4(10)	9.7	13(7)		
5.3		1.6(13)	2.5(10)	9.9	20(7)		
5.5		2.5(15)	2.6(11)	10.1	15(6)		
5.7		3.9(16)	3.3(12)	10.3	14(6)		
5.9		3.3(16)	3.2(12)	10.5	15(5)		
6.1	2(3)	4.6(18)	3.9(13)	10.7	15(6)		
6.3	1(3)	4.7(18)	4.2(14)	10.9	11(5)		
6.5	1(3)	5.9(19)	3.7(14)	11.1	15(5)		
6.7	1(5)	3.7(18)	4.1(15)	11.3	18(5)		
6.9	2(5)	5(2)	5.2(17)	11.5	19(5)		
7.1		6(2)	5.1(17)	11.7	18(6)		
7.3		6(2)	5.6(17)	11.9	15(5)		
7.5	2(6)	5(2)	6.7(15)	12.1	18(6)		
7.7	3(7)	7(2)	5.5(12)	12.3	18(6)		
7.9	2(8)	6(2)	6.0(11)	12.5	16(7)		
8.1	7(8)	8(2)	6.5(11)				
8.3	6(9)	9.3(18)					
8.5	2(9)	9.7(11)					

Branching ratios  $B_0$  for transitions to the ground state result from  $\gamma$ -ray simulations for  $^{92}\text{Mo}$ ,  $^{98}\text{Mo}$  and  $^{100}\text{Mo}$  up to the neutron-separation energy.

$E_x$ MeV	$B_0(^{92}\text{Mo})$ %	$B_0(^{98}\text{Mo})$ %	$B_0(^{100}\text{Mo})$ %	$E_x$ MeV	$B_0(^{92}\text{Mo})$ %	$B_0(^{98}\text{Mo})$ %	$B_0(^{100}\text{Mo})$ %
4.05	66(28)	70(23)	78(19)	8.45	35(8)	21(2)	
4.15	72(27)	74(19)	78(17)	8.55	35(8)	19.6(19)	
4.25	67(29)	75(20)	78(15)	8.65	34(8)	19(2)	
4.35	67(26)	72(17)	78(15)	8.75	35(5)		
4.45	64(26)	74(16)	77(16)	8.85	33(5)		
4.55	68(24)	74(16)	76(14)	8.95	33(5)		
4.65	68(24)	73(13)	76(13)	9.05	33(5)		
4.75	65(25)	74(13)	76(11)	9.15	32(5)		
4.85	68(23)	71(13)	74(12)	9.25	31(4)		
4.95	66(23)	72(11)	73(11)	9.35	32(4)		
5.05	65(23)	71(11)	72(11)	9.45	32(4)		
5.15	66(20)	69(10)	71(10)	9.55	31(4)		
5.25	66(23)	69(11)	69(9)	9.65	31(4)		
5.35	64(19)	67(11)	68(10)	9.75	30(4)		
5.45	62(19)	66(10)	67(9)	9.85	30(4)		
5.55	68(18)	65(10)	64(9)	9.95	30(3)		
5.65	61(19)	63(9)	62(8)	10.05	29(3)		
5.75	63(19)	62(9)	62(9)	10.15	29(3)		
5.85	61(16)	60(8)	59(8)	10.25	28(3)		
5.95	62(16)	58(8)	59(7)	10.35	27(3)		
6.05	62(16)	57(8)	57(7)	10.45	26(3)		
6.15	60(16)	54(7)	55(6)	10.55	25(3)		
6.25	60(14)	54(7)	53(7)	10.65	24(3)		
6.35	59(14)	53(6)	51(6)	10.75	23(2)		
6.45	58(15)	51(6)	48(6)	10.85	22(2)		
6.55	57(12)	48(6)	46(6)	10.95	21(2)		
6.65	53(13)	46(6)	45(6)	11.05	20(2)		
6.75	52(13)	44(5)	42(5)	11.15	19.4(18)		
6.85	53(13)	42(5)	41(5)	11.25	18.2(19)		
6.95	52(13)	41(5)	38(5)	11.35	17.3(18)		
7.05	51(11)	39(4)	37(4)	11.45	16.4(18)		
7.15	50(11)	37(5)	35(4)	11.55	15.3(15)		
7.25	48(10)	36(4)	33(4)	11.65	14.5(13)		
7.35	47(10)	34(4)	31(3)	11.75	14.0(14)		
7.45	47(11)	32(4)	30(3)	11.85	13.2(14)		
7.55	44(10)	31(3)	28(3)	11.95	12.2(12)		
7.65	43(10)	29(3)	26(3)	12.05	12.1(12)		
7.75	43(9)	28(3)	25(2)	12.15	11.2(9)		
7.85	41(9)	27(3)	24(2)	12.25	10.4(9)		
7.95	40(8)	26(3)	22(2)	12.35	10.3(9)		
8.05	39(8)	24(2)	21(2)	12.45	9.5(10)		
8.15	38(8)	23.1(19)	20(17)	12.55	8.8(8)		
8.25	37(8)	22(2)	18.8(18)	12.65	8.9(8)		
8.35	36(7)	21(2)					

# Bibliography

- [Adri05] P. Adrich, A. Klimkiewicz, M. Fallot, K. Boretzky, T. Aumann, D. Cortina-Gil, U. Datta Pramanik, Th.W. Elze, H. Emling, H. Geissel, M. Hellström, K.L. Jones, J.V. Kratz, R. Kulesa, Y. Leifels, C. Nociforo, R. Palit, H. Simon, G. Surówka, K. Sümmerer, and W. Waluś. Evidence for Pygmy and Giant Dipole Resonances in  $^{130}\text{Sn}$  and  $^{132}\text{Sn}$ . *Phys. Rev. Lett.* *95*, page 132501, 2005.
- [Ajze90] F. Ajzenberg-Selove. Energy levels of light nuclei  $A=11-12$ . *Nucl. Phys. A506*, page 1, 1990.
- [AlBe89] A.A. Al-Beteri and D.E. Raeside. An improved electron bremsstrahlung cross-section formula for Monte Carlo transport simulations. *Nucl. Instr. Meth. B 44*, page 149, 1989.
- [AlQu03] S.I. Al-Quraishi, S.M. Grimes, T.N. Massey, and D.A. Resler. Level densities for  $20 \leq A \leq 110$ . *Phys. Rev. C 67*, page 015803, 2003.
- [Alag55] G. Alaga, K. Alder, A. Bohr, and B.R. Mottelson. Intensity rules for beta and gamma transitions to nuclear rotational states. *Dan. Mat. Fys. Medd.* *29*, page 3, 1955.
- [Alar87] R. Alarcon, R.M. Laszewski, A.M. Nathan, and S.D. Hoblit. Photon scattering from  $^{90}\text{Zr}$  below neutron emission threshold. *Phys. Rev. C 36*, page 954, 1987.
- [Andr00] A.N. Andreyev, M. Huyse, P. Van Duppen, L. Weissman, D. Ackermann, J. Gerl, F.P. Hessberger, S. Hofmann, A. Kleinböhl, G. Münzenberg, H. Schlegel, H. Schaffner, P. Caggarda, M. Matos, S. Saro, A. Keenan, C. Moore, C.D. O’Leary, R.D. Page, M. Taylor, H. Kettunen, M. Leino, A. Lavrentiev, R. Wyss, and K. Heyde. A triplet of differently shaped spin-zero states in the atomic nucleus  $^{186}\text{Pb}$ . *Nature 405*, page 430, 2000.
- [Axel62] P. Axel. Electric Dipole Ground-State Transition Width Strength Function and 7-Mev Photon Interactions. *Phys. Rev.* *126*, page 671, 1962.
- [Bagl00] C.M. Baglin. Nuclear Data Sheets for  $A = 92$ . *Nucl. Data Sheets 91*, page 423, 2000.
- [Bart00] R. Barth, D. Yifei, H.G. Essel, R. Fritzsche, H. Göringer, J. Hoffmann, F. Humbert, N. Kurz, R.S. Mayer, W. Ott, and D. Schall. GSI Multi-Branch System. *Gesellschaft für Schwerionenforschung mbH, Darmstadt*, 2000.
- [Bart72] G.A. Bartholomew, E.D. Earle, A.J. Ferguson, J.W. Knowles, and M.A. Lone. Gamma-Ray Strength Functions. *Adv. Nucl. Phys.* *7*, page 229, 1972.
- [Bauw00] F. Bauwens. *Dipoleexcitaties naar gebonden toestanden in  $^{56}\text{Fe}$ ,  $^{58}\text{Ni}$  en  $^{92}\text{Mo}$* . University of Gent, Belgium, unpublished, 2000.
- [Beil74] H. Beil, R. Bergère, P. Carlos, Leprêtre, A. De Miniac, and A. Veyssière. A study of the photoneutron contribution to the giant dipole resonance in doubly even Mo isotopes. *Nucl. Phys. A 227*, page 427, 1974.

- [Berg87] U.E.P. Berg and U. Kneissl. Recent progress on nuclear magnetic dipole excitations. *Annu. Rev. Nucl. Part. Sci.* 37, page 33, 1987.
- [Beth50] H.A. Bethe and C. Longmire. The Effective Range of Nuclear Forces II. Photo-Disintegration of the Deuteron. *Phys. Rev.* 77, page 647, 1950.
- [Beth37] H.A. Bethe and G. Placzek. Resonance Effects in Nuclear Processes. *Phys. Rev.* 51, page 450, 1937.
- [Becv98] F. Bečvář. Simulations of  $\gamma$  cascades in complex nuclei with emphasis on assessment of uncertainties of cascade-related quantities. *Nucl. Instr. Meth. A* 417, page 434, 1998.
- [Bevi03] P.R. Bevington and D.K. Robinson. *Data Reduction and Error Analysis for the Physical Sciences*. McGraw-Hill, New York, 2003.
- [Blom85] J. Blomqvist and L. Rydström. Shell Model Description of the  $N = 50$  Isotones Between  $^{88}\text{Sr}$  and  $^{100}\text{Sn}$ . *Phys. Scr.* 31, page 31, 1985.
- [Bohl84] D. Bohle, A. Richter, W. Steffen, A.E.L. Dieperink, N. Lo Iudice, F. Palumbo, and O. Scholten. New magnetic dipole excitation mode studied in the heavy deformed nucleus  $^{156}\text{Gd}$  by inelastic electron scattering. *Phys. Lett. B* 137, page 27, 1984.
- [Bohr75] A. Bohr and B.R. Mottelson. *Nuclear Structure*. W.A. Benjamin, Massachusetts, 1975.
- [Carl74] P. Carlos, R. Bergère, Beil. H., Leprêtre, and A. Veyssièrè. A semi-phenomenological description of the Giant Dipole Resonance width. *Nucl. Phys. A* 219, page 61, 1974.
- [Chei70] E. Cheifetz, R.C. Jared, S.G. Thompson, and J.B. Wilhelmy. Experimental Information Concerning Deformation of Neutron Rich Nuclei in the  $A \sim 100$  Region. *Phys. Rev. Lett.* 25, page 38, 1970.
- [Doen05a] F. Dönau. An RPA Code for Deformed Nuclei. *Wissenschaftlich-Technische Berichte FZR-423*, page 10, 2005.
- [Doen05] F. Dönau. Suppression of Modes in the Random Phase Approximation. *Phys. Rev. Lett.* 94, page 092503, 2005.
- [Esse02] H.G. Essel. GSI Lean Analysis. *Gesellschaft für Schwerionenforschung mbH, Darmstadt*, 2002.
- [Faes90] A. Faessler and R. Nojarov. Orbital rotational vibrations in the  $A = 130$  mass region. *Phys. Rev. C* 41, page 1243, 1990.
- [Fagg59] L.W. Fagg and S.S. Hanna. Polarization Measurements on Nuclear Gamma Rays. *Rev. Mod. Phys.* 31, page 711, 1959.
- [Fede78] P. Federman and S. Pittel. Hartree-Fock-Bogolyubov study of deformation in the Zr – Mo region. *Phys. Lett. B* 77, page 29, 1978.
- [Fede79] P. Federman and S. Pittel. Unified shell-model description of nuclear deformation. *Phys. Rev. C* 20, page 820, 1979.
- [Fran03] C. Fransen, N. Pietralla, Z. Ammar, D. Bandyopadhyay, N. Boukharouba, P. von Brentano, A. Dewald, J. Gableske, A. Gade, J. Jolie, U. Kneissl, S.R. Leshner, A.F. Lisetskiy, M.T. McEllistrem, M. Merrick, H.H. Pitz, N. Warr, V. Werner, and S.W. Yates. Comprehensive studies of low-spin collective excitations in  $^{94}\text{Mo}$ . *Phys. Rev. C* 67, page 024307, 2003.

- [Fran04] C. Fransen, N. Pietralla, A.P. Tonchev, M.W. Ahmed, J. Chen, G. Feldman, U. Kneissl, J. Li, V.N. Litvinenko, B. Perdue, I.V. Pinayev, H.H. Pitz, R. Prior, K. Sabourov, M. Spraker, W. Tornow, H.R. Weller, V. Werner, Y.K. Wu, and S.W. Yates. Parity assignments to strong dipole excitations of  $^{92}\text{Zr}$  and  $^{96}\text{Mo}$ . *Phys. Rev. C* **70**, page 044317, 2004.
- [Frau93] S. Frauendorf. Tilted cranking. *Nucl. Phys. A* **557**, page 259, 1993.
- [Frau00] S. Frauendorf. Description of multi-quasiparticle bands by the tilted axis cranking model. *Nucl. Phys. A* **677**, page 115, 2000.
- [Gabr00] F. Gabriel, P. Gippner, E. Grosse, D. Janssen, P. Michel, H. Prade, A. Schamlott, W. Seidel, A. Wolf, R. Wünsch, and ELBE-crew. The Rossendorf radiation source ELBE and its FEL project. *Nucl. Inst. Meth. B* **161**, page 1143, 2000.
- [Gade03] A. Gade, D. Belic, P. von Brentano, C. Fransen, H. von Garrel, J. Jolie, U. Kneissl, C. Kohstall, A. Linnemann, H.H. Pitz, M. Scheck, F. Stedile, and V. Werner. Dipole excitations in  $^{108}\text{Cd}$ . *Phys. Rev. C* **67**, page 034304, 2003.
- [Gori98] S. Goriely. Radiative neutron captures by neutron-rich nuclei and the r-process nucleosynthesis. *Phys. Lett. B* **436**, page 10, 1998.
- [Gori02] S. Goriely and E. Khan. Large-scale QRPA calculations of E1-strength and its impact on the neutron capture cross section. *Nucl. Phys. A* **706**, page 217, 2002.
- [Gova94] K. Govaert, W. Mondelaers, E. Jacobs, D. De Frene, K. Persyn, S. Pommé, M.-L. Yoneama, S. Lindenstruth, K. Huber, A. Jung, B. Starck, R. Stock, C. Wesselborg, R.-D. Heil, U. Kneissl, and H.H. Pitz. Polarized bremsstrahlung nuclear resonance fluorescence set-up at the 15 MeV linac in Gent. *Nucl. Instr. Meth. A* **337**, page 265, 1994.
- [Gros76] R. Gross and A. Frenkel. Effective interaction of protons and neutrons in the  $2p_{\frac{1}{2}}-1g_{\frac{9}{2}}$  subshells. *Nucl. Phys. A* **267**, page 85, 1976.
- [Hage68] R.S. Hager and E.C. Seltzer. Particle Parameters. *Nucl. Data. A* **4**, page 1, 1968.
- [Hama84] I. Hamamoto and S. Åberg. Microscopic description of a low-lying  $K^\pi = 1^+$  mode in  $^{156}\text{Gd}$ . *Phys. Lett. B* **145**, page 163, 1984.
- [Hami75] W.D. Hamilton, editor. *The Electromagnetic Interaction in Nuclear Spectroscopy*. North-holland publishing company, 1975.
- [Hart04] T. Hartmann, M. Babilon, S. Kamerdzhiev, E. Litvinova, D. Savran, S. Volz, and A. Zilges. Microscopic Nature of the Pygmy Dipole Resonance: The Stable Ca Isotopes. *Phys. Rev. Lett.* **93**, page 192501, 2004.
- [Heit84] Walter Heitler. *The quantum theory of radiation*. Dover Publications, 1984.
- [Heyd87] K. Heyde, J. Jolie, J. Moreau, J. Ryckebusch, M. Waroquier, P. Van Duppen, M. Huyse, and J.L. Wood. A shell-model description of  $0^+$  states in even-even nuclei. *Nucl. Phys. A* **466**, page 189, 1987.
- [RIPL-2] <http://www-nds.iaea/RIPL-2/>.
- [Jenk01] D.G. Jenkins, D.G. Chiara, and V.I. Dimitrov. TAC Manual. *unpublished*, 2001.
- [Jenk95] R. Jenkins, R.W. Gould, and D. Gedcke. *Quantitative x-ray spectrometry*. Dekker, New York, 1995.

- [Ji88] X. Ji and B.H. Wildenthal. Effective interaction for  $N = 50$  isotones. *Phys. Rev. C* 37, page 1256, 1988.
- [Jung95] A. Jung, S. Lindenstruth, H. Schacht, B. Starck, R. Stock, C. Wesselborg, R.D. Heil, U. Kneissl, J. Margraf, H.H. Pitz, and F. Steiper. Electric and magnetic dipole excitations to bound states in  $^{70,72,74,76}\text{Ge}$ . *Nucl. Phys. A* 584, page 103, 1995.
- [Kapp89] F. Kappeler, H. Beer, and K. Wisshak. s-process nucleosynthesis-nuclear physics and the classical model. *Rep. Progr. Phys.* 52, page 945, 1989.
- [Schi03c] et al. K.D. Schilling. Beam separation magnet of the bremsstrahlung facility at elbe. *Wissenschaftlich-Technische Berichte FZR-372*, page 33, 2003.
- [Kirc93] E. Kirchuk, P. Federman, and S. Pittel. Nuclear deformation in the mass-80 and mass-100 regions. *Phys. Rev. C* 47, page 567, 1993.
- [Knei92] U. Kneissl. Parity Assignments in Photon Scattering Using Compton Polarimeters. *Prog. Part. Nucl. Phys.* 28, page 331, 1992.
- [Knei96] U. Kneissl, H.H. Pitz, and A. Zilges. Investigation of Nuclear Structure by Resonance Fluorescence Scattering. *Prog. Part. Nucl. Phys.* 37, page 349, 1996.
- [Koni04] A.J. Koning, S. Hilaire, and M.C. Duijvestijn. TALYS: Comprehensive nuclear reaction modeling. *Proc. Int. Conf. Nucl. Data for Science and Technology - ND2004, Sep. 26 - Oct. 1, 2004, Santa Fe, USA*, 2004.
- [Kran88] Kenneth S. Krane. *Introductory Nuclear Physics*. John Wiley and Sons, 1988.
- [Kran75] K.S. Krane.  $E2$ ,  $M1$  multipole mixing ratios in even-even nuclei,  $A \geq 152$ . *At. Data Nucl. Data Tables* 16, page 383, 1975.
- [Lanz51] L.H. Lanzl and A.O. Hanson.  $Z$  Dependence and Angular Distribution of Bremsstrahlung from 17-Mev Electrons. *Phys. Rev.* 83, page 959, 1951.
- [LoIu78] N. Lo Iudice and F. Palumbo. New Isovector Collective Modes in Deformed Nuclei. *Phys. Rev. Lett.* 41, page 1532, 1978.
- [LoIu01] N. Lo Iudice, A.V. Sushkov, and N.Yu. Shirikova.  $M1$  spin excitations in deformed nuclei within a microscopic multiphonon approach. *Phys. Rev. C* 64, page 054301, 2001.
- [Mant01] P.F. Mantica, A.E. Stuchbery, D.E. Groh, J.I. Prisciandaro, and M.P. Robinson.  $g$  factors of the first  $2+$  states in the transitional  $^{92,94,96,98,100}\text{Mo}$  isotopes and the onset of collectivity. *Phys. Rev. C* 63, page 034312, 2001.
- [May51] M. May and G.C. Wick. On the Production of Polarized High Energy X-Rays. *Phys. Rev.* 81, page 628, 1951.
- [Metz59] F. R. Metzger. Resonance fluorescence in nuclei. *Prog. Nucl. Phys.* 7, page 54, 1959.
- [Metz77] F.R. Metzger. Lifetimes of excited states of  $^{92}\text{Mo}$ . *Phys. Rev. C* 15, page 193, 1977.
- [Moel86] P. Möller and J.R. Nix. Atomic masses and nuclear ground-state deformations calculated with a new macroscopic-microscopic model. *At. Data Nucl. Data Tables* 26, page 165, 1981.
- [More93] R. Moreh, O. Beck, I. Bauske, R.D. Heil, U. Kneissl, J. Margraf, J. Maser, and H.H. Pitz. Precise widths of the 3089 and 3684 keV levels in  $^{13}\text{C}$ . *Phys. Rev. C* 48, page 2625, 1993.



- [Nest02] V.O. Nesterenko, J. Kvasil, and P.-G. Reinhard. Separable random phase approximation for self-consistent nuclear models. *Phys. Rev. C* 66, page 044307, 2002.
- [Nils95] S.G. Nilsson and I. Ragnarsson. *Shapes and Shells in Nuclear Physics*. Cambridge University Press, Cambridge, 1995.
- [Noja90] R. Nojarov and A. Faessler. Lo-collective scissors mode. *Z. Phys. A* 336, page 151, 1990.
- [Piet95] N. Pietralla, I. Bauske, O. Beck, P. von Brentano, W. Geiger, R.-D. Herzberg, U. Kneissl, J. Margraf, J. Maser, H.H. Pitz, and A. Zilges. Absolute level widths in  $^{27}\text{Al}$  below 4 MeV. *Phys. Rev. C* 51, page 1021, 1995.
- [Piet02] N. Pietralla, Z. Berant, V.N. Litvinenko, S. Hartman, F.F. Mikhailov, I.V. Pinayev, G. Swift, M.W. Ahmed, J.H. Kelley, S.O. Nelson, R. Prior, K. Sabourov, A.P. Tonchev, and H.R. Weller. Parity Measurements of Nuclear Levels Using a Free-Electron-Laser Generated  $\gamma$ -Ray Beam. *Phys. Rev. Lett* 88, page 12502, 2002.
- [Piet99] N. Pietralla, C. Fransen, D. Belic, P. von Brentano, C. Friebner, U. Kneissl, A. Linnemann, A. Nord, H.H. Pitz, T. Otsuka, I. Schneider, V. Werner, and I. Wiedenhöver. Transition Rates between Mixed Symmetry States: First Measurement in  $^{94}\text{Mo}$ . *Phys. Rev. Lett.* 83, page 1303, 1999.
- [Port56] C.E Porter and R.G. Thomas. Fluctuations of Nuclear Reaction Widths. *Phys. Rev.* 104, page 483, 1956.
- [Preu05] St. Preusche, F. Wüst, K.D. Schilling, N. Dohn, and H. Roß. Production of  $^{86}\text{Y}$  and  $^{56}\text{Co}$  at the Rossendorf PET cyclotron “CYCLONE 18/9”. *Wissenschaftlich-Technische Berichte FZR-424*, page 74, 2005.
- [Radf95] D. C. Radford. ESCL8R and LEVIT8R: Software for interactive graphical analysis of HPGe coincidence data sets. *Nucl. Instr. Meth. A* 361, page 297, 1995.
- [Raus04] T. Rauscher and F.-K. Thielemann. Predicted cross-sections for photon-induced particle emission. *At. Data Nucl. Data Tables* 88, page 1, 2004.
- [Rega03] P.H. Regan, C.W. Beausang, N.V. Zamfir, R.F. Casten, Jing-ye Zhang, A.D. Yamamoto, M.A. Caprio, G. Gürdal, A.A. Hecht, C. Hutter, R. Krücken, S.D. Langdown, D.A. Meyer, and J.J. Ressler. Signature for Vibrational to Rotational Evolution Along the Yrast Line. *Phys. Rev. Lett.* 90, page 152502, 2003.
- [Rich95] A. Richter. Probing the nuclear magnetic dipole response with electrons, photons and hadrons. *Prog. Part. Nucl. Phys.* 34, page 261, 1995.
- [Rick88] L. Ricken. *Der Strahlungseinfang Schwerer Ionen - Intermediäre Strukturen und Zerfall von Riesenresonanzen*. Ruhr-Universität Bochum, unpublished, 1988.
- [Ring80] P. Ring and P. Schuck, editors. *The Nuclear Many-Body Problem*. Springer-Verlag, New York, 1980.
- [Roch72] G. Roche, C. Ducos, and J. Proriol. Bremsstrahlung Cross-Section Formula Including a High-Order Coulomb Correction. *Phys. Rev. A* 5, page 2403, 1972.
- [Ruse06] G. Rusev, E. Grosse, A.R. Junghans, R. Schwengner, and A. Wagner. A Monte Carlo Code for  $\gamma$ -ray Cascade Simulations in Photon-Induced Reactions. *Wissenschaftlich-Technische Berichte FZR-442*, page 29, 2006.

- [Ruse04b] G. Rusev, A.R. Junghans, A. Wagner, and R. Beyer. Deconvolution of Bremsstrahlung Spectra Measured by Means of a NaI Detector. *Wissenschaftlich-Technische Berichte FZR-401*, page 10, 2004.
- [Ruse05] G. Rusev, R. Schwengner, F. Dönau, S. Frauendorf, L. Käubler, L.K. Kostov, S. Mallion, K.D. Schilling, A. Wagner, E. Grosse, H. von Garrel, U. Kneissl, C. Kohstall, M. Kreutz, H.H. Pitz, M. Scheck, F. Stedile, P. von Brentano, J. Jolie, A. Linnemann, N. Pietralla, and V. Werner. Decay of  $1^+$  States as a New Probe of the Structure of  $0^+$  Shape Isomers. *Phys. Rev. Lett.* *95*, page 062501, 2005.
- [Ruse04a] G. Rusev, R. Schwengner, K.D. Schilling, A. Wagner, L. Käubler, F. Dönau, S. Mallion, E. Grosse, A.R. Junghans, M. Erhard, W. Schulze, and A. Hartmann. The Bremsstrahlung Facility at the ELBE Accelerator. *BgNS Transactions* *9*, page 173, 2004.
- [Ruse03] G. Rusev, R. Schwengner, A. Wagner, L. Käubler, F. Dönau, and E. Grosse. Collimators for the BGO Escape-Suppression Shields. *Wissenschaftlich-Technische Berichte FZR-372*, page 29, 2003.
- [Saka89] H. Sakamoto and T. Kishimoto. Self-consistent effective interactions in nuclei : (I). Doubly-stretched multipole interactions in deformed nuclei. *Nucl. Phys. A* *501*, page 205, 1989.
- [Sarr93] P. Sarriguren, E. Moya de Guerra, R. Nojarov, and A. Faessler. M1 spin strength distribution in  $^{154}\text{Sm}$ . *J. Phys. G* *19*, page 291, 1993.
- [Schi51] L.I. Schiff. Energy-Angle Distribution of Thin Target Bremsstrahlung. *Phys. Rev.* *83*, page 252, 1951.
- [Schi04] K.D. Schilling, F. Dönau, M. Erhard, E. Grosse, A. Hartmann, K. Heidel, A.R. Junghans, K. Kosev, M. Langer, T. Riedel, G. Rusev, W. Schulze, R. Schwengner, A. Wagner, U. Wolf, and B. Wustmann. Improvements of the Bremsstrahlung Facility at ELBE. *Wissenschaftlich-Technische Berichte FZR-401*, page 5, 2004.
- [Schi03a] K.D. Schilling, F. Dönau, E. Grosse, L. Käubler, R. Schwengner, A. Wagner, B. Wustmann, U. Lehnert, A. Nowak, B. Rimarzig, and R. Schlenk. Radiator for the Production of Bremsstrahlung at ELBE. *Wissenschaftlich-Technische Berichte FZR-372*, page 30, 2003.
- [Schi02a] K.D. Schilling, F. Dönau, L. Käubler, A. Wagner, W. Neumann, Th. Riedel, and R. Schlenk. Bremsstrahlung Collimator for the NRF Set-Up at ELBE. *Wissenschaftlich-Technische Berichte FZR-341*, page 37, 2002.
- [Schi03b] K.D. Schilling, U. Lehnert, F. Herbrand, R. Schwengner, A. Wagner, B. Caspar, M. Langer, T. Riedel, and A. Wagner II. Steering Magnets for the Production of Polarized Bremsstrahlung at ELBE. *Wissenschaftlich-Technische Berichte FZR-372*, page 31, 2003.
- [Schi02b] K.D. Schilling, A. Wagner, F. Dönau, L. Käubler, R. Schwengner, W. Neumann, and R. Schlenk. Beam Shutter and Hardener for the NRF Set-Up at ELBE. *Wissenschaftlich-Technische Berichte FZR-341*, page 41, 2002.
- [Schl94] B. Schlitt, U. Maier, H. Friedrichs, S. Albers, I. Bauske, P. von Brentano, R.D. Heil, R.-D. Herzberg, U. Kneissl, J. Margraf, H.H. Pitz, C. Wesselborg, and A. Zilges. A sectored Ge-Compton polarimeter for parity assignments in photon scattering experiments. *Nucl. Instr. Meth. A* *337*, page 416, 1994.
- [Schw05] R. Schwengner, R. Beyer, F. Dönau, E. Grosse, A. Hartmann, A.R. Junghans, S. Mallion, G. Rusev, K.D. Schilling, W. Schulze, and A. Wagner. The photon-scattering facility at the superconducting electron accelerator ELBE. *Nucl. Instr. Meth. A* *555*, page 211, 2005.

- [Schw03] R. Schwengner, L. Käubler, M. Langer, G. Rusev, W. Schulze, and A. Wagner. Detector Setup for Nuclear-Resonance-Fluorescence Experiments at ELBE. *Wissenschaftlich-Technische Berichte FZR-372*, page 27, 2003.
- [Schw02] R. Schwengner, H. Sharma, and A. Wagner. A Polarisation Monitor for Experiments with Bremsstrahlung at ELBE. *Wissenschaftlich-Technische Berichte FZR-341*, page 39, 2002.
- [Selt85] S.M. Seltzer and M.J. Berger. Bremsstrahlung spectra from electron interactions with screened atomic nuclei and orbital electrons. *Nucl. Instr. Meth. B 12*, page 95, 1985.
- [Shod75] H. Shoda, K. Miyase, M. Sugawara, T. Saito, S. Oikawa, A. Suzuki, and J. Uegaki.  $(\gamma, p)$  cross sections and isospin splitting of the giant dipole resonance in  $N = 50$  nuclei. *Nucl. Phys. A 239*, page 397, 1975.
- [Sieg65] Kai Siegban, editor. *Alpha-, Beta- and Gamma-Ray Spectroscopy*. North-holland publishing company, 1965.
- [Sing97] B Singh. Nuclear Data Sheets for  $A = 100$ . *Nucl. Data Sheets 81*, page 1, 1997.
- [Solo97] V.G. Soloviev, A.V. Sushkov, and N.Yu. Shirikova. Low-energy dipole  $\gamma$ -ray transition rates in even-even deformed nuclei. *Phys. Rev. C 56*, page 2528, 1997.
- [Take71] H. Taketani, M. Adachi, M. Ogawa, K. Ashibe, and T. Hattori.  $0^+$  States in Mo Isotopes from  $(p, t)$  Reactions and Anomalies in the New Transitional Region. *Phys. Rev. Lett. 27*, page 520, 1971.
- [Theu90] J. Theuerkauf, S. Esser, S. Krink, M. Luig, N. Nicolay, O. Stuch, and H. Wolter. Program Tv. *Institute for Nuclear Physics, Cologne*, 1990.
- [Utsu05] H. Utsunomiya, S. Goko, K. Soutome, N. Kumagai, and H. Yonehara. Ten-tesla superconducting wiggler at SPring-8 as a photon source for nuclear astrophysics. *Nucl. Inst. Meth. A 538*, page 225, 2005.
- [Egid05] T. von Egidy and D. Bucurescu. Systematics of nuclear level density parameters. *Phys. Rev. C 72*, page 044311, 2005.
- [Wagn05a] A. Wagner, R. Beyer, M. Erhard, F. Dönau, E. Grosse, A. Hartmann, A.R. Jung-hans, L. Käubler, K. Kossev, S. Mallion, C. Nair, N. Nankov, G. Rusev, K.D. Schilling, W. Schulze, and R. Schwengner. The new bremsstrahlung facility at the superconducting electron accelerator ELBE. *J. Phys. G 31*, page S1969, 2005.
- [Wagn99] A. Wagner, F. Dönau, E. Grosse, L. Käubler, K.D. Schilling, H. Schnare, and R. Schwengner. Considerations for the Bremsstrahlung-Photon Radiator at ELBE. *Wissenschaftlich-Technische Berichte FZR-271*, page 33, 1999.
- [Wagn01a] A. Wagner, F. Dönau, E. Grosse, L. Käubler, K.D. Schilling, R. Schwengner, and W. Schulze. A Beam Dump for Energetic Photons. *Wissenschaftlich-Technische Berichte FZR-319*, page 40, 2001.
- [Wagn05b] A. Wagner, P. Evtushenko, F. Herbrand, R. Jainsch, and K. Leege. An Interface for Online Beam Parameters at ELBE. *Wissenschaftlich-Technische Berichte FZR-423*, page 27, 2005.
- [Wagn01b] A. Wagner, S. Fan, H.W. Barz, E. Grosse, and R. Schwengner. Calculating the Spectral Distribution of Bremsstrahlung. *Wissenschaftlich-Technische Berichte FZR-319*, page 38, 2001.

- [Wagn02] A. Wagner, E. Grosse, and S. Mallion. Determination of the Spectral Distribution of the Bremsstrahlung Beam at ELBE. *Wissenschaftlich-Technische Berichte FZR-341*, page 38, 2002.
- [Weiz34] C. F. v. Weizsäcker. Ausstrahlung bei Strößen sehr schneller Elektronen. *Z. Physik* 88, page 612, 1934.
- [Wern02] V. Werner, D. Belic, P. von Brentano, C. Fransen, A. Gade, H. von Garrel, J. Jolie, U. Kneissl, C. Kohstall, A. Linnemann, A.F. Lisetskiy, N. Pietralla, H.H. Pitz, M. Scheck, K.-H. Speidel, F. Stedile, and S.W. Yates. Proton-neutron structure of the  $N = 52$  nucleus  $^{92}\text{Zr}$ . *Phys. Lett. B* 550, page 140, 2002.
- [Wint94] G. Winter, R. Schwengner, J. Reif, H. Prade, J. Döring, R. Wirowski, N. Nicolay, P. von Brentano, H. Grawe, and R. Schubart. Excited states built on the  $6^-$  isomer in  $^{86}_{37}\text{Rb}_{49}$ . *Phys. Rev. C* 49, page 2427, 1994.
- [Wint93] G. Winter, R. Schwengner, J. Reif, H. Prade, L. Funke, R. Wirowski, N. Nicolay, A. Dewald, P. von Brentano, H. Grawe, and R. Schubart. Study of excited states in  $^{85}\text{Kr}$  and  $^{86}\text{Kr}$ : Evidence for neutron-core excitations in  $N = 50$  nucleus  $^{86}\text{Kr}$ . *Phys. Rev. C* 48, page 1010, 1993.
- [Wood92] J.L. Wood, K. Heyde, W. Nazarewicz, M. Huyse, and P. van Duppen. Coexistence in even-mass nuclei. *Phys. Rep.* 215, page 101, 1992.
- [Wood99] J.L. Wood, E.F. Zganjar, C. De Coster, and K. Heyde. Electric monopole transitions from low energy excitations in nuclei. *Nucl. Phys. A* 651, page 323, 1999.
- [Zawi90] D. Zawischa, M. Malcolm, and J. Speth. Magnetic dipole strength functions in heavy deformed nuclei. *Phys. Rev. C* 42, page 1461, 1990.
- [Zawi91] D. Zawischa and J. Speth. Low energy orbital magnetic dipole excitations of heavy non-spherical nuclei. *Z. Phys. A* 339, page 97, 1991.
- [Ziel02] M. Zielińska, T. Czosnyka, J. Choiński, J. Iwanicki, P. Napiorkowski, J. Srebrny, Y. Toh, M. Oshima, A. Osa, Y. Utsuno, Y. Hatsukawa, J. Katakura, M. Koizumi, M. Matsuda, T. Shizuma, M. Sugawara, T. Morikawa, H. Kusakari, A.D. Efimov, and V.M. Mikhajlov. Electromagnetic structure of  $^{98}\text{Mo}$ . *Nucl. Phys. A* 712, page 3, 2002.
- [Ziel05] M. Zielińska, T. Czosnyka, K. Wrzosek, J. Choiński, Y. Hatsukawa, J. Iwanicki, M. Koizumi, H. Kusakari, M. Matsuda, T. Morikawa, Napiorkowski, P.J., A. Osa, M. Oshima, T. Shizuma, J. Srebrny, M. Sugawara, and K. Zajac. Shape Coexistence in Even-Even Mo Isotopes Studied via Coulomb Excitation. *Acta Phys. Pol. B* 36, page 1289, 2005.
- [Zilg02] A. Zilges, S. Volz, M. Babilon, T. Hartmann, P. Mohr, and K. Vogt. Concentration of electric dipole strength below the neutron separation energy in  $N = 82$  nuclei. *Phys. Lett. B* 542, page 43, 2002.
- [Zwar85] D. Zwarts. RITSSCHIL, a new program for shell-model calculations. *Comput. Phys. Commun.* 38, page 365, 1985.

# Erklärung

Hiermit versichere ich, daß ich die vorliegende Arbeit ohne unzulässige Hilfe Dritter und ohne Benutzung anderer als der angegebenen Hilfsmittel angefertigt habe. Die als fremde Quellen direkt oder indirekt übernommenen Gedanken sind als solche kenntlich gemacht. Die Arbeit wurde bisher weder im Inland noch im Ausland in gleicher oder ähnlicher Form einer anderen Prüfungsbehörde vorgelegt. Die vorliegende Arbeit wurde am Forschungszentrum Rossendorf bei Dresden unter der wissenschaftlichen Betreuung von Prof. E. Grosse und Dr. R. Schwengner angefertigt.

*Dresden*  
*den 21. August 2006*

Gencho Y. Rusev